Flow characteristics in straight compound channels with vegetation along the main channel

Flow Characteristics in Straight Compound Channels with Vegetation along the Main Channel

Benoît Terrier

Department of Civil and Building Engineering

Loughborough University

Submitted in partial fulfillment of the requirements
for the award of Doctoral Thesis

Abstract

This study investigates the complex flow structure generated by riparian emergent vegetation along the edge of floodplain. Detailed velocity and boundary shear stress measurements were carried out for various arrangements of emergent rigid cylindric rods of 3 mm, 6 mm and 9 mm diameters and for three different rod densities. In addition, the impact of foliage on the flow field was assessed during a series of experiments where brushes were used instead of smooth rods. The results of these new experiments are first presented.

In addition to the laboratory data, field data was obtained through Acoustic Doppler Current Profiler measurements for two flood events in a stretch of the river Rhône that can be approximated to a straight compound channel with vegetated banks. The analysis of the flow structure highlights the presence of strong secondary circulation and increased vorticity on the river banks.

The rods on the edge of the floodplain increase significantly flow resistance, reducing velocity and decreasing boundary shear stress. Flow rate was seen to decrease with increasing vegetative density for all cases except when foliage was added. This suggests that an optimum threshold density, for which a smaller density would lead to an increased flow rate might exist.

Wakes trailing downstream of the vegetation stem, planform coherent structures advected between the main channel and the floodplain, and eddying motion in the flow due to enhanced turbulence anisotropy are among the defining patterns observed in the studied compound channel flows with one line of emergent vegetation along the edge of the floodplain.

The Shiono and Knight Method (SKM) was modified in order to account for the increased turbulence activity due to the rods. The drag force term was introduced in the same way as in the work of Rameshwaran and Shiono (2007). However, a new term was added to the transverse shear stress term in the form of an Elder formulation, incorporating a friction drag coefficient which can be derived from the experimental data. In this proposed version, the advection term was set to zero. Another version of the SKM, similar to Rameshwaran and Shiono (2007), was also tested with the addition of a local drag friction only applied in the rod region. The proposed SKM version without the advection term was favored as it can be more closely related to the experimental data and to physical processes.

Finally, the capabilities of Telemac-2D were tested against the experimental data for various turbulence models. The Large Eddy Simulation turbulence model highlighted some unsteady flow patterns that were observed during experiments, while satisfactorily predicting the lateral velocity and boundary shear stress distributions.

Keywords: Compound channel, Emergent vegetation, ADCP, Quasi-2D modelling, Large Eddy Simulation, Telemac-2D

Acknowledgments

The undertaking of this thesis has been above all a great human adventure, which would not have been possible without the support and friendship of many.
First, I would like to thank my supervisors at Loughborough University. It has been a privilege to receive the technical supervision from Professor Koji Shiono, who shared his wealth of knowledge and guided me. The depth of his advice and directions helped me to finish on time. I also want to thank Dr Cecil Scott for his helpful discussions, his advice on how to conduct my thesis, particularly at the early stages, and for advising me to use LaTex.

When I joined the Civil and Building Engineering Department of Loughborough, it was my surprise to find that Professor Shiono had a partnership with Cemagref and the team led by Dr André Paquier. This partnership, through the Alliance project, the external supervision of my thesis and my exchange with the Cemagref team has brought a tremendous contribution to my PhD. I would like to express my deepest gratitude to Dr André Paquier for his help with regard to many aspects in my PhD, including his review of my thesis, his advice and his help in making my stays at Cemagref both possible and enjoyable.

I wholeheartedly thank Dr Sébastien Proust for the discussions we had, his wonderful enthusiasm and his encouragements. Perhaps shall we meet on the road again. I offer profound gratitude to Dr Jérome Le Coz for his patience and his willingness to share his expertise on ADCPs and to Yann Peltier for his help in setting up the experiments in LMFA and for welcoming me in Lyon. I am also grateful to Stephanie Moore for the accommodation

she so kindly provided, for her friendship and her warm welcome.

I am indebted to the technical staff of Frank Gibb laboratory, in particular Mike Smeeton, Mick Barker, Barry Carnall, Mick Shonk, Geoffrey Russell and Alex Harrison for their help in setting up my experiments.

I want to thank the LMFA team, especially Dr Nicolas Rivière for granting me permission to carry out experiments in LMFA and for his remarks on my research. I offer thanks to Fabien and Emmanuel for their help during the experiments and Valéry for his good company during my stay.

I would like to acknowledge the Civil Engineering and Building Department of Loughborough University for granting me a studentship. I am particulary grateful to the Learning Fund for the grant I received and to Laura Penrose for her kind help. Likewise, I gladly acknowledge the contributions from the Postgraduate fund and the Royal Academy of Engineering for the grants which allowed me to attend the ICHE 2009 conference in Nagoya and to present my paper there.

I acknowledge the contribution of Dr Xin Sun, who helped me at the start of my thesis. I am also grateful to Dr Didier Bousmar for his advice on the establishment of uniform flow conditions and his work on the ICHE paper and to Dr Bram van Prooijen and Dr Catherine Wilson for our exchange.
I convey sincere appreciation to the HR Wallingford team for the help I received on Telemac-2D, especially Michael Turnbull, Kate Day and Dr Alan Cooper.

It has also been my pleasure to supervise a number of final year students and to work with external visitors, including Ish, Tom, Rebecca, Sam and

Kawanaka. I especially wish to thank Sam for the experiments carried out in the Loughborough University flume.

I thank Network rail for improving the train services during my PhD, Sprint buses of Loughborough for being punctual and Peugeot for manufacturing the good and reliable car that has served me well.

That adventure would not have been the same without those who started with me and have become my friends. Fayaz, Shafi, Nasir and all my Pakistani friends: you have shown me what true Pashto hospitality means. Thank you for the dinners we shared and for the accommodation you so generously provided. Tingting, Clare, Rene, Fiona, Massoud, Keyur: it has been a joy to work alongside you.

Thank you to my friends in WEDC and in Social Sciences. Sophie, James, Pieta, Pippa, Azaghe, Viktor, Dan, Koji. I will not forget what you have taught me about the challenges in the developing world.

I am very grateful to Anne for her help in proofreading this thesis.

Finally, I want to express my deepest feelings of gratitude towards my family for the encouragement they have given me. My wonderful parents have greatly contributed to my scientific curiosity and enthusiasm. I cannot have strong enough words of praise for my wife Stéphanie and her continued help and patience during those three years. Without her support, this project would not have been possible. Our two sons Raphaël and Timothée and their beautiful smiles have been my rays of sun. To Stéphanie, Raphaël and Timothée: *"merci d'être very very very formidables"*.

Contents

List of Tables

List of Figures

List of Symbols

Acronyms:

$ADCP$	Acoustic Doppler Current Profiler
CCD	Charge-Coupled Device
CNR	Compagnie Nationale du Rhône
$C-W$	Colebrook-White
FCF	Flood Channel Facility
ISM	Independent Subsection Method
LDA	Laser Doppler Anemometry
$LMFA$	Laboratory of Fluid Mechanics and Acoustics
LDV	Laser Doppler Velocimetry
LES	Large Eddy Simulation
$LS-PIV$	Large Scale - Particle Image Velocimetry
ODE	Ordinary Differential Equation
PIV	Particle Image Velocimetry
$RANS$	Reynolds-Averaged Navier Stokes (RANS) modelling
$SIMPLE$	Semi-Implicit Method for Pressure-Linked Equations
SKM	Shiono and Knight Method
UCL	Catholic University of Louvain-la-Neuve

Variables and coefficients:

A	Total cross-sectional area of channel $[m^2]$
A_P	Projected area on vegetation $[m^2]$
B	Total width of channel $[m]$
B_{mc}	Main channel width $[m]$

B_{fp}	Floodplain width $[m]$
B_{ss}	Width of main channel sideslope $[m]$
C_f	Friction coefficient [-]
C_D	Drag coefficient [-]
C_μ	Coefficients in the $k-\epsilon$ model [-]
C_r	Courant number [-]
C_s	Smagorinsky constant [-]
$C_{1\epsilon}$	Coefficients in the $k-\epsilon$ model [-]
$C_{2\epsilon}$	Coefficients in the $k-\epsilon$ model [-]
d	External diameter of the dynamic tube for Preston tube $[m]$
D_r	Relative depth [-]
D	Rod diameter $[m]$
f	Darcy-Weisbach friction coefficient [-] or frequency [Hz]
f_d	Drag friction factor [-]
f_{max}	Frequency of peaks in power spectrum (FFT analysis) or Threshold frequency [Hz]
F_D	Drag force $[N]$
g	Gravitational acceleration $[m/s^2]$
h_{fp}	Floodplain height $[m]$
H	Water depth in single channel $[m]$
$H(y)$	Local water depth at lateral position y $[m]$
H_{fp}	Water depth in the floodplain $[m]$
H_{mc}	Total water depth in the main channel $[m]$
H_m	Mean Water depth in the main channel and floodplain $[m]$
k	Turbulent kinetic energy $[m^2/s^2]$
k_{max}	Maximum kinematic wave number $[m^{-1}]$
k_s	Roughness height $[m]$
L	Distance between two rods, from center to center $[m]$
n	Manning's n friction coefficient $[s/m^{1/3}]$
N	Number of rods or trees [-]
P	Wetted perimeter $[m^2/s^3]$

P_t	Production term of turbulence $[m]$
Q	Total flow in channel $[m^3/s]$
Q_{fp}	Total flow in floodplain $[m^3/s]$
Q_{mc}	Total flow in main channel $[m^3/s]$
R	Hydraulic radius $[m]$
Re	Reynolds number [-]
Re_{rod}	Rod Reynolds number [-]
s	Sideslope of main channel [-]
$\|\overline{S}\|$	Filtered-field deformation tensor $[s^{-1}]$
S_0	Bed slope [-]
S_f	Friction slope [-]
S_F	Shading factor [-]
S_t	Strouhal number [-]
T_{ij}	Sub-grid stress tensor tensor $[m^2/s^2]$
u	Turbulent perturbation of longitudinal velocity $[m/s]$
U_d	Depth-averaged longitudinal velocity $[m/s]$
U_D	Apparent drag velocity $[m/s]$
$U_{Left\ wall}$	Depth-averaged longitudinal velocity on left wall $[m/s]$
U_{max}	Maximum longitudinal velocity $[m/s]$
$U_{Right\ wall}$	Depth-averaged longitudinal velocity on right wall $[m/s]$
U_*	Shear velocity $[m/s]$
v	Turbulent perturbation of transverse velocity $[m/s]$
V	Voltage of pressure transducer $[V]$
V_d	Depth-averaged transverse velocity $[m/s]$
V_{max}	Maximum transverse velocity $[m/s]$
w	Turbulent perturbation of vertical velocity $[m/s]$
x	Cartesian coordinate, longitudinal directions $[m]$
x^*	$log_{10}\left[\frac{\Delta P d^2}{4\rho\nu^2}\right]$ $[-]$
X	Longitudinal distance from inlet $[m]$
y	Cartesian coordinate, transverse directions $[m]$

y^*	$log_{10}\left[\frac{\tau_B d^2}{4\rho\nu^2}\right]$ $[-]$
z	Cartesian coordinate, vertical directions $[m]$
z_w	Water level $[m]$
α_x	Longitudinal dimensionless dispersion coefficient $[-]$
α_y	Transversal dimensionless dispersion coefficient $[-]$
β	Proportionality constant $[-]$
δ	Width of shear layer $[m]$
ΔP	Pressure difference recorded by the pressure transducer $[N/m^2]$
Δl	Characteristic sub-grid scale $[m]$
ϵ	Energy dissipation rate $[m^2/s^3]$
ϵ_d	Turbulent drag eddy viscosity $[m^2/s]$
$\overline{\epsilon_{tb}}$	Depth-averaged bottom turbulence eddy viscosity $[m^2/s]$
$\overline{\epsilon_{ts}}$	Depth-averaged transverse turbulence eddy viscosity $[m^2/s]$
ϵ_{se}	Sub-grid eddy viscosity $[m^2/s]$
ϵ_t	Turbulent eddy viscosity $[m^2/s]$
$\overline{\epsilon_t}$	Depth-averaged turbulent eddy viscosity $[m^2/s]$
Γ	Advection term or secondary current term in SKM $[N/m^2]$
κ	Von Karman constant [-]
λ	Dimensionless eddy viscosity coefficient [-]
η	Kolmogoroff's microscale $[m]$
ν	Kinematic fluid viscosity $[m^2/s]$
ν_t	Turbulent eddy viscosity $[m^2/s]$
ν_x	Longitudinal diffusion coefficient $[m^2/s]$
ν_y	Transverse diffusion coefficient $[m^2/s]$
ρ	Fluid density $[kg/m^3]$
τ_B	Bed shear stress $[N/m^2]$
τ_{Bmean}	Average bed shear stress $[N/m^2]$
$\tau_{b,x}$	Longitudinal component of bed shear stress $[N/m^2]$
$\tau_{b,y}$	Transverse component of bed shear stress $[N/m^2]$
τ_{xy}	Reynolds shear stress transverse component $[N/m^2]$

$\overline{\tau_{xy}}$	Depth-averaged Reynolds shear stress transverse component $[N/m^2]$
$\overline{\tau_{as}}$	Depth-averaged apparent shear stress $[N/m^2]$
ω	Longitudinal vorticity $[s^{-1}]$

CHAPTER 1

Introduction

"There is a willow grows aslant a brook
That shows his hoar leaves in the glassy stream;" Hamlet, Shakespeare

1.1 The Main Channel - Floodplain Ensemble in Floods

Flood disasters are responsible for approximately a third of the financial losses due to natural disasters throughout the world and account for more than half of the fatalities. Analyses of the trends in the occurrence of disasters suggest that these figures have been increasing significantly in recent years (Berz, 2000). In the twentieth century, river engineers tended to resort to hard and heavy engineering solutions in order to mitigate the effects of flooding (Purseglove, 1988). Most of these solutions consisted in attempts to contain the flow in river channels and typically took the form of embankments, channel straightening or detention reservoirs. However, such methods often failed to fulfil their objectives. Floodplains, which had been developed, continued to flood in spite of costly flood alleviation schemes. A more open approach to flood control focusing on the main channel - floodplain ensemble rather than solely the main channel began to be advocated (Islam, 2001).

In the UK, the DEFRA policy"Making Space for Water", initiated in 2003, is a step towards a more sustainable use of floodplains. The vital role of floodplains in

flood alleviation strategies is recognised and the re-creation of natural floodplains is being promoted. For flood engineers, a prerequisite to applying this policy is a sound understanding of the hydrodynamic processes that link a floodplain to its channel.

The flow interaction between a river channel and its floodplain is complex. At a discharge high enough for the adjacent plains to be inundated, the main channel flow and the floodplain flow together generate a complicated flow structure. In practice, the modelling of such typically three-dimensional flow structures, for example for design purposes, usually has to be simplified. Research in open channel hydraulics and fluid mechanics has contributed to an increase in the understanding of compound channel flows, providing valuable models to river engineers.

1.2 Influence of Vegetation along the Main Channel

Traditionally, the presence of vegetation on the floodplain has been regarded by flood engineers as a problem which hinders flow capacity. Yet, the ecological role of riparian vegetation is very much recognised. Today, river engineers are encouraged to preserve vegetation found in river banks and floodplains.

The presence of vegetation within the floodplain, however, adds an additional degree of complexity into the analysis of compound channel flows. The magnitude of drag force exerted by flow on the plants is such that it generally cannot be neglected when dealing with the modelling of main channel - floodplain ensembles. Observations of river banks reveal that one-line vegetation growing along the edge of floodplain is a common arrangement. Such vegetation may be trees or bushes of different species and may be spaced in different ways. Figure 1.1 provides a typical illustration in the form of a single array of mature trees, somewhat regularly spaced out, along the left bank of the river Nene in England. A single line of riparian vegetation may be used for bank stabilisation, to promote environmental diversity or for landscape amenity purposes (Hubble *et al.*, 2009). Today however, little is known about the impact of

Figure 1.1: Stretch of the River Nene showing an example of one-line of riparian trees at the interface of a compound channel

such arrangements on the flow structures in the vicinity of such vegetation. In order to bring flood protection and environmental requirements together, a better knowledge of the hydraulic effects of such arrangements is required.

1.3 Research Approach

The high economic, social and political stakes justify the significant amount of research that has been carried out on compound channel hydraulic modelling with and without vegetation on the floodplain, particularly in the second half of the twentieth century. In order to assess a state of the art in vegetated compound channels, a review of the current knowledge in this subject is first summarised in this report. Stemming from this review, a research gap can be identified and detailed objectives can be laid out. The objectives of this thesis are presented in Section 2.7 and are briefly summarized below together with the research approach that has been adopted.

The review of past research studies highlights the lack of experimental data on the impact of one line emergent vegetation on the edge of floodplain. In particular, boundary shear stress measurements for this type of configuration are rare. Yet, data collection is of primary importance in order to understand the hydraulic behaviour if pertinent hydraulic models are to be tested or developed. Therefore, a robust experimental data set composed of velocity and boundary shear stress measurements needs to be collected. To set up the relevant experiments, vegetation needs to be scaled into the physical model. Furthermore, such a data set must investigate the influence of key parameters on the flow structure, such as stem diameter, vegetation density, and water depth.

Until recently, the use of Acoustic Doppler Current Profilers (ADCP) was mostly restricted to oceanographic applications. However, technological advances have also enabled velocity measurements in shallower fluvial environments to be obtained during flood events (Muste *et al.*, 2004). Such data sets can now complement laboratory experiments in providing insight into the hydraulics of rivers. In this research, ADCP measurements carried out during two flood events in the river Rhône in France were obtained in a stretch of the river that can be approximated to a straight compound channel.

The analysis of the data sets collected through laboratory and field work studies established the main characteristics of the studied flows. To complete the synergy between experimental and field investigations, the numerical modeling of the studied flows will be undertaken using the Shiono and Knight Method and Telemac-2D. The quasi two-dimensional modelling through the Shiono and Knight Method requires the modelling of the transverse shear stress term to be reconsidered to better account for the effect of drag force. Telemac-2D is a numerical package widely used both in research and in the industry. However, its ability to model flows in vegetated compound channels remains largely untested. In particular, the relevance of the different turbulence models in the Telemac-2D code needs to be assessed. The large eddy simulation turbulence model of Telemac-2D has the potential to model the unsteady patterns present in the

flow field and will therefore be further investigated in the present study.
A typology of the flow patterns observed in the case of one line vegetation on the edge of floodplain may emerge from the analysis of experimental, field and numerical work and conclusions may then be drawn.

1.4 Thesis Structure

The thesis is divided into eight chapters and the scope is succinctly summarised as follows.

In chapter two, the literature on compound channel hydraulics relevant to this thesis is reviewed.

The third chapter describes the experimental set up used in the methodology adopted.

The fourth and fifth chapters describe and provide an analysis of the experimental results obtained in the compound channels of Loughborough University and LMFA respectively.

Chapter six presents field data obtained from the ADCP measurements in the Rhone River as well as the results and findings.

Chapter seven is a presentation of theoretical developments and quasi two-dimensional modelling using the Shiono and Knight Method. The results of the numerical modelling using Telemac-2D are also presented.

Finally, the conclusions of this study are summarised and some further research is suggested in Chapter eight.

CHAPTER 2

Literature Review

"There is no part of hydrodynamics more perplexing to the student than that which treats the resistance of fluids". Lord Rayleigh (1876)

2.1 Introduction

The main focus of this research is the study of flows in straight compound channels in presence of one-line rigid emergent vegetation along the edge of floodplain. In order to reach an understanding of the intricate flow characteristics observed in this type of flow, it is necessary to comprehend cases of intermediate complexity, namely the inbank and overbank flow cases without vegetation. Hence, the main patterns of straight simple and compound channel flows are briefly summarised in this Chapter.

Numerous studies have focused on the impact of emergent floodplain vegetation on compound channel flows. As a result, the significance of such flow resistance on the compound channel flow structure can be well appreciated through selected previous studies, which are then presented.

This study will also benefit from the background understanding of flow behaviour observed in an array of emergent cylinders. Important findings on flow characteristics of such a configuration have primarily been achieved through experimental research and are summarised. Aligned emergent cylinders, however, were mostly studied in straight

rectangular channels. Only a few, recent, studies have focused on the influence of emergent line of vegetation placed along the main channel. The main results of such research are also presented and discussed hereafter.

This Chapter is divided into the reviews of the following aspects that are relevant to the flows studied in this thesis.

- Sections 2.2 and 2.3 present the flow characteristics in straight compound channels for inbank and overbank cases respectively;
- Section 2.4 summarises the flow patterns of straight compound channels in presence of vegetation on the floodplain;
- Research on flow characteristics in an array of aligned cylinders in straight channel is presented in Section 2.5;
- Section 2.6 summarises the flow characteristics in straight compound channels in presence of one-line rigid emergent vegetation along the banks;
- The conclusion of the literature review are drawn and discussed in Section 2.7 so that the research gap is clearly identified, which then leads to the aims and objectives of this study.

2.2 Inbank Flows in Straight Channels

2.2.1 Introduction

In order to understand the more complex hydraulic characteristics of compound channel flow, a basic understanding of inbank flow is necessary. Therefore, the main characteristics of flow in straight inbank channels are briefly reviewed in this section. As illustrated in the next paragraphs, even for a simple geometry such as that of a rectangular channel, open-channel flows are characterized by elaborated flow structures. The aspect ratio, defined as the ratio between the width of the channel (B) and the depth of

the flow (H), has an obvious impact on the hydrodynamic behaviour of open-channel flows.

2.2.2 Longitudinal Velocity Distribution

One of the most interesting aspects of the longitudinal velocity distribution in straight rectangular channels is the unexpected points of inflection in the isovels and the fact that the maximum velocity occurs below the free surface.

The isovels in straight rectangular open-channels bulge towards the sidewalls and the corner due to the presence of secondary currents. Naot and Rodi (1982) investigated numerically the effect of the aspect ratio on the isovels of the longitudinal velocity. This is illustrated in Figure 2.1, which shows how the bulging of the isovels changes with the aspect ratio. The velocity contour lines are also bulged towards the juncture between the sidewall and free surface (Kang and Choi, 2006a). This is caused by inner secondary currents in the vicinity of the juncture.

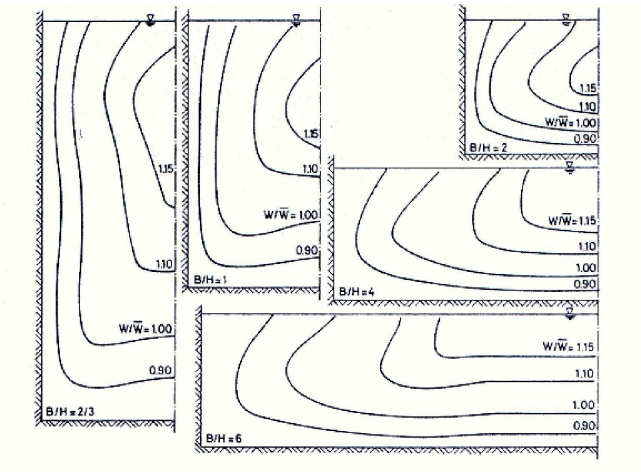

Figure 2.1: Calculated longitudinal velocity contours in open channels under various width-to-depth ratio conditions (after Naot and Rodi 1982)

Thomson (1878) discovered that the maximum velocity occurs below the free surface as early as in 1878. This phenomenon is commonly referred to in literature as "velocity-dip". The mechanisms of generation underlying the "velocity-dip" phenomenon are not well understood. However, it is generally recognized that this phenomenon is caused by the secondary currents occurring in open-channels. The "velocity-dip" is more pronounced for narrow channels (Nezu and Nakagawa, 1993) and for an aspect ratio less than 2, the maximum velocity is located at 60% of the water depth for both subcritical and supercritical flows. On the other hand, for an aspect ratio of 8, Wang and Cheng (2005) observed the velocity-dip near the sidewall region only.

2.2.3 Secondary Currents

Secondary currents are defined as flow normal to the longitudinal flow direction. They affect the longitudinal velocity pattern and boundary shear stress distribution.

Secondary flows have been formally classified into two categories by Prandtl (1952). One is secondary flows of first kind, which are derived from mean flow skewing and by centrifugal forces. The secondary flows of first kind exist either in the laminar or turbulent conditions. Secondary flows of second kind are caused by the transverse non-homogeneity of turbulence and are a result of turbulence anisotropy. They are observed in straight channel or non-circular ducts and can be initiated by sidewall effect, free surface effect or bed variation.

The secondary currents in straight rectangular channels do not usually exceed 3% of the maximal longitudinal mean velocity U_{max} and are typically about 2-3% of U_{max} (James and Wark, 1992; Naot and Rodi, 1982; Tominaga *et al.*, 1991). Nevertheless, their influence on the longitudinal velocity is obvious.
In narrow open-channels with a small aspect ratio (e.g. $\frac{B}{H} < 5$), with a fixed bed, vortices are first observed at the corners because of the sidewalls. These vorticies are stretched in the lateral direction which leads to streamwise vorticies of a scale similar to the water depth H. These secondary flows are referred to as 'corner flows'. This is

illustrated in Figure 2.2.

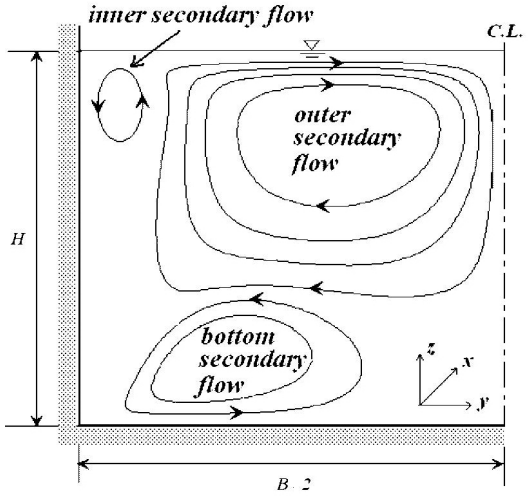

Figure 2.2: Schematic view of secondary flows in open rectangular channel (after Kang and Choi 2006)

Secondary-currents are also observed in straight wide open channels. They are characterized by their counter-rotating flow cells and are termed cellular secondary flows. The cell width is usually of the same range as H.

The importance of the aspect ratio on the secondary current distributions was also investigated by Naot and Rodi (1982). Figure 2.3 shows secondary current streamlines in a rectangular straight open channel for various channel aspect ratios. The vortex near the free surface is stronger than the bottom vortex and transports high momentum from the water surface downwards. The bottom vortex located between bottom and corner bissectors, transports the low momentum fluids from near the walls towards the channel centre. The inner secondary currents described in the previous section are missing. As mentioned, the inner secondary currents are very weak and are difficult to measure and to model even with the most sophisticated turbulent models available (Kang and Choi, 2006a). As the aspect ratio increases, the vortex near the free surface becomes stronger and eventually suppresses the lower bottom vortex. The secondary flow patterns remain similar when the aspect ratio is greater than 4. On the other

hand, the lower vortex becomes dominant when the aspect ratio decreases below 2. When the aspect ratio is smaller than 1, i.e. when the channel is very narrow, the upper vortex eventually splits into smaller weaker vortices.

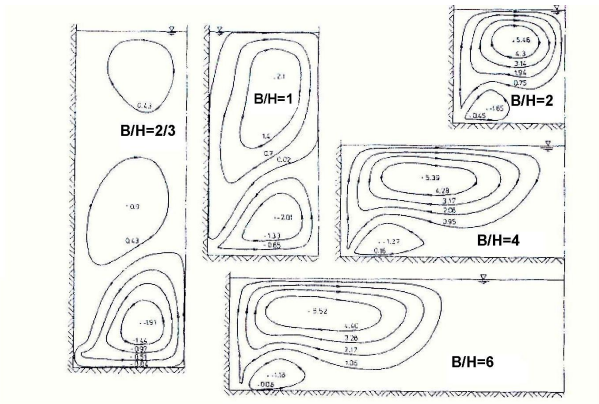

Figure 2.3: Calculated secondary current streamlines in open channels under various width-to-depth ratio conditions (after Naot and Rodi 1982)

Knight *et al.* (2007) investigated the secondary flow distribution in straight trapezoidal channels. A typical distribution of secondary flow is given in Figure 2.4. The number of secondary flow cells was found to be dependant on the aspect ratio. For aspect ratios less than 2.2, the number of secondary cells in a trapezoidal channel was found to be three, two located over the side slope region and one over the flat bed region. For aspect ratios greater than 4, the number of secondary flow cells was found to be four, two located over the side slope region and two over the flat bed region. No experiment for aspect ratio between 2.2 and 4 was available.

2.2.4 Boundary Shear Stress

The distribution of boundary shear stress in the cross-section depends on the turbulent structure of flow and on the roughness and shape of the solid boundaries.

Typical distributions of boundary shear stress in straight rectangular open channels for different aspect ratios are illustrated in Figure 2.5. The waviness of the boundary

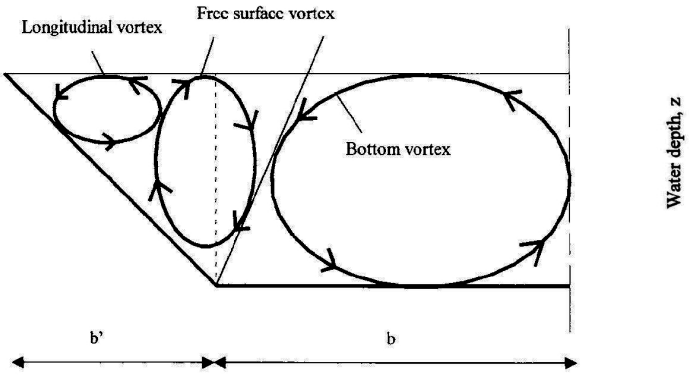

Figure 2.4: Secondary flow cells in half simple trapezoidal channel (from Knight et al. 2007)

shear stress distributions measured by Knight *et al.* (1984) is obvious. It is caused by secondary currents. These secondary currents are controlled by the heterogeneity of the roughness distribution and the shape of the cross-section. This wavy aspect is a characteristic that has led some scientists (Ikeda, 1981) to model these secondary currents using sinusoidal functions to account for that particular distribution.

2.3 Flows in Straight Compound Channels

2.3.1 Introduction

In this section, the main flow characteristics present in straight compound channels are reviewed. In nature, river channels commonly have floodplains that extend laterally away from them. A sound understanding of the flow interaction between a river channel and its floodplain is an essential part of river management, and is a pre-requisite to appreciate the impact of floodplain vegetation on flow structure. Since the 1960s, compound channels have been studied intensively and a brief summary of the main findings is presented below.

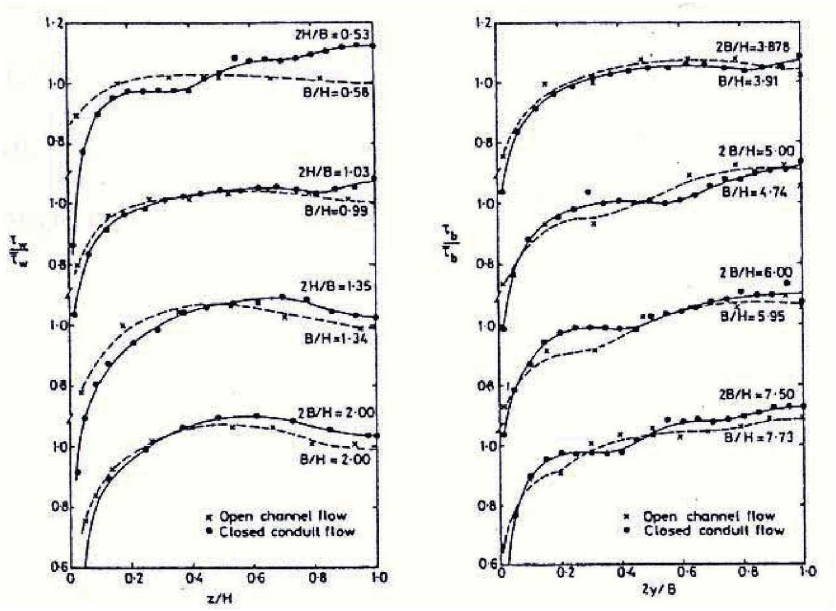

Figure 2.5: Distributions of wall shear stress and bed shear stress in open channels (after Knight et al. 1984)

2.3.2 General Flow Structure and Mechanisms

When the flow in the main channel exceeds bankfull flow, the floodplain becomes inundated. The velocity difference between the deeper and faster main channel flow and the usually rougher and slower floodplain flow leads to the formation of a shear layer near the interface between the main channel and the floodplain. The exchange of momentum taking place between the main channel and the floodplain acts as an apparent shear stress that causes additional resistance to the flow (Myers, 1978).

A complex turbulent flow structure develops and large vertical vortices are observed at the interface between the main channel and the floodplain. This is illustrated in Figure 2.6. These vertical vortices were identified by Sellin (1964) using the photographs of aluminium powder scattered on the water surface and taken by a camera moving downstream at a constant speed. An illustration is provided in Figure 2.7. These vortices transport the high momentum fluid from the main channel towards the floodplain. As a result, the conveyance in the main channel decreases while the conveyance in the adjacent floodplain increases. This phenomenon has been termed “kinematic effect”.

Figure 2.6 also illustrates the helical secondary currents observed in the longitudinal direction of the main channel. These helical secondary currents also contribute to the momentum exchange between the floodplain and the main channel.

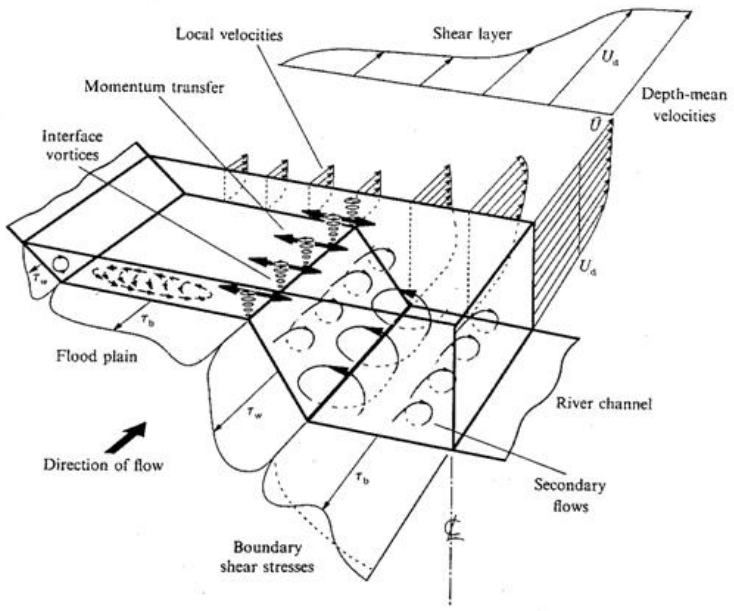

Figure 2.6: Flow structure in a compound channel (after Shiono and Knight, 1991)

The relative depth D_r is defined as the ratio between the floodplain water depth H_{fp} and the main channel water depth H_{mc}. The intensity of the interaction between main channel and the floodplain is highly dependent on the relative depth. Strong interactions have been observed for relative depths comprised between 0.1 and 0.3 (Knight and Shiono, 1996).

2.3.3 Secondary Currents

In compound channels, like in simple straight channels, secondary currents are generated by anisotropic turbulence and their characteristics are influenced by many factors, such as the channel cross-section geometry and aspect ratio, relative depth and turbulence activity (Shiono and Knight, 1991).

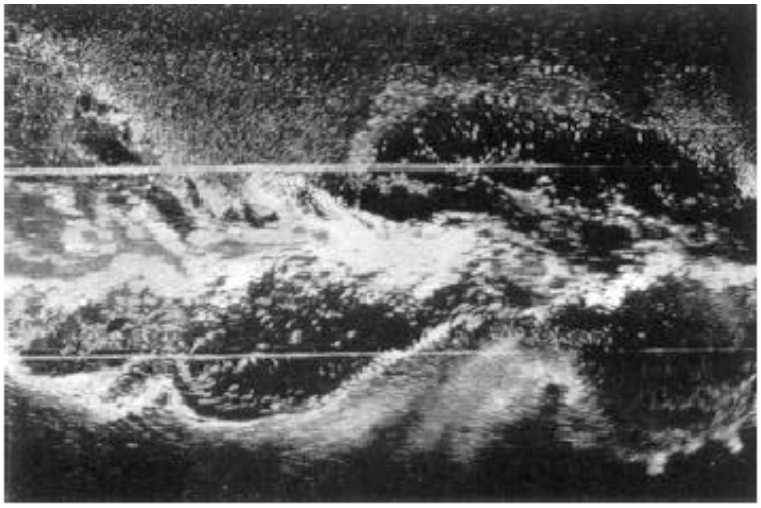

Figure 2.7: Large vortices observed at the interfaces between the main channel and the floodplains of a compound channel (Sellin, 1964)

Tominaga and Nezu (1991) carried out experiments in rectangular compound channels and reported that the size and position of secondary currents is largely dependant upon the channel's geometry. By contrast, floodplain roughness, which was investigated with a roughened floodplain of ks=2 mm, was not found to affect the structure of secondary currents. However, this statement only results from one experiment with a roughened floodplain, carried out in a rectangular compound channel for only one relative depth and would therefore need to be confirmed.

For the shallow case and a relative depth of Dr=0.50, the authors found a pair of secondary currents, namely a main channel and a floodplain vortex, as well as a free surface vortex observed near the sidewall of the main channel. For Dr=0.75, the floodplain vortex appeared stronger and reached the free surface, while secondary currents near the free surface prevailed over the main channel vortex. For Dr=0.25, the main channel vortex stretched laterally.

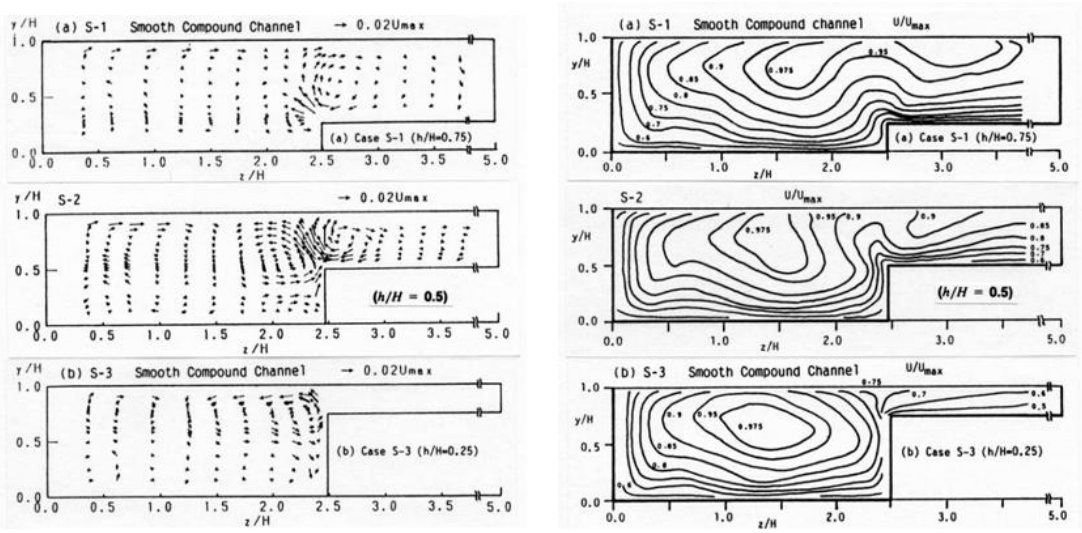

(a) (b)

Figure 2.8: Flow patterns for straight compound channels for different relative water depths (a) Secondary flow circulations (b) corresponding isovels of primary flow velocity

Shiono and Knight (1989) investigated the influence of the shape of the cross-section on the secondary currents in the case of symmetrical wide compound channels. They observed that the flow cell extending across the floodplain existed regardless of the shape of the cross-section. In addition, smaller cells were found in the far corner of the floodplain. Two secondary current cells were located in the rectangular main channel: a larger counter-clockwise cell in the upper part of the main channel and a weaker clockwise cell in the corner. In the trapezoidal channel, one clockwise secondary current cell was located in the main channel while a smaller counter-clockwise cell was observed near the interface between the main channel and the floodplain.

Tominaga and Nezu (1991) found that the magnitude of secondary currents $\sqrt{V^2 + W^2}$ reaches approximately 4 % of the maximum longitudinal velocity U_{max}. This magnitude is stronger than the magnitude of secondary currents observed in the inbank case, which typically reach 2-3 %, as seen in Section 2.2. Despite their somewhat small magnitudes, secondary currents exert some influence on the other hydraulic parameters such as longitudinal velocity (Figure 2.8b), boundary shear stress (Nezu and Nakagawa, 1993) and turbulence (Kang and Choi, 2006b).

2.3.4 Boundary shear stress

The boundary shear stress in straight compound channels has been measured by many researchers (Knight and Demetriou, 1983; Myers and Elsawy, 1975; Shiono and Knight, 1991; Sun, 2006). In these studies, a Preston tube was the instrument used to obtain direct measurements of boundary shear stress. Figure 2.9 shows a typical distribution of boundary shear stresses in shallow, compound channel flows (Yuen, 1989).

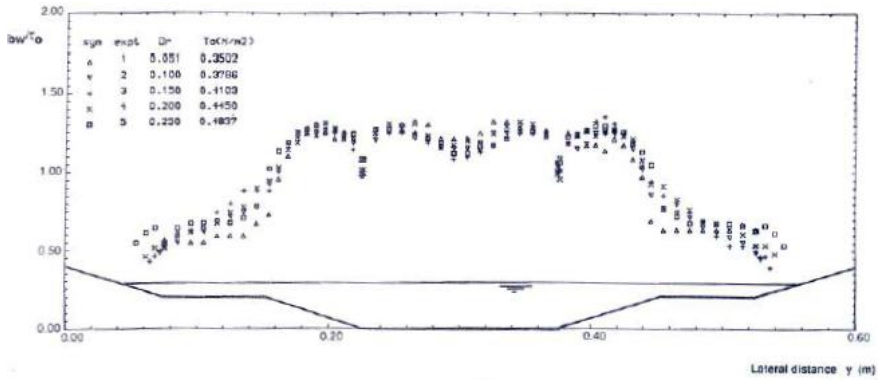

Figure 2.9: Distributions of boundary shear stress in compound trapezoidal channels under various relative water depth conditions (Yuen, 1989)

The measurements were carried out for shallow cases and relative depths varying from 0.051 to 0.250. The values of bed shear stress $\overline{\tau_{bw}}$ normalised by the overall measured boundary shear stress $\overline{\tau_0}$ tend to decrease in the main channel and increase on the floodplain as the relative water depth increases. The waviness in the distributions of boundary shear stress is striking and is generated by the momentum exchange and the complex distribution of secondary current cells (Knight *et al.*, 1994). The bed shear stress τ_B differs from the standard two-dimensional value $\rho g H S_0$ due to the transverse gradient of the apparent shear stress (Shiono and Knight, 1991). The boundary shear stress on the main channel bed is usually observed to be smaller than $\rho g H S_0$ and larger on the floodplain (Tominaga and Nezu, 1991) and (Knight and Shiono, 1996). As early as 1975, Myers and Elsawy (1975) found that the average boundary shear stress in the main channel could reduce by up to 22%, and could increase by up to 200% on the floodplain for low water depth cases in the compound channel compared

with the single channel case. This discrepancy has been attributed to the gradients of the depth-averaged Reynolds stress and the secondary current in the lateral direction (Shiono and Knight, 1991).

The boundary shear stress can be expressed by means of a friction coefficient C_f for two dimensional flows with the following two components:

$$\tau_{b,x} = \frac{1}{2}\rho C_f \sqrt{U_d^2 + V_d^2}|U_d| \tag{2.1}$$

$$\tau_{b,y} = \frac{1}{2}\rho C_f \sqrt{U_d^2 + V_d^2}|V_d| \tag{2.2}$$

where $\tau_{b,x}$ and $\tau_{b,y}$ are the longitudinal and transverse components of the boundary shear stress respectively. Equations 2.1 and 2.2 are widely used in two dimensional numerical models to represent boundary shear stress, the only difference usually lying in the choice of the friction coefficient. Thus, boundary shear stress varies with the streamwise velocity U and friction but is also directly affected by secondary circulation.

2.3.5 Turbulence

The anisotropic turbulence near the interface between the main channel and the floodplain is largely responsible for the generation of secondary currents (Ikeda, 1981). The anisotropy of the turbulence is reflected in the discrepancies between the transversal and vertical turbulent intensities, as seen in Figure 2.10.
The results highlight the complexity of turbulent intensities driven by secondary flows and the anisotropic turbulent behaviour in the junction region. Figure 2.11 shows the distribution of the turbulent kinetic energy (TKE) calculated from the results of Figure 2.10. A high energy containing area that spreads near the edge of the junction can clearly be observed.

Figure 2.12 shows the cross sectional distributions of the Reynolds stresses for various depths under overbank conditions obtained by Shiono and Knight (1991). The relative magnitudes of τ_{yx} to τ_{zx} at the junction for each case suggest that the lateral

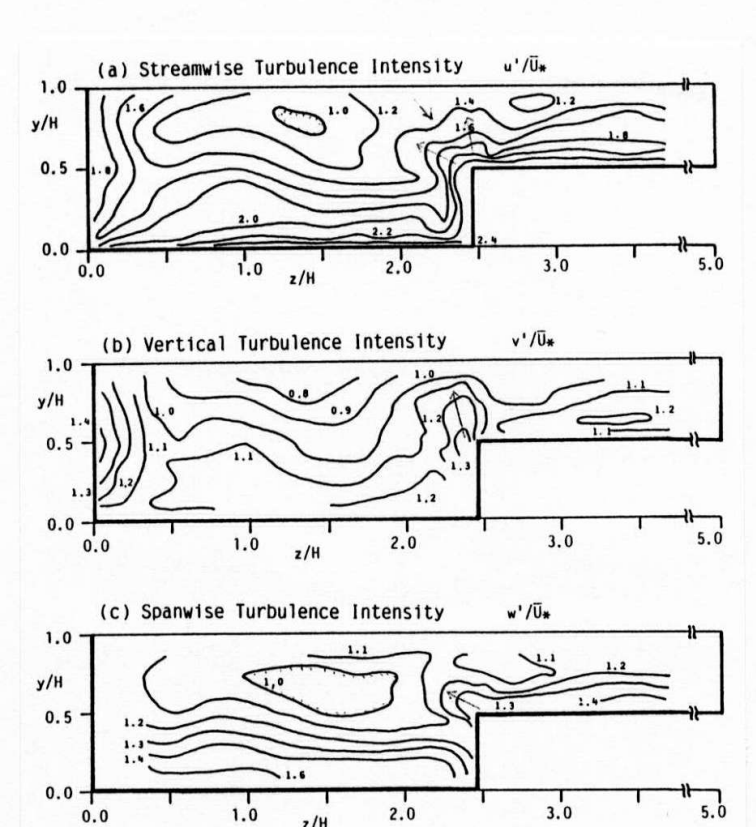

Figure 2.10: Turbulence intensities in a straight compound channel (Tominaga and Nezu, 1991)

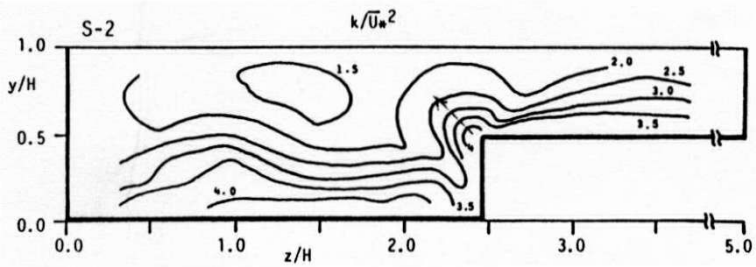

Figure 2.11: Turbulent Kinetic Energy (TKE) in a straight compound channel (Tominaga and Nezu, 1991)

mixing caused by the main channel - floodplain interaction dominates the bed generated vertical mixing and that this interaction is more intense when the depth on the floodplain is shallow, in which case the velocity difference between the main channel

and the floodplain is higher than for deeper cases.

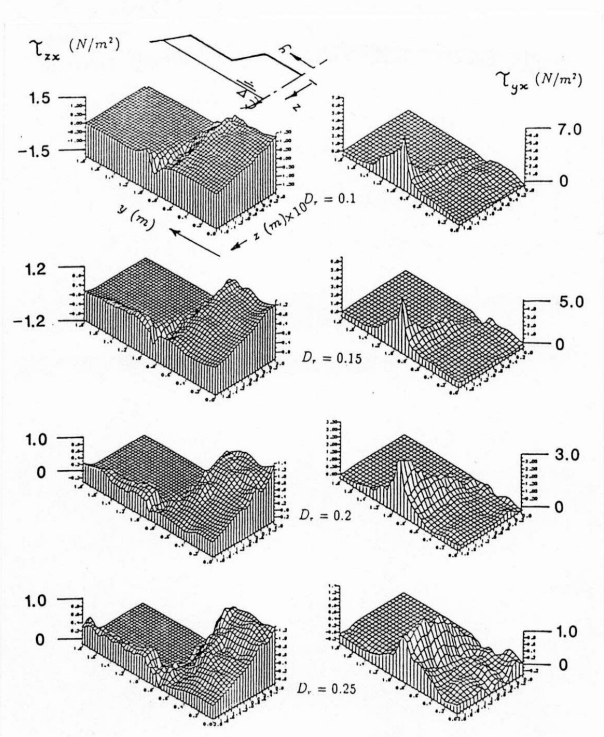

Figure 2.12: Reynolds stresses τ_{zx} and τ_{yx} in a straight compound channel with various relative depths (Shiono and Knight, 1991)

2.3.6 Apparent Shear Stress

Myers (1978) defined the apparent shear stress acting at the interface of a compound channel on the basis of bed shear stress measurements. The apparent shear stress can be seen as a measure of the momentum transfer taking place laterally between the floodplain and the main channel (Christodoulou, 1992). The depth mean apparent shear stress τ_a can be defined by Equation 2.3 after (Shiono and Knight, 1991).

$$\tau_a = -\frac{1}{H}\int_0^y \left[\rho g H S_0 - \tau_B \left(1 + \frac{1}{s^2}\right)^{\frac{1}{2}}\right] dy \tag{2.3}$$

The apparent shear force is the product of the apparent shear stress and the water depth. As summarised in (Christodoulou, 1992) many authors have attempted to de-

rive empirical relationships to obtain τ_a. Such formulae typically include cross-section geometry and a velocity gradient accounting for the difference of velocity in floodplain and main channel, which is at the source of the momentum transfer mechanism.

Figure 2.13 presents the lateral variations of apparent shear stress derived for Series 03 of the FCF by Shiono and Knight (1991). The apparent shear stress varies approximately linearly in the main channel. The amplitude of τ_a at the interface increases as relative depth decreases, thereby reflecting the stronger transverse shearing observed for the shallow flows.

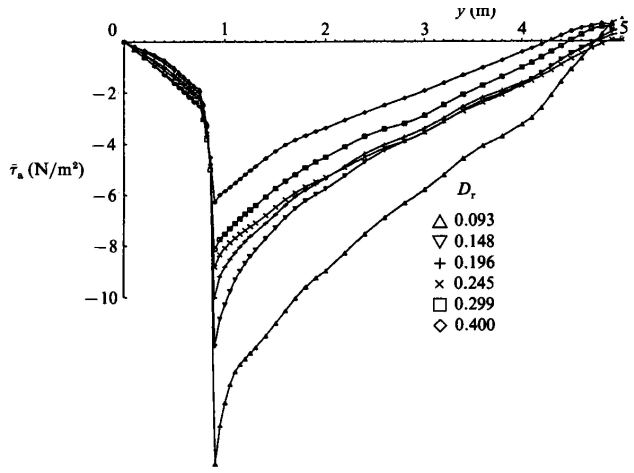

Figure 2.13: Lateral variations of depth-mean apparent shear stress τ_a for different relative water depths, in Series 03 (Shiono and Knight, 1991)

2.4 Vegetated Compound Channels

2.4.1 Introduction

Vegetation on the floodplain of a river can usually be classified into rigid vegetation (typically trees) and flexible vegetation such as grass. The stems of flexible vegetation can be deformed by the flow, while the stems of rigid vegetation remain in their original state in the flow. This research is focused on rigid vegetation and flexible vegetation is

not investigated.

In addition, studies focusing on flow with vegetation can be usually classified into two groups: flow over submerged, short vegetation and flow through non submerged, tall vegetation. This research focuses on emerged vegetation.

2.4.2 Drag due to vegetation

2.4.2.1 Definition of drag

First, it is important to recall that the drag force experienced by a single cylinder placed into water is usually divided into two components: frictional drag and pressure drag (Schlichting and Gersten, 1968). Frictional drag comes from friction between the fluid and the surfaces over which it is flowing, and is associated with the development of boundary layers. On the other hand, pressure drag is related to the turbulent eddying motions set up in the fluid and is associated with the formation of a wake. Frictional drag and pressure drag are caused by different flow phenomena. Frictional drag is important for attached flows (when there is no separation), and is related to the surface area exposed to the flow. Pressure drag is significant for separated flows, and it is related to the cross-sectional area of the body. At large Reynolds numbers, the drag exerted by fluid on cylinder rods is dominated by the pressure losses in the wake (Figure 2.14).

The boundary layer, through its interaction with the local pressure gradient, plays a major role in affecting the flow over a cylinder (Smits, 2001). The mechanisms involved in flow separation are illustrated in Figure 2.15 and are succinctly summarised as follows.

Near the shoulder of the cylinder, the pressure gradient varies from negative (decreasing pressure from D to E) to positive (increasing pressure from E to F). The force caused by pressure differences changes from being accelerating to retarding and the flow slows down in response. However, the fluid in the boundary layer has already lost some momentum because of viscous losses and strong viscous friction and cannot overcome

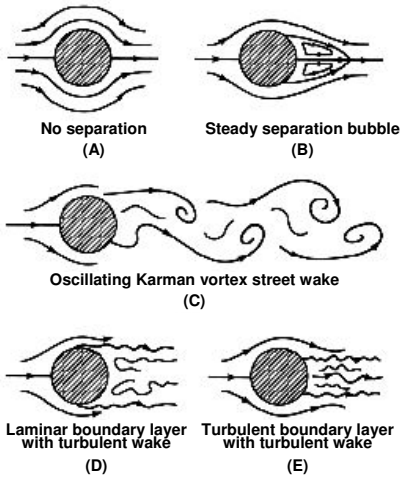

Figure 2.14: Flow patterns for flow over a cylinder: (A) Reynolds number = 0.2; (B) 12; (C) 120; (D) 30,000; (E) 500,000, (Smits, 2001)

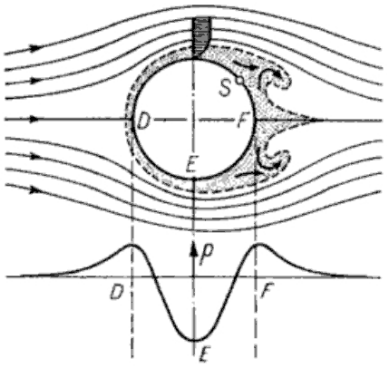

Figure 2.15: Separation of boundary layer and vortex formation at a circular cylinder. S is the separation point (Schlichting and Gersten, 1968)

the retarding force. This leads to some fluid near the boundary actually reversing direction and the flow separates (at point S in Figure 2.15).

Near the boundary, a turbulent boundary layer carries more momentum than a laminar boundary layer because turbulence is a very effective mixing process. Importantly, turbulent transport of momentum is very effective at replenishing the near-boundary momentum. Therefore, compared to a laminar flow, a turbulent boundary layer en-

tering a region of adverse pressure gradient can persist for a longer distance without separating. This is due to the momentum near the boundary being greater from the start, and to the continuous and prompt replenishment caused by turbulent mixing. In fully turbulent flows such as flows in nature with vegetation, with a thin boundary layer, flows passing vegetation stems or tree trunks are separated flows and the pressure drag will drop substantially compared to laminar flow because of flow separation (Jarvela, 2002).

2.4.2.2 Drag force

Considering a tree placed in a flow, the total force which acts on that body consists of the normal pressures and the shear stresses acting on the surface of the body. If F is the component of the total force in any given direction, a dimensionless force coefficient can be formed by choosing $\frac{F}{\rho A U^2}$ where A is a characteristic surface of the rod, usually taken as the face of the tree in the flow direction (A_P), and U is a characteristic velocity, which can be taken as the depth-averaged velocity U_d. If $\frac{\rho U_d^2}{2}$ is chosen instead of ρU_d^2, the dimensionless drag coefficient is obtained (Equation 2.4)where F_D is the drag force (Schlichting and Gersten, 1968).

$$C_D = \frac{F_D}{\frac{\rho A_P U_d^2}{2}} \tag{2.4}$$

The drag force, which acts on the surface area A_P, may therefore be defined as:

$$F_D = \frac{1}{2}\rho C_D A_P U_d^2 \tag{2.5}$$

As highlighted by Jarvela (2002), the drag coefficient is the result of the pressure and friction drag described in the previous section. The drag coefficient for an isolated element, C_D, is affected by the wake structure, and depends on the rod Reynolds number Re_{rod}. Figure 2.16 presents a change of C_D for a range of Reynolds numbers. The influence of the Reynolds number is further discussed in Section 2.5.3.

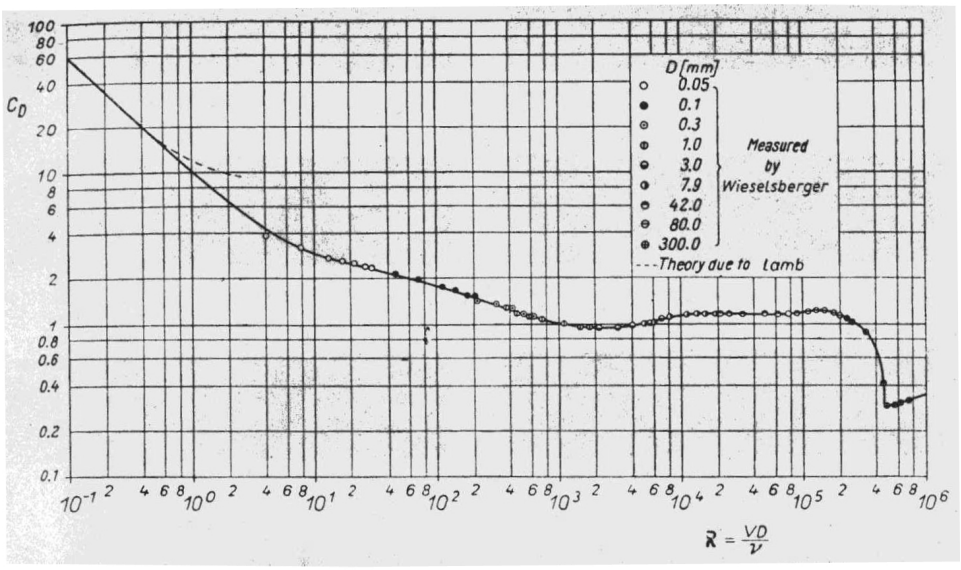

Figure 2.16: Drag coefficient as a function of the rods Reynolds number for an infinite circular cylinder (Schlichting and Gersten, 1968)

Armanini *et al.* (2005) and James *et al.* (2008) investigated the effects of foliage on the resistance to flow through emergent vegetation. Armanini *et al.* (2005) recommended that a value of drag coefficient close to unity was reasonable for the range of experimental flows tested with emergent willow vegetation, i.e. for $Re \in [2,000; 20,000]$. In other words, the value of C_D for a rigid, smooth, indefinite cylinder remained a reasonable approximation. However, values of drag coefficients for foliated stems were found to be significantly higher than for bare stems by James *et al.* (2008). For example, James *et al.* (2008) investigated the values of the plant drag coefficient for a single reed stem with different degrees of foliage. For vegetative Reynolds number in the region of $850 \sim 900$, the plant drag coefficient increased from approximately 5.4 for a stem with 6 leaves to 7.5 for a stem with full foliage. Jarvela (2004) investigated the flow resistance of non-submerged leafless woody vegetation and suggested that a drag coefficient increased to 1.5 should be used to account for the branch structure of the plant. Therefore, while it is common to recommend a constant value of C_D typically close to unity, natural vegetation with branches or foliage can exceed these values considerably.

2.4.3 Overall Flow characteristics

The drag exerted by fluid on vegetation has a significant impact on the flow characteristics of a compound channel. The mean flow of vegetated areas is reduced when compared to non vegetated areas while the flow depth can also increase (e.g. Darby, 1999). James and Makoa (2006) carried out experiments in a straight single channel with different strips of vegetation patterns. It was found that the overall resistance increased with the number of interfaces between clear and vegetated flows zones, suggesting that the flow interaction across the interfaces is a major source of resistance in partially vegetated channels (Figure 2.17).

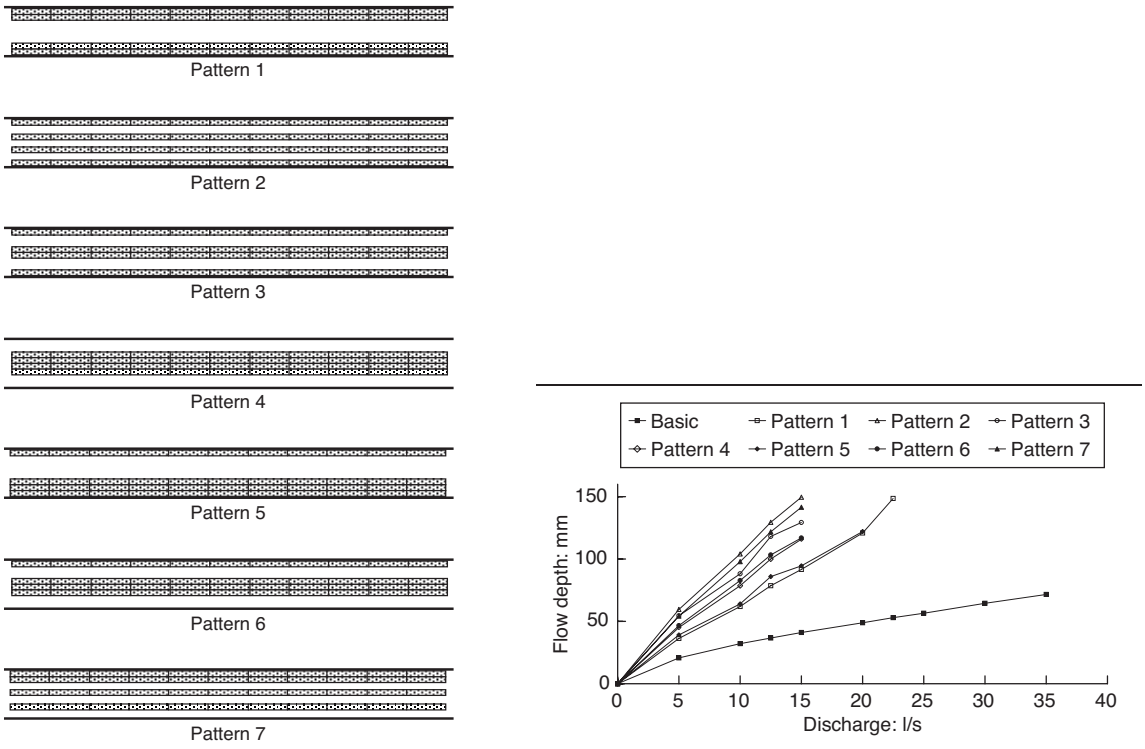

(a) (b)

Figure 2.17: (a) Vegetation strip patterns in plan (b) Stage discharge curves (after James and Makoa, 2006)

Within the wakes of the vegetation stems, the mean kinetic energy is converted to turbulent kinetic energy, which has for effect to augment the turbulence intensity (Nepf, 1999). The primary source of turbulence production is from the stem wakes. The turbulence length scale is of the order of the stem diameter. The turbulence intensities increase with the introduction of sparse vegetation due to the wake, but decrease as the vegetation density increases due to the reduced velocity.

Tsujimoto (1992) measured turbulence in a partially vegetated rectangular channel where vertical cylinders were used to represent vegetation. Under the water depth of 4.5 cm, the mean velocity was reduced by over 30% and the transverse Reynolds stress was approximately 40% higher when the vegetation density was increased by a factor of approximately 6.0. The velocity difference between the vegetated zone and non-vegetated zone increased as the vegetation density increased.

Naot *et al.* (1996) investigated the hydrodynamic response of turbulent flow in a rectangular compound channel with a vegetated floodplain. Densities were expressed as $N = 100nHD$, where n is the average vegetation density (rods per unit area), H is the depth of water and D is the diameter. An algebraic stress model accounting for the drag force caused by vegetation was used. Figure 2.18 presents the calculated streamwise velocity normalised by the maximum velocity. As the density of the vegetation gradually increases, the maximum velocity in the main channel also gradually moves away from the interface with the vegetated floodplain and a bulging towards the side wall can be observed. The authors attribute this shift in the location of the maximum velocity to an increase in secondary currents as vegetation density increases.

As the vegetation density increases, it is observed that the maximum of the turbulence kinetic energy, developing at the free shear layer at the floodplain threshold, also increases. Naot *et al.* (1996) introduced a length scale l_v characterising the vegetated zone structure in their algebraic stress turbulence model that relates to the wakes formed behind the rods. Analysing the hydrodynamic behavior of the vegetated compound

channel, the role of this length scale l_v is highlighted as l_v increases with vegetation diameter and decreases when vegetation density increases.

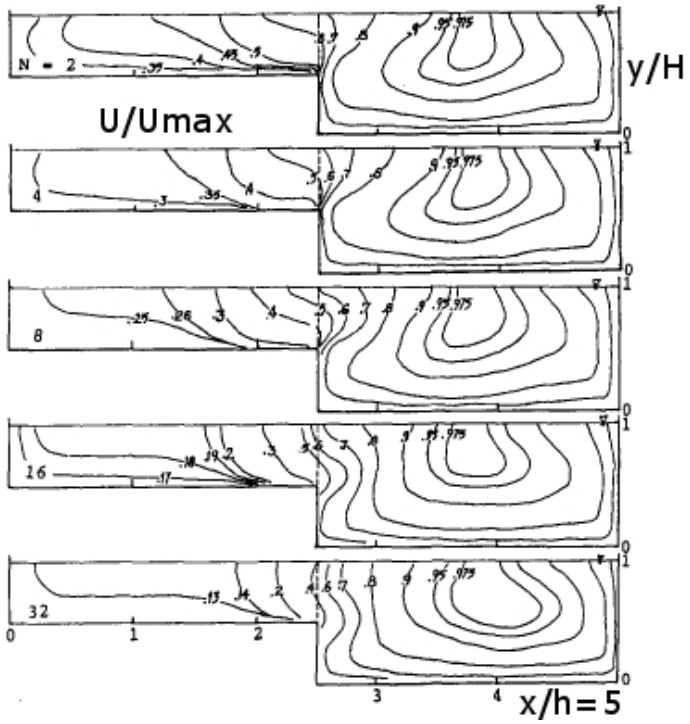

Figure 2.18: Calculated streamwise velocity contours for densities of vegetation for N=2, 4, 8 16 and 32 (after Naot *et al.*, 1996)

As underlined by Pasche and Rouve (1985), who conducted experiments applying an LDV and a Preston tube, the intensive momentum transfer between the vegetated floodplain and the main channel is reflected by the coherent structures that can be observed in the flow. This mechanism of interaction bears similarity with the interaction observed in compound channel with uniform roughness, as described in the previous section. However, the scale of these vortex structures is different from those found in the smooth floodplain case due to the additional drag forces caused by trees on the floodplain. The emergent vegetation increases flow resistance on the floodplain and induces a larger velocity difference between sub-sections, leading to stronger lateral momentum exchange.

2.4.4 Secondary currents

Kang and Choi (2006b) developed a three dimensional Reynolds Stress Model that was validated on experimental data sets for cases without vegetation. The model was then developed to account for the effect of vegetation by adding a drag term to the momentum equations. In the absence of detailed turbulence measurements for vegetated compound channel flow, the model was compared to the model developed by Naot *et al.* (1996). Figure 2.19 presents the secondary current vectors for different densities of vegetation on a floodplain. The intensity of the secondary currents near the vegetated floodplain interface is found to increase with the vegetation density. The results indicated that the simulated maximum magnitudes of secondary current vectors were 3.4%, 3.75%, 4.0%, and 5.1% of the maximum streamwise velocity for vegetation densities of 0.25, 0.5, 1.0 and 4.0 m^{-1}, respectively.

Nezu and Onitsuka (2001) measured secondary currents with LDA in a vegetated corner of a simple open channel. The secondary currents measured during the experiments exhibited different characteristics from those in smooth open channels. The results, presented in Figure 2.20, show that a large counterclockwise secondary circulation exists in the channel. High-momentum fluid from the non-vegetated zone is moved to the top of the vegetated zone and then into the vegetated zone and finally to the non-vegetated zone. They also found that the secondary currents are generated by an anisotropic turbulence and that the strength of secondary currents near the free surface over the vegetation zone is of appreciable size. The strength of the secondary currents increases as the Froude number increases.

White and Nepf (2007) undertook Laser Doppler Velocimetry measurements in a partially vegetated single channel, in which 6 mm wooden rods were placed in staggered arrangements. The rods covered a width of 0.4 m, in a 1.2 m wide flume. Although carried out in a partially vegetated single channel, the results obtained by White and

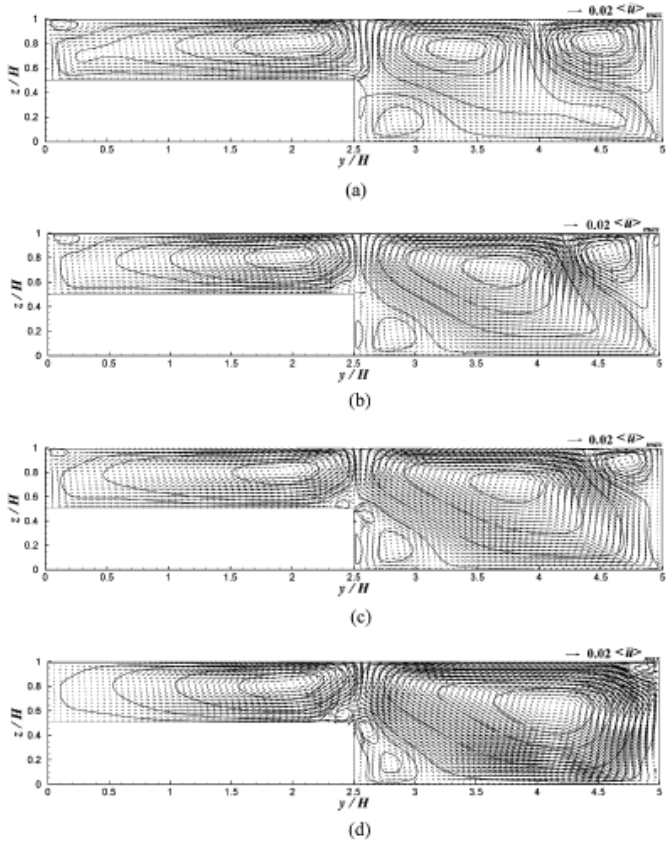

Figure 2.19: Impact of vegetation density on secondary currents: (a) for a = 0.25 m^{-1}; (b) for a = 0.5 m^{-1}; (c) for a = 1.0 m^{-1}; (d) for a = 4.0 m^{-1} (after Kang *et al.*, 2006)

Nepf (2007) are particularly relevant to the current research. Figure 2.21 presents the time series of the longitudinal and transverse velocities U and V, and of the free surface fluctuation h measured 3 cm outside the interface between the rods and the rest of the channel. The temporal oscillations of U, V and h reveal a near periodicity and the magnitude of fluctuations is remarkable. The oscillations of transverse secondary currents V correlate the oscillations of U and h as V and h peak at the same time and U reaches a minimum value.

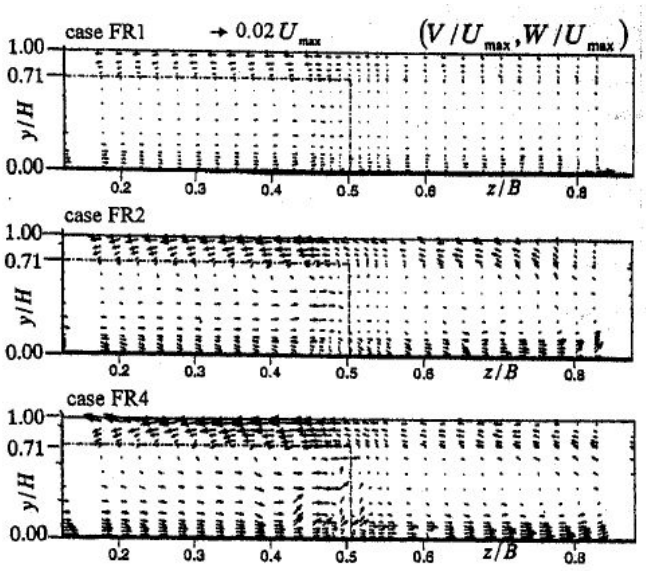

Figure 2.20: Vector description of secondary currents (V,W) (after Nezu and Onitsuka, 2001)

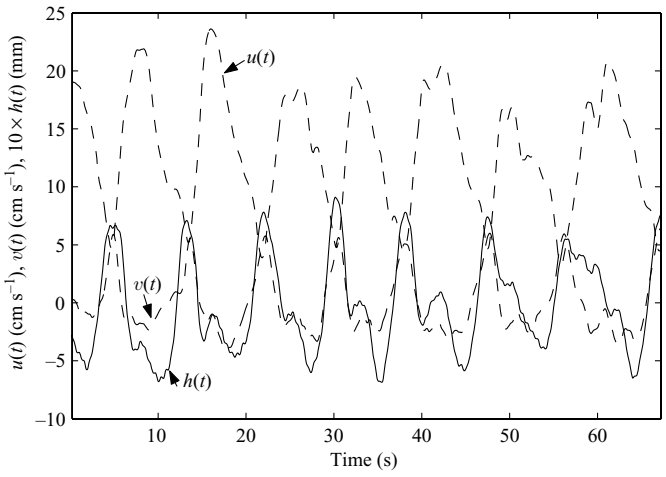

Figure 2.21: Temporal oscillations of the longitudinal and transverse velocity and free surface elevation for a flow depth of 7.8 cm (after White and Nepf, 2007)

2.4.5 Boundary shear stress

One significant effect of vegetation is to increase the total drag by absorbing momentum from the flow, thereby reducing bed shear stress. As a result, boundary shear stress on

the vegetated bed is generally smaller than that in the non-vegetated bed as there is a reduction in the mean velocity due to drag force.
The boundary shear stress distribution in the vegetated zone depends on many factors including vegetation density, channel geometry and water depth, as stated in Nezu and Onitsuka (2001) and Crawley and Nickling (2003).

Vegetation on the floodplain has a significant impact on the boundary shear stress distribution, as shown in Figure 2.22. Vegetation in the floodplain reduces boundary shear stress both in the floodplain and in the main channel. The peak in boundary shear stress is shifted towards the sidewall and is decreased. For the vegetation density $a = 1\ m^{-1}$, the peak in boundary shear stress is shifted by approximately 0.5 H and is decreased by 19%.

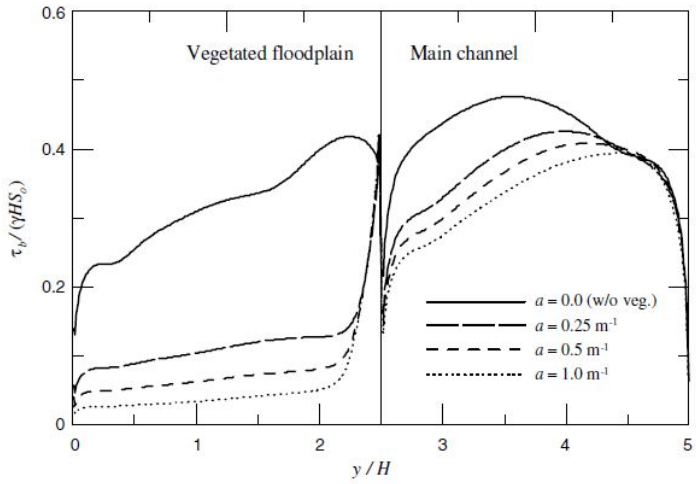

Figure 2.22: Impact of vegetation density on boundary shear stress: (a) for a = 0.25 m^{-1}; (b) for a = 0.5 m^{-1}; (c) for a = 1.0 m^{-1}; (d) for a = 4.0 m^{-1} (after Kang *et al.*, 2006)

Bed shear stress in the vegetated bed area often exhibits similar characteristics to that observed over a roughened surface. This explains why many experiments related to vegetated compound channel have been successfully conducted with roughened floodplain instead of actual vegetation. Nonetheless, bed shear stress measurements in vegetated

sections can prove difficult to measure. Instead, bed shear stress in vegetated channels can be indirectly determined using force balance method. For uniform flow in vegetated channels, the bed shear stress can be obtained from the balance between the shear force on the bed, drag force on the vegetation and the weight component of the flow (Jordanova and James, 2003). However, the problem is then shifted to the measurement of drag force, which can be equally, if not more, complicated to carry out.

Nezu and Onitsuka (2001) extended the continuity equation and steady Reynolds equations to open channel flow in order to predict the lateral distributions of bed shear stresses in a partly-vegetated simple open channel. The results are shown in Figure 2.23.

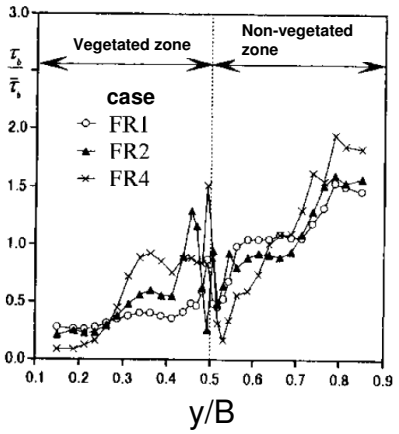

Figure 2.23: Bed shear stress derived from momentum equation (Nezu and Onitsuka, 2001)

The bed shear stress on the non-vegetated bed was larger than that on the vegetated bed, and varied greatly near the interface between the main channel and the floodplain due to the secondary currents and complex momentum exchange. The resulting momentum equation agreed well with the log-law in the non vegetated part of the channel. However, it could not be validated in the vegetated area where the log-law is not valid. The method would therefore need to be further verified against bed shear stress measurements.

2.4.6 Modelling approaches

2.4.6.1 Introduction

Ikeda and McEwan (2009a) have recently reviewed various modelling approaches available to tackle compound channel flow modelling. The Shiono and Knight Method (SKM) was identified as a robust method that can be used to predict the lateral distributions of depth-averaged velocity and bed shear stress in straight compound channel. Rameshwaran and Shiono (2007) modified the SKM to incorporate drag force and this attempt is presented in this Section.

As previously highlighted in this Chapter (Sections 2.3 and 2.4), the large-scale turbulence structures near the interface between the main channel and the floodplain are an essential feature of compound channel flow. In this context, large eddy simulations have yielded promising results and previous work related to large eddy simulations applied vegetated compound channel is reviewed in Section 2.4.6.3.

2.4.6.2 Extended Shiono and Knight Method (Rameshwaran and Shiono, 2007)

Under the assumption of steady uniform turbulent flow, the equation for the longitudinal streamwise component of momentum on a fluid element combined with the continuity equation leads to:

$$\rho\left[\frac{\partial UV}{\partial y}+\frac{\partial UW}{\partial z}\right]=\rho gSo+\frac{\partial\left(-\rho\overline{uv}\right)}{\partial y}+\frac{\partial\left(-\rho\overline{uw}\right)}{\partial z} \tag{2.6}$$

where x, y, z are the streamwise, lateral and normal directions respectively, U, V, W are the corresponding temporal mean velocity components and u, v, w are the related turbulent perturbations of velocity, ρ is the density of water, g is the gravitational acceleration, and So is the bed slope gradient.

The integration of the previous equation over the water depth H gives, assuming that $W(0) = W(H) = 0$ (Shiono and Knight, 1991):

$$\frac{\partial H\left(\rho UV\right)_d}{\partial y} = \rho g H So + \frac{\partial H \tau_{yx}}{\partial y} - \tau_b \left(1 + \frac{1}{s^2}\right)^{\frac{1}{2}} \tag{2.7}$$

where $U_d = \frac{1}{H}\int_{z=0}^{H} U dz$, τ_b is the bed shear stress and s is the side slope. τ_b is modelled using the Darcy-Weisbach friction factor f as $\tau_b = \rho\left(\frac{f}{8}\right)U_d^2$.
An analytical solution of Equation 2.7 can be obtained and is presented in Shiono and Knight (1991).

Rameshwaran and Shiono (2007) extended the SKM to model the effects of vegetation interacting with the flow by adding the drag force due to vegetation as an additional momentum sink term in the Navier Stokes equation. Let F_i be the drag force per unit fluid volume generated by the vegetation type i. F_i can be defined as:

$$F_i = \frac{1}{2}\rho\left(C_D S_F A_P\right)_i U_d^2 \tag{2.8}$$

where C_D is the drag coefficient, S_F is the shading factor and A_P is the projected area of i plants per unit volume. Thus, the addition of drag force into the depth-averaged equation previously obtained becomes:

$$\alpha\frac{\partial H\left(\rho UV\right)_d}{\partial y} = \alpha\rho g H So + \alpha\frac{\partial H\overline{\tau}_{yx}}{\partial y} + \alpha\tau_b\left(1 + \frac{1}{s^2}\right)^{\frac{1}{2}} - \sum_i \frac{1}{2}\rho\left(C_D S_F A_P\right)_i U_d^2 \tag{2.9}$$

In Equation 2.9, the porosity α was introduced to account for the blockage effects on the flow by the vegetation and is defined as $\alpha = 1 - \sum\left(N_v A_v\right)$ where A_v is the average cross-sectional area of i vegetation stems and N_v is the averaged i vegetation density per unit area. The last term on the right hand side is the drag force term. In the drag force term, S_F is the shading factor. The transverse shear stress term was defined via a depth-averaged eddy viscosity $\overline{\epsilon_t}$ such that $\tau_{yx} = \rho\overline{\epsilon_t}\frac{\partial U_d}{\partial y}$.
The input parameters were therefore a calibrated friction factor (f), the secondary current term Gamma ($\Gamma = \frac{\partial H(\rho UV)_d}{\partial y}$), the depth-averaged eddy viscosity $\overline{\epsilon_t}$ and the drag coefficient and the shading factor that define the drag force component.
Rameshwaran and Shiono (2007) applied the model to the data collected in the Flood Channel Facility (FCF) series A for smooth main channel and floodplain case and B

for smooth main channel and roughened floodplain. Several eddy viscosity models were tested, ranging from an Elder model to a combination of Elder and mixing length models. The best results were obtained with the combination of Elder and mixing length models. It was found that the addition of the mixing length helped to capture the velocity difference between the main channel and the vegetated floodplain caused by the flow resistance.

2.4.6.3 Large Eddy Simulation (LES)

The governing principle of Large Eddy Simulation is the separation of flow variables into resolved and unresolved parts (Lesieur *et al.*, 2005). While large-scale quantities are resolved, small scale quantities are modelled with a sub-grid model. LES simulations can therefore capture the unsteady characteristics of large eddies. The turbulent flow characteristics can be better modelled than through a Reynolds Averaged Navier-Stokes (RANS) approach. In addition, this numerical modelling method requires less significant computational power than Direct Numerical Simulation (DNS).

Using the SDS-2DH model presented in Nadaoka and Yagi (1998), Bousmar (2002) investigated the characteristics of large eddies in compound open channels with no vegetation under different relative water depth conditions. In this model, close to a LES turbulence model, the small-scale turbulence effect is implicitly modelled through an eddy-viscosity corresponding to the so-called Sub-Depth-Scale turbulence. The numerical computation was also initiated from an unperturbed uniform flow. The mechanism of eddy generation in compound channels was qualitatively reproduced. The vortex wavelength estimated from the modelling results agrees well with that from the hydrodynamic stability analysis and that from the experiments. The averaged velocity and bed shear stress profiles were well predicted in the shear layer. In the central part of the main channel, the velocities were under-predicted for relative depths under 0.15 and over-predicted for relative water depths exceeding 0.20. The velocities on the floodplain were under-predicted, especially for high relative water depth conditions.

Stoesser *et al.* (2009) and Guillermo *et al.* (2008) performed three dimensional LES modelling of vegetation in open channel flow for submerged and emerged vegetation respectively. Each individual vegetation element was resolved in the mesh and it was found that LES can elucidate the large-scale coherent structures associated with the modelled flows. While instantaneous flow structures such as von-Karman type vortices and horseshoe vortex formation were found to be responsible for bed-shear stress peaks, most of the energy losses were shown to be due to the drag exerted by fluid on plants.

Sun (2006) applied LES Telemac-2D to model vegetated compound channel flow. One case of emergent vegetation placed on the edge of floodplain was modelled for a relative depth of Dr=0.5. The results obtained highlighted the potential of LES Telemac-2D to resolve the unsteady characteristics of the flow. The large eddies simulated from an unperturbed uniform flow exhibited realistic time and length scales. The simulated depth-averaged velocity and boundary shear stress distributions were compared with experimental data obtained in a trapezoidal flume. Although the results were encouraging, the profiles could not be well reproduced. At the vegetated interface in particular, both depth-averaged velocity and boundary shear stress were very significantly underestimated, while the maximum main channel and floodplain maximum velocities were overestimated. The model generated better predictions when applied to the corresponding no vegetation case.

2.5 Flow Characteristics of One-Line Cylinders in a Rectangular Channel

2.5.1 Introduction

This section briefly summarises the flow patterns on aligned cylinders relevant to the current project. Numerous studies on flow characteristics around aligned cylinders have been carried out. At first, studies tended to focus on cylinders arranged in tandems. Then third, fourth and fifth cylinders were added. As highlighted by Zdravkovich

(1987), the addition of a third or fourth cylinder to aligned two cylinders almost does not affect the flow around the first two cylinders. This led him to conclude that the flow patterns might be regarded as typical for any additional number of rods aligned in an array. The conclusions drawn from the studies of two to five aligned rods are therefore relevant to the current work.

2.5.2 Notion of critical spacing

Zdravkovich (Zdravkovich, 1977) defined a critical spacing $\frac{L}{D}$ around which flow characteristics change. The discontinuity is caused by a sudden change between two stable flow patterns. For $\frac{L}{D}$ values lower than $3.5 \sim 3.8$, the shear layer separated from the upstream cylinder reattaches onto the downstream cylinder. Vortex shedding does not occur between the two cylinders. Instead, quasi-stationary vortices are observed.
Beyond the critical spacing, periodic vortex shedding is observed. Many researchers have focused on the flow patterns occurring for $\frac{L}{D}$ ratios lower than the critical value of 3.5. For that range of $\frac{L}{D}$ ratios, complex sub-patterns can be observed but only one main type of flow pattern is reported for higher $\frac{L}{D}$ values. Slaouti and Stansby (1992) showed that for cylinders in tandem arrangement, four different flow patterns could be identified for $\frac{L}{D} \leq 3.4$ while cylinders shed vortices independently for $\frac{L}{D} > 3.8$. The results are presented in Figure 2.24, which summarises how $\frac{L}{D}$ affects vortex shedding.

Hetz (1991) attempted to show that all sub-patterns observed for subcritical flow oscillations can be explained by the interaction of three types of flow configurations presented in Figure 2.25, namely cavity oscillations, gap shedding and bluff-body shedding. For $\frac{L}{D} > 3.24$, unobstructed shedding as illustrated in sketch (d) in Figure 2.25, is observed.

2.5.3 Reynolds number

The Reynolds number Re_{rod} is a dimensionless number that plays an important role in defining flow structures in presence of vegetation and a number of researchers have

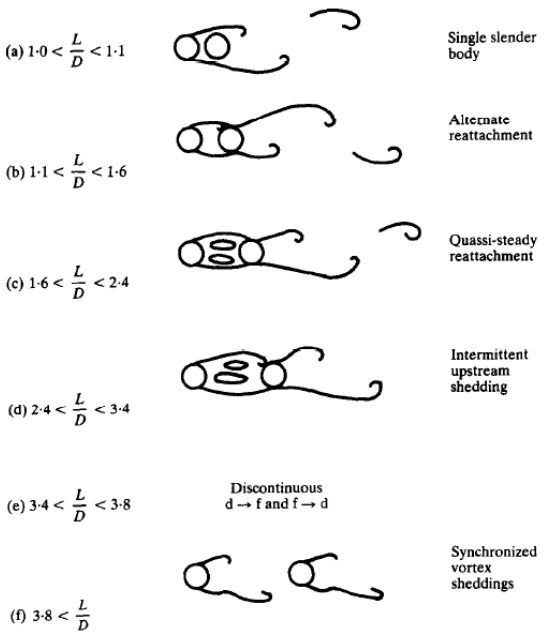

Figure 2.24: Classification of flow regimes in tandem arrangement (Slaouti and Stansby, 1992)

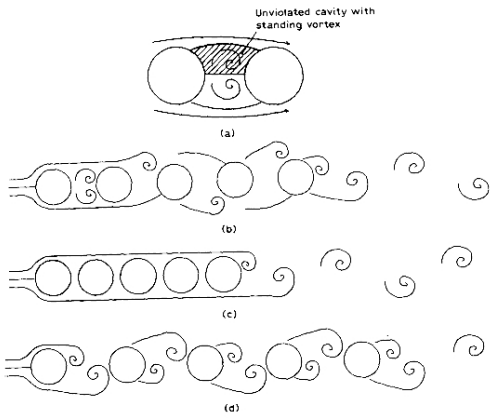

Figure 2.25: Schematic of cavity flow and flow over a pentad of cylinders (a) cavity flow; (b) gap shedding; (c) inactive gaps; (d) unobstructed shedding. (Hetz, 1991)

defined flow patterns in terms of the rod Reynolds number only. The Reynolds number Re_{rod} is defined by:

$$Re_{rod} = \frac{U_d D}{\nu} \tag{2.10}$$

where D is the rod diameter, ν is the kinematic viscosity and U_d is the uniform depth-averaged velocity.

Williamson (1992) described the details of the laminar to turbulent transition for a single isolated cylinder in a uniform flow for a range of Reynolds numbers. The cylinder wake remains laminar up to $Re_{rod} \approx 200$, although vortex shedding is initiated at $Re_{rod} \approx 50$. For $Re_{rod} > \approx 200$, vortex instability causes the wake to become turbulent. Lateral shear in the flow upstream of an isolated cylinder can delay the onset of vortex shedding to $Re_{rod} = 200$ (Tamura *et al.*, 1980), and because vortex shedding is a precursor to wake instability (Williamson, 1992), the transition to a turbulent wake will also be delayed. Within a cylinder array, Nepf *et al.* (1997) observed that vortex shedding was initiated at $Re_{rod} = 150 \sim 200$ for the large range of studied cylinder densities. They attributed the delay to shear associated with upstream wakes. However, as the array density declines, the critical Re_{rod} values should return to those of an isolated cylinder. From the above observations, the transition from laminar to turbulent wake structure within the array is expected to occur at $Re_{rod} \approx 200$. The wake structure (laminar versus turbulent) is important in defining the contribution of the wake to turbulent kinetic energy and diffusion within the array.

2.5.4 Drag coefficient

As stated in Wang (2006), the increased level of turbulence generated by an upstream rod decreases the drag force generated by the consecutive rod. The turbulence reinforced by the wake moves the point of separation on the downstream cylinder further downstream, which results in a lower pressure drop around the cylinder and thus a lower drag. Igarashi (1984b) studied the evolution of drag coefficients of three aligned rods in function of the ratio $\frac{L}{D}$ for a given Reynolds number of $2.2X10^4$ (Figure 2.26). After a jump occurring at the critical spacing ratio, the drag coefficients of the downstream two rods become similar as the ratio $\frac{L}{D}$ increases and approaches 4. It is noticeable that the drag coefficients of the downstream two rods are much reduced (being approximately halved) when compared to the upstream rod.

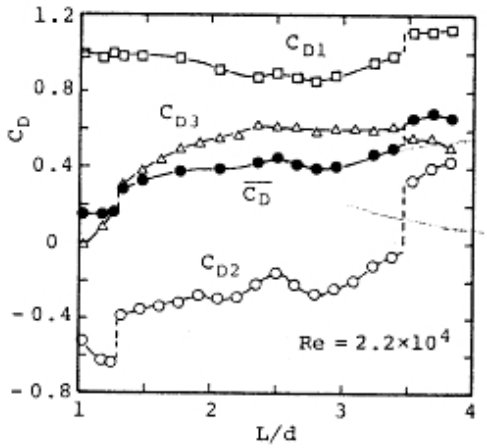

Figure 2.26: Drag coefficients CD1, CD2 and CD3 of three cylinders inline and combined drag coefficient $\overline{CD}$ (Igarashi, 1984b)

Similarly, experiments on cylinders in tandem have demonstrated how the wakes of an upstream cylinder can suppress the drag coefficient on the downstream cylinder, as illustrated in Figure 2.27 and summarised in Nepf (1999).

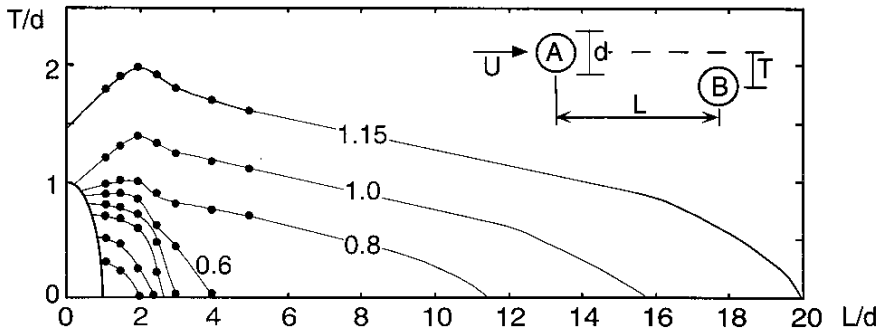

Figure 2.27: Contours of drag coefficient, C_D, on trailing cylinder B, showing the suppression of C_D due to wake interaction, after Nepf, 1999

2.6 Impact of One-Line Vegetation on Flow Structures in Compound Channel

Research on the impact of a single line of emergent vegetation placed on the edge of the floodplain in a compound channel is scarce. Sun (2006), Sun (2008) and Sun and Shiono (2009) studied the impact on flow structures of emergent one-line vegetation placed on the edge of a compound channel. Sun carried out experiments in the small compound channel flume of Loughborough University. Velocity and boundary shear stress were measured using a Pitot tube and a Preston tube respectively. 9 mm diameter wooden rods were placed on the edge of the floodplain and the flow structures in the flume without vegetation and with 9 mm diameter rods were compared. Spacing ratios of $\frac{L}{D} = 4.4$ and 13.3 were investigated.

Figure 2.28: Experiments from Sun (2006) with 9 mm rods in the compound channel flume of Loughborough

Sun noted that the emergent rods strongly affected the flow structure in such a way that it becomes "*totally different from that in the compound channel without rods on the floodplain under similar, relative water-depth conditions.*" The measured lateral distributions of boundary shear stress and depth-averaged velocity in the rod-case were noticeably different compared to the no rod case. Figure 2.29 illustrates the impact of the line of rods by comparing the lateral distributions of depth averaged velocity and boundary shear stress for a relative depth of 0.52 and a spacing ratio of 4.4.

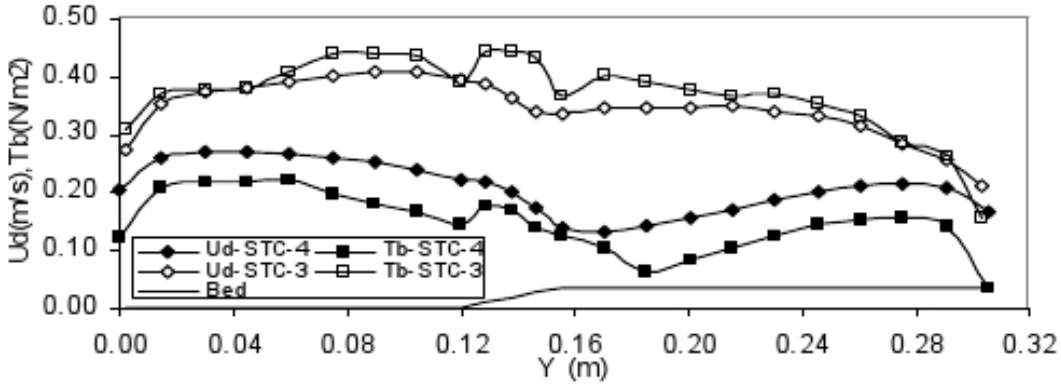

Figure 2.29: Lateral distributions of depth-averaged velocity and bed shear stress in vegetated (STC4) and non-vegetated (STC3) channels under Dr = 0.52

In the compound channel with one-line emergent rods along the main channel, Sun observed two shear layers in the floodplain and the main channel separately. The total shear layer width in the rod case was 0.083 m as opposed to only 0.030 m in the no-rod case.

Sun (2006) applied the SKM using a similar approach to Rameshwaran and Shiono (2007). The only significant, but important, difference with Rameshwaran and Shiono (2007) was in the introduction of wall velocities, which were found to significantly improve velocity predictions. Sun (2008) related the advection term to drag force and found that the advection term normalised by the gravity term $\rho g H S_0$ varied approximately linearly in the main channel and in the floodplain. The magnitudes of the advection term appeared large and were attributed to the transverse mixing due to drag force at the interface rather than secondary flow. Nonetheless, it was felt that the definition of the physical processes behind the advection term remained to be elucidated.

The analytical formulae (Equation 2.8) was found to provide significantly different results when compared to force balance (Sun and Shiono, 2009). The analytical formulae underestimated drag force by factors ranging from 8.5 for the shallow case to 2.8 for the deeper case. The interpretation of this discrepancy is not straightforward and

the applicability of this formulae to an array of rods placed on the edge of a compound channel floodplain should be further investigated.

2.7 Summary and Discussion

The literature review highlighted an number of important parameters to be considered in order to study more comprehensively flows in vegetated compound channels. These parameters include the channel aspect ratio, Reynolds number (Re), spacing ratio ($\frac{L}{D}$), stem diameter (D), foliage and relative depth (Dr).

Sections 2.2 and 2.3 illustrated how the channel aspect ratio influences secondary currents in single and compound channels. It is a determining factor in the number and in the organisation of secondary flow cells. Therefore, efforts should be made in this research to investigate a range of aspect ratios.

Reynolds number plays a significant role in the flow structure and in the variations of drag coefficient, as seen in Section 2.5 in particular. Experiments carried out with Reynolds numbers greater than 200 would most likely ensure that a turbulent wake structure is reached, thus focusing on flow cases which are closer to those observed in nature.

As emphasized in Sections 2.5 and 2.6, the spacing and the diameter of the rods also need to be studied as these affect the flow blockage, alter the turbulence between the rods and change the quantity of drag force in the force balance. Spacing ratios greater than the upper limit of the critical ratio of 3.8 should be considered, on the condition that these remained consistent with spacing ratios found in the field.

As highlighted in Sections 2.3 and 2.6, the turbulent shear at the interface of a compound channel varies with relative depth. Shallow, deep and intermediate experimental flow cases therefore need to be investigated to identify possible changes in flow patterns due to relative depth.

Section 2.4 suggested that the analysis would also benefit from a comparison between bare, smooth cylinders and foliated modelled vegetation as foliage is seen to increase

flow resistance. Experiments with and without foliage should be carried out for similar relative depth, spacing ratio and main stem diameter to allow for direct comparisons.

From a modelling viewpoint, the SKM requires further assessment against experimental data with vegetation on the floodplain. A few researchers, Bousmar (2002); Proust (2005); van Prooijen *et al.* (2005), highlighted that caution was needed to apply the SKM using the advection term $\Gamma = \frac{\partial \rho H \overline{UV}}{\partial y}$. Indeed, it is felt that the interpretation of the advection term requires more specific research (Ikeda and McEwan, 2009a). Instead, the reconsideration of the transverse shear term, as explored by van Prooijen *et al.* (2005) in the no vegetation case, provides an interesting alternative modelling approach.

Large Eddy Simulation appears as an intermediate modeling strategy between RANS and DNS models. From an engineering perspective, three dimensional modelling approaches are still out of reach for most field case applications despite the latest advances in numerical techniques and the promises of parallel computing (Lesieur *et al.*, 2005). In addition, if the large eddies in shallow compound-channel flows are mainly two dimensional, a depth-averaged model will be sufficient to describe this phenomenon at a much less expensive computational cost. The capabilities of two dimensional LES can be explored through Telemac-2D. Although this numerical model has become extensively applied to both research and industrial applications, the capabilities of its LES turbulence model remain largely unexplored. Furthermore, a comparison of the different turbulence models available in Telemac-2D could prove useful in assessing the performance of the model.

This research would also benefit from the analysis of field data that would complement data obtained by laboratory experiments. Field data is now more accessible as advances in Acoustic Doppler Current Profilers (ADCP) have enabled velocity measurements in shallow flow conditions. In particular, ADCPs have provided valuable data collected during flood events. Such data can be more directly related to compound channel flows studied in laboratory.

Research gaps have been identified so that the detailed objectives of this thesis can be defined as follows:

1. To carry out detailed velocity and boundary shear stress measurements to assess the impact of emergent one line vegetation on the edge of floodplain on velocity and boundary shear stress distributions;

2. To investigate the impact of aspect ratio, relative depth, diameter, spacing ratio and foliage on the flow field and on drag force;

3. To assess the applicability of the drag force analytical formulae to the studied flow cases;

4. To investigate the flow structure in vegetated rivers through the analysis of ADCP field data;

5. To extend the SKM to account for the effects of drag on the flow field and assess the capabilities of the proposed SKM to model the flows studied experimentally. Analytical solutions of a proposed modified SKM should be explored;

6. To investigate the capabilities of Telemac-2D to model the flows studied experimentally, through the application of Large Eddy Simulation and other turbulence models.

Thus, this thesis aims to advance the previous research in the area of compound vegetated open channel flow by investigating experimentally and numerically how a single line of emergent vegetation placed on the edge of floodplain affects the flow structure.

CHAPTER 3

Experimental Apparatus and Measuring Methodologies

"We must measure what is measurable and make measurable what cannot be measured."
Galileo Galilei

3.1 Introduction

In this chapter, the apparatus and methodologies used in the experimental part of this study are presented. Section 3.2 describes the experimental apparatus, which consists of straight compound channel flumes with vegetated floodplain in the Laboratory of Loughborough University and in the Laboratory of Fluid Mechanics and Acoustics in Lyon. Section 3.3 presents measurement techniques that are involved in the data collection. The instrumentation includes two Pitot tubes and a micro-propeller to measure velocity, a point gauge and a pressure sensor to measure water elevation, a Preston tube to measure boundary shear stress and high definition cameras to carry out Large Scale PIV analysis.
The main aim of this chapter is to demonstrate a sound understanding of the apparatus and instrumentation used in the experiments in this study. In particular, the setting of quasi-uniform flow conditions for the studied cases was carefully verified.

3.2 Experimental Set-up

3.2.1 Loughborough compound channel flume

3.2.1.1 Flume characteristics

Measurements were conducted in a 12 m long perspex titling flume in the Frank Gibb hydraulic laboratory of Loughborough University. Figure 3.1 shows a cross-section of that flume, in which the geometrical parameters are $B_{mc} = 0.120$ m, $B_{ss} = 0.036$ m and $B_{fp} = 0.150$ m for a sideslope of 1 in 1.

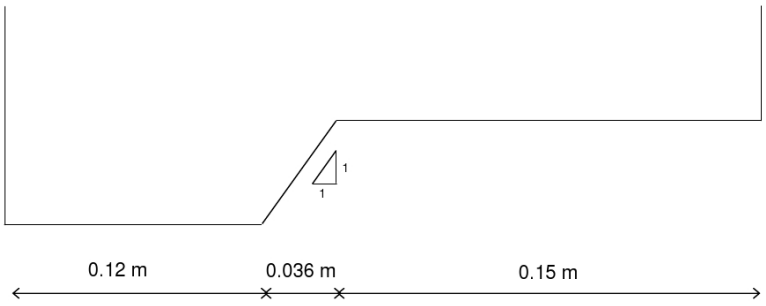

Figure 3.1: Cross-section of the flume used in Loughborough University

A schematic representation of the hydraulic system for the flume in Loughborough Frank Gibb Laboratory is given in Figure 3.2. The water is pumped from a 3.0 m long to 1.3 m wide outlet tank through a PVC circular pipe and into an inlet tank upstream from which the water flows into the flume. The flow rate into the channel was controlled using a digital flow meter.

The flume has an adjustable bed slope S_0 which was set to 0.001 using a total station. Four points were surveyed every meter, two in the main channel, at y = 3.5 cm and y = 10.5 cm, and two in the floodplain, at y =17.5 cm and y = 27.5 cm, to verify the longitudinal and transverse bed slopes. After initial surveying, the flume was carefully adjusted by turning the screws under the channel. The results of the flume surveyed before and after adjustments are presented in Figure 3.3. The longitudinal

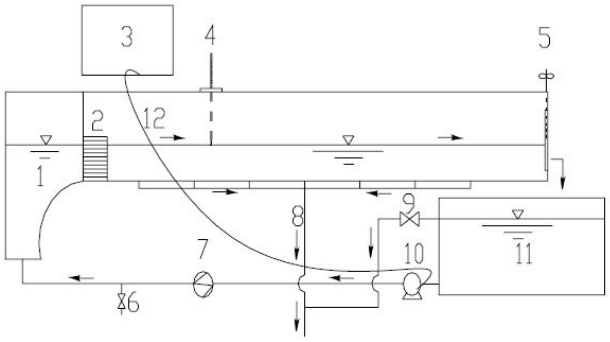

1-Inlet tank 2-Kraft honeycomb 3-Pump controller 4-Point gauge
5-Adjustable weir 6-Discharge valve 7-Pump control valve 8-Leakage tube
9-Overflow valve 10-Centrifugal pump 11-Storage and outlet tank

Figure 3.2: Schematic representation of the hydraulic system for the flume Loughborough Frank Gibb Laboratory

slope was double checked after having left water running for 8 hours in the flume. After further adjustment, the final longitudinal bed slope matched the theoretical bed slope with satisfying accuracy. Locally, the maximum discrepancy with the theoretical bed slope was 0.26 mm.

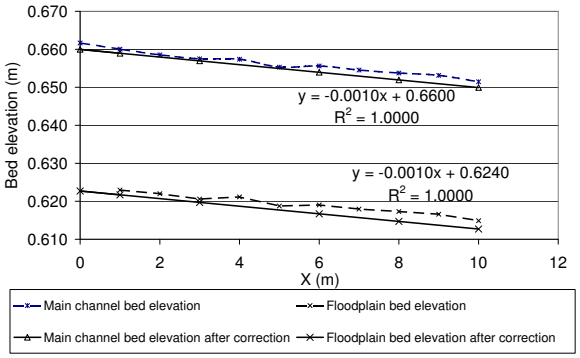

Figure 3.3: Leveling of the flume bed slope on the floodplain and main channel

Figure 3.4 shows photographs of the compound channel flume, the downstream tailgate, the outlet tank, the Kraft honeycomb blocks placed at the entrance of the

flume.

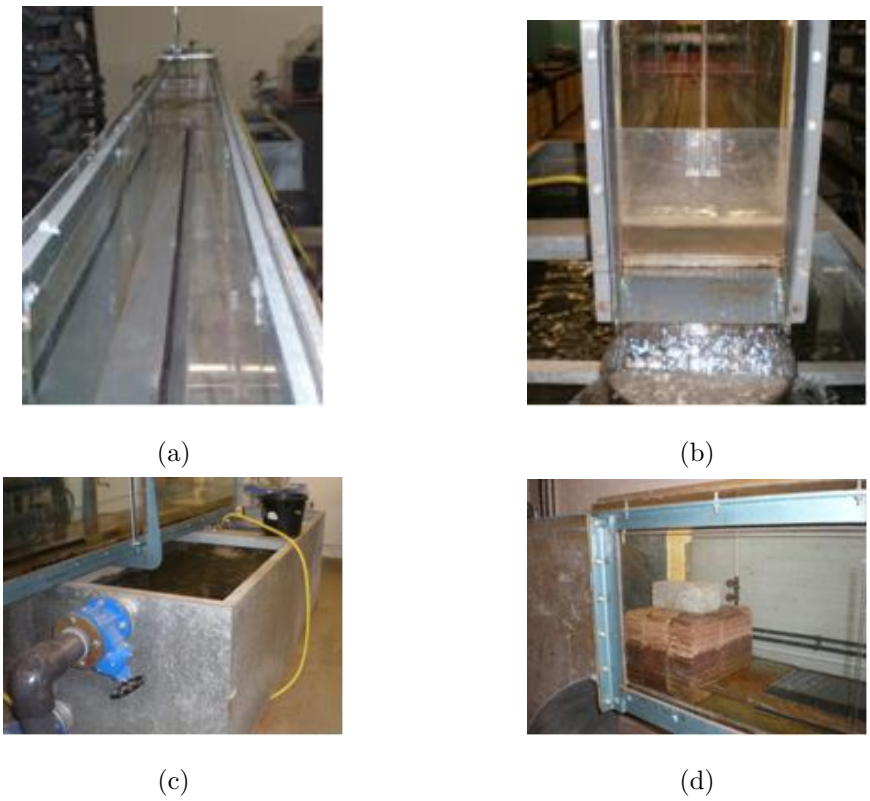

(a) (b)

(c) (d)

Figure 3.4: (a) View of the compound channel flume (b) Downstream tailgate (c) Outlet tank (d) Kraft honeycomb upstream.

3.2.1.2 Inlet turbulence

To minimize the effects of inlet turbulence on flow development, three 0.1 m long by 0.2 m high and 0.3 m, wide Kraft honeycombs with small uniform hexagonal holes were placed at the inlet to straighten the flow and reduce the disturbances due to inlet turbulence. The effects of Kraft Honeycombs on depth-averaged velocity and isovels were studied by (Sun, 2006) in the Loughborough flume for a discharge of 0.015 m^3/s. The results are presented in Figure 3.5.

The effects of the Kraft honeycombs on the depth-averaged velocity and isovels are significant. When the honeycombs were used the velocity pattern appears to be sym-

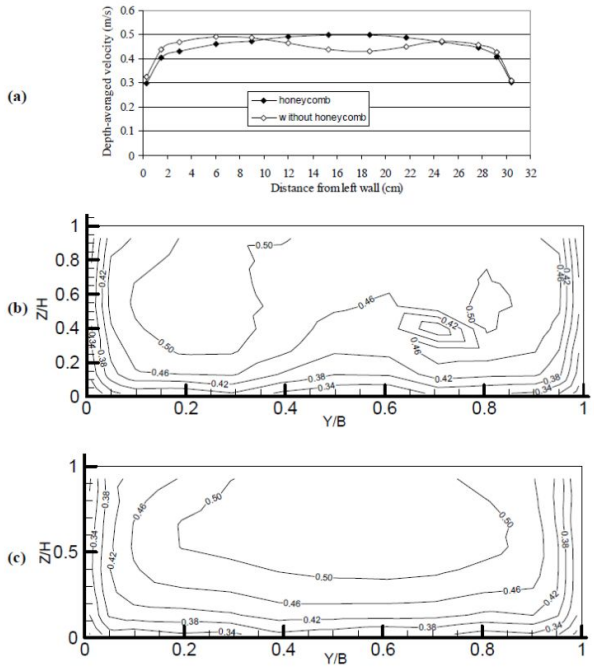

Figure 3.5: Effect of honeycomb on the velocity distributions at aspect ratio 2.9. (a) Depth-averaged velocity with and without honeycomb; (b) Isovels without honeycomb: (c) Isovels with honeycomb.

metrical. The Kraft honeycombs therefore contribute significantly to the setting of quasi uniform flow conditions.

3.2.1.3 Setting of quasi uniform flow conditions

The assumption of quasi-uniform flow forms the basis of most research in open channel flow. The experiments carried out in this research make no exception and it is assumed that quasi-uniform flow conditions are achieved at the measuring section. The importance and difficulties in obtaining such flow conditions are discussed in more detailed in Appendix A.

Great care was taken to establish quasi-uniform flow conditions. First, the water

surface slope was set parallel to the bed slope by adjusting the opening of a tailgate located at the flume outlet. Water levels were measured with a point gauge between x = 4.0 m and x = 9.0 m every meter with 0.5 m interval either side of the measuring section at 8.25 m. If the readings were within ±0.25 mm in the flume at the required flow depth the first stage of setting up quasi-uniform flow conditions was considered to be completed.

Once the water surface slope was set parallel to the bed slope, the quasi-uniformity of the flow was verified by inspecting the isovels of the mean longitudinal velocity. The longitudinal velocity was measured between rods at 7.25 m, 9.25 m and at 8.25 m i.e. at the measuring section. If the relative discrepancy between the velocities measured at the upstream and downstream sections with those at the measuring section were less than 5%, then the flow was regarded as quasi-uniform. The results of this test for a relative depth of Dr = 0.25, the dense vegetation case and rods of 3 mm diameter are presented in Figures 3.6 and 3.6

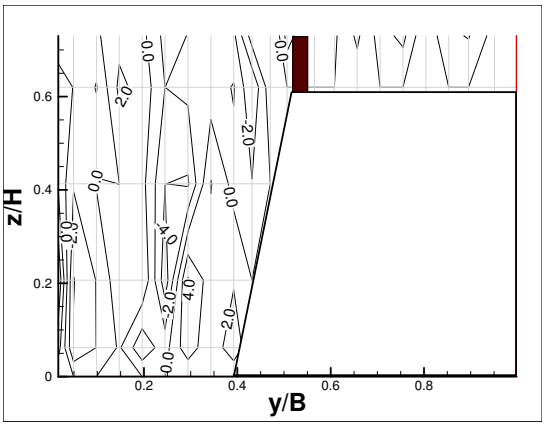

Figure 3.6: Percentage relative difference between velocities at x = 7.25 m and x = 8.25 m (%)

Clearly, the measured velocities remain stable and do not vary by more than 4%. Therefore, the assumption of quasi-uniform flow appears to be valid for this case. A similar test was carried out for the deeper and dense case with the 6 mm rods. The

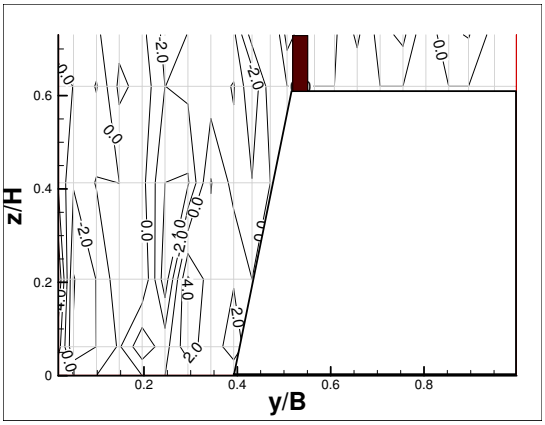

Figure 3.7: Percentage relative difference between velocities at x = 8.25 m and x = 9.25 m (%)

relative discrepancies did not exceed ±5% hence confirming that the measuring section was adequately located.

3.2.2 Laboratory of Fluid Mechanics and Acoustics Compound Channel Flume

3.2.2.1 Flume characteristics

Measurements were also conducted in a relatively flume of the LMFA laboratory in Lyon (France). A cross-section of the flume is given in Figure 3.8.

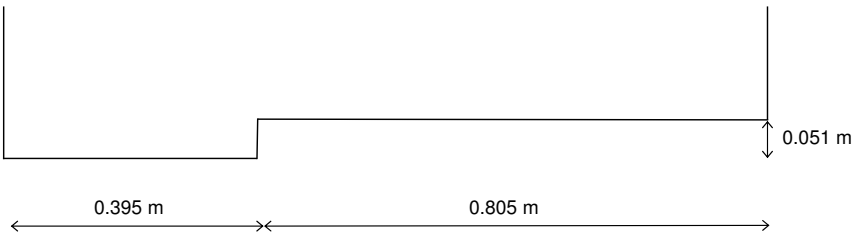

Figure 3.8: Cross-section of the LMFA flume

The flume is a rectangular straight compound channel. The flume is 7.98 m long and

has a main channel width of $B_{mc} = 0.395$ m and a floodplain width of $B_{fp} = 0.805$ m. The longitudinal slope is 1.810^{-3} m/m.

3.2.2.2 Setting of quasi uniform flow conditions

In LMFA uniform flow conditions without rods were demonstrated to be achieved at approximately x = 3.1 m Proust *et al.* (2006). For this research the measuring section of reference was located at approximately 5.5 m.

The flow rate corresponding to the available uniform flow conditions without vegetation was kept as upstream condition, while the water level was adjusted to set quasi-uniform flow conditions. The water surface elevation was measured between rods at 1 m intervals in the longitudinal direction and at 0.100 m interval in the lateral direction. The measurements were further conducted at every 0.5 m either side of the measuring section in the flow direction and near the interface at intervals of 0.05 m in the lateral direction. Quasi-uniform flow conditions were considered to be achieved if the water depth did not vary by more than 0.5 mm at $\pm 1.0m$ from the measuring section.

Once the water surface profile was set up, the velocity was measured between two consecutive rods at cross-sections located approximately at x = 1.5 m, 3.5 m, 4.5 m, 6.5 m, at the reference section at 5.5 m. The relative differences of the measured velocities between the velocities measured at 4.5 m and at the measuring section and the velocities measured at 6.5 m and at the measuring section are given in Figure 3.9.

All the relative differences for the measured velocity data points are below $\pm 5\%$ to the exception of a few measured data points located near the interface, which exhibit relative differences up to 6.06%.
The relative differences between the depth-averaged velocity profiles at 4.5 m and 6.5 m with the velocities measured at the measuring section are presented in Figure 3.10.

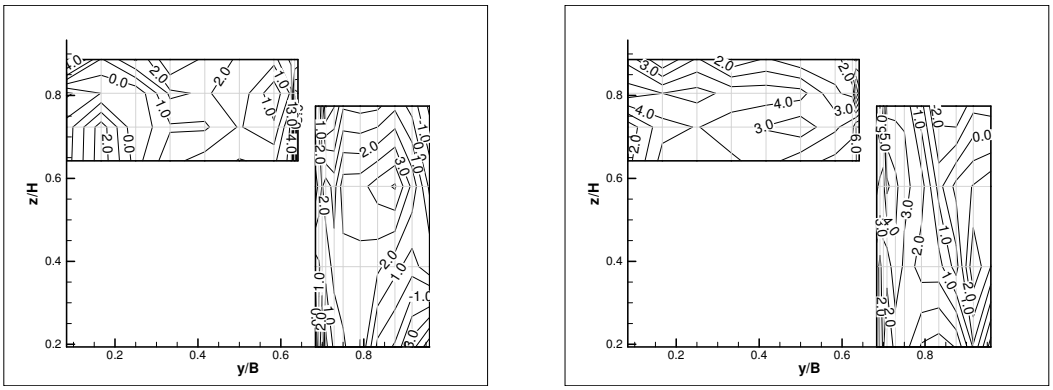

(a) (b)

Figure 3.9: Relative differences (%) between the velocities measured for Dr = 0.44 and $\frac{L}{D}$=8.0 between 5.5 m and (a) 4.5 m (b) 6.5 m.

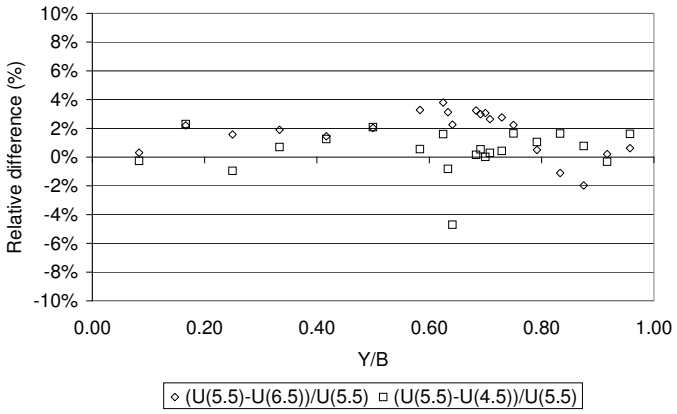

Figure 3.10: Relative difference (%) between depth-averaged velocities at x = 4.5 m, 6.5 m and at the measuring cross-section between rods x=5.5 m for Dr = 0.44 and $\frac{L}{D} = 8.0$

In this case, the highest relative difference is -4.7% and occurs near the interface between the main channel and the floodplain. The comparison of depth-averaged velocity profiles does not provide a validation as sound as the comparison of isovels graphs. For instance, some vertical dispersion could be masked in the integration of velocities over the vertical.

3.2.3 Reasoning Behind the Modelling Strategy of Vegetation in Experimental Flume

The configurations of the rods to be used in experiments are defined by the diameter D of the rods and the spacing L between two consecutive rods. As discussed in Section 2.5, L and D are used to define the non-dimensional spacing ratio $\frac{L}{D}$ used (usually in conjunction with the Reynolds number) to characterise the change in flow patterns between two cylinders in tandem (Igarashi, 1984a). In order to ensure that the studied configurations are realistic and representative of engineering situations, the following considerations on L and D are made.

3.2.3.1 Diameters D of the rods in the experiments

Sun (2006) carried out experiments with one rod diameter, namely 9 mm. The impact of the rods on the flow parameters were shown to be significant. The lateral distributions of depth-averaged velocity profiles were very different to the non vegetation case, suggesting that drag force drastically changes the flow structure. The effect of vegetation was for example reflected in the sharp decline of the depth-averaged velocity profiles near the wall. The maximum velocities were also pushed towards the sidewalls in the main channel and in the floodplain. This may have been in part due to the narrowness of the flume and the somewhat large 9 mm diameter of the rods used in experiments.

In this research, two smaller diameters of 3 mm and 6 mm were used in Loughborough laboratory to allow for comparison with the 9 mm rods. The 6 mm rods were made of wood, which is similar to the 9 mm wooden rods. However, wood proved to be unsuitable for the 3 mm rods as the wooden rods were too fragile. Instead, fiber glass plastic 3 mm diameter rods were used. Both sets of rods were approximately 100 mm high.

An attempt was also made to physically model vegetation with foliage along the floodplain. For that purpose, a series of test tube brushes from Fisher Scientific (code BUR-610-030G) with 3 mm diameter steel tube and 35 mm brush strand diameter as shown in Figure 3.11 were also lined along the floodplain edge to represent trees.

Figure 3.11: Brush used for the modelling of tree with foliage

Each brush was prepared for the experiments by cutting the cotton end with wire cutters to obtain a constant density along the length of the brush. The final brushes were 50 mm high. An analysis using Autocad confirmed that the bristles were uniformly distributed in space along the brush (Figure B.6 in Appendix (B). Compared to natural foliage, such a dense uniform spatial distribution is likely to be more representative of deciduous shrubs and trees observed during estival conditions in England for example (Vincent, 2005). The bristles are rigid and together with the 3 mm diameter rod represent an effective frontal area of 72%. The use of 3 mm diameter brushes allowed direct comparison with the 3 mm fiber glass plastic rod without foliage, as shown in Figure 3.12.

The rods and brushes were placed so that their bases touched the floodplain and no water could seep below. The 3 mm diameters rods and brushes were placed into a strip of wood with 3 mm diameters holes spaced evenly at 24 mm spacing. The 6 mm diameters rods were placed evenly in a strip of wood of 6 mm diameter holes spaced every 48 mm.

Finally in LMFA, where the flume is 1.2 m wide, 9 mm diameter wooden rods were fitted to the channel. A strip of wood with holes drilled spaced every 48 mm was used.

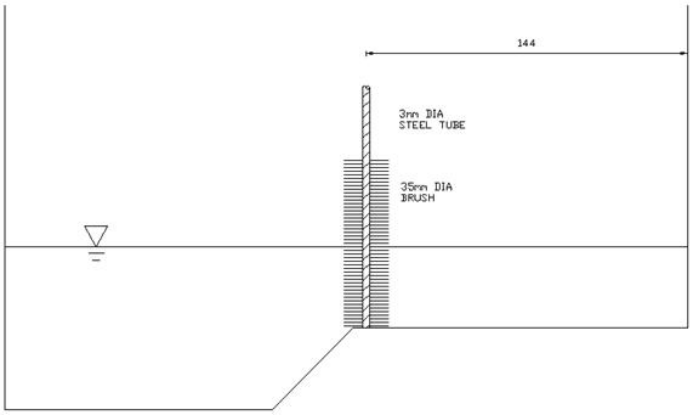

Figure 3.12: Positioning of the rods and brushes along the floodplain

Rotating wooden bars were nailed at the end of the strips, abutting the sidewalls of the flumes as shown in Figure 3.13.

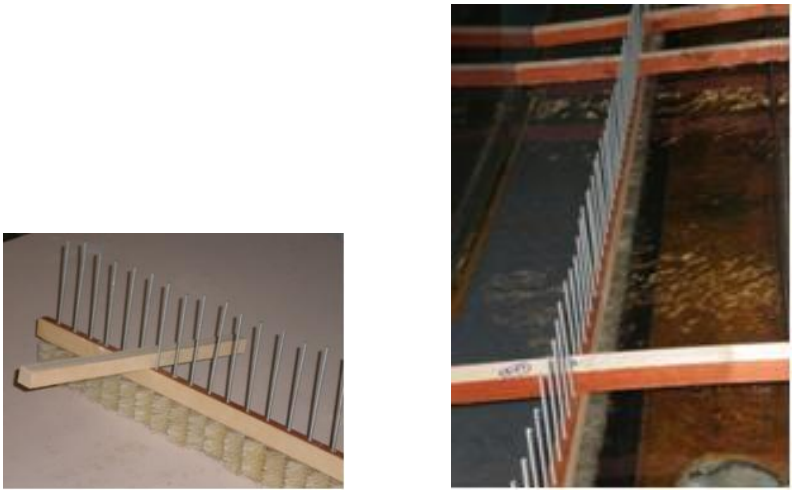

(a) (b)

Figure 3.13: (a) and (b) Brushes anchorage device.

The diameters of the rods in relation to the main channel width B_{mc} compare favorably with natural conditions. The experimental ratios $\frac{D}{B_{mc}}$ for smooth rods vary between 0.75% and 1.96%. For example, along the River Nene, in Figure 1.1, the ratio $\frac{D}{B_{mc}}$ varies between 1.6% and 3.3%. In the stretch of the River Rhône studied in Chapter 6, $\frac{D}{B_{mc}}$ is on average 0.5%. For the brushes, the ratio between the spread

of the bristles and the rod diameter is approximately 11.7, which which is in line with the range of observations made on site. Figure B.6, in Appendix B, summarises the different rods used in the experiments.

3.2.3.2 Spacing L between rods

Sun (2006) first decided to investigate a configuration based on the so-called critical spacing $\frac{L}{D} = 3.5 \sim 3.8$ (Igarashi, 1984a) and adopted $\frac{L}{D} = 4.4$. The dataset was then completed with $\frac{L}{D} = 13.3$.

In Loughborough laboratory, spacing ratios of $\frac{L}{D} = 8.0$ and 16.0 were used to investigate the effects of vegetative density on the flow. In LFMA laboratory, the measurements were carried out with spacing ratios of $\frac{L}{D} = 16.0$ and 32.0. These spacing ratios are much greater than the critical spacing ratios mentioned in 2.5.2. The spacing ratios were confirmed for applicability via literature review and the collection of spacing ratios of trees in field studies.

First, guidelines on planting trees found in literature (Landcare Notes, 1998) were studied to define applicable spacing ratios of rods. Spacings between 8 to 16 times the diameter of trees were found to be representative.

In addition, tree spacing surveyed along three rivers in Japan (Shiono *et al.*, 2009), whose results are shown in Figure 3.14, confirmed that such tree spacings provided a realistic configuration.

Spacing ratios of trees along the floodplain of a part of the river Thames were also collected. These ratios were derived by taking photos of trees along the river bank and scaling the ratios between trees so that the frequency diagram shown in Figure 3.15 could be produced.

Finally, tree survey was conducted along the banks of the river Rhone in the area of Pierre-Bénite on the right bank. The average tree diameter in this case was found to be 0.5 m with an average spacing ratio $\frac{L}{D}$ of 10.

The vegetation surveys along rivers were conducted in three different countries, namely

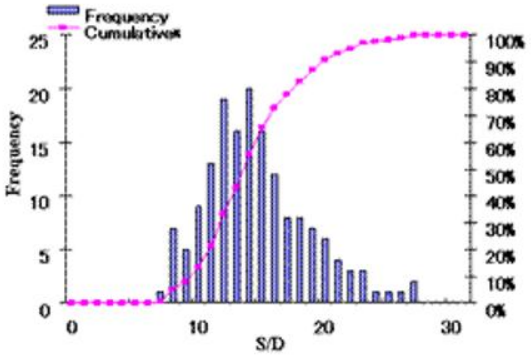

Figure 3.14: Spacing ratio from vegetation survey along three rivers in Japan

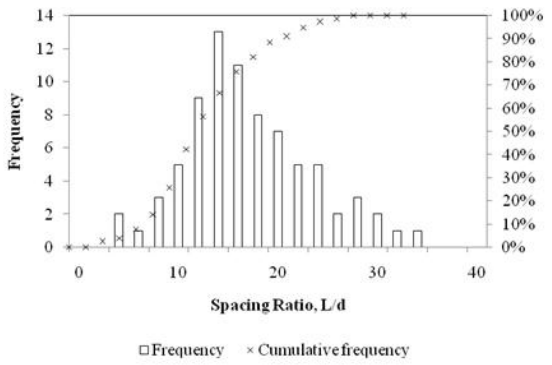

Figure 3.15: Spacing ratio from vegetation survey along the Thames River

England, France and Japan. The results appear to be consistent despite the geographical differences of the survey sites. Therefore the selected spacing ratios are confirmed as applicable to natural rivers.

3.3 Measuring Techniques

3.3.1 Stage-discharge

In Loughborough laboratory, a point gauge fitted to a digital caliper as presented in Figure 3.16 was used to measure the water depth with an accuracy of 0.01 mm. Once quasi uniform flow condition was set up, the water level was watched during the experiments to ensure that it remained constant.

The pump that is fitted to the flume is linked to an electronic flowmeter. The flowmeter was used to calibrate the flow rate with the motor frequency. That calibration curve was used to estimate directly the flow rate. However, uncertainties arose as to the reliability of the frequencies displayed digitally for the low flows. All flow rates were therefore also measured between four and eight times for each configuration by weighing the water on a scale for a given time. The digital caliper and the flowmeters are shown in Figure 3.16.

(a) (b)

Figure 3.16: (a) Digital caliper (b) Flowmeter.

In LMFA, the water surface elevations were measured using a pressure sensor measuring the air column between the sensor and the water surface. The water depth is obtained by subtracting the measured elevation with the corresponding bed surface elevation. The sensor has a sampling frequency of 50 Hz and a sampling diameter of 1 cm by 1 cm.

Two flowmeters controlled electronically by a command control board were fitted to the pipes bringing water to the main channel and the floodplain. Time-series of the readings from the flowmeters were acquired throughout the experiments via LabView.

3.3.2 Data Acquisition

3.3.2.1 TracerDaq

To measure boundary shear stress and velocity distributions, a computer software package is required which enables the pressures to be calculated in the flow. In Loughborough laboratory, the recordings from the Pitot-static and Preston tube were processed using the data acquisition software TracerDaq, by Coleman-Parmer. TracerDaq allows the voltage time-series to be input directly into a spreadsheet. This spreadsheet allowed all of the results across the channel to be easily stored and manipulated. The sampling rate was set at 1.00 samples/second and the accuracy was set to 0.0001 Volts.

3.3.2.2 LabView

LabView was used in LMFA to obtain the time-series outputted from the flowmeters, the pressure gauge, the micro-propellers, the Pitot tube and the Preston tube. The automatic displacement was also commanded through LabView.

3.3.3 Pressure transducer

The recordings taken by the Preston and Pitot-static tubes were passed through an LPM5480 low-range pressure transducer which measures the pressure difference in the instruments. Two compartments in the pressure transducer are separated by a diaphragm which flexes with the change in differential pressure. The displacement of the diaphragm due to a pressure difference Δp can be converted into a voltage. This principle was used to calibrate the pressure transducer.

The voltage (V) and the pressure difference Δp were calibrated by changing the water level from 10 mm to 50 mm in a calibration tank. A digital caliper was used to adjust the height of the water column. The calibrated relationship between Δp and (V) was expressed as:

$$\Delta p = 68.9130V - 3.5209 \tag{3.1}$$

Before any readings were taken in the flume, the pressure transducer was completely flushed of air using the tap valves to ensure that it did not affect the readings. After every flushing event, the transducer was left for 1 hour to allow the internal membrane to settle.
As mentioned in 3.3.2.1, the output from the transducer was read using TracerDaq, which produced a graph of voltage against time. The transducer was mounted so that the membrane was above the flow and stagnant bucket water level to prevent negative pressures being induced, causing suction of air into the transducer.

3.3.4 Pitot tube

3.3.4.1 Principle

The Pitot tube is a pressure instrument to measure longitudinal fluid flow velocity. The principle of the Pitot tube was discovered in the early 1700s by the French engineer Henry Pitot. The Pitot tube is an inexpensive instrument and its ease of use has made it a popular instrument in the field of hydraulics. The main purpose of the experiments carried out in this study is to obtain isovels and depth-averaged velocity profiles.

The L-shaped Pitot tube used in this study has an inner tube diameter of 2.2 mm and four outside holes, placed perpendicular to the flow, of diameter 0.75 mm. It was connected to a low range pressure transducer Drück of range 0 to 5 mBar and output 0 to 10 Volt. A photograph of the pressure transducer and the Pitot tube is given in Figure 3.17.

The pressure difference (Δp) is obtained from the output of the pressure transducer. The relationship linking the flow velocity U to the pressure difference stems from the Bernoulli Equation. The Bernoulli Equation 3.2 states that the static pressure plus one half the density times the velocity U squared is equal to the total pressure. Hence:

$$U = \sqrt{\left(\frac{2\Delta p}{\rho}\right)} \tag{3.2}$$

(a) (b)

Figure 3.17: (a) Drück Pressure transducer (b) Pitot tube plunged into beaker and horizontal ruler

where ρ is the fluid density.

Before the measurements, a reference pressure was determined by placing the Pitot tube in a plastic beaker for five minutes. The submerged Pitot tube was then moved into the flowing water of the flume by carefully placing it into a small container. The Pitot tube has to remain submerged so that air does not enter the pipes system. The reverse of this procedure was performed before transferring the instrument from main channel into floodplain and at the end of the measurements. The background pressure would then be measured and compared to the background pressure at the start of the experiments. If the discrepancy proved to be more than 5% the experiment had to be repeated. Although rare, the entrance of air into the measuring system can be the cause of the such discrepancy.

During measurements, the Pitot tube was placed perpendicular to the flow direction

and the pressure difference between static and dynamic pressures was measured.

3.3.4.2 Convergence graphs

The membrane of the pressure transducer requires some time to respond to the movements of the Pitot tube. Tests were performed at several points for the deeper and dense rod case of relative depth $Dr = 0.50$ and $\frac{L}{D} = 8.0$. Figure 3.18 shows the evolution of the typical response time to the movements of the Pitot tube to four positions.

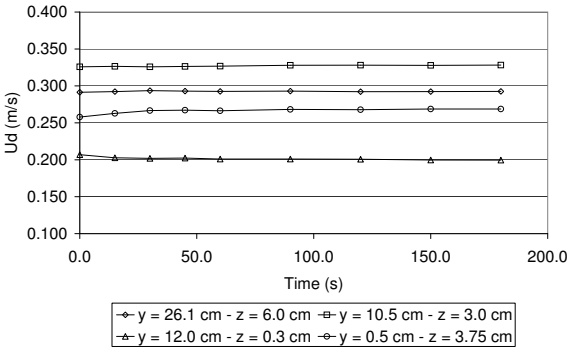

Figure 3.18: Evolution of measured velocity in function of response time

The velocity measurements clearly become stable after one minute so that the response time was chosen to be one minute.

The record time was selected after several tests. Figures 3.19 and 3.20 show the relative discrepancies between the velocity measurements at 30 s and 60 s respectively with measurements taken at 120 s for the deeper and dense rod case of relative depth $Dr = 0.50$ and $\frac{L}{D} = 8.0$. The measurements at the interface, in the wake area of the rods and near the boundaries were the ones that required the longest record time before the mean signal remained constant. The relative differences of most velocity measurements between the recording time of 60 s and 120 s were within $\pm 2\%$ and all these relative

differences were comprised between ±4.7%. Consequently, the record time was set to one minute for all measurements.

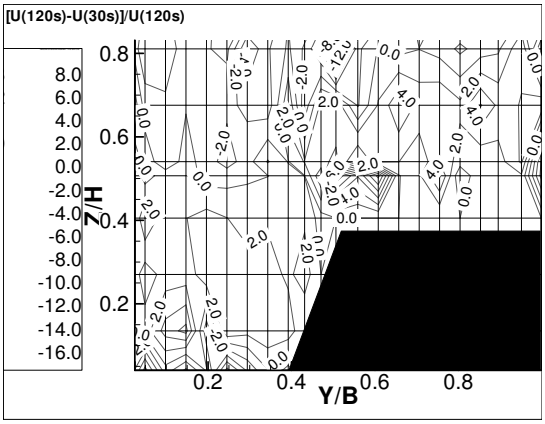

Figure 3.19: Relative difference (%) between velocities measured after a recording time of 120 s and 30 s

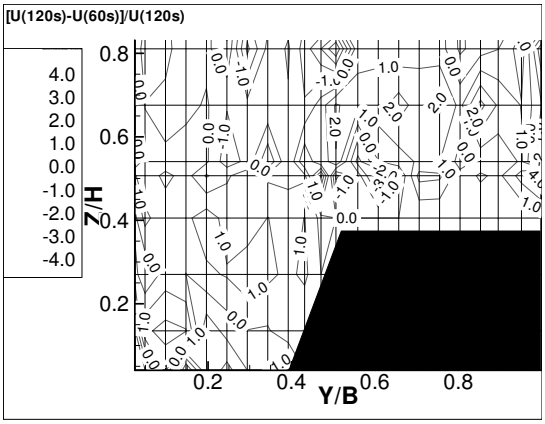

Figure 3.20: Relative difference (%) between velocities measured after a recording time of 120 s and 60 s

The velocities were integrated to calculate the flow rate. The results were then directly compared with the flow measured from the flowmeter. The estimated accuracy of the Pitot tube is of the order of 3% , which is the typical error between integrated and measured flow values. All the integrated values were comprised between 0.4% and 5.7% and some errors were only marginally over 5%.

3.3.5 Micro-propeller

3.3.5.1 Principle

In LMFA, velocities were measured using a micro-propeller. The instrument was mounted on the automatic displacement. The propeller had a diameter of 15 mm.

The measured velocity fields were integrated to calculate the flow rate and to allow comparison with the discharge imposed by the flowmeters. The discrepancies were typically between 0.4% and 4.6%.

3.3.5.2 Measurement grids

In Loughborough, measurements with the Pitot tube were carried out at a lateral interval of 1.5 cm. On the sideslope and near the interface, the measurement spacing was refined to every 1.2 cm. The measurements on the vertical were carried out at intervals of approximately $\frac{H}{7}$ with a refined resolution near the floodplain height, as seen in Figure 3.21.

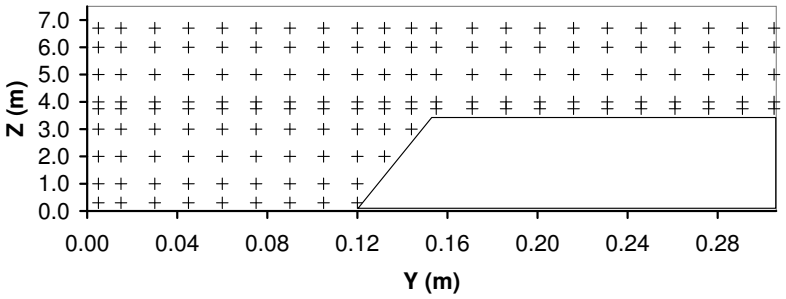

Figure 3.21: Measurement grid for Pitot tube in Loughborough for a relative depth of Dr = 0.51

In LMFA, measurements were carried out every 5 cm and every 1 cm within $\pm 5cm$ of the interface area. The measurements were made at 20%, 40%, 60% and 80% of the flow depth in the main channel H_{mc} and H_{fp} floodplain as illustrated in Figure 3.22.

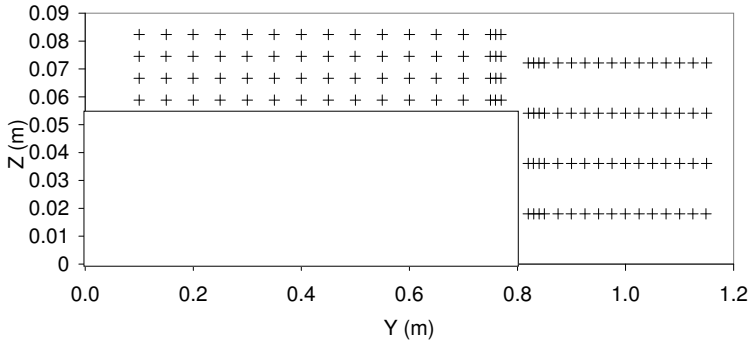

Figure 3.22: Measurement grid for micro-propeller in LMFA for a relative depth of Dr = 0.43

3.3.6 Preston tube

3.3.6.1 Principle

The Preston tube was developed by Preston (Preston, 1954) and has been widely used in experimental studies, especially in the UK. Its principle is the following: the boundary shear stress τ_B can be obtained from the pressure difference between the dynamic and static pressures ΔP in the Preston tube pipes when the Preston tube lies on the boundary. The Preston tube requires great care when used and needs to lie flat on the boundary. The Preston tube has been shown to provide a measurement accuracy of +/- 6% (Patel, 1965).

The diameters of the static and dynamic pressure pipes of the Preston tube used in this study are 3.00 mm and 2.72 mm respectively. There are four circular holes of diameter 0.54mm on the side of the static pressure pipe.

3.3.6.2 Calibration

In order to determine the boundary shear stress τ_B from the measured pressure difference ΔP, Patel's method (Patel, 1965) was used. Patel derived the following relationships:

$$y^* = 0.50x^* + 0.037y^*,\ y^* < 1.50 \tag{3.3}$$

$$y^* = -0.0060x^{*3} + 0.1437x^{*2} - 0.1381x^* + 0.8287,\ 1.50 < y^* < 3.50 \tag{3.4}$$

$$x^* = y^* + 2\log_{10}\left(1.95x^* + 4.02\right),\ 3.50 < y^* < 5.30 \tag{3.5}$$

where:

$$x^* = \log_{10}\left(\frac{\Delta P d^2}{4\rho\nu^2}\right) \tag{3.6}$$

and

$$y^* = \log_{10}\left(\frac{\tau_B d^2}{4\rho\nu^2}\right) \tag{3.7}$$

where d is the external diameter of the dynamic tube. Patel's method was found suitable in studies that used Preston tube of similar diameter to the one used in this study (Sutardi and Ching, 2001) and was therefore adopted.

The offset value of the Preston tube was determined before each experiment by putting the tube into still water in a plastic beaker. Then the Preston tube was moved into flowing water in the channel and fixed on a holder. The Preston tube was held in place using a clamp, which was attached to the vertical point gauge rod. When measurements were taken, the position of the Preston tube across the channel was controlled by a horizontal ruler spanning the width of the channel at the top of the tube. Visual checks were carried out to ensure that the Preston tube was correctly lying on

the channel boundaries.

The offset value was verified after measuring a sub-section and at the end of each experiment to ensure consistency in the measurements. If the relative difference between the offset value at the start and the end of the experiment was greater than 5% the measurements were repeated.

While velocity measurements can be validated to some extent against the experimental discharge by integration, boundary shear stress measurements cannot be directly validated when the rods are in place. As mentioned, boundary shear stress can be integrated and compared to the two-dimensional boundary shear stress value $\rho g R S_0$ for uniform flow conditions in absence of vegetation. However, force balance cannot be applied to verify the boundary shear stress measurements because drag force could not be measured directly. That is why the procedure of control described above, namely the check on the offset values is important. During the course of the experiments, another procedure of control was performed at the start of the measurements. In order to use the Preston tube with confidence, a check was performed at bank-full conditions. This allowed a comparison between the total shear stress obtained derived from the measurements and the theoretical value two-dimensional value $\rho g R S_0$ where R is the hydraulic radius. Bankfull conditions were chosen for ease of setting up. If the results were within $\pm 5\%$ of each other then the Preston tube was considered to perform satisfactorily.

3.3.6.3 Convergence graphs

In order to define a suitable response time and record time, the same testing methodology as used for the Pitot tube was employed.
The response time of the pressure transducer to the Preston tube movement was assessed by moving the Preston tube from still water to the fast moving water of the main channel center. Then the Preston tube was moved to the slow moving water to

the floodplain edge. Finally, the Preston tube was moved to the interface at the edge of the rod alignment. The results are presented in Figure 3.23.

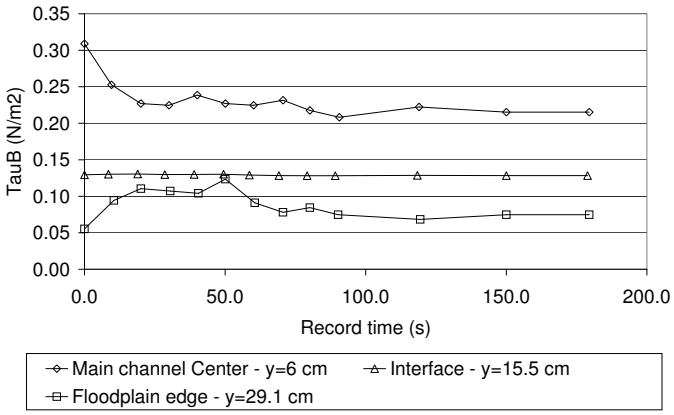

Figure 3.23: Boundary shear stress evolution in relation to response time

The response time increases when the Preston tube moves from areas where the flow velocity changes significantly. Based on the results, a response time of 2 min proves suitable for the measurements.

The measurements were first carried out for the dense case $\frac{L}{D} = 8.0$ and for the 6 mm diameter rods for the whole cross-section for a recording time of up to 240 s. The results are presented in Figures 3.24 and 3.25. Figure 3.24 shows the typical evolution through time of boundary shear stress in the main channel (y=6 cm), in the floodplain (y=24.6 cm) and at the interface (y=15.6 cm). Figure 3.25 presents the relative difference between the boundary shear stress derived after 240 s with that derived after 30 s, 60 s, 120 s and 150 s across the channel. The results of the boundary shear stress appear to remain stable from 120 s. A record time of three minutes was adopted for all measurements.

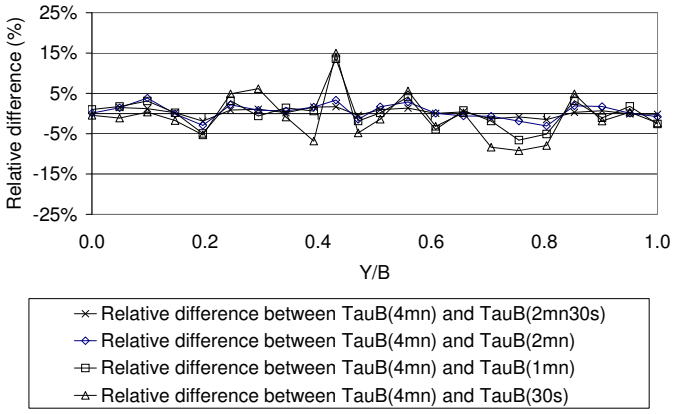

Figure 3.24: Boundary shear stress evolution in relation to recording time across the channel

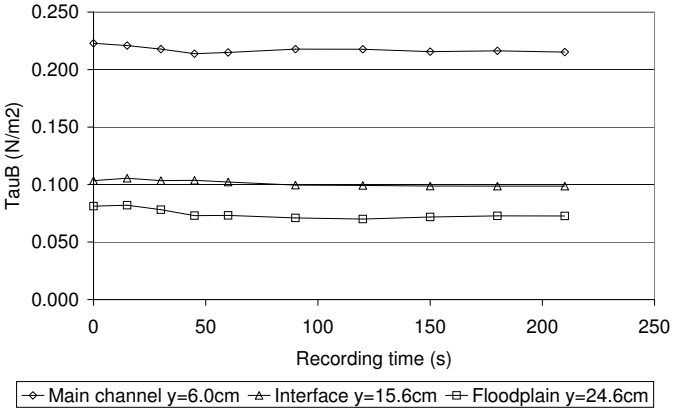

Figure 3.25: Boundary shear stress evolution in relation to recording time at three locations

3.3.7 LS-PIV

3.3.7.1 Experimental Set-up and apparatus

Velocities at the water surface were calculated using a large-scale PIV method. In the narrow flume of Loughborough University, saw dust was spread uniformly on the surface using a sieve and video clips were recorded for two minutes at a resolution of

720 x 576 and a frequency of 25 frames per second using a hard disk camera recorder Everio JVC GZ-175 (3.26).

Figure 3.26: Everio Camrecorder used in Loughborough University for LS-PIV

The Everio JVC GZ-175 camrecorder cannot record progressive movie clips and only offers an interlaced mode. This means that each camrecorder image is cut into two parts, called fields. One field contains the odd-numbered scan lines of the image, while the other contains the even-numbered ones, and the recorded video-clip displays them alternately. This is an important factor to consider when analysing the video clips.
Six targets were set on the walls of the flume that appear on the camera field. The positions of these targets and the location of the camera were surveyed. An example of the LS-PIV set-up is given in Figure 3.27.

Figure 3.27: Example of LS-PIV set-up at Loughborough University

The Large Scale PIV software developed by Tsubaki and Fujita from Kobe university was adopted for the post-processing of the data Tsubaki and Fujita (2007). This software includes a simple de-interlace algorithm. The algorithm deletes the original even field and interpolates the even field from the odd field image. The interpolation is carried out by averaging each neighboring two odd lines.

Velocities at the water surface were also calculated at LMFA using large-scale PIV method. The Panasonic HDC-SD9, as seen in Figure 3.28, was used to carry out the LS-PIV. The HDC-SD9 provides full high definition resolution at 1920 x 1080 with progressive recording at 25 frames per second. Two types of seedings were tried, namely grass seeds and confetti.

Figure 3.28: Panasonic HDC-SD9 progressive camrecorder used for LS-PIV at LMFA

Video clips of 1 min to 2 min duration were recorded. The dataset was analysed using the LS-PIV postprocessing software developed by Hauet (Hauet, 2006).

3.3.7.2 Principles of Large Scale PIV

The principles underlying the Large Scale PIV technique are summarised in Hauet *et al.* (2007). When a camera records an image, the camera maps the luminosity of the captured area to its CCD sensor. The information collected from the field is converted into image coordinate system using equations 3.8 and 3.9:

$$u - u_0 = d_u \frac{m_{11}(x - x_0) + m_{12}(y - y_0) + m_{13}(z - z_0)}{m_{31}(x - x_0) + m_{32}(y - y_0) + m_{33}} \tag{3.8}$$

$$v - v_0 = d_v \frac{m_{21}(x - x_0) + m_{22}(y - y_0) + m_{23}(z - z_0)}{m_{31}(x - x_0) + m_{32}(y - y_0) + m_{33}} \tag{3.9}$$

where [x,y,z] are the 3D field coordinate of visible point relative to the Cartesian coordinate system, [u,v] are the 2D pixel coordinate of the same point in the image, u_0 and v_0 are the pixel coordinates of the centre of the image; $[x_0, y_0, z_0]$ are the space coordinates of the camera and d_u and d_v are coefficients relating horizontal and vertical scale factors to the effective focal length of the camera. The factors m_{ij} are the elements of the so-called transformation matrix M.

The two main stages to process the data consists in the geometric transformation of the images and the calculation of the water surface velocity.

In order to carry out the geometric transformation, the video clips are first split into images. These images are geo-referenced by using ground reference points or targets of known physical coordinates. Assuming that the water surface is horizontal, the inverse of Equations 3.8 and 3.9 write:

$$x = \frac{a_1 u + a_2 v + a_3}{a_7 u + a_8 v + 1} \tag{3.10}$$

$$y = \frac{a_4 u + a_5 v + a_6}{a_7 u + a_8 v + 1} \tag{3.11}$$

Four geo-reference points are sufficient to determine the a_i parameters in Equations 3.10 and 3.11. Five and six reference points were used to reference the data in this study and Equations 3.10 and 3.11 were solved using least square estimation.

Once the geometric transformation is completed a set of transformed geo-referenced images of same height and width is obtained and the PIV analysis can start. The principle of the PIV analysis is based on the search of a maximum correlation between an interrogation area centered on a point $P_{i,j}$ in the first image at time t and the searching area centered on a point $Q_{i,j}$ on the second image at time $t+dt$. The most probable

displacement of a particle of fluid from point $P_{i,j}$ during the lapse of time dt is the one for which the correlation coefficient is maximum. The calculation is carried out on a calculation grid defined by the user.

The main sources of error in the steps that lead to the derivation of surface velocity are:

- The accuracy of the reference points or targets used to geo-reference the images;
- The size of the interrogation area which must scale with the flow patterns to identify;
- The seeding that needs to provide enough contrast with the water surface so that displacement can be tracked.

In this study, these issues were addressed in the following way. The reference points were surveyed accurately using a total station in Loughborough to reference the targets. In LMFA the reference points were known surveyed markers related to the flume (screws, canal edges, interface between floodplain and main channel).
Lighting proved to be an important factor in this research. Initial inadequate lighting in Loughborough caused the experiments to be repeated. To improve the contrast created by the seeding, two flood lights placed either side of the flume were used in Loughborough.

3.3.8 Summary of measuring techniques

Table 3.1 summarises the instruments used during the experiments carried out in Loughborough University and LMFA flumes.

In this research, the geometry of the flumes and the instruments used to measure velocity and boundary shear stress limit the choice of relative water depths. Indeed, measurements with the Preston tube and micro-propeller in particular cannot be carried out for relative water depths less than $0.2 \sim 0.25$. Below these relative water depths, the water depth on the floodplain becomes too small to use the Preston tube

Table 3.1: Summary of measuring techniques

Instrument	**Characteristics**	**Derived quantity**	**Case**
Pressure sensor	Sampling frequency set to 50 Hz	Water level	LMFA flume
Point gauge	Fitted to a digital caliper	Water level	Loughborough flume
Electronic flowmeters	Two flowmeters used in LFMA, to control main channel and floodplain flow rates	Flow rate	LMFA and Loughborough flume
Pitot tube	Inner diameter 2.2 mm and outer diameter 0.75 mm	Velocity	Loughborough and LMFA flumes
Micro-propeller	15 mm diameter	Velocity	LMFA flume
Preston tube	Static and dynamic pressure pipe diameters of 3.00 mm and 2.72 mm respectively	Boundary shear stress	Loughborough and LMFA flumes
Everio JVC GZ-175 Camrecorder	Interlaced mode, recording at 25 frame per second	Surface velocities	Loughborough flume
Panasonic HDC-SD9 Camrecorder	Progressive mode, recording at 25 frame per second	Surface velocities	LMFA flume

and not enough data points can be measured with the micro-propeller to obtain a representative vertical velocity profile. In nature, most floods occur at small relative water depths, typically in the range $0.05 \sim 0.25$ like the actual flood events investigated in Chapter 6, so that the studied flow cases correspond to extreme flood events.

CHAPTER 4

Experiments in Loughborough University Laboratory

"Remember, when discoursing about water, to introduce first experience, then reason".
Leonardo da Vinci

4.1 Introduction

In this chapter, the results of experiments carried out in Frank Gibb Laboratory of Loughborough University are presented. Section 4.2 explains the rational from an engineering perspective behind the analysis of the experimental results. Section 4.3 succinctly recalls the results of the no rod case and Section 4.4 summarises the characteristics of flow structures identified in the compound channel flume with smooth rods and brushes along the floodplain. Finally, Section 4.5 summarises the main findings of the experiments.

4.2 Methodology

The rational behind the different steps taken in the data analysis is presented in this Section.

From a flood defence perspective, the water depth in the channel is one of the main engineering input required to design flood defence structures and in flood mapping. When setback flood defence embankments have been built on a floodplain, riparian trees might be planted along the main channel for amenity and ecological purposes. It is therefore important to know the impact of basic parameters such as tree types and density on flood water levels. Hence, the impact of rods along the main channel on the main channel and floodplain water depths (H_{mc} and H_{fp}) and on discharge (Q) is first examined. The rational behind the choice of the rod and brush diameter and density used in experiments has already been laid out in Chapter 3.

The isovels and the depth-averaged longitudinal velocity (U) are then derived from measurements. Velocities on the floodplain are also an important parameter in the planning of new development and in risk assessment. For example, Strategic Flood Risk Assessments in England and Wales require the definition of so-called Rapid Inundation Zones, assessing the risks caused by velocity on floodplains.

Reynolds stresses could not be directly measured in the experiments carried out in Loughborough as the studied flows were too shallow for the available instrumentation (ADV). However, horizontal depth-averaged Reynolds stress ($\overline{\tau_{xy}}$) were modelled from depth and velocity measurements. The horizontal Reynolds stress gives an indication of the momentum transfer between the main channel and the floodplain, while also reflecting the level of mixing occurring in the flow field. Hence, indication of the impact of rods on Reynolds stresses can help engineers to better handle issues related to pollutant transport and sediment transport.

Boundary shear stress (τ_B) measurements are then analysed. The differences in amplitude of boundary shear stress due to rods give an indication of the impact of trees on erosion along the main channel, as boundary shear stress is directly related to the entrainment of sediment particles. The difference between ($\tau_B - \rho g H S_0$) is associated with

momentum transfer, as discussed in Shiono and Knight (1991) and is therefore investigated. The apparent shear stress is then calculated and its amplitude is also analysed.

Finally, drag force is calculated from the boundary shear stress and water depth measurements, and is compared to analytical formulae used by engineers. At the cross-section scale, drag force competes with boundary shear stress to offer resistance to the gravity driven flow. The relative weight of drag force in the balance of forces highlights the significance of vegetation in flood management.

4.3 Flow Characteristics without Vegetation (Sun, 2006)

The flow structure of non-vegetated compound channels in the trapezoidal straight compound channel of Loughborough University Laboratory have been investigated for three relative depths, namely 0.24, 0.37 and 0.50. The results of these experiments have been summarised in Sun (2006) and only the main findings are recalled in this paragraph.

The results of the depth-averaged velocity and of the boundary shear stress are presented in Figures 4.1.

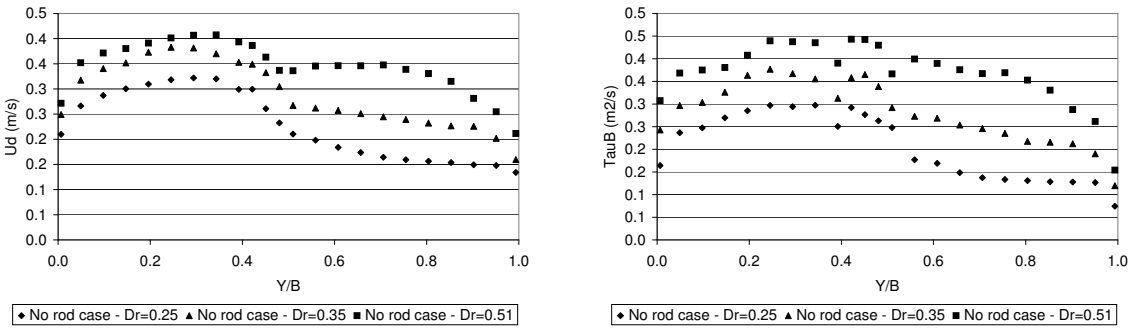

(a) (b)

Figure 4.1: Results of no rod flow cases in Loughborough (a) Depth-averaged velocity profiles (b) Boundary shear stress profiles

The results of three dimensional flow structure (Sun and Shiono, 2009) showed strong velocity bulging at the interface between the main channel and the floodplain and near the corner. This is caused by the momentum transfer between the main channel and the floodplain via secondary currents. In this study, the velocity bulging was observed to be stronger for the higher relative depths.

The apparent shear stress was observed to peak near the interface, and the ratio of the apparent shear stress to $\rho g H S_0$ decreased as the relative water depth increased, which indicated that the lateral shear becomes weaker under deep-water conditions.

In the compound channel without rods, the bed shear stresses were smaller than $\rho g H S_0$ in the main channel and larger on the floodplain, which was attributed by Sun (2006) to the gradients of the modelled Reynolds shear stress $\frac{H\partial\tau_{xy}}{\partial y}$ and secondary current $\frac{H\partial(UV)_d}{\partial y}$. The values of $\frac{H\partial\tau_{xy}}{\partial y}$ and $\frac{H\partial(UV)_d}{\partial y}$ were much larger near the junction between the main channel and the floodplain than those outside this region and this indicated that the effect of $\frac{H\partial(UV)_d}{\partial y}$ can be neglected outside the interface area in modelling.

4.4 Flow Characteristics in Presence of One-Line Vegetation

4.4.1 Summary of experiments

Three series of experiments were carried out in the 12 m long straight trapezoidal compound channel flume of Frank Gibb laboratory in Loughborough. Series 1 involved experiments with 6 mm diameter rods, Series 2A involved experiments with 3 mm diameter rods and in Series 2B brushes of diameter 3 mm were used to simulate vegetation with foliage. The experiments in each series were carried out for three relative depths

(Dr), namely Dr=0.25, 0.35 and 0.51, and for two spacing ratios of $\frac{L}{D} = 8.0$ and 16.0, for which the letter a and b are used respectively in the series designation. Thus, Series 1a-25 designates the experiment with 6 mm diameter rod for $\frac{L}{D} = 8.0$ and Dr=0.25. Series 2Bb-51 refers to the experiment carried out for with the 3 mm diameter brushes, for $\frac{L}{D} = 16.0$ and Dr=0.51. A summary of the experiments carried out is given in Table 4.1.

The Reynolds number is calculated as:

$$Re = \frac{4RU_{mean}}{\nu} \tag{4.1}$$

where R is the hydraulic radius and ν is the kinematic fluid viscosity.

The values of porosity α can be defined as in Section 2.4.6.2 by $\alpha = 1 - \sum (N_v A_v)$. In Loughborough, rod density varies between 34 rods per m^2 for $\frac{L}{D} = 16.0$ and $D = 6\ mm$ and 136 rods per m^2 for $\frac{L}{D} = 8.0$ and $D = 3\ mm$. The corresponding porosity values are close to unity and thus vary between 0.9981 for Series 1a and 0.9990 for Series 2A.

4.4.2 Nature of the studied flows

Manning's equation is commonly employed by flood engineers. However, as shown by Gioia and Bombardelli (2002), the development of the Manning formula assumes that the flow to which it is applied is hydraulically rough. This assumption therefore needs to be checked. Hydraulically rough regimes have been characterized by Kolmogorov (1941) through the introduction of a length scale η, also known as the Kolmogorov length. At the scale of the Kolmogorov length, viscous effects cannot be neglected anymore and molecular dissipation processes tend to dominate over the inertial energy transfer from larger eddies to smaller ones. On the other hand, if roughness elements are higher than the Kolmogorov length scale η, viscous effect becomes negligible and the flow is characterized as hydraulically rough.

Based on dimensional analysis, the Kolmogorov length η [m] can be shown to be written as a function of the kinematic viscosity ν $[m^2/s]$ and the turbulent kinetic energy (TKE) dissipation rate ϵ $[m/s^3]$:

Table 4.1: Experiments with one-line vegetation in Loughborough straight compound channel flume

Series name	Relative depth	Reynolds number	Flow (m^3/s)	Rod diameter (m)	Rod spacing (m)	Spacing ratio
Series 1a-25	0.25	15915	0.00200	0.006	0.048	8
Series 1a-35	0.35	22148	0.00279	0.006	0.048	8
Series 1a-51	0.51	36200	0.00434	0.006	0.048	8
Series 1b-25	0.25	17474	0.00215	0.006	0.096	16
Series 1b-35	0.35	23051	0.00293	0.006	0.096	16
Series 1b-51	0.51	38417	0.00470	0.006	0.096	16
Series 2Aa-25	0.25	18446	0.00180	0.003	0.024	8
Series 2Aa-35	0.35	24848	0.00252	0.003	0.024	8
Series 2Aa-51	0.51	38728	0.00412	0.003	0.024	8
Series 2Ab-25	0.25	19435	0.00196	0.003	0.048	16
Series 2Ab-35	0.35	25897	0.00264	0.003	0.048	16
Series 2Ab-51	0.51	31458	0.00431	0.003	0.048	16
Series 2Ba-25	0.25	12850	0.00183	0.003	0.024	8
Series 2Ba-35	0.35	17040	0.00225	0.003	0.024	8
Series 2Ba-51	0.51	25825	0.00330	0.003	0.024	8
Series 2Bb-25	0.25	13228	0.00178	0.003	0.048	16
Series 2Bb-51	0.35	15946	0.00210	0.003	0.048	16
Series 2Bb-51	0.51	22567	0.00273	0.003	0.048	16

$$\eta \sim \left(\frac{\nu^3}{\epsilon}\right)^{\frac{1}{4}} \tag{4.2}$$

Kolmogorov (1941) showed that, assuming that the energy dissipation rate ϵ at the Kolmogorov scale equals the energy input rate at larger scales, η can then also be written as a function of hydraulic radius R, viscosity and the average flow velocity U:

$$\eta \sim \left(\frac{\nu^3}{\epsilon}\right)^{\frac{1}{4}} \tag{4.3}$$

Combined with

$$\epsilon \sim \frac{U^3}{R} \tag{4.4}$$

implies:

$$\eta \sim \left(\frac{R\nu^3}{U^3}\right)^{\frac{1}{4}} \tag{4.5}$$

Since the Manning formulae assumes a hydraulically rough regime, the roughness height k_s should be greater than the Kolmogorov length, hence:

$$k_s > \eta \Rightarrow k_s > \left(\frac{R\nu^3}{U^3}\right)^{\frac{1}{4}} \tag{4.6}$$

Manning formulae is written as:

$$U = \frac{R^{\frac{2}{3}}\sqrt{S_0}}{n} \tag{4.7}$$

Equation 4.8 defines an empirical relation between the Manning's n coefficient and the roughness height k_s that has proved sound (Ackers, 1991).

$$n = \frac{k_s^{\frac{1}{6}}}{8.25\sqrt{g}} \tag{4.8}$$

Combining Equation 4.7 and 4.8, one eventually reaches:

$$U = 8\left(\frac{R}{k_s}\right)^{\frac{1}{6}}\sqrt{gRS_0} \tag{4.9}$$

By combining relations 4.6 and 4.9, one obtains the condition for a hydraulically rough regime on the roughness height k_s defined by inequation 4.10 (Huthoff and Augustin, 2006).

$$k_s^7 > \frac{\nu^6}{8^6 R^2 (gS_0)^3} \tag{4.10}$$

S_0=0.001 for the compound channel flume. For the range of wetted perimeters observed in the studied flows (Table 4.1), $\frac{\nu^6}{8^6 R^2 (gS0)}$ varies between 2.2x10^{-5} and 2.6x10^{-5}. The roughness length k_s reported by Sun (2006) is 0.0003, so $O(10^{-4})$, which is one

order of magnitude larger. One can therefore conclude that the studied flows are hydraulically rough.

4.4.3 Phenomenology of the flow cases studied in Loughborough laboratory

Based on flow visualization (Terrier, 2010), the following three patterns were clearly observed for all the experiments carried out regardless of rod diameter, spacing ratio or relative depth. They are illustrated and numbered in Figure 4.2.

1. Wake action

   Wake action was observed in the trail of the flow passing each rod and was reflecting clear flow separation. Observing from aside the flow field, wakes could be seen to deform the water surface elevation by generating vertical amplitudes in the order of a few millimeters. Looking from above at the flow field, the wakes left visible rounded V shapes extending downstream of each rod.
   The intensity of the wakes was seen to increase with relative depth and rod diameter. The increases in intensity were translated in more pronounced wake patterns due to larger deformations of the water surface.

2. Planform coherent structures advected from floodplain to main channel and vice-versa

   Planform coherent structures of characteristic length larger than two to three times the distance between two consecutive rods L were observed for all studied cases. These structures move from the floodplain to the main channel and from the main channel to the floodplain leaving an overall wavy pattern either side of the interface. Even when the wake action was strongest, at high relative depth and for the 6 mm diameter rods, intense momentum exchange seemed to take place in the form of those planform flow structures. Although not measured, the effect of secondary circulation in the entrainment of the planform structures was

obvious.

These structures are bound to influence the flow separation point and the pressure distribution on the rods.

3. Planform eddying motion

   Eddying motion was observed for all cases in the vicinity of the vegetated interface. The characteristic length of these eddies is smaller than or of the order magnitude of the distance between two rods. These were located either side of the line of rods and bear some similarity with the planform vorticies described by Shiono and Knight (1991), although they were not approximately centered on the interface between the main channel and the floodplain.

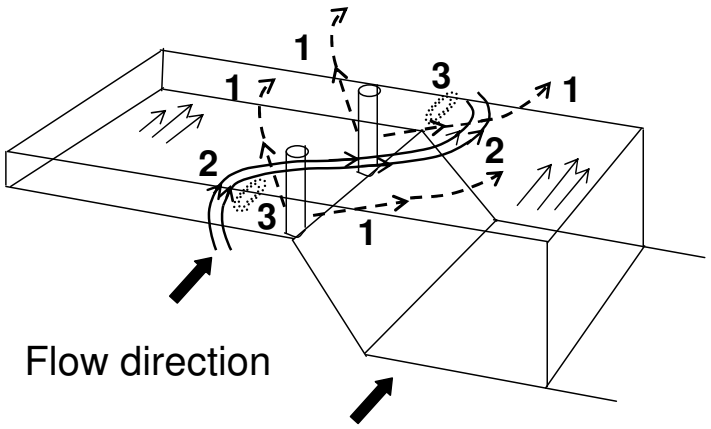

Figure 4.2: Flow patterns observed for all Series in Frank Gibb laboratory 1) wake 2) planform coherent structures 3) planform eddying motion

The local Froude numbers for all cases varied between 0.24 to 0.50, with Series 2A exhibiting the highest Froude numbers. All flows were therefore subcritical. These Froude numbers are smaller than those observed in the no rod case which reached 0.61. This is because one impact of the rods was to reduce the velocity and the experiments with rods were carried out at the same relative depths as with the no rod cases.
The fact that planform vortices moving either side of the interface were observed for all

cases demonstrates that the wake structures behind each rod could not prevent mixing between floodplain and main channel by the planform coherent structures.

4.4.4 Stage-discharge relationships

The stage discharge relationships obtained for the different cases are presented in Figure 4.3.

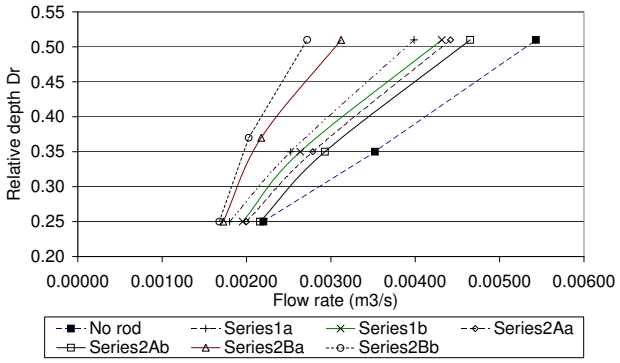

Figure 4.3: Stage-discharge relationships

As rod density and rod diameter decrease, the rating curve approaches that of the no rod case. However, it is significant to note how rods with a diameter D as small as 3 mm can reduce the flow rate when compared to the no rod case. For Series 2Aa, the reduction is about 9% for $Dr = 0.25$ and 19% for $Dr = 0.51$. Yet, a 3 mm diameter rod accounts for approximately 1.0% of the total flow width. These results confirm that vegetation along the main channel of a river does have a detrimental effect in terms of flood defence.

For smooth rods, rod diameter seems to have slightly more impact on flow reduction compared to rod spacing but the difference remains little. The average relative differences between the flow rates of Series 1a and Series 2Aa, and Series 1b and 2Ab are 9.7% and 8.9% respectively as opposed to 6.2% and 7.1% for Series 2Aa and 2Ab, and 1a and 1b respectively. This supports the results from Jordanova *et al.* (2006) who found that increasing the diameter or the vegetation density up to 75% produced very similar

effects on the stage discharge relationship with emergent reeds. However, Jordanova *et al.* (2006) also showed that when decreasing the diameter and the rod spacing by up to 75%, rod spacing proved to have a more significant effect on the stage discharge, hence providing a contrasted overall sensitivity analysis. However, like Jordanova *et al.* (2006), the conclusion that rod diameter and spacing need to be considered in design holds.

For the Series 2Ba and 2Bb, the channel discharge is seen to increase as the flow depth increases, with the brushes providing a drop in total discharge compared to smooth cylinders, which agrees with the findings of Heanen *et al.* (2004). The brushes significantly decrease the channel's total discharge in the compound channel when compared to smooth cylinders for all cases. The flow reduction due to the brush compared to smooth rods increases with relative depth. Between Series 2Aa and 2Ba, flow reductions ranges from 18.5% to 28.4% for Dr=0.25 and Dr=0.51 respectively, compared to 20.2% to 38.3% for Series 2Ab and 2Bb. Interestingly, the increase in vegetative density along the floodplain edge leads to a greater discharge for all channel stages when compared to the less dense vegetation. It had been expected that increasing the brush density would lead to an increase in the chances of flooding, as was the case for Series 1a and b and Series 2Aa and b with smooth rods. However, these results suggest that there is a threshold at which closer spacing of brushes can result in an increase in discharge, thereby reducing flooding effects (Terrier *et al.*, 2010).
One explanation for the increase in discharge with the increase in brush density might lie in the very much reduced momentum transfer between the main channel and the floodplain for increased brush density. As brush density increase, both main channel and floodplain exhibit behaviors closer to independent sections, without the so-called kinematic effect and might therefore have higher discharge compared to the less dense case. The brushes become responsible for the main macroscale turbulence across the flume.

Figures 4.4 and 4.5 give a breakdown of the percentage of total discharge carried by the main channel and the floodplain for the smooth rods and brushes respectively.

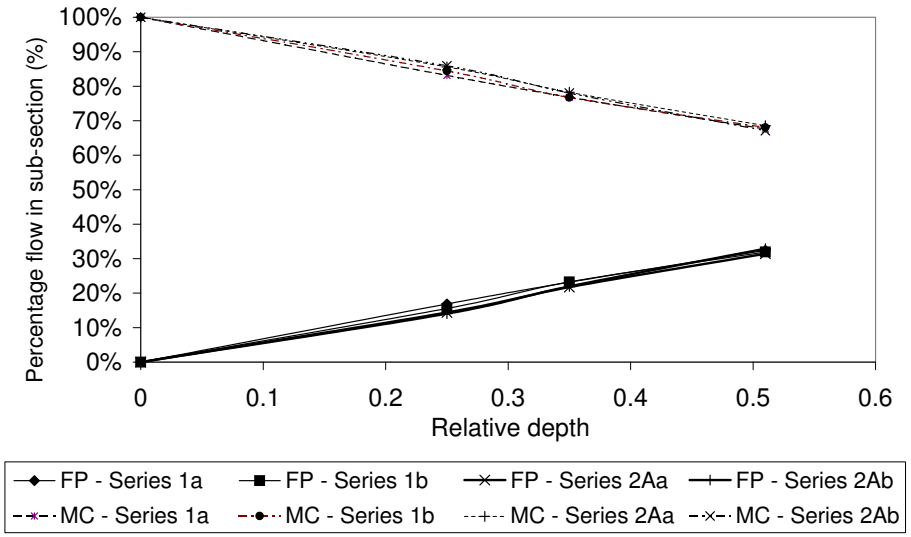

Figure 4.4: Flow distribution in floodplain (FP, solid line) and main channel (MC, dotted line) for the Series 1 and 2A

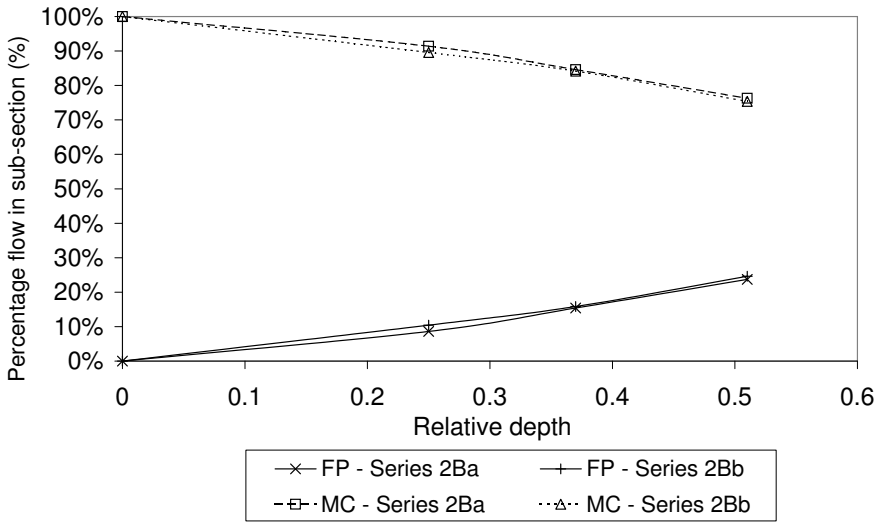

Figure 4.5: Flow distribution in floodplain (FP, solid line) and main channel (MC, dotted line) for the Series 2B

The discharge distribution is derived by the integration of depth-averaged velocities over the main channel and floodplain areas. As relative depth increases towards unity,

the percentage of discharge in each section of the channel tends towards 51% and 49% for the main channel and floodplain respectively. One impact of the brushes is to increase the contribution of the main channel compared to smooth rods. At a relative depth of 0.51, the contribution of main channel to flow distribution for Series 2B is 13.7% greater than in Series 1 and 2A. This might be attributed to the very limited momentum transfer taking place between main channel and floodplain due to the line of brush. In a smooth compound channel, one impact of the lateral shear between main channel and floodplain would be to decrease main channel conveyance (Christodoulou, 1992). In Series 1 and 2A, albeit to a lesser extent, momentum transfer between the compound channel subsections might appear more significantly promoted than in Series 2B.

As depth increases, the increase in discharge is found to be largely provided by the floodplain, whose discharge increases at a much faster rate than the main channel. This correlates the findings of Helmio (2002).

The overall Manning's n values were calculated using the Manning equation (Equation 4.11), whose applicability was verified in 4.4.2.

$$n = \frac{AR^{\frac{2}{3}}S_0^{\frac{1}{2}}}{Q} \tag{4.11}$$

The results are presented in Figure 4.6.

For all rod cases, the Manning's n values increase with the relative depth and the rod density. For Series 2A, the overall Manning's n values are comprised between 0.0102 and 0.0136 for Dr=0.25 and Dr=0.51 respectively. Manning's n values are comprised between 0.0113 and 0.0150 for Series 1. The brushes have for effect to increase significantly the Manning's n values, as the latter are comprised between 0.013 and 0.022 for Series 2B. These increases in Manning's n with relative depth and density, in the case of Series 1 and 2A, translates the effects of the increase in drag force. In Series 2B, the decrease in flow with increasing density explains the corresponding decrease in Manning's n between Series 2Ba and 2Bb.

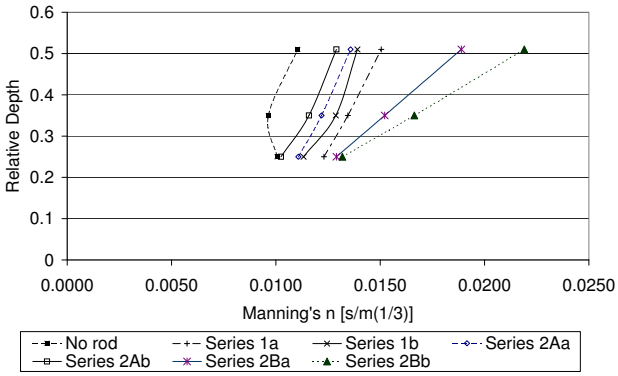

Figure 4.6: Overall Manning's n for the different cases

4.4.5 Velocity distribution

The isovels for the 18 cases of Series 1, 2A and 2B are presented in Appendix B in order to lighten the presentation of this Chapter. Compared to the no rod case, the maximum velocity is clearly shifted towards the outer boundary walls. As density, rod diameter and relative depth increase, there is also a trend for the maximum velocity to be shifted away from the interface. However, the relative depth seems to be a more contributing factor to the displacement of maximum velocity than density, and to a lesser extent than rod diameter. As the water depth increases, the drag force due to rods also increases as well as the effects of wakes and of Prandtls second kind's secondary currents due to the presence of rods. As a result, the magnitude of turbulent intensity in the lateral direction increases but the turbulence intensity in the vertical direction remains similar due to the existence of free surface (Nezu and Onitsuka, 2001). Hence, turbulence anisotropy is enhanced. The secondary currents are therefore strengthened at higher relative water depth regardless of rod density. The shifting of maximum velocity is also determined by the following two factors:

1. the large transverse shear stress generated by the rods, as compared with transverse shear stress generated by the left main channel wall and floodplain wall (Sun and Shiono, 2009).

2. the planform coherent structures advected from the main channel to the floodplain and vice-versa.

For Series 2B, the position of the mean velocity isovel in the main channel appears to change very little between different densities while floodplain flow is seen to be relatively greater for the less dense vegetation. The maximum velocities are suppressed further as flow depth increases, with it being pushed closer to the boundary wall with increasing flow depth in the main channel as observed with smooth rods. However, maximum velocities are pushed towards the centre of the channel in the floodplain which is contrary to the smooth rod cases. The velocity in the brush area is more affected by the smaller depths as vegetation density is changed.
The depth-averaged velocity U_d can be calculated using Equation 4.12:

$$U_d(y) = \frac{1}{H(y)} \int_{z=0}^{H(y)} U(y,z)dz \tag{4.12}$$

The lateral distributions the depth-averaged velocity for the different cases are presented in Figures 4.7 and 4.8.

The results clearly show that the shear layer characterising the momentum exchange in typical compound channel flows is significantly affected by the one-line vegetation. Instead of the typical profiles found in the no rod case, the depth-averaged velocity profiles "dive" towards the interface, where the rods are located. This corresponds to the free shear layer alongside the vegetative interface zone as observed by Pasche and Rouve (1985) and Sun and Shiono (2009). For Series 1 and 2A, the magnitude of depth-averaged velocity decreases when the rod diameter and rod density increase. Rod density has more impact on the velocities measured with 6 mm diameter rods compared to those measured with 3 mm diameter rods. For example, the average velocity increase between Series 1a and 1b is 7.0% as opposed to 4.8% for Series 2Aa and 2Ab. Rod diameter is a slightly more influential factor in the reduction of velocity in the

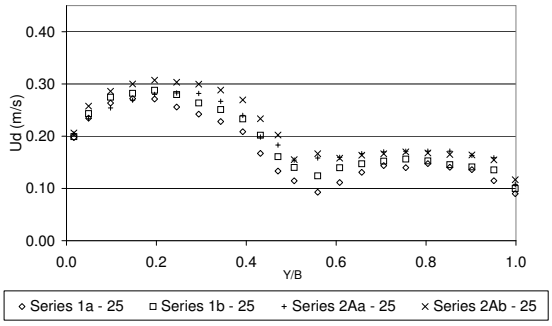

(a)

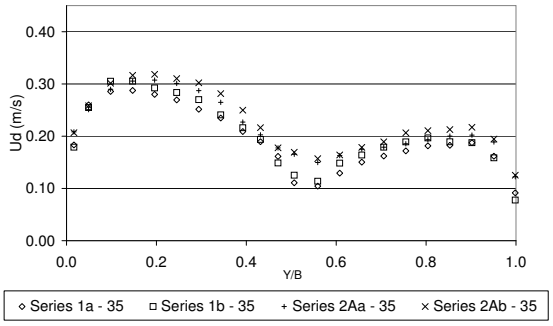

(b)

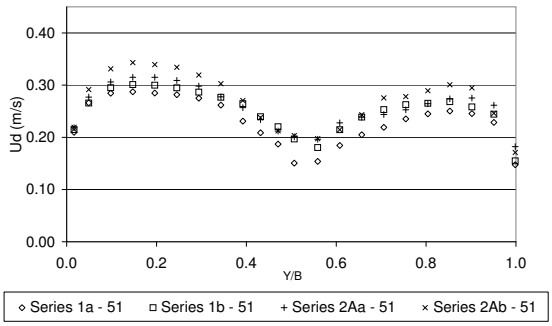

(c)

Figure 4.7: Depth-averaged velocity profiles for (a) Dr=0.25 (b) Dr=0.35 (c) Dr=0.51

tested cases, thus correlating the results observed on stage discharge distributions.

The lateral distributions of the depth-averaged velocity for Series 2B are presented in Figure 4.8.

Series 2Ba indicates a larger discharge through the main channel than for Series 2Bb, and shows a slight increase generally in the floodplain area. At the point of vegetation, the velocity is slightly smaller for the denser vegetation, which is to be expected. For each case, the velocity in the main channel is greater at lower flow depths whereas in the floodplain the greatest velocity occurs for the larger flow depths. The decrease in average velocity between smooth rods and the corresponding brush flow case increases

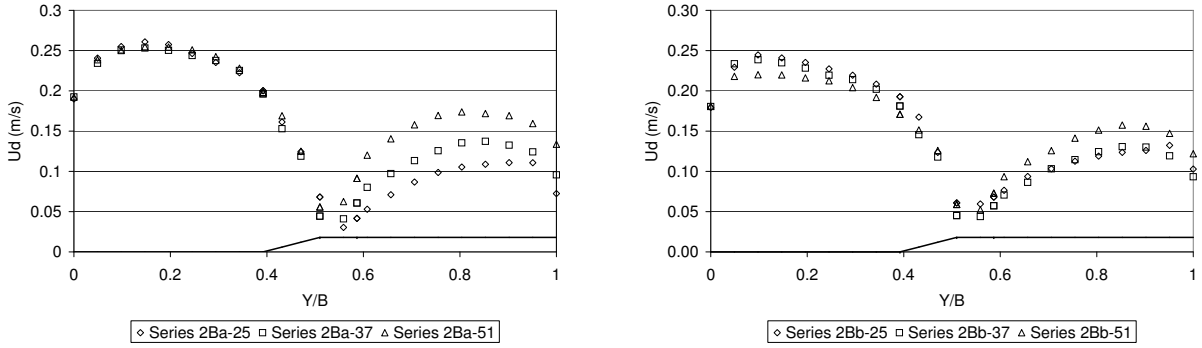

(a) (b)

Figure 4.8: Depth-averaged velocity for (a) Series 2Ba and (b) Series 2Bb

with relative depth. Brushes reduce the velocity by a minimum of 13.7% between Series 2Aa-25 and Series 2Ba-25 to a maximum of 37.6% between Series 2Ab-25 and Series 2Bb-51. Although the brushes have a clear detrimental effect on the water levels from an engineering viewpoint, they contribute to lower the velocities and would help to prevent erosion for example. These experimental results also suggest a seasonal effect of vegetation on velocity, if rods are compared to trees in winter and the brushes to a more estival type of vegetation, i.e. when foliage is present. It is interesting to note that the addition of foliage affects the flow structure further when compared to the smooth rods and no rod cases.

4.4.6 Large Scale-PIV

Large Scale PIV was carried out and the results of the surface velocities obtained. An example of mean surface velocity results, derived from video clips averaged over 2 min, is given in Figures 4.9 and 4.10 for the 3 mm rod diameter for Series 2Ab - 25.

The mean surface velocity results derived from LS-PIV were found in good agreement with the measured surface velocities, thus providing further confidence in the velocity measurements.

Figure 4.11 illustrates the type of time variations observed for the transverse velocity

Figure 4.9: Example of Large Scale PIV results

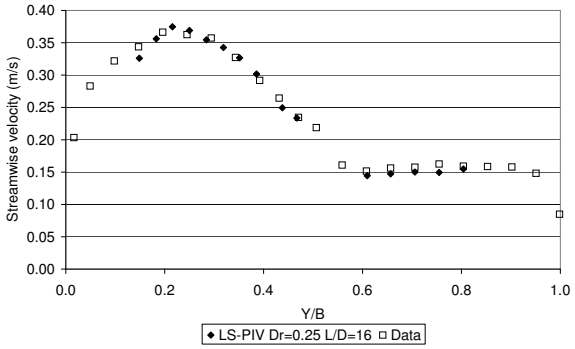

Figure 4.10: Large scale PIV for Series 2Ab-25 $\frac{L}{D} = 16$

at the surface near the interface between the main channel and the floodplain. The variations of transverse velocity from positive to negative values reflect the coherent structures moving from the main channel to the floodplain and vice-versa.

4.4.7 Eddy viscosity and Reynolds stress

In the no rod case, the depth-averaged Reynolds shear stress $\overline{\tau_{xy}}$ is commonly modelled using a simple eddy viscosity approach. Although more sophisticated models have been put forward, the modelling of the depth-averaged Reynolds shear stress through this type of approach remains the most popular in engineering applications. $\overline{\tau_{xy}}$ is usually related to the gradient of the depth-averaged velocity $\frac{\partial U_d}{\partial y}$ via a depth-averaged tur-

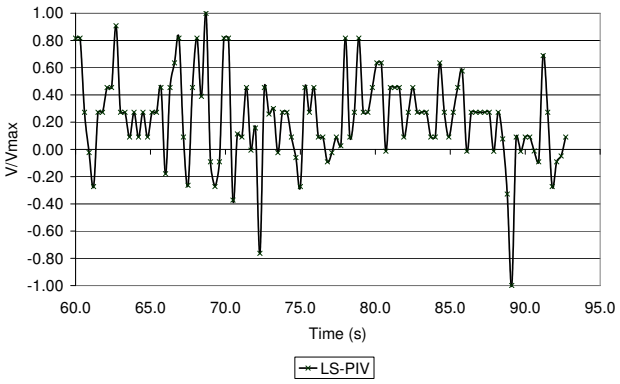

Figure 4.11: Example of time variations of transverse velocity V normalised by the maximum transverse velocity V_{max} from Large Scale PIV analysis of Series 2Ab-25

bulent eddy viscosity $\overline{\epsilon_t}$. The modelling of momentum exchange is thus shifted to the determination of an appropriate eddy viscosity $\overline{\epsilon_t}$.

The depth-averaged eddy viscosity $\overline{\epsilon_t}$ can be divided between the contributions made by bottom turbulence (Shiono and Knight, 1991) and transverse shear (van Prooijen *et al.*, 2005), as seen in Equation 4.13.

$$\overline{\epsilon_t} = \overline{\epsilon_{tb}} + \overline{\epsilon_{ts}} \tag{4.13}$$

The depth-averaged eddy viscosity due to bottom turbulence $\overline{\epsilon_{tb}}$ is modelled by Equation 5.6:

$$\overline{\epsilon_{tb}} = \overline{\lambda_{tb}} \left(\frac{f}{8}\right)^{\frac{1}{2}} U_d H \tag{4.14}$$

The depth-averaged eddy viscosity due to the transverse shear $\overline{\epsilon_{ts}}$ is modelled by 4.15:

$$\overline{\epsilon_{ts}} = \frac{H_m}{H} \beta^2 \delta^2 \left|\frac{dU_d}{dy}\right| \tag{4.15}$$

The value of $\overline{\lambda_{tb}}$ is taken as 0.068 (approximately $\frac{\kappa}{6}$) (Shiono and Knight, 1991), and the value of the proportionality constant β is taken as 0.08 (van Prooijen *et al.*,

2005). δ is the width of the shear layer, determined following the definition given in van Prooijen *et al.* (2005). δ is defined as twice the distance between the position $y_{25\%}$ at which $U_{y_{25\%}} = U_{m,fp} + 0.25(U_{m,mc} - U_{m,fp})$ and $y_{75\%}$ at which $U_{y_{75\%}} = U_{m,fp} + 0.75(U_{m,mc} - U_{m,fp})$. $U_{m,mc}$ and $U_{m,fp}$ are the maximum depth-averaged velocities in the main channel and floodplain respectively.

The results of the mean eddy viscosity modelled using Equations 4.13 to 4.15 are presented in Table 4.2.

Table 4.2: Mean eddy viscosity $\overline{\epsilon_t}$

Case	$\overline{\epsilon_t}$ (10^{-5} m^2/s)	Case	$\overline{\epsilon_t}$ (10^{-5} m^2/s)
Series 1a - 25	3.98	Series 1b - 25	3.66
Series 1a - 35	6.04	Series 1b - 35	5.16
Series 1a - 51	6.39	Series 1b - 51	6.29
Series 2Aa - 25	3.39	Series 2Ab - 25	3.64
Series 2Aa - 35	5.41	Series 2Ab - 35	4.95
Series 2Aa - 51	7.31	Series 2Ab - 51	6.89

The mean eddy viscosity $\overline{\epsilon_t}$ increases with relative depth for all Series. There is also a clear tendency for $\overline{\epsilon_t}$ to increase when the rod density increases, which corresponds to the finding of Nezu and Onitsuka (2001) who measured an increase in turbulence activity with vegetation density. The mean eddy viscosity increases for Series 1 compared to Series 2A for relative depth 0.25 and 0.35 but decreases for the deeper case thereby suggesting that the combined effects of rod diameter and rod spacing on eddy viscosity change as water depth increases.

The results of the modelling of the depth-averaged Reynolds shear stress $\overline{\tau_{xy}}$ using the measured velocity U and the estimated mean eddy viscosity $\overline{\epsilon_t}$ are presented in Figure 4.12.

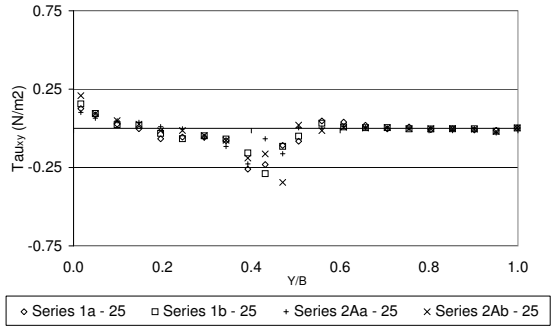

(a)

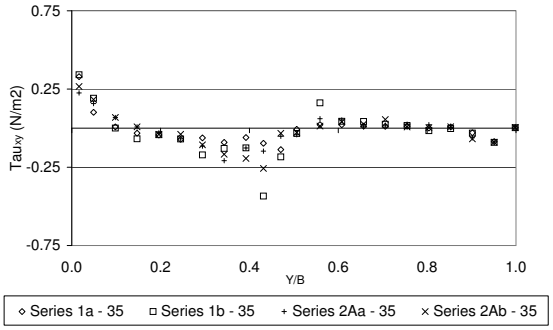

(b)

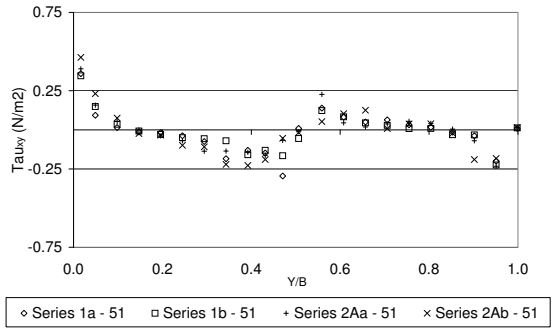

(c)

Figure 4.12: Reynolds stresses distributions for (a) Dr=0.25 (b) Dr=0.35 (c) Dr=0.51

The horizontal Reynolds stresses modelled by this approach exhibit little variations between the different cases. The values of $\overline{\tau_{xy}}$ remain small, of the order of $O(10^{-2})$ in centre of floodplain and reach minimum and maximum values either side of the line of rods. On the floodplain, the values of $\overline{\tau_{xy}}$ increase more significantly with relative depth, especially in the rod region, but no clear trend can be noticed in the main channel. The depth-averaged Reynolds shear stress reaches minimum values on the sidelope, decreasing with an approximately constant gradient from the main channel wall to that minimum value.

It can be seen from Figure 4.12 that the Reynolds stresses reach 0 in the main channel and on the floodplain where the maximum depth-average velocity is observed. This is to be expected as the Reynolds stress is modelled as a product containing the depth-averaged velocity gradient.

The ratios between the eddy viscosity due to transverse shear $\overline{\epsilon_{ts}}$ to the eddy viscosity due to bottom turbulence $\overline{\epsilon_{tb}}$ peak in the rod area and reach values in the range $1.3 \sim 5$. The average ratios $\frac{\overline{\epsilon_{ts}}}{\overline{\epsilon_{tb}}}$ are presented in Table 4.3 for the different flow cases. $\frac{\overline{\epsilon_{ts}}}{\overline{\epsilon_{tb}}}$ decreases with relative depth, rod density and diameter, the only exception being when comparing Series 2Aa-25 and 2Ab-25, for which this average ratio increases as density increases.

Table 4.3: Average ratios $\frac{\overline{\epsilon_{ts}}}{\overline{\epsilon_{tb}}}$

Case	$\frac{\overline{\epsilon_{ts}}}{\overline{\epsilon_{tb}}}$	Case	$\frac{\overline{\epsilon_{ts}}}{\overline{\epsilon_{tb}}}$
Series 1a - 25	1.059	Series 1b - 25	0.896
Series 1a - 35	0.896	Series 1b - 35	0.701
Series 1a - 51	0.244	Series 1b - 51	0.142
Series 2Aa - 25	0.313	Series 2Ab - 25	0.452
Series 2Aa - 35	0.689	Series 2Ab - 35	0.342
Series 2Aa - 51	0.277	Series 2Ab - 51	0.109

The Reynolds stresses results for Series 2B are presented in Figure 4.13. The extrema in Reynolds stresses appear either side of the line of brush and exhibit similar variations to those observed for smooth rods. The amplitude of Reynolds stresses either side of the line of brushes is higher for the denser rod case. However, the Reynolds stresses are smaller in the main channel and greater in the floodplain compared to smooth rods, as turbulent activity seems enhanced in the brush cases. The increase in turbulent kinetic energy due to foliage has for overall effect to increase the turbulent intensities in the channel (Nepf, 1999).

The ratios between the eddy viscosity due to transverse shear $\overline{\epsilon_{ts}}$ to the eddy viscosity due to bottom turbulence $\overline{\epsilon_{tb}}$ also exhibit a behaviour similar to that observed for smooth rods. The ratios peak near the vegetated interface and reach values in the range $1.3 \sim 11.5$. They decrease significantly with relative depth. This pattern suggests stronger shearing for the shallower relative depths, which was also noticed in the

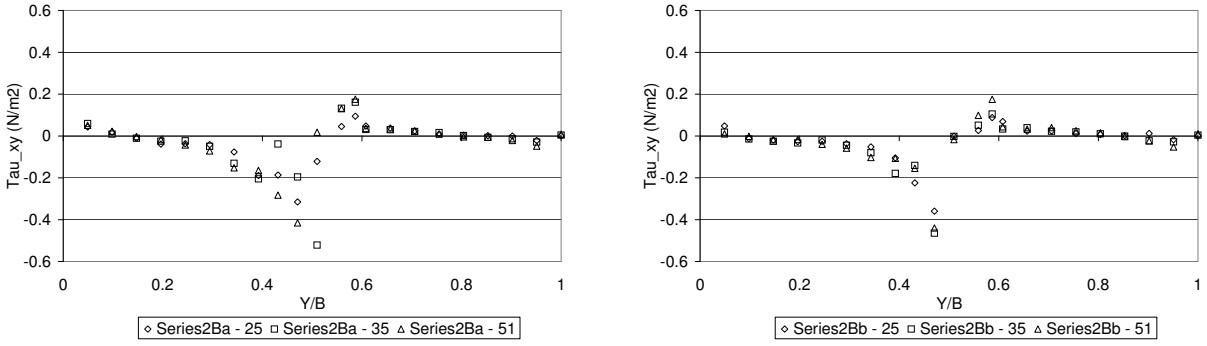

(a) (b)

Figure 4.13: Lateral distributions of the Reynolds shear stress for (a) Series 2Ba and (b) Series 2Bb

no rod case. However, the ratios are stronger in the less dense case, i.e. for Series 2Bb compared to the dense case which is different from the smooth rod cases.

4.4.8 Boundary shear stress analysis

The results of bed shear stress measurements are presented in Figure 4.14. The lateral distributions of boundary shear stress tend to follow the distributions of depth-averaged velocity. The maximum values of boundary shear stress are shifted away from the interface when compared to the no rod case and the locations of boundary shear stress maxima coincide with the locations of depth-averaged velocity maxima.

The relative differences of boundary shear stress between the different cases were compared in order to identify the most influential factors responsible for boundary shear stress variations. The results show that the change in diameter from 6 mm to 3 mm has more impact on the results than the change in spacing ratio from 8.0 to 16.0, as boundary shear stress was 17.3% greater on average compared to 13.2% for the corresponding flow cases. The change in rod density has a more profound impact on boundary shear stress in the case of the 6 mm rods, with an averaged bed shear stress increase of 16.0% compared to 10.4% for the 3 mm rods when rod density is increased.

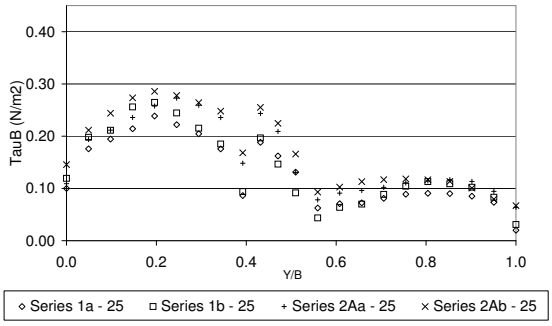

(a)

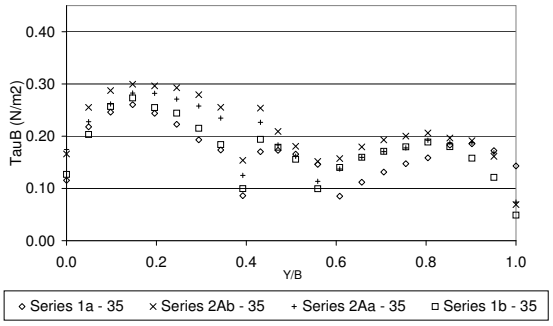

(b)

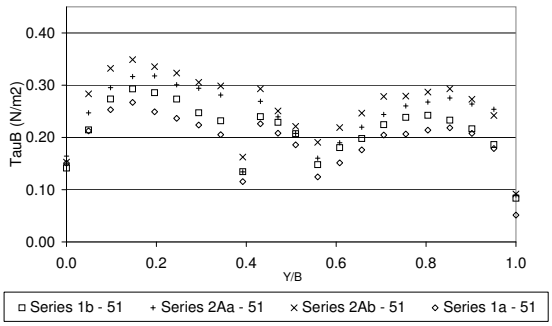

(c)

Figure 4.14: Boundary shear stress distributions for (a) Dr=0.25 (b) Dr=0.35 (c) Dr=0.51

The discrepancies between the measured boundary shear stress τ_B and the gravity term $\rho g H S_0$, which corresponds to the gravity term for a two-dimensional flow case with equivalent depth, were calculated for all cases. The lateral distributions of $\rho g S H - \tau_B \left(1 + \frac{1}{s^2}\right)^{\frac{1}{2}}$ normalised by $\rho g H S_0$ are presented in Figure 4.15.

In the no rod scenario, presented in Figure 4.16, the difference $\rho g H S_0 - \tau_B \left(1 + \frac{1}{s^2}\right)^{\frac{1}{2}}$ remains negative on the sideslope and in the floodplain and positive elsewhere in the main channel for all relative depths. That difference normalised by $\rho g H S_0$ is minimum for the shallow case as it reaches -1.24 at the interface. As mentioned in Section 4.2, the variations of $\rho g H S_0 - \tau_B \left(1 + \frac{1}{s^2}\right)^{\frac{1}{2}}$ are associated with momentum transfer. The

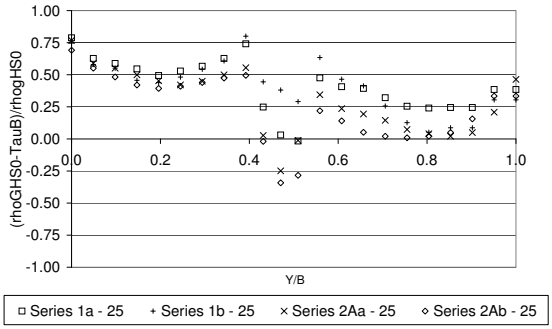

(a)

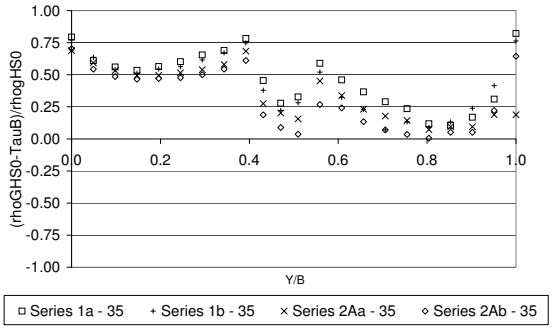

(b)

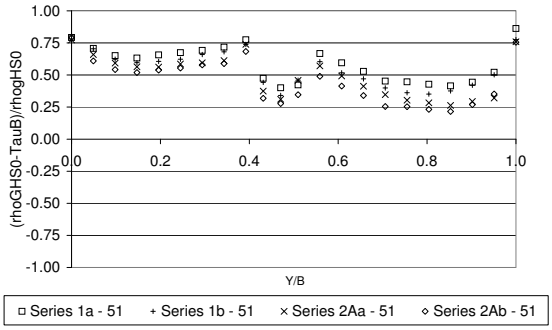

(c)

Figure 4.15: $(\rho g H S_0 - \tau_B \left(1 + \frac{1}{s^2}\right)^{\frac{1}{2}})$ normalised by $\rho g H S_0$ for (a) Dr=0.25 (b) Dr=0.35 (c) Dr=0.51

variations of depth-averaged Reynolds stresses and secondary currents directly account for this behavior (Shiono and Knight, 1991).

However,the variations of $\rho g H S_0 - \tau_B \left(1 + \frac{1}{s^2}\right)^{\frac{1}{2}}$ are different when rods are placed on the edge of floodplain. The difference between the boundary shear stress $\tau_B \left(1 + \frac{1}{s^2}\right)^{\frac{1}{2}}$ and the gravity term $\rho g H S_0$ remains positive across the entire section of the compound channel, except for one datapoint in Series 2A-25 and two datapoints in Series 2B-25, all located on the sideslope. This difference decreases with rod diameter and density, which correlates the observations of Sun and Shiono (2009). In the rod case, the bed shear stress is always smaller than the two-dimensional value $\rho g H S_0$, which can be directly attributed to the impact of drag force.

The depth-mean-averaged momentum equation can be rearranged so that:

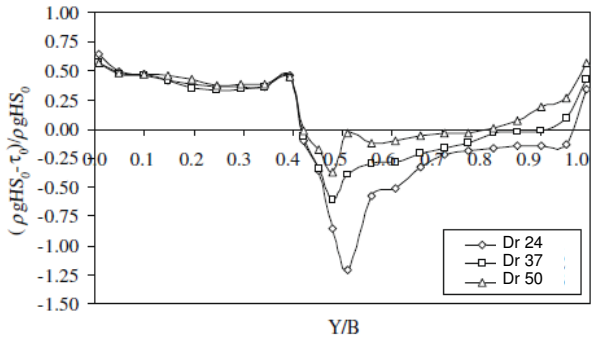

Figure 4.16: $(\rho gHS_0 - \tau_B \left(1 + \frac{1}{s^2}\right)^{\frac{1}{2}})$ normalised by ρgHS_0 for the no rod cases

$$\rho gSH - \tau_B \left(1 + \frac{1}{s^2}\right)^{\frac{1}{2}} = \frac{\partial}{\partial y}\left(H\rho(UV)_d - H\tau_{xy}\right) + F_D \tag{4.16}$$

The drag force term complicates the analysis of the left hand side term $\rho gS_0H - \tau_B \left(1 + \frac{1}{s^2}\right)^{\frac{1}{2}}$. In the no-rod case, this term was solely function of the partial derivative of $(UV)_d - \tau_{xy}$, which itself has two distinct components, the first one arising from transverse velocity and the other one from turbulence.

A depth-averaged apparent shear stress τ_a is defined following Shiono and Knight (1991)'s definition in a no-rod case.

$$\tau_a = -\frac{1}{H}\int_0^y \left(\rho gS_0H - \tau_B \left(1 + \frac{1}{s^2}\right)^{\frac{1}{2}}\right) dy \tag{4.17}$$

Equation 4.17 can be solved provided boundary conditions are given. In this study, we will assume that the depth-averaged apparent shear stress at $y = 0$ is equal to the left mean wall shear stress $\tau_{lwall,mean}$ (Equation 4.18). Similarly, we will assume that the depth-averaged apparent shear stress at $y = B$ is equal to the opposite of the right mean wall shear stress $\tau_{rwall,mean}$ (Equation 4.19).

$$\tau_a(0) = \tau_{lwall,mean} \tag{4.18}$$

$$\tau_a(B) = -\tau_{rwall,mean} \tag{4.19}$$

The lateral variations of τ_a are presented in Figure 4.17.

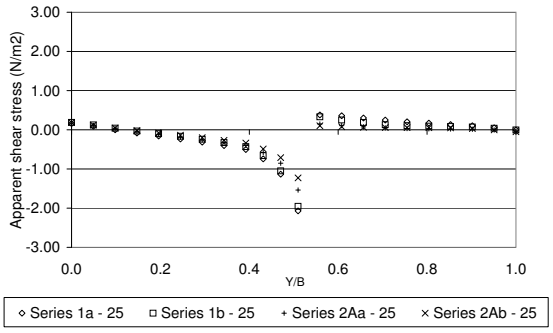

(a)

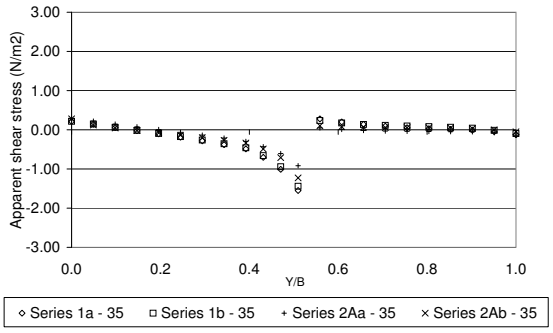

(b)

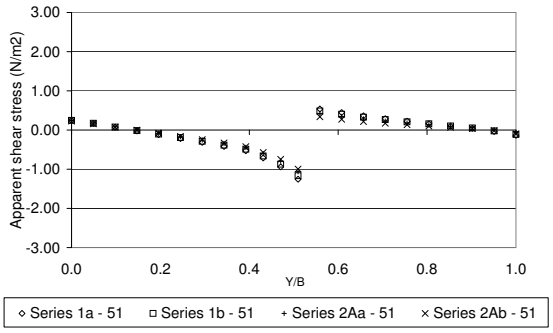

(c)

Figure 4.17: Apparent shear stress for (a) Dr=0.25 (b) Dr=0.35 (c) Dr=0.51

The distributions of the apparent shear stress do not vary significantly for a given relative depth. The apparent shear stress decreases from the main channel left wall to reach a minimum value near the interface, and increases from the floodplain right wall to reach a maximum at the interface. The apparent shear stress is consistently lower in the main channel and greater in the floodplain when the rod density and rod diameter increase. The minimum value of apparent shear stress decreases when the relative depth decreases, which is similar to the no vegetation case.

The results of bed shear stress measurements for Series 2B are presented in Figure 4.18. For both vegetative densities, the boundary shear stress distributions in the

main channel are similar for all relative depths. On the floodplain, the larger relative depths provide a larger boundary shear stress with the maximum moving closer to the boundary wall with smaller relative depths.

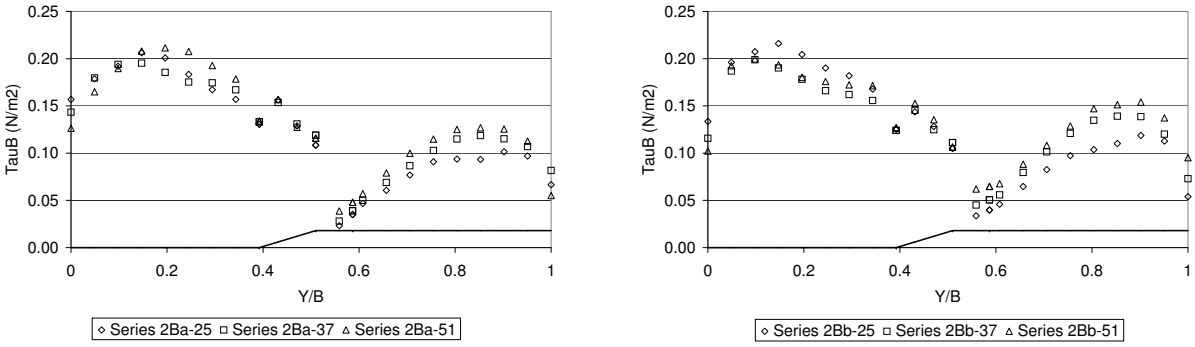

(a) (b)

Figure 4.18: Boundary shear stress distributions for (a) Series 2Ba and (b) Series 2Bb

The lateral distributions of $\rho g S_0 H - \tau_B \left(1 + \frac{1}{s^2}\right)^{\frac{1}{2}}$ normalised by $\rho g S_0 H$ are presented in Figure 4.19. This difference remains always positive for all cases. Decreasing the density in Series 2Bb does not affect the difference significantly in the main channel while this difference reduces in the floodplain compared to the same relative depth.

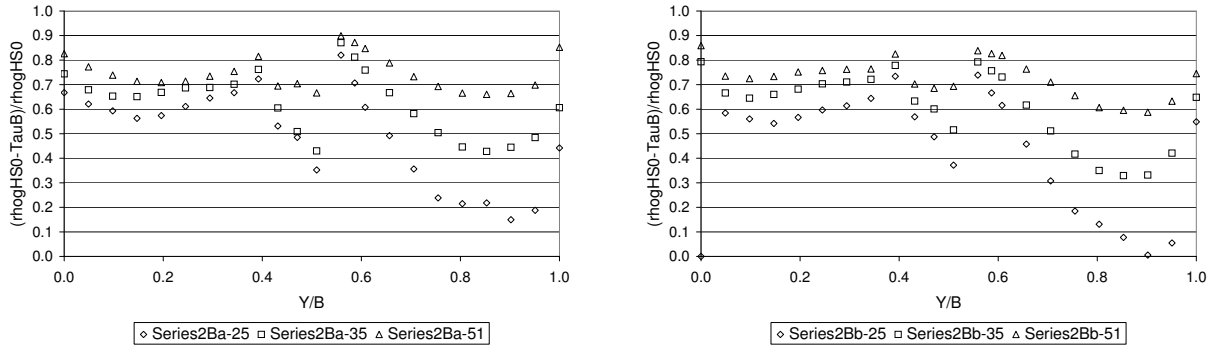

(a) (b)

Figure 4.19: Lateral distributions of $\rho g S_0 H - \tau_B \left(1 + \frac{1}{s^2}\right)^{\frac{1}{2}}$ normalised by $\rho g S_0 H$ for (a) Series 2Ba and (b) Series 2Bb

The lateral variations of τ_a are presented in Figures 4.20. The addition of foliage to the rods has for clear impact to increase the amplitude of apparent shear stress either side of the line of brush. For each spacing ratio, the apparent shear stress remains similar in the main channel although one notes a slight decrease when relative depth increases. The apparent shear stress increases somewhat remarkably with relative depth in the floodplain.

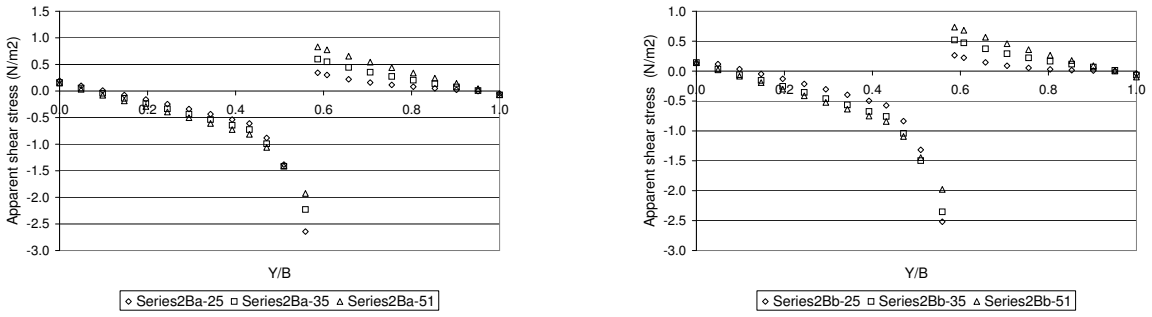

(a) (b)

Figure 4.20: Lateral distributions of the depth-averaged apparent shear stress for (a) Series 2Ba and (b) Series 2Bb

4.4.9 Drag force calculations

4.4.9.1 Drag coefficient

The drag coefficients for a circular cylinder corresponding to the rod Reynolds number $Re_{rod} = \frac{U\ D}{\nu}$ of the experiments can be extracted from Figure 2.16. In the definition of Re_{rod}, U is the upstream velocity approaching the rod (Schlichting and Gersten, 1968). The rod Reynolds numbers for the studied cases vary from 256 to 1132 and the corresponding drag coefficients vary from 1.00 to 1.27. The largest values of drag coefficient are observed for Series 2B, and are 1.23 on average compared to 1.09 for

Series 1A and 2A. However, as highlighted in Section 2.5, these drag coefficients do not take the effects of shading and suppression due to wakes into account. Hence, they should be regarded as upper limits of the actual bulk drag coefficients.

4.4.9.2 Drag force estimates

Drag force can be estimated by a force balance approach or via an analytical formulae commonly used for drag force calculations.

The force balance approach considers the forces in equilibrium exerted on a control volume for quasi uniform flow conditions. The driving force is gravity while the forces balancing gravity are boundary forces and drag force. This is expressed by equation 4.20, where the drag force F_D is expressed per unit length.

$$F_D = \rho g A S_o - \int_{WettedPerimeter} \tau_B(y) dy \tag{4.20}$$

In Equation 4.20, τ_B is averaged over a control volume length. The results of force balance are presented in Figure 4.21.

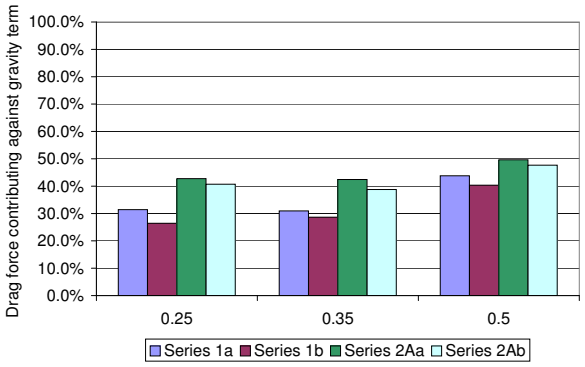

Figure 4.21: Drag force estimates normalised by gravity term derived from force balance

This approach is straightforward and can be applied where stage and boundary shear stress measurements have been carried out.

The results show that drag force increases almost linearly with water depth, with correlation coefficients for linear regressions varying from 94.6% for Series 2A to 97.5% for Series 1a.

The drag force per unit length can also be defined by the following analytical formulae:

$$F_D = \frac{1}{2}\frac{\rho C_D S_f A_P H U_{d,p}^2}{\frac{L}{D}} \tag{4.21}$$

where S_f is the shading factor, A_P is the projected area of the rod under water, that is HD, and $U_{d,p}$ is the approaching depth-averaged velocity. Considering drag coefficients derived from studies on a unique cylinder placed in two dimensional flows, like those presented in 4.4.9.1 or taking the approach of Sun and Shiono (2009), are likely to overestimate drag force calculations. Instead, the bulk drag coefficient ($C_D S_F$) was determined using the results presented in Figure 2.27 for aligned tandem of rods. For a spacing ratio 8.0 and 16.0, the bulk drag coefficients are approximately 0.715 and 1.015 respectively. $U_{d,p}$ is taken as the velocity surrounding the rods, averaging the measurement points the closest either side of the rod.

The comparisons between both approaches are presented in Figure 4.22:

The analytical formulae overestimates the drag force value compared to force balance method. The best results are obtained for the 3 mm rod in Series 2Aa with an average relative difference of 11.4%. Series 1b and 2Ab, with the spacing ratio of 16.0, have the worst fits between the two methods of calculations with average relative differences of 27.7% and 36.2% respectively. This overestimation of the analytical formulae is attributed in large part to the bulk drag coefficient, whose values seem too high and do not fully account for the shading effects.

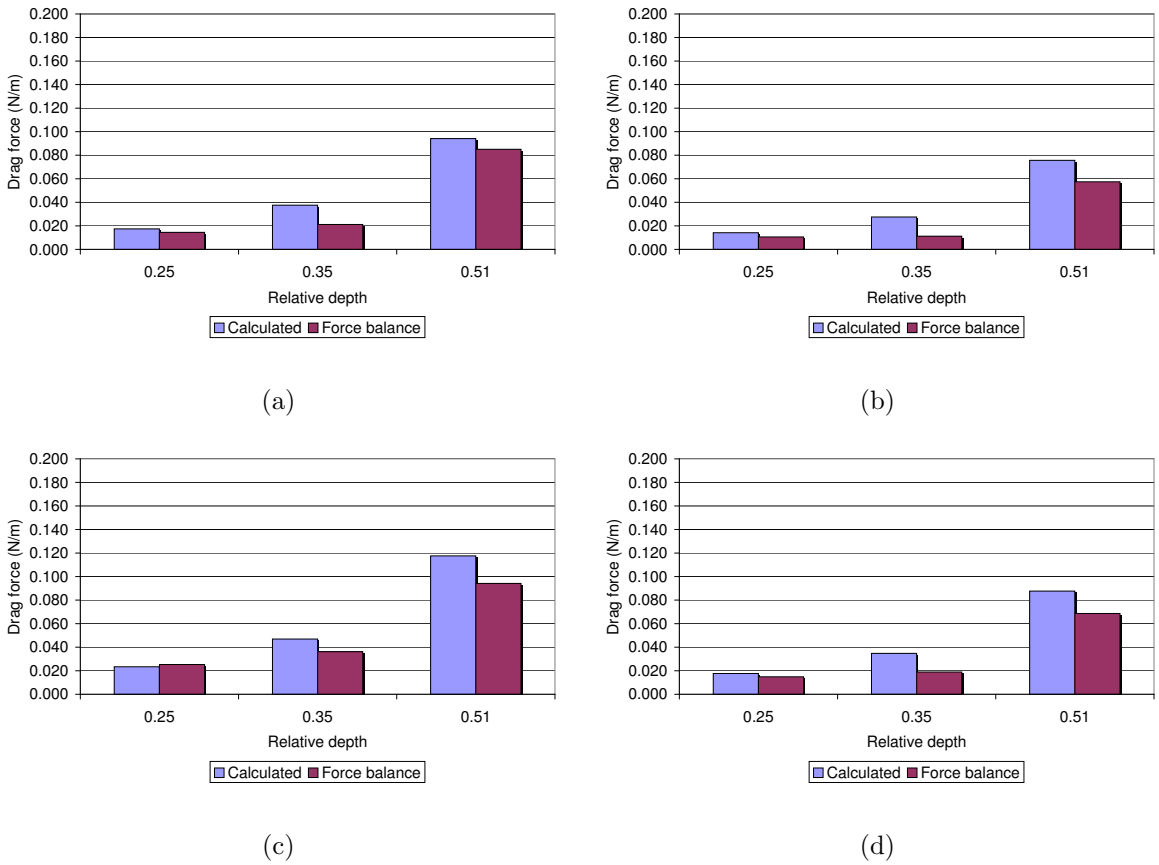

Figure 4.22: Drag force calculated by force balance and analytical formulae for (a) Series 1a (b) Series 1b (c) Series 2Aa and (d) Series 2Ab

The results of drag force calculations for Series 2B using force balance approach are presented in 4.23. As water depth increases, the boundary shear force changes very little but drag force increases very rapidly for both vegetative densities.

The addition of foliage to the smooth rods contributes to a greater drag force element to the total channel resistance compared to smooth rods, which is supported by published literature (e.g. James *et al.*, 2008; Nepf, 1999).

As shown in Figure 4.24, drag force varies linearly with relative depth for both series.

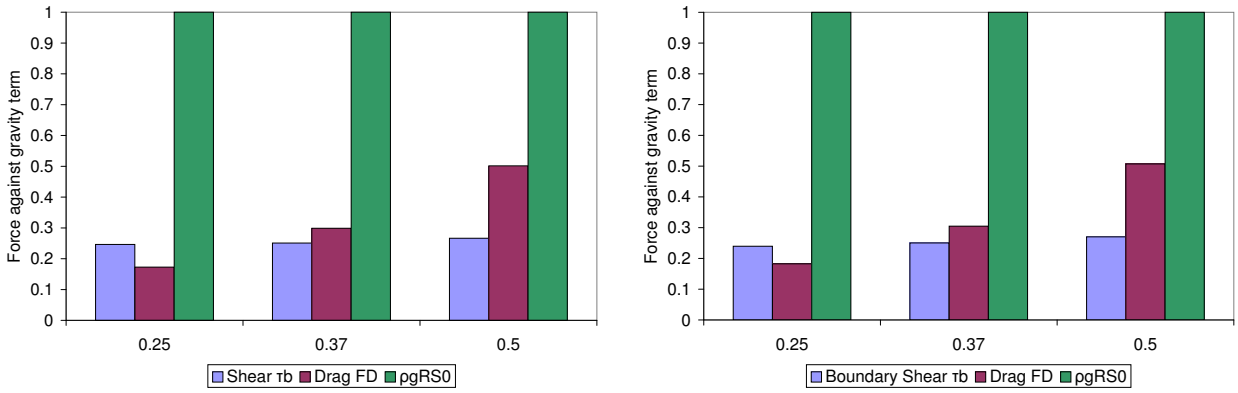

(a) (b)

Figure 4.23: Force balance for (a) Series 2Ba and (b) Series 2Bb

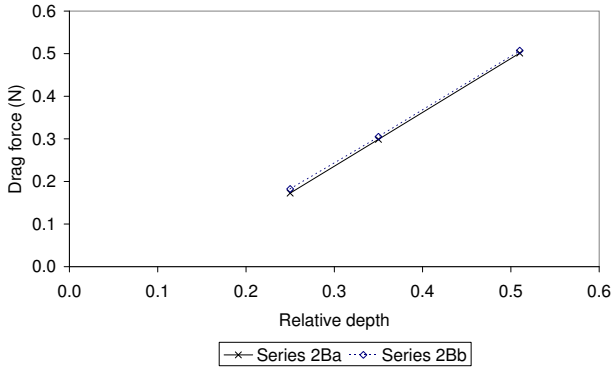

Figure 4.24: Drag force results in function of relative depth

4.4.9.3 Further evaluation of the drag coefficient in drag force analytical formulae

In the analytical drag force Equation 4.21, various possibilities are available to calculate the so-called approaching velocity $U_{d,p}$. A sensitivity test was carried out by comparing the drag coefficient resulting by the averaging of velocity 1) Across the whole section 2) In the main channel 3) In the floodplain 4) taking the measurement points either side of the rod, as in Section 4.4.9.3. The resulting drag coefficients were calculated using Equation 4.22 for all cases, including (Sun and Shiono, 2009) dataset.

$$C_D = \frac{F_{D,force\ balance}}{\frac{1}{2}\frac{\rho A_P H U_{d,p}^2}{\frac{L}{D}}} \tag{4.22}$$

The results are shown in Figure 4.25.

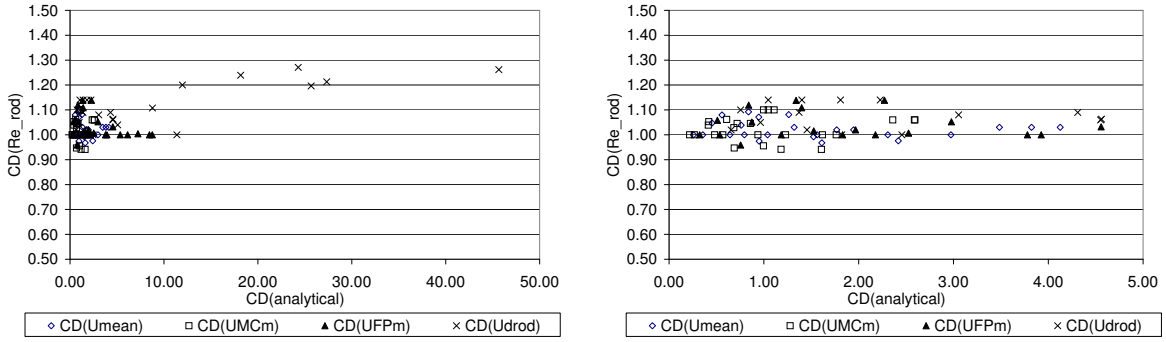

(a) (b)

Figure 4.25: C_D results (a) For all cases (b) Zoom on results

The drag coefficients exhibit a very significant scatter. The largest values, reaching $C_D = 45.7$ for Series 2B are obtained for $U_{d,p}$ taken near the rods and reflect the much slowed down velocities in the brush area. For the smooth rods, the largest values of C_D are obtained for (Sun and Shiono, 2009) data, with C_D reaching 11.4 for a spacing ratio $\frac{L}{D} = 13.3$ and Dr=0.25. The drag coefficients the closest to unity are obtained for Series 2Aa and 2Ab.

Therefore, the choice of the area to determine $U_{d,p}$ has a significant impact on the values of the drag coefficients.

4.4.9.4 Further analysis using force balance principle

In the no rod case, Equation 4.23 expresses the principle of force balance. Equation 4.23 is also the integration of the SKM Equation assuming the advection term Γ can be neglected.

$$-\int_0^{y_L}(\rho g S_0 H_{mc} - \tau_B(y))\,dy + \tau_{left\ wall}H + \tau_{right\ wall}h + \int_0^{y_L}\frac{\partial \tau_{xy}H}{\partial y}dy = 0 \quad (4.23)$$

The first integral deals with the terms of force balance that can be calculated exactly, i.e. the gravity and the bed shear stress terms. The second integral represents the transverse shear term and has been modelled using van Prooijen *et al.* (2005) adopting the model constants as $\lambda = 0.07$ and $\beta = 0.08$. Equation 4.23 can therefore be used to control that the Reynolds stress term has been correctly modelled, assuming measurements are correct. Figure 4.26 presents the results of the two integrals, both taking account of wall shear stress at the wall boundaries. The integrations were carried out from the left wall to the right wall.

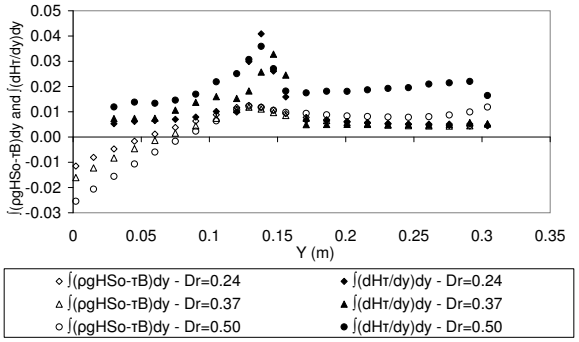

Figure 4.26: Evolutions of $\int_0^{y_L}(\rho g S_0 H_{mc} - \tau_B(y)dy)$ and $\int_0^{y_L}\frac{\partial \tau_{xy}H}{\partial y}dy$ in the no rod case

At the end of the integration, both integrals are approximately equal for Dr=0.24 and Dr=0.37, with relative errors of -0.3% and 1.3% respectively. For the deeper case Dr=0.51, the relative difference is higher and reaches 27.9%. The results suggest that the Reynolds shear stress has been correctly modelled for Dr=0.24 and Dr=0.37, while it is overestimated in the deeper case and constant β in the modelling of transverse shear contribution might need to be adjusted. The discrepancy for Dr=0.51 might be due to the measurement errors as the measurement of boundary shear stress on walls is somewhat awkward to carry out.

Apparent shear force can also be integrated in the no rod case from each sidewall to the interface. The results are presented in Figure 4.27. At the interface, there is some discrepancy in the apparent shear force in that $\tau_{as}h|_{y=int^-} \neq \tau_{as}h|_{y=int^+}$. The largest discrepancy can be observed for Dr=0.52, thereby strengthening the case for possible measurement errors.

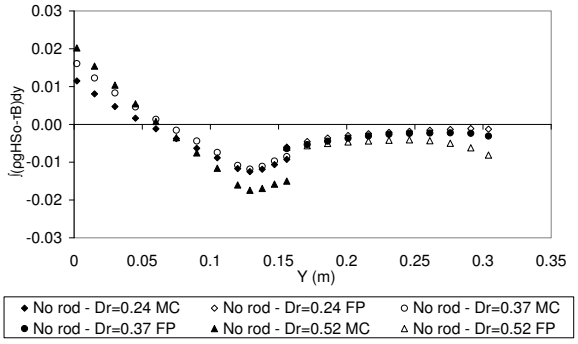

Figure 4.27: Evolutions of $\int_0^{y_L} (\rho g S_0 H_{mc} - \tau_B(y)dy)$ in each subsection in the no rod case

Equation 4.23 can be rewritten so that in the main channel, one obtains an expression for the depth-averaged transverse shear stress given in Equation 4.24.

$$\overline{\tau_{xy}}H = -\int_0^y (\rho g S_0 H_{mc} - \tau_B(y))\, dy + \tau_{left\ wall}H \tag{4.24}$$

or,

$$\rho\overline{\epsilon_t(y)}H(y)\frac{\partial U}{\partial y} = -\int_0^y [\rho g S_0 H_{mc} - \tau_B(y)]\, dy + \tau_{left\ wall}H \tag{4.25}$$

The depth-averaged turbulent eddy viscosity $\overline{\epsilon_t(y)}$ can be expressed by Equation 4.26.

$$\overline{\epsilon_t(y)} = \frac{-\int_0^y [\rho g S_0 H_{mc} - \tau_B(y)]\, dy + \tau_{left\ wall}H}{\rho H(y)\frac{\partial U}{\partial y}} \tag{4.26}$$

For $y = y_{int}$, one obtains the value of the depth-averaged eddy viscosity $\overline{\epsilon_t}$ at the interface. This eddy viscosity accounts for the effects of drag and transverse turbulent

shear. In order to express the enhanced turbulence due to drag, a drag eddy viscosity could be introduced. This idea will be developed further in Chapter 7.

4.4.10 Wakes

In the case of a unique rod as shown in Figure 4.28, the wake at a distance x from the rod centre can be characterised by a length a. This length is evenly split either side of the rod longitudinal axis in the case where the wake structure is symmetrical, like for the simple case of a rod located in a infinite plane. In this case, if U_{us} is the mean velocity upstream of the rod, $U(x,t) = U_{us} + u(x,t)$ is the instantaneous velocity in the wake of the rod where u is the perturbation velocity when compared to the upstream velocity. Let $\bar{u}$ and $\acute{u}$ be the average of the perturbations and turbulent part of the perturbation so that $u(x,t) = \bar{u}(x) + \acute{u}(x,t)$.

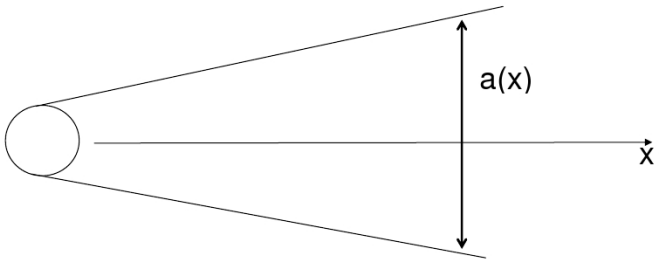

Figure 4.28: Sketch of a wake behind a rod

The component according to the x axis of the flow is of the order of magnitude of U_{us} while the transverse component is of the order of $\bar{u}$. This leads to $\frac{da}{dx} \approx \frac{\bar{u}}{U_{us}}$. Assuming that the wake is homogeneous, the lift can be neglected. The drag force F_d has an order of magnitude of $F_d = \rho \bar{u} U_{us} a^2$. Therefore, $\frac{da}{dx} \approx \frac{F_d}{\rho U_{us}^2 a^2}$. Following integration, a relation defining the spread of the wake a with x is obtained in Equation 4.27.

$$a \approx \left(\frac{F_d}{\rho U_{us}^2} x \right)^{\frac{1}{3}} \tag{4.27}$$

This first order approximation shows that the characteristic length of the wake a grows like $x^{\frac{1}{3}}$. In Figure 4.29, the results of F_D and average longitudinal velocity in the floodplain and main channel have been used to calculate the simplified wake field for Series 1b - 51 and 2Ab - 25. The approximation of U_{us} as the average floodplain velocity and main channel velocity translates the asymmetry due to the difference in velocity either side of the line of rods.

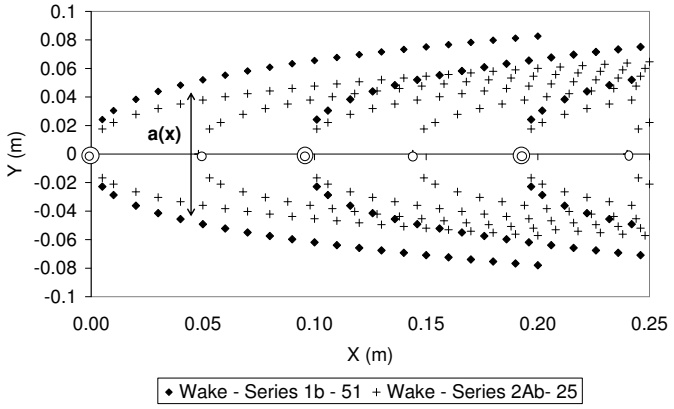

Figure 4.29: Modelled wake growth behind a rod

The asymmetry in the wake field is more pronounced for the shallow cases as the difference in longitudinal velocities in the main channel and in the floodplain is greater. The spread in wakes increases when drag force increases which also confirms experimental observations.

During the experiments, wakes were most clearly visible through light reflection on the free surface. Figure 4.30 presents a black and white photograph of wakes, particularly visible upstream in the main channel (bottom right of the photograph).

Using photographs such as Figure 4.30, direct comparisons of computed wakes with experimental data was possible. The wakes proved to be approximately well predicted within the first three to five rod spacings. However, wakes often reflected against the side walls during experiments which was not reproduced with this first order approxi-

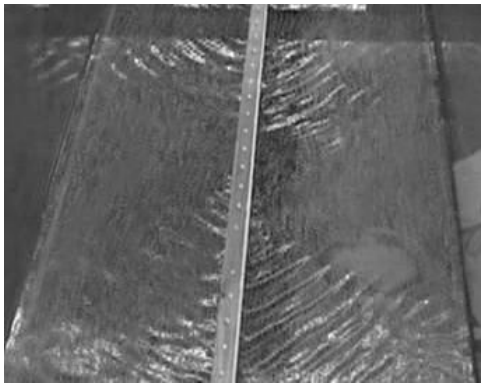

Figure 4.30: Wakes visible on the free surface in Series 2Ab - 25

mation. In addition, wakes often exhibited oscillations that are not taken into account in this simple model.

4.5 Summary

From flow visualization, three flow patterns were clearly observed for all the experiments. These are composed of wake action observed in the trail of the flow separating downstream of the rods, planform coherent structures advected from the floodplain to the main channel and vice-versa and eddying motion near the vegetated area.

The overall characteristics of lateral depth averaged and boundary shear stress distributions caused by one-line of smooth rods in the narrow straight compound channel of Loughborough University are similar to those observed by Sun and Shiono (2009). The depth-averaged velocity is reduced in the rod area. The maximum velocity in the sub-sections moves away from the interface as rod density and relative depth increase. Relative depth was seen to be a more contributing factor to the displacement of maximum velocity than density and rod diameter. This is because drag force and the effects of wakes and of Prandtl's second kind's secondary currents due to the presence of rods increase significantly with relative depth. As a result, the magnitude of turbulent intensity in the lateral direction increases but the turbulence intensity in the vertical direction remains similar due to the free surface, thereby enhancing turbulence

anisotropy. The secondary currents are therefore strengthened at higher relative water depth regardless of rod density.

Increasing vegetative density in the case of brushes can lead to an increase in the total channel discharge. This suggests that, although increasing vegetative density can lead to an increase in the chances of flooding, there is also a point at which closer spacing of trees can result in an increase in discharge and thereby reducing flooding effects. It is therefore important to consider how the vegetative density and discharge relate to flow depth when planting trees instead of simply increasing the spacing ratio with the aim of reducing the cumulative drag effects.

A change in diameter from 6 mm to 3 mm has more impact on the results than the change in spacing ratio from 8.0 to 16.0 as boundary shear stress was 17.3% greater on average compared to 13.2%. The change in rod density had a more profound impact on boundary shear stress in the case of the 6 mm rods, with an averaged bed shear stress increase of 16.0% compared to 10.4% for the 3 mm rods when the rod density is increased. Hence, both diameter and density need to considered in planning riparian vegetation as both are seen to have an impact on boundary shear stress.
The apparent shear stress τ_{as} was calculated following the method laid out in Shiono and Knight (1991), including wall shear stress. The distribution of apparent shear stress remains linear in the floodplain and in the main channel, which was also reported by Sun and Shiono (2009). The amplitude of apparent shear stress was seen to increase with relative depth. The amplitude of apparent shear stress increased with brush compared to the smooth rod cases. This relates to the increase in drag and turbulent activity generated by foliage.
The results suggest that the drag force induces a sharp decrease in boundary shear stress. Drag force was seen to vary linearly with relative depth for all cases. Drag force values calculated using the analytical formulae can differ significantly from the drag force values derived from force balance. These results confirm that the analytical formulae should be applied with caution to calculate drag force in the case of one-line

vegetation along the main channel. The approaching velocity $U_{d,p}$ used in the analytical formulae changes significantly the results, depending on whether $U_{d,p}$ is averaged in the rod area, in the main channel or floodplain. The use of velocities at the rods or in the floodplain leads to high drag coefficients in order to validate the analytical formulae against force balance method.

The drag on the flow due to brushes contributes to additional turbulence, hence slowing down the channel and increasing the secondary current's magnitude. This effect is reflected in the higher magnitude of Reynolds stresses calculated for Series 2B compared to smooth rods cases. This means that riparian trees with foliage are likely to induce further turbulence to that already seen due to momentum transfer, aiding in the reduction of flow velocity compared to a smooth channel.

CHAPTER 5

Further Investigations on Complementary Experimental Data

5.1 Introduction

Complementary experimental data were obtained in the Laboratory of Fluid Mechanics and Acoustics (LMFA) in Lyon. The main objectives of this complementary data set were:

- to analyze the impact of one-line vegetation in channels of different aspect ratios and bed slope on flow structures. The LMFA flume has an aspect ratio ($\frac{B_{mc}}{h_{fp}}$) of 7.75 while the narrow flume in Loughborough has an aspect ratio of 4.33;
- to identify the possible influence of bed slope and Froude number on the flow structure. The LMFA flume is steeper than that of Loughborough University ($S_0 = 0.0018$ against 0.001). The studied flows in LMFA have much higher Froude numbers (Fr=0.54 $\sim$ 0.81) than those observed in Loughborough University (Fr=0.21 $\sim$ 0.50);

- The impact of a smaller density of rods on flow characteristics, with a ratio $\frac{L}{D} = 32$, was studied in LMFA. The results of tree surveys (Figure 3.14) indicated that this configuration is occasionally found in the field. One might expect that as the ratio $\frac{L}{D} = 32$ increases, flow characteristics would approach those observed in uniform flows without rods. In particular, the intuitive assumption that a smaller rod density promotes momentum transfer between subsections needs to be assessed;

5.2 Experiments in LMFA

5.2.1 Experimental conditions

Flow characteristics of three cases with one line-vegetation were investigated in the LMFA, in addition to two cases without vegetation. The vegetation was modelled with 9 mm diameter smooth wooden rods. Porosity values for the three cases with the line of rods range from 0.9996 and 0.9998.The flows for all cases were quasi uniform as the water surface profile was adjusted to be parallel to the bed slope. Velocities were measured using a micro-propeller and a Pitot tube. Boundary shear stress were measured for the rod cases only using a Preston tube.
The detailed flow conditions of the three cases investigated are presented in Table 7.5. They are reviewed against the corresponding no rod cases.

Table 5.1: Experiments in the LMFA straight compound channel flume

Relative depth	Reynolds number	Hydraulic Radius (m)	Manning's n (s/m(1/3))	Flow (L/s)	Rod diameter (m)	Rod spacing (m)	L/D
0.211	41165	0.027	0.0103	17.3	N/A	N/A	N/A
0.217	41748	0.028	0.0104	17.3	0.009	0.28	32
0.423	129889	0.063	0.0129	36.3	N/A	N/A	N/A
0.431	131020	0.064	0.0134	36.3	0.009	0.14	16
0.439	130590	0.064	0.0134	36.3	0.009	0.28	32

5.2.2 Data analysis

5.2.2.1 Velocity distributions

Figures 5.1 and 5.2 show the normalised velocity (U/U_m) patterns for the no rod and rod cases respectively. The depth mean velocity was calculated using the measured local velocities and plotted in Figures 5.3 and 5.4 for the low and high relative depths cases respectively. For the low relative depth case, the no rod case and the rod case exhibit similar flow characteristics. The relatively faint double peak observed in the uniform flow case is attributed to the presence of secondary currents of Prandtl's second kind in the main channel. This double peak structure is not present anymore in the rod case as the turbulence flow field in the main channel has been strongly affected by the rod wakes.

There is a decrease in velocity near the rod area for all cases. For the shallow case, the depth-averaged velocity profile retains similar characteristics to those observed for the no rod case, indicating the presence of a shear layer extending either side of the interface between the main channel and the floodplain. Interestingly, this pattern suggests that this rod configuration still allows momentum transfer to occur between the main channel and the floodplain. On the other hand, the contrast between the rod and no-rod case is much more pronounced for the higher relative depths cases. The depth-averaged velocity profiles "plunge" in the rod area. The decrease in velocity is stronger for the greater density as the velocity decreases by 24.2% and 14.7% 3 cm away from the rods, in the main channel. The presence of rod causes strong secondary currents and wake generated turbulence, which in turn cause a decrease in the streamwise depth-averaged velocity in the rod area.

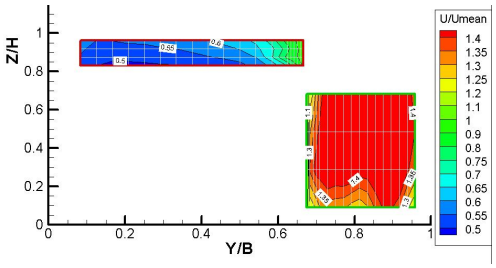

(a)

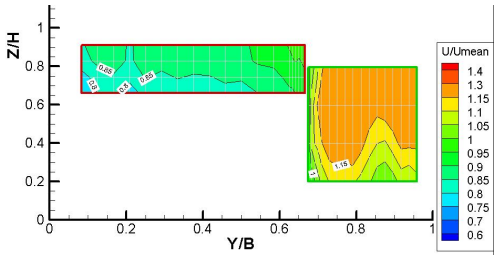

(b)

Figure 5.1: Isovels for the no rod flow conditions for relative depths of (a) Dr=0.21 and (b) Dr=0.42

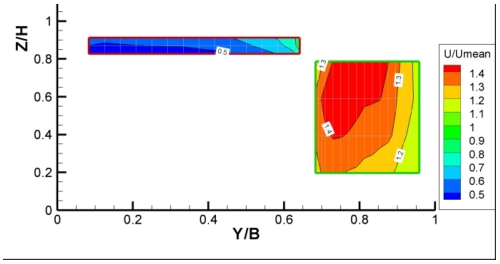

(c)

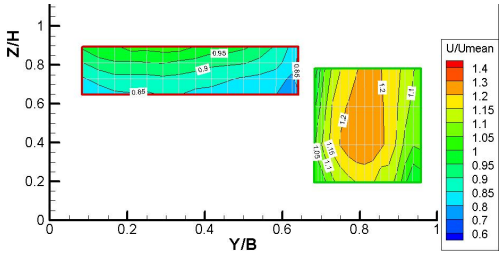

(d)

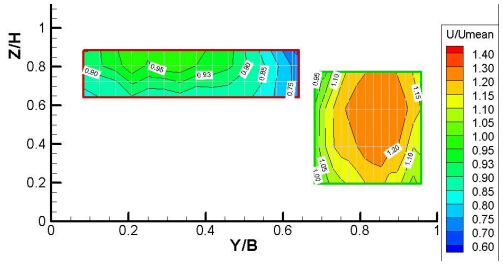

(e)

Figure 5.2: Isovels for one line of rods for cases (c) L/D=32 and Dr=0.22, (d) L/D=32 and Dr=0.43 and (e) L/D=16 and Dr=0.44

One noticeable difference between the no rod flow case and the one-line of rods cases lies in the position of the maximum velocity for the higher relative depths. This is illustrated by the arrows in Figure 5.4 and in Table 5.2.

As seen in Figure 5.4, for the deeper cases the location of maximum depth-averaged velocity is pushed 5.0 cm and 10.0 cm towards the side wall in the main channel for the rod density $\frac{L}{D} = 16$ and 32 respectively. In the floodplain, the maximum velocity has moved 5 cm towards the sidewall for both rod densities. This can be attributed to

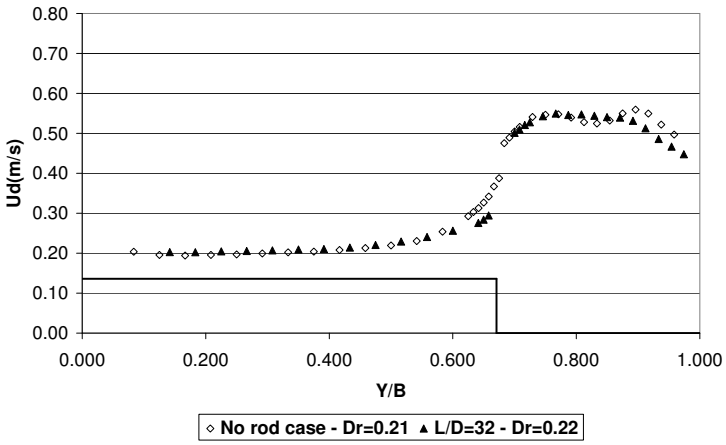

Figure 5.3: Lateral variations of depth-averaged velocity for the shallow water depth flow cases

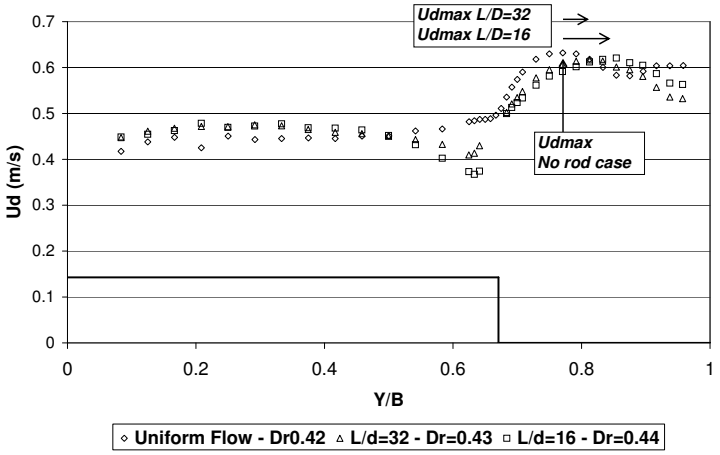

Figure 5.4: Lateral variations of depth-averaged velocity for deeper water depth flow cases

a direct impact of drag force on the velocity flow field.

5.2.2.2 Boundary shear stress distributions

Figure 5.5 presents the distribution of boundary shear across the measured sections. The distribution of boundary shear stress follows somewhat closely that of depth-

Table 5.2: Position of maximum velocity in the main channel and in the floodplain for the higher relative depths cases

Case	Position of maximum velocity in main channel (m)	Position of maximum velocity in floodplain (m)
Uniform flow case Dr=0.42	0.925	0.300
Dr=0.43 - L/D=32	0.975	0.250
Dr=0.44 - L/D=16	1.025	0.250

averaged streamwise velocity. The peaks of boundary shear stress occur at y=0.925 m, y=0.975 m and y=1.025 m for the rod cases with relative depths Dr=0.22, 0.43 and 0.44 respectively, thus coinciding with the peaks of maximum depth-averaged velocity. In the deeper cases, the boundary shear stress distribution does not vary significantly over the whole cross-section with the rod density. In the rod area, the boundary shear stress increases by 11% when the spacing ratio $\frac{L}{D}$ is doubled. The gravity component of the flow, $\rho g H S_0$ remains similar for both rod densities since the water depth increases only by 0.8%. This suggests that the change in drag force in the force balance equation is mainly compensated for by the change in bed shear stress.

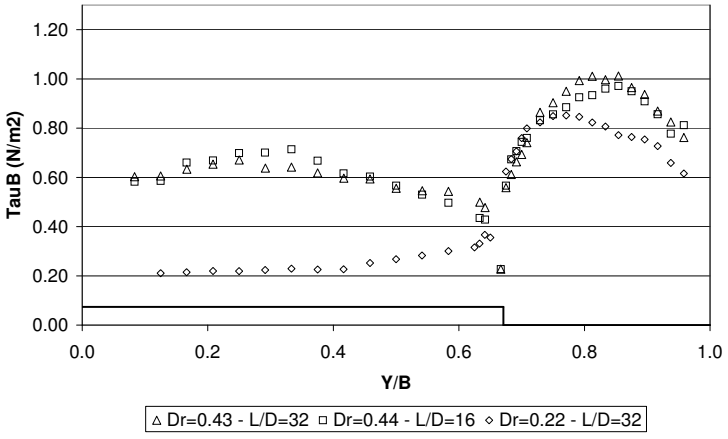

Figure 5.5: Boundary shear stress distributions

The discrepancy between the measured boundary shear stress τ_B and the gravity term

$\rho g H S_0$, which corresponds to the gravity term for a two-dimensional case with equivalent depth, were calculated for the rod cases. The results are presented in Figure 5.6.

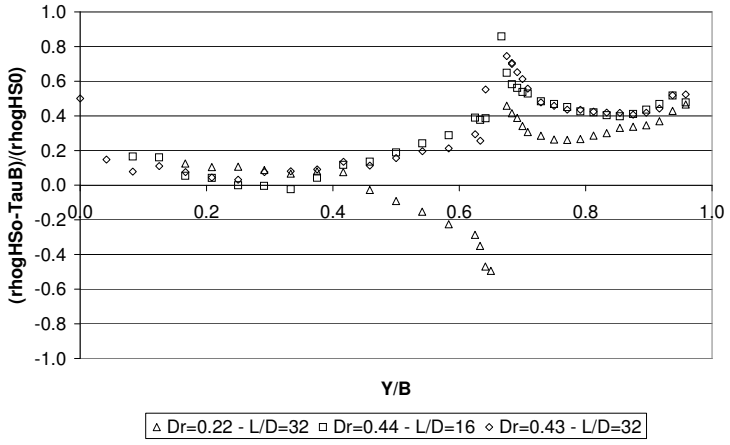

Figure 5.6: Distributions of $(\rho g H S_0 - \tau_B)$ normalised by $\rho g H S_0$

For the higher relative depth cases, the difference between the boundary shear stress τ_B and the gravity term $\rho g H S_0$ remains positive across the compound channel. However, this difference becomes negative in the shallow and less dense rod case. This variation in the difference between the gravity term and the boundary shear stress term has been associated with momentum transfer from main channel to floodplain and the presence of secondary currents, and has been explained by Shiono and Knight (Shiono and Knight, 1991). These results confirm that the shallower and less dense case approaches the corresponding no rod case.

The average values of bed shear stress in the main channel and in the floodplain were also compared to the average theoretical bed shear stress corresponding to a two-dimensional quasi-uniform flow $\rho g H S_0$ without rods. The results are presented in Figure 5.7. For the shallow case, the average bed shear stress in the floodplain is inferior to the two-dimensional value by only 3%. For the deeper cases, the average bed shear stress in the floodplain represents 86% and 83% of $\rho g H S_0$ for spacing ratios

$\frac{L}{D} = 32$ and $\frac{L}{D} = 16$ respectively. On the other hand, in the narrower main channel, the average bed shear stress represents 66% of $\rho g H S_0$ in the shallow case and approximately half of the theoretical two-dimensional value for the deeper cases. The results therefore suggest that the drag force induces a sharp decrease in the overall boundary shear stress distribution, even in a relatively wide channel such as the LMFA flume.

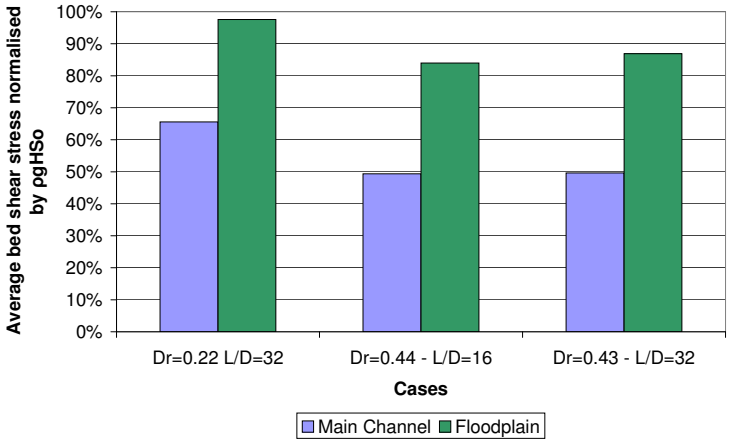

Figure 5.7: Average τ_B in main channel and floodplain normalised by $\rho g H S_0$

The apparent shear force was calculated by integrating the difference $\tau_B - \rho g H S_0$ from the main channel wall to the rod in the main channel and from the floodplain wall to the rod in the floodplain through equation 5.1:

$$\overline{\tau_{as}(y)} H(y) = \left[- \int_0^y \left(\rho g H(y) S_0 - \tau_B \left(1 - s^2\right)^{\frac{1}{2}} \right) dy + \overline{F_{wall}} \right] \tag{5.1}$$

where y is the lateral coordinate starting from the main channel wall, $H(y)$ is the local water depth and $\overline{F_{wall}}$ is the wall shear force acting on the main channel wall. The distribution of apparent shear force per unit length is shown in Figure 5.8:

The distributions of the apparent shear force exhibit linear distributions in the main channel and are approximately linear on the floodplain outside the rod area. The linearity of the apparent shear stress is characteristic of its distribution in compound channel flow. However, in compound channel flow without rods, the apparent shear

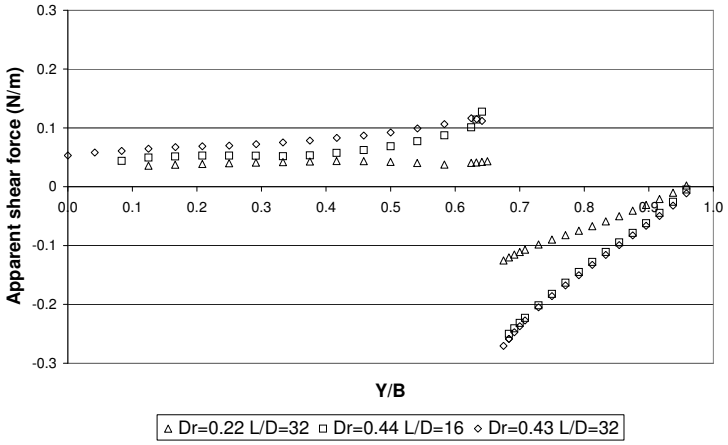

Figure 5.8: Distributions of apparent shear force per unit length

force is continuous and the gradient of its distribution changes sign at the interface (Shiono and Knight, 1991). Figure 5.9 shows some typical distributions of apparent shear stress from data collected in the FCF in Series 02. Therefore, the presence of rods at the interface changes radically the distribution of apparent shear force across the channel.

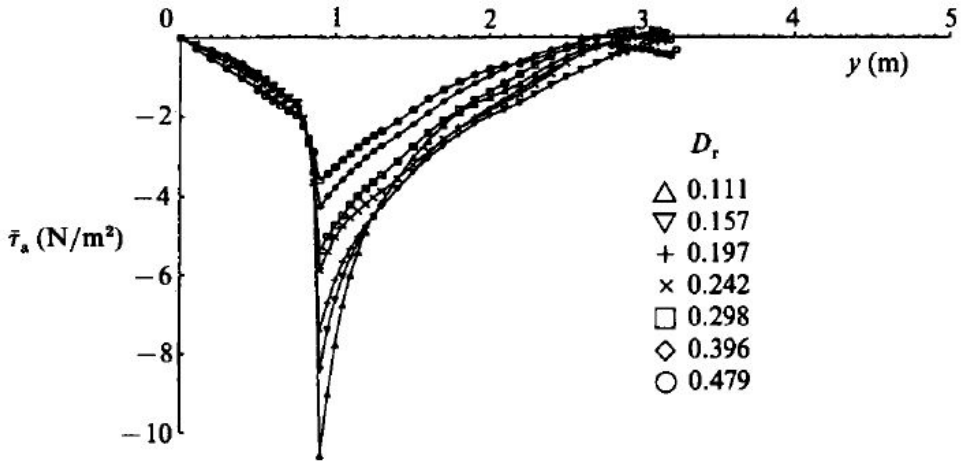

Figure 5.9: Distributions of apparent shear force per unit length in FCF Series 02, after (Shiono and Knight, 1991)

The methodology for obtaining the friction factor in LMFA is outlined below. The skin friction of the smooth channel surface was obtained from experimental data by Proust (2005). Figure 5.10 shows the Manning's n coefficient values in the main channel and in the floodplain for the no rod cases. These are comprised between 0.00889 and 0.00957. The equivalent sand grain roughness was calculated from the relationship given in Equation 5.2 (Ackers, 1991):

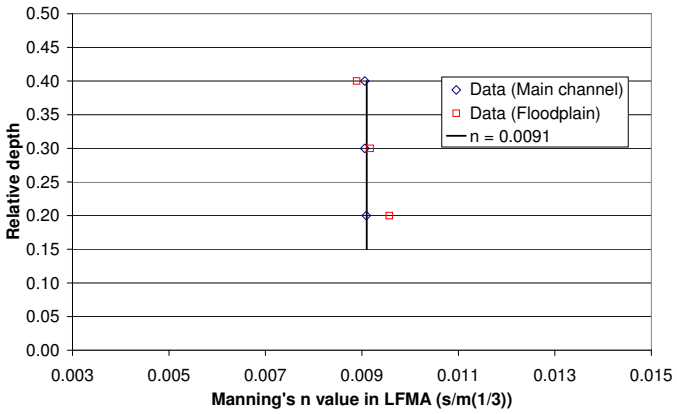

Figure 5.10: Calibrated Manning's n coefficients in LFMA flume

$$n = \frac{k_s^{\frac{1}{6}}}{8.25\sqrt{g}} \tag{5.2}$$

The calculated roughness height k_s was used in the Colebrook-White equation (C-W) to calculate the friction factor f. The C-W equation writes (Equation 5.3):

$$\frac{1}{f} = -2log\left(\frac{3.02}{Re\sqrt{f}} + \frac{k_s}{12.3H}\right) \tag{5.3}$$

where Re is the Reynolds number calculated locally with:

$$Re = \frac{4U_dH}{\nu}. \tag{5.4}$$

Given $U_* = \sqrt{gHSo}$ and $f = \frac{8U_*^2}{U_d^2}$ the expression for f can be rearranged as (Rameshwaran and Shiono, 2007):

$$f = \frac{1}{\left[-2log\left(\frac{3.02\nu}{\sqrt{128gH^3So}} + \frac{k_s}{12.3H}\right)\right]^2} \tag{5.5}$$

The validity of this formulation is assessed against the experimental data. Figure 5.11 presents the friction factors calculated from the collected dataset $\left(f = \frac{8\tau_B}{\rho U_d^2}\right)$ in the main channel and in the floodplain against the calculated friction factors using equation 5.5.

The values on the main channel tend to be underestimated by the formulae, especially towards the side wall. For the shallow case, the friction factor also tends to be underestimated on the floodplain. Nevertheless, there is a reasonable agreement between the experimental and calculated friction factors. The relative discrepancies on the average friction factor across the section are 6.4%, 2.6% and 1.4% between the experimental and calculated friction factors for cases $Dr = 0.22$, $Dr = 0.43$ and $Dr = 0.44$ respectively.

5.2.2.3 Eddy viscosity

The depth-averaged eddy viscosity $\overline{\epsilon_t}$ can be divided between the contributions made by bottom turbulence (Shiono and Knight, 1991) and transverse shear (van Prooijen *et al.*, 2005), as applied in Chapter 4.

The depth-averaged eddy viscosity due to bottom turbulence $\overline{\epsilon_{tb}}$ is modelled by Equation 5.6:

$$\overline{\epsilon_{tb}} = \overline{\lambda_{tb}}\left(\frac{f}{8}\right)^{\frac{1}{2}} U_d H \tag{5.6}$$

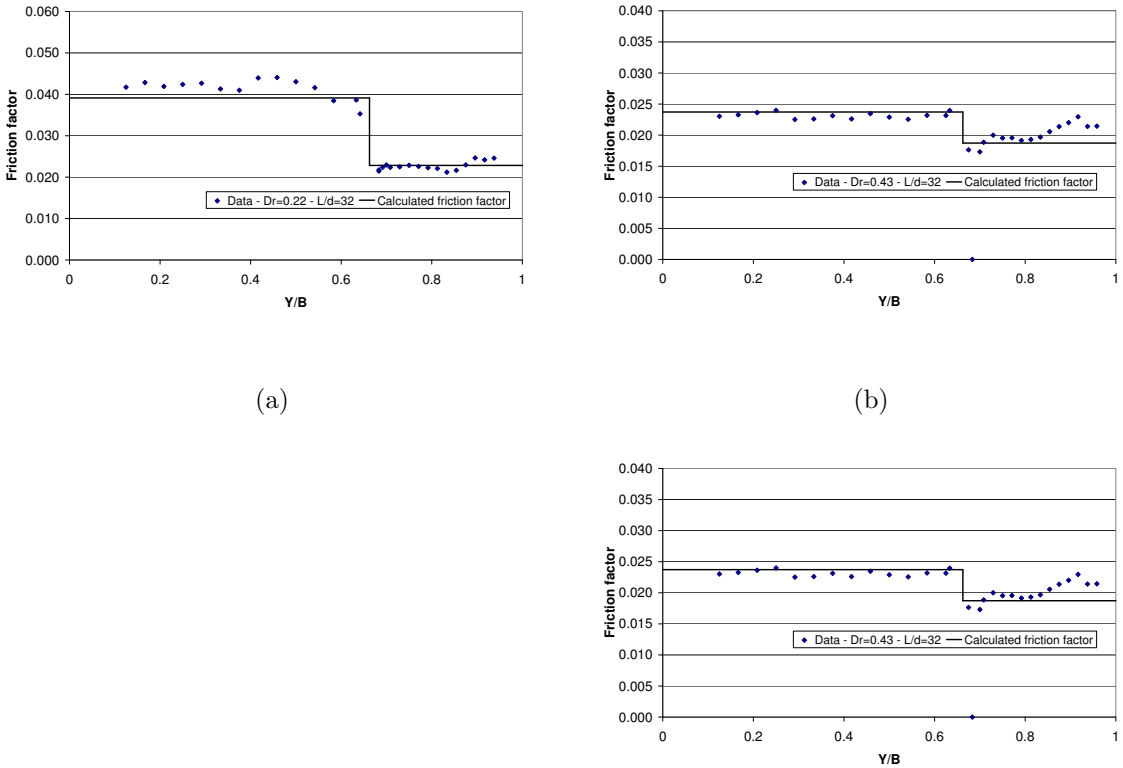

(a) (b)

(c)

Figure 5.11: Friction factor distribution for (a) L/D=32 and Dr=0.22, (b) L/D=32 and Dr=0.43 and (c) L/D=16 and Dr=0.44.

The depth-averaged eddy viscosity due to the transverse shear $\overline{\epsilon_{ts}}$ is modelled by Equation 5.7:

$$\overline{\epsilon_{ts}} = \frac{H_m}{H}\beta^2\delta^2\left|\frac{dU_d}{dy}\right| \tag{5.7}$$

The value of $\overline{\lambda_{tb}}$ is taken as 0.068 (approximately $\frac{\kappa}{6}$) (Shiono and Knight, 1991), and the value of the proportionality constant β is taken as 0.08 (van Prooijen *et al.*, 2005).

Figures 5.12 and 5.13 present the results of the calculated eddy viscosities for the no rod cases and for the rod cases respectively. No bed shear stress measurements were available for the no rod cases. As a result, the friction factor f could not be derived from $f = \frac{8\tau_B}{\rho U_d^2}$. Therefore, the eddy viscosity due to the contribution of bottom turbulence

in equation 5.6 was calculated for the two no rod cases using a friction factor derived from equations 5.2, 5.3 and 5.5.

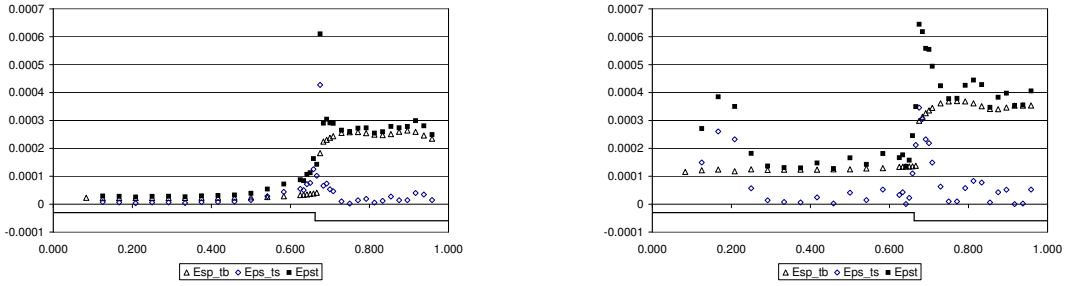

(a) (b)

Figure 5.12: Modelled eddy viscosity due to bottom turbulence and transverse shearing for (a) Dr=0.21 and (b) Dr=0.42.

The results show that for all cases, bottom turbulence is much greater, by a factor of 3 for the deeper cases, in the main channel than in the floodplain. This observation can be explained by equations 5.6 and 5.7, as bottom turbulence varies directly with the water depth H and the depth-averaged velocity U_d while the transverse shearing is a function of $\frac{H_m}{H}$ and the velocity gradient. In their analysis of the Flood Channel Facilities data, van Prooijen *et al.* (2005) also noticed this pattern when comparing bottom and transverse shear turbulence in the main channel and the floodplain in the absence of vegetation.

The transverse shearing accounts for most of the eddy viscosity at the interface and continues to dominate in the part of the floodplain located near the interface, which is consistent with van Prooijen *et al.* (2005). This is particularly the case for the shallow case, where the transverse shear turbulence is approximately 6.710^{-3} (m^2/s) which is two order of magnitude higher than bottom turbulence. For the deeper case, transverse shear turbulence is greater than bottom turbulence by approximately one order of magnitude. These results suggest that as drag force becomes greater, momentum

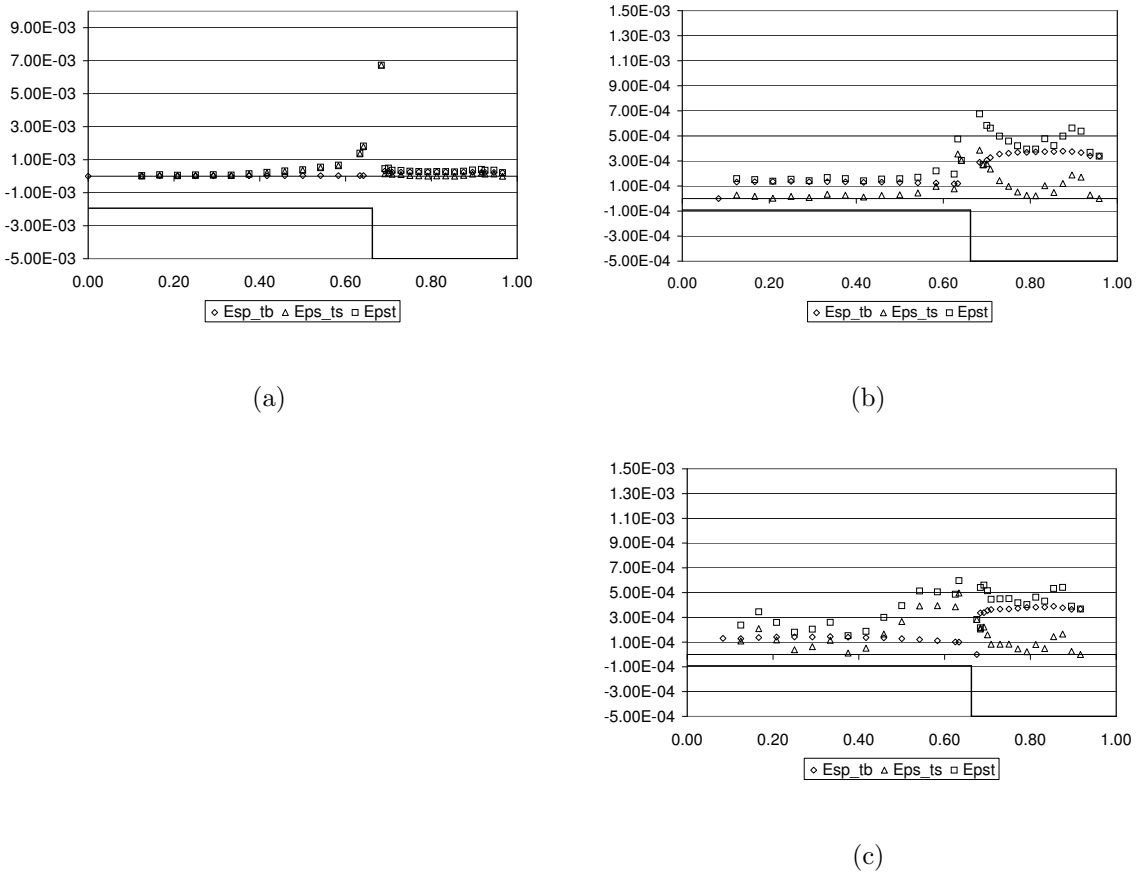

(a) (b)

(c)

Figure 5.13: Modelled eddy viscosity due bottom turbulence and transverse shearing (a) $\frac{L}{D}$=32 and Dr=0.22, (b) $\frac{L}{D}$=32 and Dr=0.43 and (c) $\frac{L}{D}$=16 and Dr=0.44.

transfer through horizontal eddies might be impeded.

For all cases however, the gradient $\frac{dU_d}{dy}$ varies significantly in the vicinity of the interface and becomes high, thereby contributing to the increase in $\overline{\epsilon_{ts}}$.

5.2.2.4 Drag force

The force balance method can be used to calculate the total drag force in vegetated compound channel. Under quasi uniform flow condition, the weight component of flow is equal to the sum of the total boundary shear force and the total drag force in vegetated compound channel. This is expressed in terms of force per unit length in Equation 5.8:

$$\rho g A S_0 = \int_P \tau_B dP + F_D \tag{5.8}$$

where P is the wetted perimeter and A is the cross-sectional area. Using the measured boundary shear stress and water level, the total drag force per unit length can be calculated exactly using Equation 5.8.

Alternatively, the drag force can also be calculated analytically using Equation 4.21:

$$F_D = \frac{1}{2} \frac{\rho C_D S_f A_P H U_{d,p}^2}{\frac{L}{D}}$$

The bulk drag coefficient ($C_D X S_F$) was determined using the results of presented in Figure 2.27 for aligned tandem of rods. For a spacing ratio 16.0 and 32.0, the bulk drag coefficients are approximately 1.015 and 1.20 respectively. The bulk drag coefficient for $\frac{L}{D} = 32.0$ was estimated by extrapolating the results for the aligned tandem of rods.

The results comparing the total drag forces obtained with force balance equation and analytically are presented in Table 5.3:

Table 5.3: Drag forces calculated from force balance and analytically for the rod cases in LMFA

Relative depth	L/D ratio	Drag force from force balance	Drag force from analytical formulae
0.21	32	0.084	0.103
0.43	32	0.324	0.158
0.44	16	0.331	0.246

The drag forces calculated from force balance for the deeper cases are similar, with $F_D = 0.324$ N/m and $F_D = 0.331$ N/m for the less dense and denser cases respectively. These close values are due to the fact that the magnitudes of the boundary shear stress distributions for the two rod densities only vary locally, namely in the rod area, while the magnitudes away from the interface are very similar, as seen in Figure 5.5. The

integrated boundary shear stress is therefore also very similar for both cases while the increase in water depth between the two cases is +0.6 mm (0.8%), as presented further in Table 5.4.

The different components of the force balance equation normalised by the gravity term $\rho g H S$ are presented in Figure 5.14.

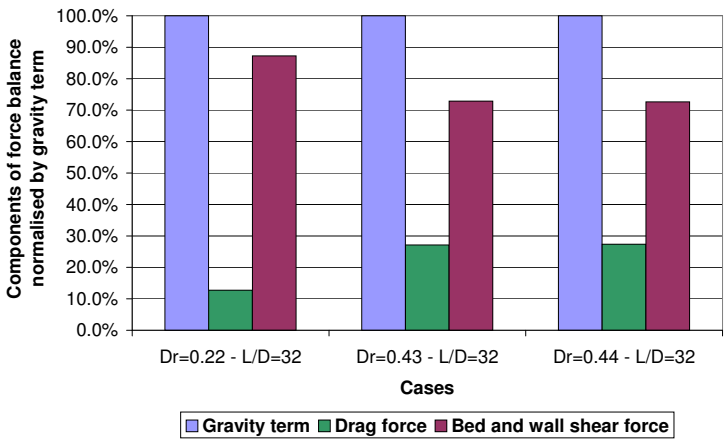

Figure 5.14: Force balance analysis

The analytical formulae produces the best estimation for the less dense and shallow water case while it underestimates significantly the results for the deeper cases. Sun and Shiono (2009) obtained the least discrepancy between the analytical formulae and the force balance method in the narrower flume of Loughborough laboratory for the higher relative depths. However, the discrepancies remained very high between analytical formulae and force balance results since the best agreement was obtained for the denser case of $\frac{L}{D} = 4.4$ and the higher relative depth of Dr=0.52 with a relative difference of 32.3%. Force balance method consistently overestimated drag force compared to analytical formulae, which is also the case in this study for the deeper cases. The analysis by Sun and Shiono (2009) was carried out with rod diameters of 9 mm which were large compared to the flume width (2.9% as opposed to 0.75% in LMFA), smaller $\frac{L}{D}$ ratios and smaller Froude numbers. In these studies, some uncertainty lies in the

estimation of the bulk drag coefficient for the studied configurations. In addition, Sun and Shiono (2009) interpreted the discrepancy between the analytical formulae and force balance method by considering the effects of shearing between the main channel and floodplain area as the water depth decreases. The shear might enhance the wakes caused by the rods, thereby increasing form drag. The enhanced wakes might move the separation point on the rod perimeter forward, hence increasing the pressure drop around the rod. The higher drag given by force balance would therefore come from the increased pressure drop around the rod.

In the LMFA study, a better approximation is achieved through the analytical formulae for the shallower water depth and less dense case. For this case, the flow characteristics are closer to those of uniform flow case, for which stronger momentum transfer is observed. These results suggest that the definition of drag force in such a three-dimensional flow field is complex and requires further research.

5.2.2.5 Stage - flow relationship

One of the impacts of one-line of rods along the main channel is to increase the water depth. Table 5.4 presents the increase in water level for the studied cases:

Table 5.4: Average Water depth in the uniform flow case and in the rod cases

Case	Water depth (m)	Increase due to rods compared to uniform flow (mm)	Percentage increase compared to uniform flow (%)
Uniform flow case Dr=0.21	0.0647	N/A	N/A
Dr=0.22 - L/D=32	0.0651	+ 0.4	0.6
Uniform flow case Dr=0.42	0.884	N/A	N/A
Dr=0.43 - L/D=32	0.0902	+ 1.7	2.0
Dr=0.44 - L/D=16	0.0909	+ 2.3	2.8

The addition of the one line of rods has for effect to increase the water depth. In terms of flood defence, this is arguably an adverse impact.

5.2.2.6 Water surface time-series

The ultrasound probe was used to measure water surface time-series in the rod wake areas for each case. The probe was placed between two rods to a distance of approximately $\frac{L}{4}$ of the upstream rod, and moved laterally within ± 10 cm so that it was recording the water surface profile in the field left by the wake. The recording time of the time series was set to 3 minutes. The sampling frequency of the probe was 50 Hz. Three sets of three-minute time-series were recorded for the deeper cases and six sets were recorded for the shallow case. The data was collected in both the main channel and the floodplain for the shallow case. The data was only collected in the main channel for the deeper and dense case, and in the floodplain for the deeper and less dense case.

A Fast Fourier Transform analysis was carried out on the collected dataset in order to identify periodic structures in the time-series data. Let $z(t)$ be the function of time representing the free surface elevation. The function was sampled at N times $t_k = h\Delta t$ where $k = 0, 1, ...N - 1$. From these N measurements, h_k, N complex amplitudes H_n are calculated:

$$H_n = \sum_{k=0}^{N-1} h_k e^{ik\frac{2\pi n}{N}} \tag{5.9}$$

The sampled function then has the discrete Fourier expansion:

$$h_k = \frac{1}{N} \sum_{n=0}^{N-1} H_n e^{-in\frac{2\pi k}{N}} \tag{5.10}$$

The right hand side of 5.10 is the discrete analogue to the complex form of the Fourier expansion as expressed in 5.11

$$h_t = \sum_{n=-\infty}^{+\infty} c_n e^{-in\omega t} \tag{5.11}$$

where the complex coefficients c_n are defined as $c_n = \frac{1}{T}\int_0^T h_t e^{in\omega t} dt$ and $\omega t = \frac{2\pi}{T}$. The number of samples used in the time-series for the analysis was set to 4096. The magnitudes of the Fourier coefficients were calculated. Figure 5.15 is a representative example of the magnitude of the Fourier coefficient against the frequency.

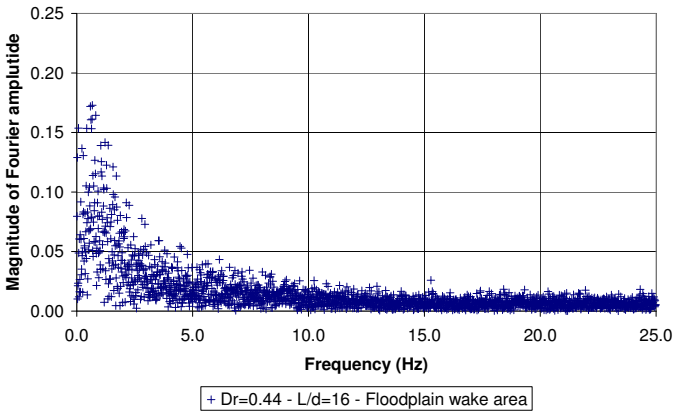

Figure 5.15: Example of magnitude of Fourier coefficient against frequency - Dr=0.44 $\frac{L}{D} = 16$

The power spectrum at a given frequency is the square of the Fourier coefficient. An example of Fourier power spectrum against frequency is given in Figure 5.16

The peaks in the magnitude of the Fourier coefficients and in the corresponding power spectrum consistently occur for frequencies comprised between 0.15 Hz and 1.1 Hz. The Strouhal numbers St for the frequencies f_{max} corresponding to these maximums is defined by equation 5.12:

$$St = \frac{f_{max} D}{U_d} \tag{5.12}$$

The results of the analysis are given in Table 5.5:

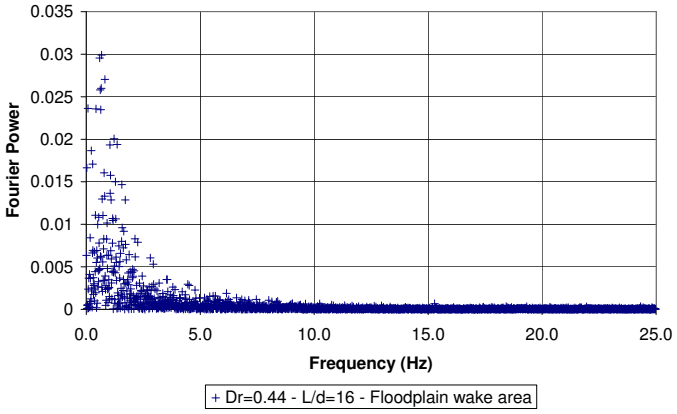

Figure 5.16: Example of Fourier Power against frequency - Dr=0.44 $\frac{L}{D} = 16$

Table 5.5: Summary of the Fast Fourier Transform analysis

Case	Average Frequency of peak	Average Magnitude of coefficient	Average Power	Average Strouhal number	Standard deviation on St
Dr=0.22 - $\frac{L}{D} = 32$ Main channel	0.366	0.145	0.021	0.012	0.0018
Dr=0.22 - $\frac{L}{D} = 32$ Floodplain	0.362	0.154	0.024	0.006	0.0011
Dr=0.44 - $\frac{L}{D} = 16$ Floodplain	0.435	0.257	0.068	0.010	0.0017
Dr=0.43 - $\frac{L}{D} = 32$ Main channel	0.870	0.190	0.037	0.015	0.003

No data based on water surface time-series was available in literature for direct comparison with the results. Hetz (1991) presented Strouhal numbers based on recorded velocity time-series for five in-line cylinders. The velocities were measured using hot wire. The magnitudes of velocity fluctuation were derived and peaks in the plots revealed frequencies at which the vortices form and shed around the cylinders. The Strouhal numbers were then calculated by normalising these frequencies with $\frac{U}{D}$. The results are provided in Table 5.6:

Table 5.6: Summary of Strouhal numbers from the five in-line cylinders (Hetz, 1991)

L/D ratio	Strouhal numbers
1.1	0.084
1.25	0.071
1.5	0.102
1.8	0.124

The results are approximately one order of magnitude higher than those presented in Table 5.5. However, these were obtained in straight channel non-compound configurations, for $\frac{L}{D}$ ratios of one order of magnitude smaller, Reynolds numbers (Re_{rod}) that varied between 10^4 and 5.10^4, and using the fluctuations of the velocity spectrum instead of the water free surface. More data is required to investigate the frequencies associated with wake flapping and the corresponding Strouhal numbers. The results could be compared to the frequencies of the turbulence motion of the flow field to assess possible correlations.

5.2.2.7 LS-PIV analysis

Confetti were used as seedings to carry out LS-PIV in the LMFA laboratory. The action of wakes on the confetti was evident, as shown in Figures 5.17, 5.18 and 5.19. These Figures are examples taken from the orthorectified photographs used for the LS-PIV analysis. The floodplain is at the top of the photographs, the main channel at the bottom and the flow direction is from right to left. Due to the strong effect of wakes, it proved impossible to ensure a consistent seeding in the vicinity of the rod. This is particularly obvious for the main channel, where only a few points could be calculated.

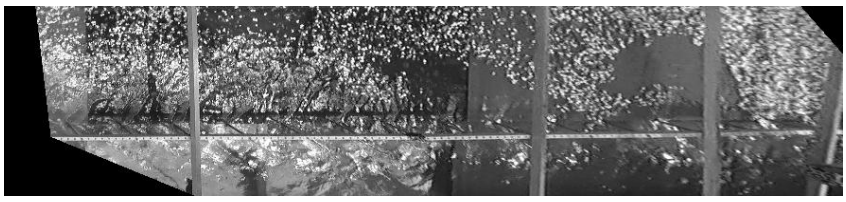

Figure 5.17: Dr = 0.22 - $\frac{L}{D} = 32$ - Action of wakes evident on the confetti seedings.

Figure 5.18: Dr = 0.44 - $\frac{L}{D} = 16$ - Orthorectified image

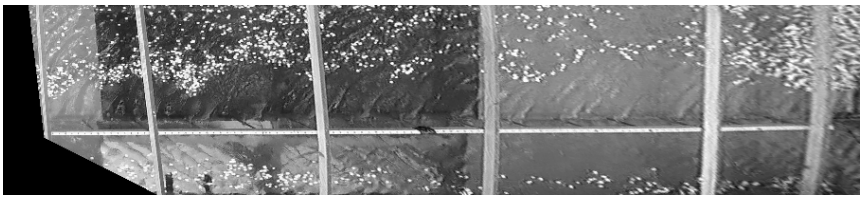

Figure 5.19: Dr = 0.43 - $\frac{L}{D} = 32$ - Orthorectified image

Surface velocities across the channel were calculated by averaging the results over 60 seconds. The surface velocities calculated by LS-PIV are compared with the measured top velocities and shown in Figure 5.20. There is generally a good agreement between the results, which gives confidence in the velocity measurements.

In the video recordings, the seedings on the water surface produce easily identified patterns. These patterns can also be used to estimate the direct area of influence of the rods. This area is obtained by measuring the widths, either side of the rods, up to which the seedings are pushed aside. This width varies through time so the envelop of the different estimates was taken from the recordings and is given approximately at ±5 cm interval. The results are presented in Table 5.7.
The stronger wake action produced at the higher relative depths explains why the width of influence of the rods tends to be larger than for the shallower case. The width of influence in the main channel is smaller than in the floodplain for all cases. This width does not vary significantly with the rod density for the deeper case.

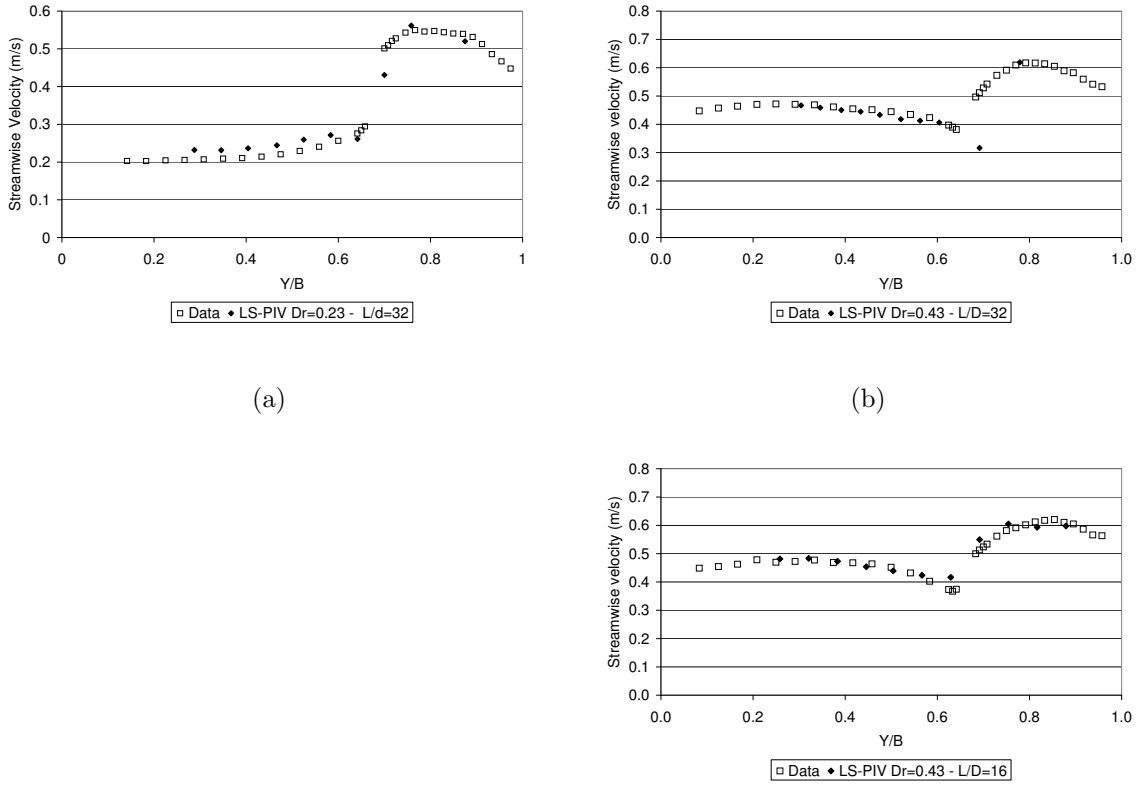

Figure 5.20: Comparison between LS-PIV surface velocities and measured data for (a) L/D=32 and Dr=0.22, (b) L/D=32 and Dr=0.43 and (c) L/D=16 and Dr=0.44

Table 5.7: Approximate widths of influence of the rods

Case	Width in main channel (m)	Width in floodplain (m)
Dr=0.22 - $\frac{L}{D} = 32$	0.25	0.31
Dr=0.44 - $\frac{L}{D} = 16$	0.31	0.42
Dr=0.43 - $\frac{L}{D} = 32$	0.30	0.31

5.3 Summary of Experiments in the LMFA Compound Channel

The overall flow characteristics generated by one-line of rods in the wider straight compound channel of LFMA are similar to the flow characteristics observed in the narrow flume of Loughborough. The depth-averaged velocity is reduced in the rod area. The

maximum velocity in the sub-sections moves away from the interface as the density of rods and the relative depth increase.

The results suggest that the drag force induces a sharp decrease in boundary shear stress, which confirms the results found in Loughborough University. This decrease in boundary shear stress is found at the sub-section scale, even in a relatively wide channel such as the LMFA flume. Drag force calculation using the analytical formulae best predicted drag force in the shallow and less dense case when compared to the force balance method. For the deeper cases, however, the analytical formulae overestimated the drag force by 24.6% and 51.1% for the spacing ratio of $\frac{L}{D} = 16$ and 32 respectively. When the rod density doubles, the drag force calculated by the analytical formulae also approximately doubles for the two deeper cases. The measured boundary shear stress between the two densities remains approximately the same. Since the weight component also remains approximately the same, so does the drag force calculated by force balance. This pattern is similar to the pattern found for the experiments in Loughborough. This discrepancy in the drag force calculation by the analytical formulae could be due in part to an approximate estimation the bulk drag coefficient, which does not suitably account for the suppression caused by the wakes.

Momentum transfer between the floodplain and the main channel increases as the density of rods decreases, as illustrated by the shallower case in LMFA. Visual observation of seedings on the water surface also confirms the presence of coherent structures that have generated some great interest in past literature (e.g. Fukuoka and Watanabe, 1997). Planform vortices were observed moving from one sub-section to another for the shallow case. However, these planform vortices were not observed for the deeper case. These results suggest that momentum transfer between the floodplain and the main channel is highly dependent upon the density of rods and the relative depth. The distributions of $\rho g H S_0 - \tau_B$ for the three studied cases also support this assumption.

The distribution of apparent shear force remains quasi linear in the floodplain and in the main channel, as observed in the uniform flow case. The apparent shear force for a larger aspect ratio therefore exhibits a similar pattern as to that observed for the smaller aspect ratio of the Loughborough flume. Bottom turbulence is dominant in the floodplain and in the main channel away from the interface. However, the transverse shear turbulence is preponderant at the interface in the rod area. This increased transverse shear turbulence observed near the interface is characteristic of a shear layer.

The Fast Fourier Transforms of the water surface time-series in the rod area have peak frequencies in the power spectrum that are consistently in the order of 0.3 to 0.9 Hz. The corresponding Strouhal numbers are in the order of $1.0\text{x}10^{-2}$. More data is necessary to correlate the water surface fluctuations and the frequencies associated to wake flapping with Strouhal numbers and the characteristics of the turbulent flow field.

CHAPTER 6

Analysis of Acoustic Doppler Current Profiler measurements

"Altissima qusque flumina minimo sono labi (The deepest rivers flow with the least sound)." Q. Curtius, vii. 4. 13

6.1 Introduction

One of the greatest problems in research on compound channel hydraulics stems from the lack of confrontation between experimental and field data. Elaborated theories on flow structures in compound channels might be derived by laboratories, but their applicability and their engineering value can remain questionable as long as they have not been exposed to field cases.

Significant technological progress has been made in the field of instrumentation over the past decade. Field measurements have now become more routinely used by river engineers. However, such measurements are often restricted to in-bank flow cases. Measurements carried out during overbank flow events, particularly in large rivers, pose a serious challenge in terms of health and safety. Data sets such as those used in this chapter, collected on the river Rhône in France or the river Derwent in England, are sill rare.

In this chapter, based on the field data collected in the river Rhône for two overbank flow events and in the river Derwent for one overbank flow event, the flow structures in compound channel with vegetation on the floodplain are analysed. Section 6.2 presents the benefits and limitations of the vessel-mounted Acoustic Doppler Current Profilers used in the river Rhône. Section 6.3 lays out the methodology adopted to analyse the measured data. The flow structures of the two overbank flow events are presented. In Section 6.4, the methodology derived to analyse the flow structure in the river Rhône is validated on the data measured in the river Derwent. The benefits of Acoustic Doppler Profilers and of their stationary mode are presented. The characteristics of the flow at Derby Saint Mary's are analysed. Section 6.5 summarises the results from analysis of field data. These results are used in Chapter 7 to confront the modified Shiono and Knight method to field data.

6.2 Acoustic Doppler Current Profilers in Fluvial Applications

6.2.1 Introduction

Until recently, applications related to Acoustic Doppler Current Profilers (ADCP) were mainly restricted to the study of flow in oceans and estuaries. However, the range of application of ADCPs has widened since the 1990s and the development of broadband, multi-pulsed ADCPs. They are now commonly used in shallow waters and provide high spatial resolution data. Vessel-mounted ADCPs are used to gauge river flow and to update or validate stage-discharge rating curves. They have also been used successfully in a wide range of applications, including the investigation of dispersion coefficients in rivers (Carr and Rehmann, 2007).

Vessel-mounted ADCPs can potentially be used in the analysis of mean velocities, turbulence characteristics (intensities, Reynolds stresses) and velocity distribution in addition to discharge measurements. However, there are limitations inherent to the nature of the instrument. The limitations have been widely discussed in literature (e.g.

Dinehart (2003), Muste *et al.* (2004), Dinehart and Burau (2005), Sime *et al.* (2007), Le Coz *et al.* (2007)). The limitations include the impossibility to measure near water surface due to contamination in the return signal, some dispersion in the measurements inversely proportional to the ultrasound frequency, the size of the bin and the number of independent measures, and a low sampling frequency. In spite of these limitations, the data collected from vessel-mounted ADCPs provide useful information in the analysis of river flows.

6.2.2 Understanding the limitations of vessel mounted ADCP data

The limitations of ADCP applied in rivers are listed and discussed more fully below.

1. Assumption of homogeneous velocity field

   The most questionable assumption of velocity measurement by ADCP lays that the water currents are horizontally homogeneous within the spread of the beams. Exceptions to this assumption can be substantial in rivers because of the ubiquity of sediment suspension by macroscale turbulence throughout the water column (Dinehart, 2003). The uncertainty in velocity components that can arise when crossing a highly turbulent flow field is reduced by the use of multiple pings (Gordon, 1996). Although velocity ensembles derived from multiple pings may mask the inclusion of ambiguity velocities, the net effect is that velocity directions become more uniform.

2. Size of sampling window

   ADCP measures radial velocities in a sample window which is determined by the diameter of the acoustic transducer, the angular width of the beam and the depth of the cell height (Muste *et al.*, 2004). The smallest expected turbulent eddies in a river flow are several orders of magnitudes smaller than the sample window. The smaller turbulent fluctuations are dampened so that the turbulent scales which are smaller than the measurement volume cannot be resolved and become source of noise.

3. Range

   In vessel mounted ADCP in multiple pings mode, the measurement volume increases proportionally with the vessel translation velocity. Also, the beam spread, and consequently the magnitude of error, increases when the distance from the instrument increases. In other words, the data sampled in the lower part of the channel depth has a greater uncertainty when ADCP is used from the water surface.

4. Side-lobe

   The beam angle of the main lobe of an ADCP transducer is 20° or 30° off the vertical. This means that the distance to the boundary along the ADCP centerline is shorter than the distance to the boundary along a beam. Most boundaries will tend to reflect much more strongly than the scatterers. As a result, so-called sidelobe energy can travel the shorter path directly to the surface and thereby contaminate the measurements. An ADCP with a 20° beam angle has a potential for sidelobe contamination at (distance to the boundary)*cos(20°), or equivalently, the last 6% of the profile. Typically, the bottom part of the measurements therefore has to be excluded.

5. Blanking distance

   Measurements near the surface are also subject to ringing errors. After transmission, the ADCP electronics and transducer require some finite time to dampen the transmit energy. During this time, any signal return will be contaminated. A blank zone is defined near the head of the ADCP, usually corresponding to the minimum distance required to avoid collecting the potentially contaminated data (Muste *et al.*, 2004).

6. Doppler noise

   ADCP measuring technique also generates a random error that is referred to as a Doppler noise. When the measuring cells are too small, the Doppler noise tends too increase and velocity profiles can appear more dispersed and present some

abberations. This dispersion is inversely proportional to the ultrasound frequency, the size of the bin and the square root of the number of independent averaged measures (Le Coz *et al.*, 2007). For example the dispersion for a RioGrande 1200 kHz ADCP with a bin size of 40 cm is 9 cm. This dispersion is reduced to 4.5 cm if four independent measurements have been carried out.

7. Sampling frequency

   The vessel mounted ADCPs still have a relatively low sampling frequency processing compared to the high sampling frequency of laser Doppler for example, commonly used in laboratories. Nezu and Nakagawa (1993) have defined the maximum response frequency recommended to study turbulence (Equations 6.1 and 6.2):

$$f_{max} = k_{max} \frac{U_m}{2\pi} \tag{6.1}$$

$$f_{max} \geqslant \frac{100 U_m}{2\pi L_x} \simeq \frac{50}{\pi} \left(\frac{U_m}{h} \right) \tag{6.2}$$

   where k_{max} is the kinematic wave number, U_m is the mean bulk streamwise velocities, L_x is the macroscale of turbulence and h is flow depth in the outer region. Equation 6.2 assumes that the macroscale of turbulence L_x scales with the flow depth, assumption also common in experimental studies. The recommendation is that the data processing should be chosen to satisfy the condition $f \geq 2 f_{max}$ in order to allow for the elimination of data aliasing.

6.3 Analysis of ADCP Measurements carried out on the River Rhône (France)

6.3.1 Introduction

ADCP measurements were carried out on the River Rhône in April 2006 for two overbanks flows. Transverse profiles were taken at three cross-sections and one longitudinal

section in the area of Pierre-Benite on the 4^{th} and the 11^{th} of April 2006. The transverse profiles were taken at kilometer points 7.1 km and 7.7 km on the 4^{th} of April and at kilometer points 7.1 km and 7.85 km on the 11^{th} of April. Figure 6.1 is a location plan of the cross-sections at the kilometer points 7.1 km, 7.7 km and 7.85 km. On the 11^{th} of April, the downstream profile should have been taken at the same location as for the 4^{th} of April, i.e. kilometer point 7.7 km. However, the conditions were such that the exact location was difficult to identify, which resulted in a shift of 150 m in the profile location.

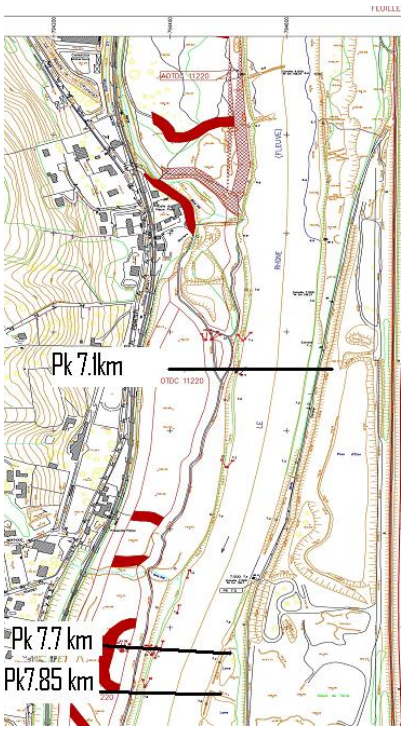

Figure 6.1: Location plan

6.3.1.1 Description of the channel

This stretch of the River Rhône is relatively straight and behaves as a compound channel. The downstream end of the stretch, at kilometer points 7.7 and 7.85, the floodplain on the right bank tends to be slightly converging while the floodplain on the left bank

is slightly diverging. The floodplain remains dry most of the year. The flow in this part of the river is controlled upstream by the dam of Pierre-Bénite at kilometer point 5.0 km.

At kilometer point 7.1 km, the main channel and the floodplain are approximately 130 m and 60 m wide respectively. The cross-section of the main channel approaches that of a trapezoidal channel. Further downstream, at kilometer point 7.7 km, the main channel is 130 m wide and is divided in two parts: the main part is 100 m wide and is separated from the second part by an 8m wide embankment. The floodplain is just over 52 m wide. At kilometer point 7.85 km, the main channel is 145 m wide and the floodplain is 50 m wide. The aspect ratio of the channel is approximately 18.3 upstream and 20.6 downstream. The river Rhône in the study area is therefore a wide river.

The density of trees on the floodplain was estimated using the results from a tree survey carried out in June 2007. The density of trees in the study area was estimated to be 3 trees per 10 m^2 with an average tree diameter of 0.5 m. These figures are used in the modelling carried out in Chapter 7. Figure 6.2 shows a typical tree arrangement.

Figure 6.2: Illustration of floodplain vegetation

6.3.1.2 Description of the two overbank flood events

The peak flows were estimated to be 1600 m^3/s and 2400 m^3/s on the 4^{th} and 11^{th} of April 2006 respectively. Figure 6.3 presents the flow time-series derived using the rating curves available at the kilometer points 5.5 km (blue line), 7.5 km (green line) and further downstream at 15.2 km. The inspection of the discharge time-series suggests that the flow of this large river remains relatively constant on a scale of one hour and can therefore be regarded as a steady state condition for both events.

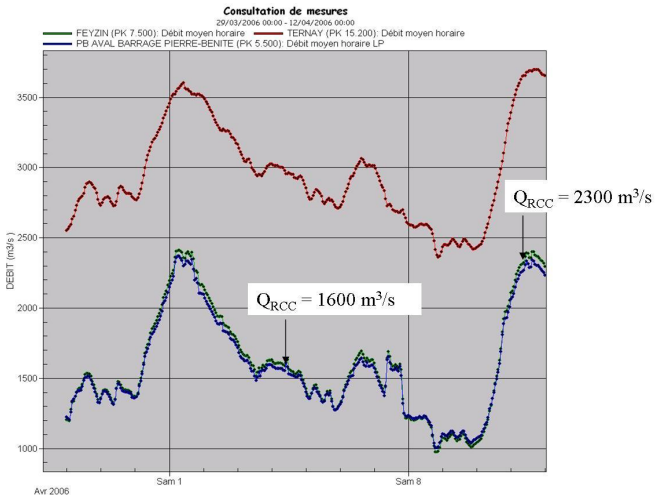

Figure 6.3: Flow time-series at kilometer points 5.5 km, 7.5 km and 15.2 km between 29/03/2006 and 12/04/2006

On the 4^{th} of April, the relative depth ratio $\left(\frac{H_{mc}-h_{fp}}{H_{mc}}\right)$ at this stretch of the river was approximately 0.09. On the 11^{th} of April, the relative depth ratio was 0.22. The slope of the water profile was 1/2000 for both events.

6.3.1.3 Characteristics of the measurements

Two different ADCP recorders were used to measure the velocities in the floodplain: a 1200 kHz vessel-mounted RioGrande and a 2400 kHz vessel-mounted StreamPro. For the main channel, a 600 kHz vessel-mounted RioGrance was used. The measurements

were carried out by the CNR (Compagnie Nationale du Rhône).

The main characteristics of the operational procedures used for each ADCP are described in Table 6.1. The StreamPro ADCP and the two RioGrance ADCPs used 6 and 5 pings per ensemble respectively.

Table 6.1: Main characteristics of the operational procedures used for the ADCP

$Operational Characteristics$	$StreamPro$	$RioGrande 1200kHz$	$RioGrande 600kHz$
Number of pings per ensemble	6	5	5
Sampling frequency (Hz)	1	0.8	0.6
Blanking distance (cm)	3	10	15
Depth of cell length (cm)	10	10	35

On the 4th of April, the depth of water in the floodplain was shallow (less than 1 meter) and the use of the ADCP RioGrande 1200 kHz was not appropriate, as confirmed by Serge Françon from CNR (*Phone conversation, 22/06/2007*). The data collected with this instrument were discarded. Therefore, the data analysis was carried out with the data obtained from the StreamPro 2400 kHz, more suited to shallow water measurements.

6.3.2 Flow characteristics and limitations of the vessel mounted ADCP used in the study

6.3.2.1 Overall flow characteristics

Table 6.2 presents the characteristics of the flow measured at the three cross-sections in the floodplain and in the main channel. The velocity on the floodplain is very low due to the presence of vegetation.

The Froude numbers range from 0.02 to 0.203 and the flows are therefore subcritical, like the flows studied in the experimental flumes presented in Chapters 4 and 5. The Froude numbers in the floodplain are typically lower than 0.05 and are therefore smaller than the Froude numbers from experimental flows. However, the Froude numbers in

Table 6.2: Flow characteristics

Case	Mean velocity (m/s)	Maximum Water depth (m)	Reynolds number	Froude number
Pk 7.1km - 04/04/06 - Main channel	1.07	5.50	$23.459\ 10^6$	0.145
Pk 7.1km - 04/04/06 - Floodplain	0.06	0.88	$0.203\ 10^6$	0.020
Pk 7.7km - 04/04/06 - Main channel	1.17	5.77	$27.086\ 10^6$	0.156
Pk 7.7km - 04/04/06 - Floodplain	0.10	1.27	$0.368\ 10^6$	0.035
Pk 7.1km - 11/04/06 - Main channel	1.78	7.81	$55.619\ 10^6$	0.203
Pk 7.1km - 11/04/06 - Floodplain	0.17	2.20	$1.473\ 10^6$	0.036
Pk 7.85km - 11/04/06 - Main channel	1.70	7.97	$54.098\ 10^6$	0.192
Pk 7.85km - 11/04/06 - Floodplain	0.19	1.99	$1.522\ 10^6$	0.043

the main channel are of the order of $0.15 \sim 0.20$, which is comparable to the Froude numbers observed during the experiments carried out in Loughborough University.

The Reynolds numbers range from $0.203\ X\ 10^6$ to $55.619\ X\ 10^6$ and the flows are therefore highly turbulent. Although all experimental flows were fully turbulent, these Reynolds numbers are significantly higher than the Reynolds numbers obtained experimentally. In the main channel, the Reynolds numbers are two orders of magnitude higher than the flows studied in the LMFA flume.

These results suggest that the flows analysed in this chapter are of the same nature as the flows studied in experimental flumes, i.e. subcritical and fully turbulent.

6.3.2.2 Size of flow structures

Many studies have shown that the overall channel geometry dictates the size of the largest scale of turbulent motion (e.g. Knight *et al.*, 2007). Typically, the size of secondary circulation is of the order of the size of the flow depth as the secondary circulation cells extend from the channel bed to the water surface.

6.3.2.3 Limitations of the vessel mounted ADCP used in the study

Based on the flow characteristics presented in Table 6.2, the maximum kinematic wave number k_{max} and the threshold frequencies f_{max} derived from Equations 6.1 and 6.2 can be calculated. The results are presented in Table 6.3.

Table 6.3: Threshold frequencies recommended to investigate turbulence

Case	Maximum kinematic wave number $k_{max}(m^{-1})$	Threshold frequency f_{max} (Hz)
Pk 7.1km - 04/04/06 - Main channel	18.19	3.09
Pk 7.1km - 04/04/06 - Floodplain	45.38	1.04
Pk 7.7km - 04/04/06 - Main channel	17.32	3.23
Pk 7.7km - 04/04/06 - Floodplain	113.53	1.88
Pk 7.1km - 11/04/06 - Main channel	12.80	3.63
Pk 7.1km - 11/04/06 - Floodplain	45.38	1.21
Pk 7.85km - 11/04/06 - Main channel	12.55	3.39
Pk 7.85km - 11/04/06 - Floodplain	45.38	1.59

The maximum response frequencies of all the ADCPs used in the study were below or equal to 1Hz, which is much smaller than the frequencies estimated in Table 6.3. Hence, fine turbulence could not be expected to be resolved. It is important to note that the ADCP used in the study would normally not meet the criteria set by Equation 6.2 for a typical river.

6.3.3 Data analysis

6.3.3.1 Data post-processing methodology

The collected data was processed according to the following methodology:

The location of each data point is referenced with North-East Earth coordinates. The data for all crossings at a particular location is plotted and a suitable axis of projection is defined by applying a least squared trendline to the data set.

The profiles are then superimposed. Correct superimposition is achieved by checking that the bathymetry profiles for each crossing match each other.

The streamwise and transversal components of the instantaneous velocities are obtained by projection from the North-East recorded components. The instantaneous velocity vectors are fully defined for each crossings by adding the vertical component, which is left unchanged.

An interpolation mesh is defined and is used to interpolate the results of each crossings. For the main channel, a resolution of 0.4 m in the vertical direction by 1 m in the transverse direction was selected. For the floodplain, a resolution of 0.1 m and 1 m were selected in the vertical and transverse direction respectively. This corresponds approximately to the resolution of the measurement mesh. A test on the mesh resolution was carried out. For the upstream cross-sections for instance, these

measurement densities correspond to vertical resolutions of $\frac{H}{13.8}$ to $\frac{H}{19.5}$ and horizontal resolutions of $\frac{B}{130}$ to $\frac{B}{145}$. In laboratory experiments, this resolution can be regarded as rather dense as vertical resolutions investigated in this research were in the order of $\frac{H}{4}$ to $\frac{H}{10}$ and horizontal resolutions of $\frac{B}{24}$ up to $\frac{B}{100}$ locally near the interface between the main channel and floodplain.

In order to obtain a sufficient representation of the secondary circulation, the relatively fine resolution adopted in this study was found suitable.
A simple inverse distance interpolation algorithm was used for the interpolation. A test on the density of neighboring points to be used for the interpolation was carried out. For a high enough number of points (higher than 32), the variation of the results becomes insignificant. For this study, 128 points were selected for the interpolation. The results were validated by comparing the measured discharge with the discharge integrated after interpolation. Typically, the discrepancy is around 5% for each profile which was regarded as acceptable.

The mean velocity components are obtained by combining the profiles on the interpolation grid, using $U_i = \frac{1}{n}\sum_{j=1}^{n} u_{i,j}$, where j refers to the j^{th} crossings, n is the number of crossings and u_i is a given velocity component. The velocity fluctuations can then be calculated as well as the other turbulent characteristics of the flow. These calculations are detailed in the next sub-section.

The analysis of the longitudinal section profiles was carried out using a spatial averaging over the entire length of the profiles for each cell depth.

The following general comment applies to the data collected for this study. There is usually some discrepancy in the track followed by the boat to cross the river, due to the difficult navigation conditions. Although special attention was paid on site to have similar Made Good distances for all crossings at a given location, this sometimes masks spatial discrepancies between crossings. The Made Good distance is defined as the measure of the actual distance between the platform and the start point (i.e. variations in the course track removed). Variations between crossings can exceed 10 meters in the

East or North directions. This is reflected in the spread around the trendline used as a projection axis. Nevertheless, the superposition of bathymetry data gave satisfactory results. Only two profiles were excluded from the analysis because of mismatch in the bathymetry.

6.3.3.2 Example: application to the upstream cross-section for the high flow event

The methodology described above in the subsection 6.3.3.1 was applied to the whole dataset. The processing of the data and the analysis of the results obtained for the high flow event on 11th of April 2006 at kilometric point 7.1 km are detailed below.

For the main channel, the four available profiles were used. A comparison between the implementation plan and the recorded East-North coordinates of the boat tracks shows a good agreement between the four crossings (two "right bank - left bank" crossings and two "left bank - right bank" crossings). The overall Distance Made Good remains similar for all crossings and is about 190 m. The projection axis is defined from the scatter data points. The data is projected and the profiles are re-aligned in order to superimpose the bathymetry. The results of the bathymetry adjustments are presented in Figure 6.4.

The same process was repeated for the floodplain data. The results for the full cross-section were obtained by combining the results obtained for the main channel and floodplain.

The instantaneous measured velocity fields of each cross-section were then projected on the defined axis. The mean velocity field, composed of the three velocity components, was calculated by combining the four projected instantaneous velocity fields using an inverse-distance interpolation method.

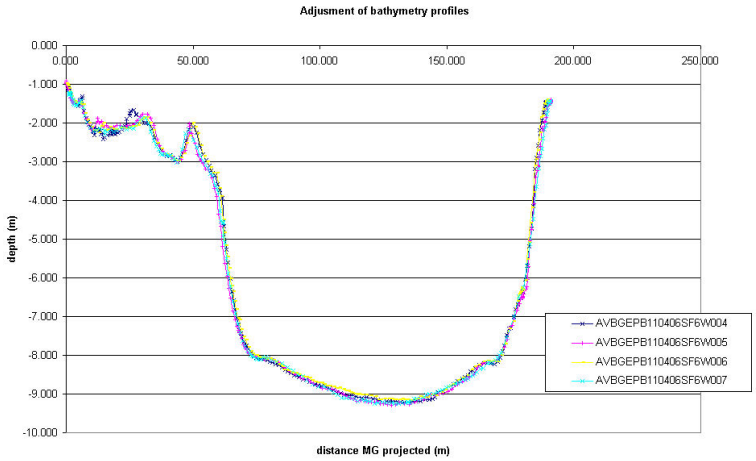

Figure 6.4: Superposition of the bathymetry profiles for the upstream cross-section during the high flood event

6.3.4 Results

6.3.4.1 Mean flow

The streamwise depth-averaged velocity at a particular transverse location y is calculated using Equation 6.3:

$$U_d(y) = \frac{1}{H(y)} \int_{z=0}^{H(y)} U(y) dz \tag{6.3}$$

The results of the depth-averaged velocity are presented in Figures 6.5. The streamwise depth-averaged velocity reaches the maximum values at the centre of the main channel and decreases somewhat abruptly from the edge of the main channel side slopes to the river banks. Despite a certain degree of spikiness, the results are in broad agreement with the results published in the literature related to flows in compound channels (e.g. Abril and Knight, 2004).

6.3.4.2 Estimation of Shear Velocity and Roughness

The shear velocity U_* can be estimated using a reach-averaged value calculated as 6.4:

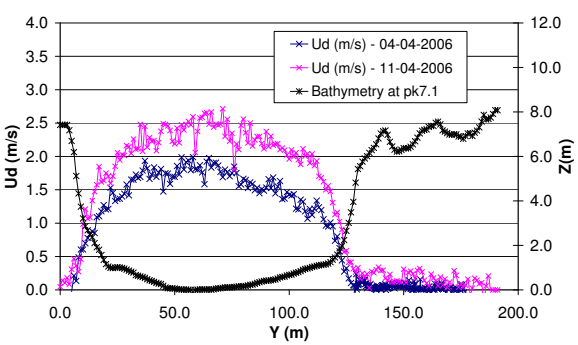

(a)

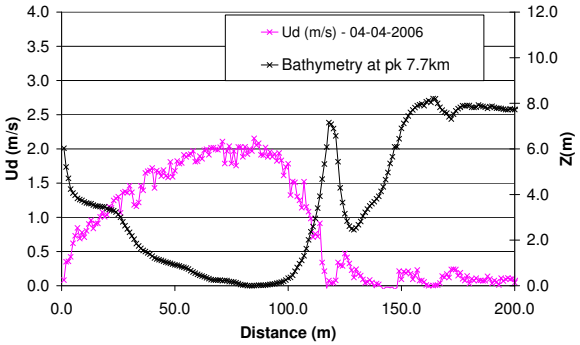

(b)

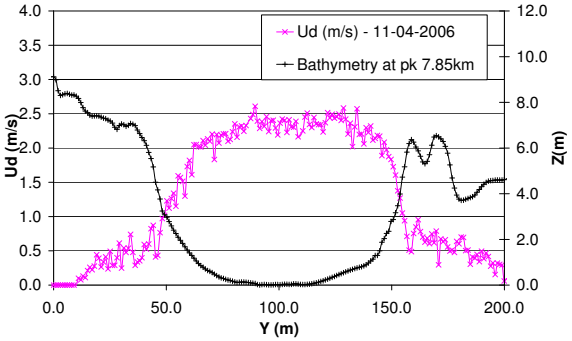

(c)

Figure 6.5: Depth-averaged Velocity U_d (m/s) at pk 7.1 km, 7.7 km, and 7.85 km respectively.

$$U_* = \sqrt{gRS_f} \tag{6.4}$$

where R is the hydraulic radius, g is the gravitational acceleration and S_f is the friction slope. Assuming uniform flow conditions, 1) the bed friction slope, the energy slope and the bottom slope are equal 2) the bottom slope and the water surface slope are equal. Thus, S_f can be approximated by the water profile slope S_0 in the centre of the main channel. In addition, the approximation $R \approx H$ holds as the studied channel is sufficiently wide ($\frac{B_{mc}}{H_{mc}} \geq 12$).

Where the flow is mainly two-dimensional, that is in the centre of the main channel, the local shear velocity can also be estimated from the vertical distribution of the mean streamwise velocity U assuming that the vertical profile follows the logarithmic law of the wall (Babaeyan-Koopaei *et al.*, 2002). At a height z above the bed, the vertical profile of U follows Equation 6.5.

$$\frac{U}{U_*} = \frac{1}{\kappa} \ln\left(\frac{z}{Zo}\right) \tag{6.5}$$

where κ is the von Karman's constant (taken as 0.41) and Zo is the characteristic roughness length.

U_* and Zo were obtained by plotting the previous data in its semi-logarithnic form and fitting a least square regression to the profile. U_* and Zo are calculated from the slope and the intercept of the linear regression.

The log-law was applied to the vertical profiles of the streamwise mean velocity in the main channel. In order to smooth out the irregularities, the vertical profiles used at a given y location across the channel are averaged over a width of $y \pm 2m$. The profiles for which the low-law had a least square fit R^2 inferior to 75 % were excluded from the calculations. The average values of Z_0 obtained from the log-law are given in Table 6.4:

The bed shear stress τ_b is calculated from the shear velocity using the quadratic relationship 6.6:

$$\tau_b = \rho U_*^2 \tag{6.6}$$

Considering the crude approach adopted in this study, the cross-section averaged-value τ_{b0} and the average bed shear stress derived from the log-law fitting are in reasonably close agreement, the difference between both values lying below or around 5 %.

Table 6.4: Comparison of the different roughness values using the ADCP Rhône data

	04-04-06 pk7.1	04-04-06 pk7.7	11-04-06 pk7.1	11-04-06 pk7.85
Average Z_0 (m)	0.032	0.045	0.035	0.072
Cross-section averaged bed shear stress Tb (N/m^2)	35.9	39.4	42.9	42.6
Average bed shear stress Tb (N/m^2)	33.4	37.2	42.1	40.9
Average least square fit R^2	0.95	0.96	0.91	0.96
Standard deviation of boundary shear stress (N/m^2)	5.50	3.84	10.41	10.71

The cross-sectional variation of the bed shear stress obtained from the log-law fitting are presented in the Figure 6.6.

The bed shear stress typically varies between 0.7 τ_{Bmean} and 1.3 τ_{Bmean} in the upstream sections. These variations are similar to those measured by Nezu *et al.* (1993) in the wide channel of the Biwako-Sosui River. The authors found that the variations of boundary shear stress in that river lies between 0.65 τ_{Bmean} and 1.3 τ_{Bmean}, as shown in Figure 6.7. It is interesting to note that the Biwako-Sosui River, having an aspect ratio of 8, also belongs to the wide channel category. This undulation of bed shear stress is significant when considering sediment or pollutant transport in rivers.

Variations of bed shear stress would normally be interpreted in relation to the secondary current patterns. As highlighted by Nezu and Nakagawa (1984), one would expect the bed shear stress to become largest at the downflow ($W < 0$) and to become smallest at its upflow ($W > 0$). However, in the present dataset, the correlation between bed shear stress and upflow - downflow gave mixed results. In particular the areas of

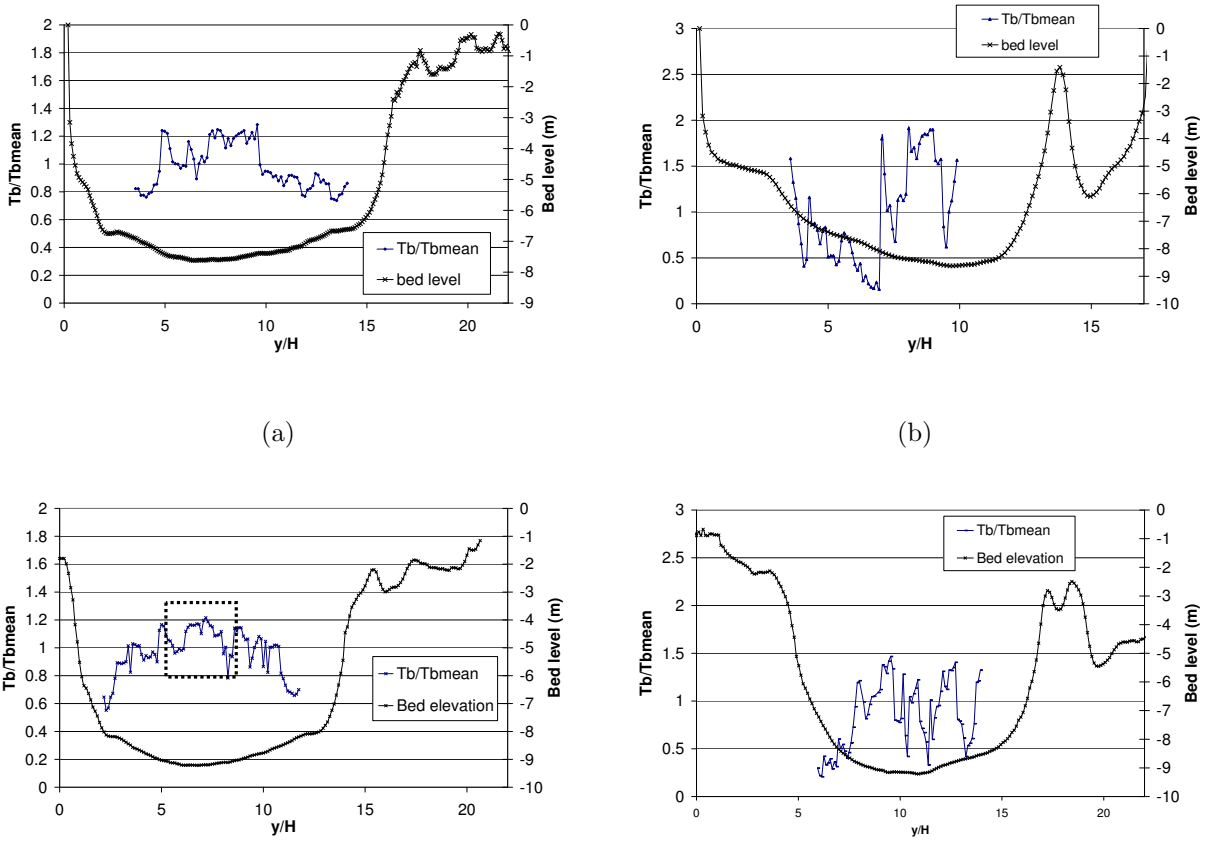

Figure 6.6: Bed shear stress $\tau_B(N/m^2)$ for the low flow event at pk 7.1 km, 7.7 km, and for the high flow event at pk 7.1 km and 7.85 km respectively. Results in the area within the dashed rectangle of Figures (c) are presented in Figure 6.8

upflow proved difficult to relate with decreasing bed shear stress. This may be due to inaccuracies in the projection of the velocity field. An example of correlations between secondary currents and bed shear stress is given in Figure 6.8.

6.3.4.3 Secondary current and vorticity

The secondary currents V and W in a straight channels are governed by the vorticity equation, which writes in the streamwise direction as Equation 6.7:

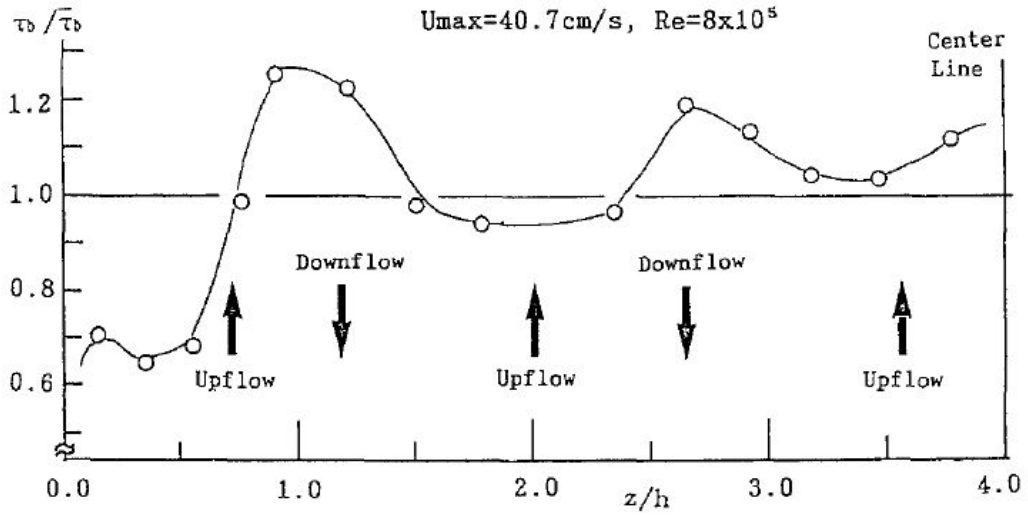

Figure 6.7: Spanwise variation of bed shear stress in Biwako-Sosui river, after Nezu *et al.* (1993)

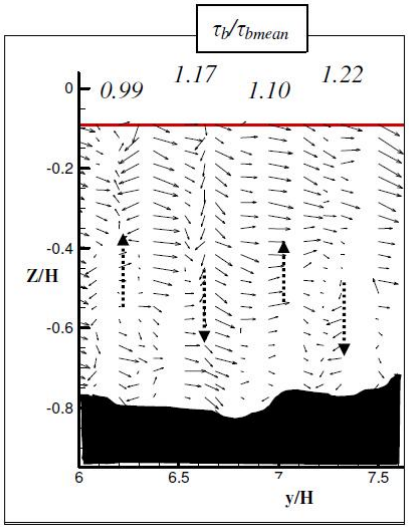

Figure 6.8: Example of correlation between boundary shear stress variations (arrows) and secondary currents (vectors) at pk 7.1 km for the high flow event in the main channel

$$V\frac{\partial \omega_x}{\partial y} + W\frac{\partial \omega_x}{\partial z} = \frac{\partial^2}{\partial y \partial z}\left(\overline{w^2} - \overline{v^2}\right) + \left(\frac{\partial^2}{\partial y^2} - \frac{\partial^2}{\partial z^2}\right)\overline{vw} + \nu\nabla^2\omega_x \qquad (6.7)$$

where ω_x is the streamwise vorticity defined by Equation 6.8:

$$\omega_x = \frac{\partial W}{\partial y} - \frac{\partial V}{\partial z} \tag{6.8}$$

$(x; y; z)$ are the streamwise, lateral and vertical directions respectively,$(U; V; W)$ are the corresponding temporal mean velocity components and $(u; v; w)$ are the related turbulent perturbations of velocity. The secondary currents influence the streamwise velocity U and their gradient affects the bed shear stress.

Some secondary currents are very noticeable across the measured sections, with areas of upflow and downflow. In order to characterise the magnitude of the secondary currents, the ratio $\frac{\sqrt{V^2+W^2}}{U}$ was calculated. On average, the values in the main channel are commonly $7\% - 12\%$, which is higher than typical values expected for uniform flow in straight compound channels (Nezu and Nakagawa, 1993). Local maxima of up to 25 %- 35 % were observed.

The secondary currents appear to be strong on the side slopes between the main channel and the floodplain. In order to investigate the distribution of secondary currents in the cross-sections, the streamwise vorticity ω_x was plotted. Figure 6.9 presents the results for the upstream section during the high flood event.
"Pockets" of positive and negative vorticity values are found in the channel. The lowest and highest values of vorticity can be found on the main channel side slopes, where relatively high secondary circulation was observed. For example, for the high flow event, the highest vorticity values were observed on the side slope with values normalised by the maximum vorticity greater than 0.85 while most values in the main channel are between -0.1 and 0.1. This phenomenon has been observed in the laboratory study carried out by Sun (2006).

6.3.4.4 Longitudinal section profile

Data for one longitudinal section profile for each event was collected. The boat was moving from downstream to upstream on the right bank. When the measurements took

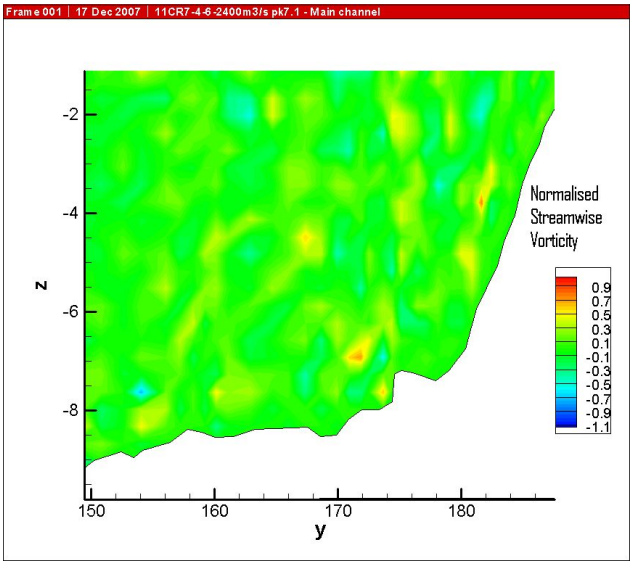

Figure 6.9: Example of streamwise vorticity on the right bank at pk 7.1 km on 11-04-2006

place, the water level for the longitudinal section profile collected at the high flood event (11/04/2006) was on average approximately 1.75 m higher than that observed at the lower flood event.

The same methodology as that used for processing the measurements made at cross-sections was adopted. The bed levels and velocity fields of both data sets were plotted on the same graph and a common projection was defined by applying a least squares regression. The profiles were then projected on the projection axis previously defined.

The bed level was determined using the Bottom Track option of the ADCP. The bed level is the average of 4 measurements from the 4 beams used for that mode. Both longitudinal profiles overlap the cross-sections at which measurements were made. The longitudinal section profile for the low flow event (04-04-06) is about 1000 m long. The longitudinal section profile measured during the high flood event (11-04-2006) extends both upstream and downstream of the studied cross-sections and is approximately 1600 m long.

The projected bed profiles of both longitudinal sections were superimposed. The results of the bathymetry superimposition are presented in Figure 6.10.

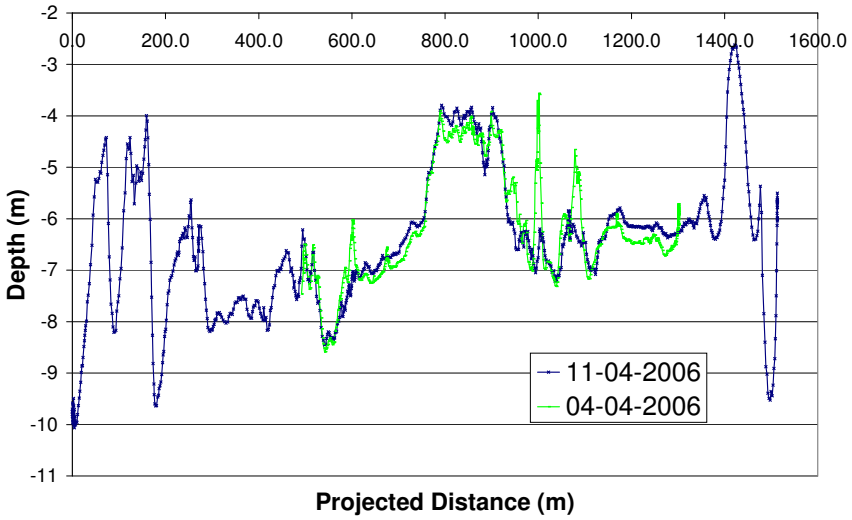

Figure 6.10: Superimposition of the bathymetries measured for the low and high flow events

The inspection of the bathymetry superposition reveals some significant discrepancies, although the overall shape of the longitudinal section remains similar for both profiles.

The longitudinal profiles exhibit large variations in the depth of the bed, which is in contradiction with the fairly homogeneous topography of the right bank observed during the field inspection. These discrepancies are attributed to the boat lateral displacements while the operators attempted to follow the right bank. The recorded boat tracks suggest that the boat moved along the right bank with shifts of $\pm 5m$ each side. Such lateral shifts are enough to produce significant shifts in the bed level in areas of steep sideslopes.

The streamwise velocity was averaged for each water depth H_k cells over the entire longitudinal profile length to non-dimensionalise the data. That is, the mean streamwise velocity U for a given depth H_k was defined as:

$$U_{H_k} = \frac{1}{L} \sum_{i=1}^{n} u_{i,k} \tag{6.9}$$

Results of plots of the longitudinal section for the streamwise and transversal velocities U and V normalized by the mean value of U defined by Equation 6.9 presented in Figures 6.11 and 6.12 for depths of 1 m and 1.98 m, for a length of 200 m. This stretch was chosen because the bed level in that area remains more stable, without exhibiting some of the large discrepancies noted in Figure 6.10.

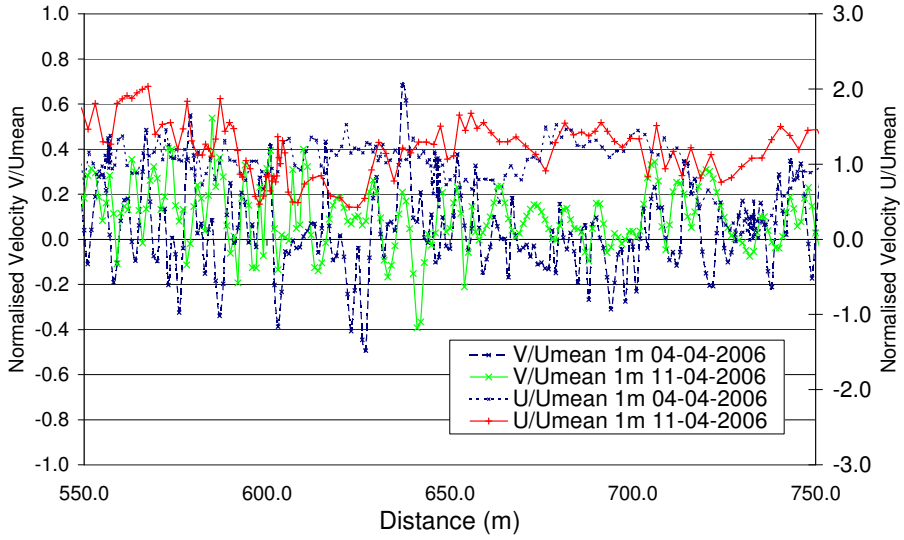

Figure 6.11: Variation of the transversal velocity along the right bank at both events results at a depth of 1 m below surface

With a certain regularity, the transversal velocity clearly oscillates between positive and negative values and the positive and negative peaks are of close amplitudes. The period of the oscillations varies for distances from just over 2 m to 8 m, which correspond to the peaks in the power spectrum calculated with a Fast Fourier Transform Analysis.

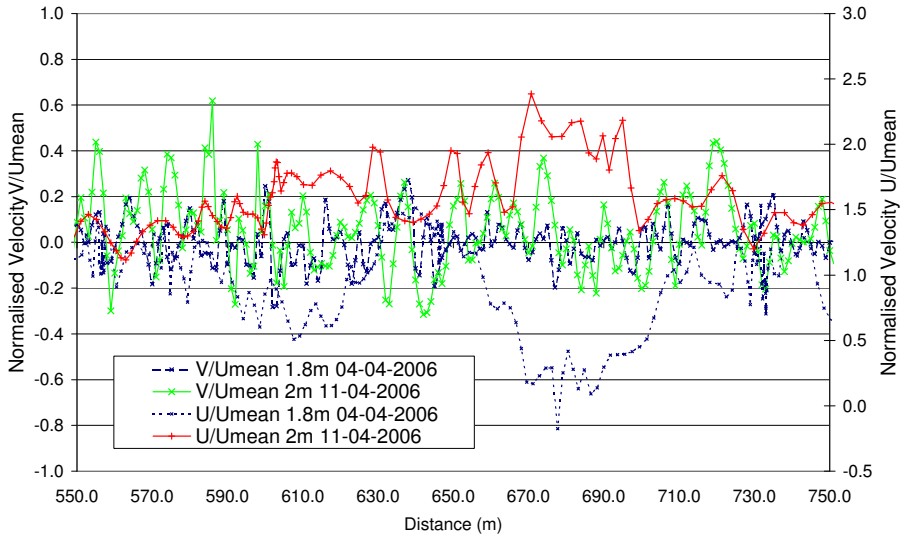

Figure 6.12: Variation of the transversal velocity along the right bank at both events results at a depth of 2m below surface

An example of such analysis is presented in Figure 6.13 for a depth of 1.33 m measured at the high flood event. Interestingly, these variations of transversal velocity correlates the visual observations and the LS-PIV results obtained in laboratory experiments, for the Loughborough flow cases and for the shallow case in the LMFA flume.

The strength of these secondary currents increased noticeably during the high flood event. On average, for measurements at a depth of 1.8 m and 2.03 m for the low and high flood event respectively, the average strength of secondary currents was 6.7 % and 13.5 % respectively with standard deviations of 5.8 % and 9.0 %. This represents a doubling in the intensity of secondary currents at the high flood event near the interface, which is very significant. Such a strong change in intensity has important consequences for the river bank stability and erosion.

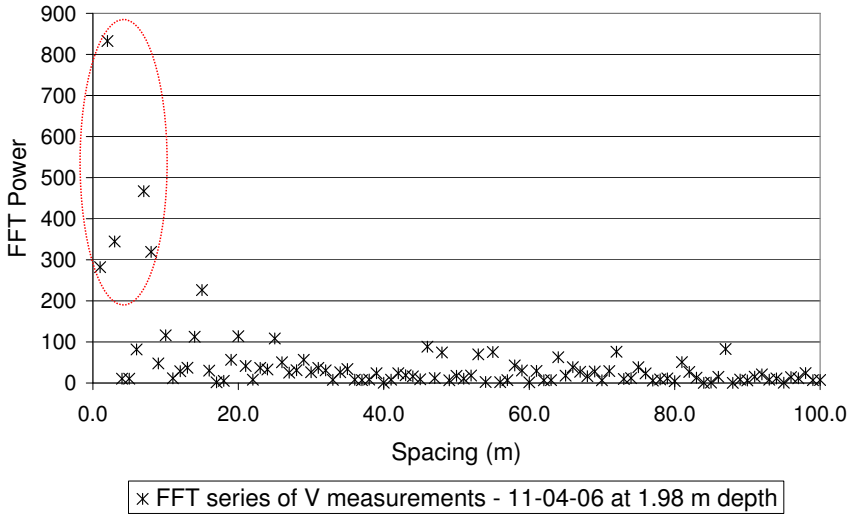

Figure 6.13: Example of FFT of the Transverse velocity for 11-04-06 at 1.98 m depth

6.4 Acoustic Doppler Profiler (ADP) Postprocessing Validation and Analysis of Flow Structures at Derby Saint Mary's

6.4.1 Introduction

Acoustic Doppler Profiler (ADP) data were provided for one flood event in Derbyshire (England) by SonTek, with the permission of the Environment Agency (EA). This set of data was used to validate the postprocessing methodology applied to the river Rhône data set. During the summer 2007 flood, the EA commissioned SonTek to carry out high flow gaugings in River Derwent at Derby St Mary's. SonTek Stationary mode was used to collect the results.

6.4.1.1 Differences between ADCP and ADP

The main manufacturer of ADCPs remains RD Instruments while ADPs were later introduced on the market by SonTek. Both series of instruments exhibit very similar characteristics. There are, however, some unique differences.

The most noticeable difference is the use of three transducers instead of four. Only three beams are necessary to measure three dimensional velocity profiles and the abandon of the fourth transducer reduces the costs of the instruments. However, three transducers do not provide a safety factor in the advent of a transducer failure. The loss of the fourth beam also implies that the ability to compute velocity quality control on the measurements is no longer available Appell (1996).

The major effect that the choice of three or four beams has on velocity data is in the conversion of beam velocity data (the projection of the 3D velocity onto the beam axis) to 3D velocities. Two factors affect the conversion of beam velocity to 3D velocity the number of beams and the beam-mounting angle. The SonTek system uses three beams mounted 25° off vertical. The ADCP system used for the Rhône data has four beams mounted 20° off vertical. The 25° angle allows profiling of approximately 91% of the water column as opposed to 94% for the 20° angle, which means it has a slightly reduced accuracy per ping.

6.4.1.2 Description of the site

The measurements were carried out on 26 June 2007 from a bridge which has no piers in the channel, near the gauging station of Saint Mary's on the river Derwent. The river channel in this location is approximately 50 m wide and 3.5 m deep. The aspect ratio of the channel $\left(\frac{B_{mc}}{H_{fp}}\right)$ is approximately 15.8 and the channel can therefore be considered as wide. The left and right floodplains are narrow with setback defences and are approximately 7 m and 50 m wide respectively. They are vegetated with mature trees, with one line on the left floodplain and patches of trees on the right floodplain. No detailed vegetation survey was undertaken at this site. However, a distance to diameter ratio $\frac{L}{D}$ of 12 and a mean tree diameter of 0.5 m was regarded as a representative approximation of the tree density in the area. Figure 6.14 presents a view of the upstream area.

Figure 6.14: River Derwent at Derby Saint Mary's

6.4.1.3 Characteristics of the measurements

In order to gauge the flows, a 3.0 MHz ADP (Acoustic Doppler Profiler) was deployed from the downstream side of road bridges using a single rope and the SonTek Stationary-Measurement system was used. Photograph of the ADP used is shown in Figure 6.15. Measurements were only performed in the main channel as the floodplain flow was too shallow. The relative depth ratio at the time of measurements was estimated to be 0.13.

Six profiles were collected twice at near cross-sections, at approximately one hour interval. The operational characteristics of the ADP used for the measurements are provided in Table 6.5:

Table 6.5: Main characteristics of the operational procedures used for the ADP

OperationalCharacteristics	*StreamPro*
Data collection time for stationary mode (s)	6
Sampling frequency (Hz)	0.55
Blanking distance (cm)	30
Depth of cell length (cm)	35

Figure 6.15: ADP used on the River Derwent at Derby Saint Mary's

The Stationary-Measurement system uses an alternative approach to the standard moving boat method of measuring water currents and discharge. Both methods use an ADP to measure water currents. However when using the Stationary-Measurement software, the ADP operates from a fixed mounted position, stationary vessel or platform. Measurements are made at stationary positions, usually along a tagline, to obtain a more precise representation of the mean velocity profile.

As previously mentioned in paragraph 6.2.2, in order to measure flow accurately using a Doppler system that uses the moving boat method, a reference is needed to relate the water velocities to a known geographical feature. This reference is normally taken as the bed of the river, which in most cases is rightly assumed to be fixed. However in some circumstances, especially during floods, the system will detect a moving bed. If such a condition arises the total discharge that is calculated will be less than the true discharge.

In the case of the stationary mode, the bottom tracking element of the navigation is removed due to the fact that the measurement platform is stationary and that the horizontal position is input by the user. The moving bed element is therefore completely removed from the equation and the actual velocity profiles are directly computed. The

stationary mode software package originally rose from the need to make true discharge measurements in places where moving bed conditions exist.

At Derby St Mary's the bed was detected as constantly moving. The stationary mode and the standard moving boat method computed flows of $90m^3/s$ and $265m^3/s$ respectively (Martin, 2007), the standard moving boat method thus significantly overestimating the actual flow rate.

6.4.2 Data analysis

The same methodology as that described in 6.3.3.1 was used to postprocess the results obtained from the ADP measurements. However, the use of the stationary mode simplifies the obtention of the mean velocity components. Each measurement is carried out at the same fixed location for each of the collected profiles. Therefore, the velocity field is measured at the measurements grid. Figure 6.16 presents the measurement grid used to measure the velocity.

No interpolation of the results on an interpolation grid before combining the profiles is necessary. In addition, the ADP was aligned so that it faced the current by referencing the Azimuth (or compass heading) of the ADP from the left bank to the right bank. The velocity field was rotated accordingly and the mean velocity components were then obtained by directly averaging the three velocity components of the measured profiles.

6.4.3 Results

6.4.3.1 Flow characteristics of the flood event at Derby Saint-Mary's

Table 6.6 presents the characteristics of the flow measured in the main channel.

The Reynolds number is large and exceeds $25\ X\ 10^6$ so the flow is highly turbulent. The Froude number is approximately 0.285 and is comparable to the Froude numbers

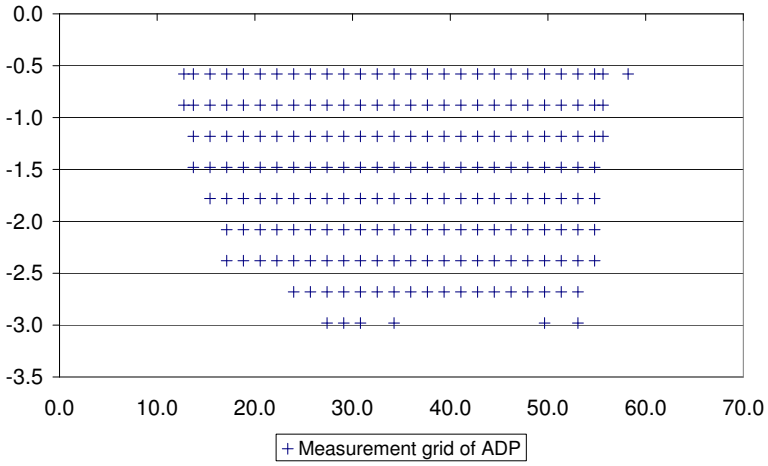

Figure 6.16: Depth averaged velocity at Derby Saint Mary's - 26-06-2007 at 13:46 and 14:43

Table 6.6: Flow characteristics at Derby Saint Mary's

Case	Mean velocity (m/s)	Maximum Water depth (m)	Reynolds number	Froude number
Derby Saint Mary's 26/06/07 at 13:46- Main channel	1.70	3.70	$25.160\ X\ 10^6$	0.282
Derby Saint Mary's 26/06/07 at 14:43	1.77	3.74	$26.479\ X\ 10^6$	0.292

observed in the laboratory of Loughborough University.

The kinematic wave number and the maximum response frequency are calculated using Equations 6.1 and 6.2. The results are presented in Table 6.7:

The frequencies given in Table 6.7 are well above the maximum sampling frequency of 2 Hz of the ADP used in this study. Therefore the collected data is not suited for the analysis of turbulence.

Table 6.7: Threshold frequencies at Derby Saint Mary's

Case	Maximum kinematic wave number $k_{max}(m^{-1})$	Threshold frequency f_{max} (Hz)
Derby Saint Mary's 26/06/07 at 13:46 - Main channel	27.02	7.31
Derby Saint Mary's 26/06/07 at 14:43 - Main channel	26.73	7.53

6.4.3.2 Estimation of shear velocity and Roughness

The bathymetry was measured for both series at the six profiles. The mean bathymetry was calculated by averaging the bathymetry of the six profiles. The results are given in Figure 6.17.

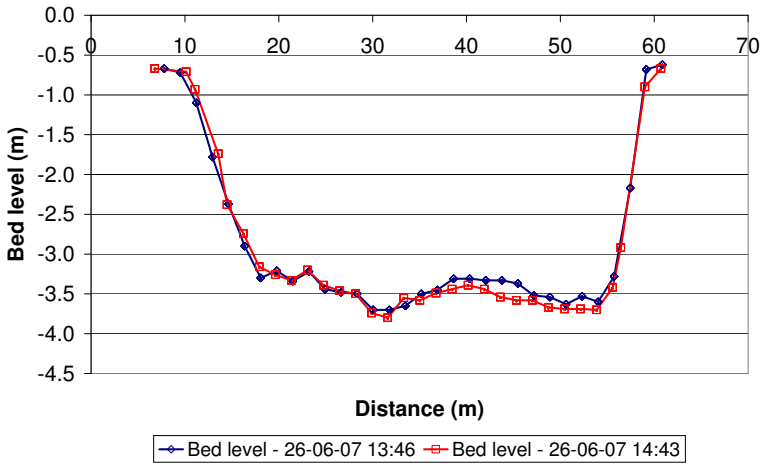

Figure 6.17: Bathymetry profiles derived at Derby Saint Mary's - 26-06-2007 at 13:46 and 14:43

The channel geometry approaches that of a symmetrical trapezoidal cross-section with sideslopes of approximately 1 in 3 slopes.

The depth-averaged velocity profiles are presented in Figure 6.18.

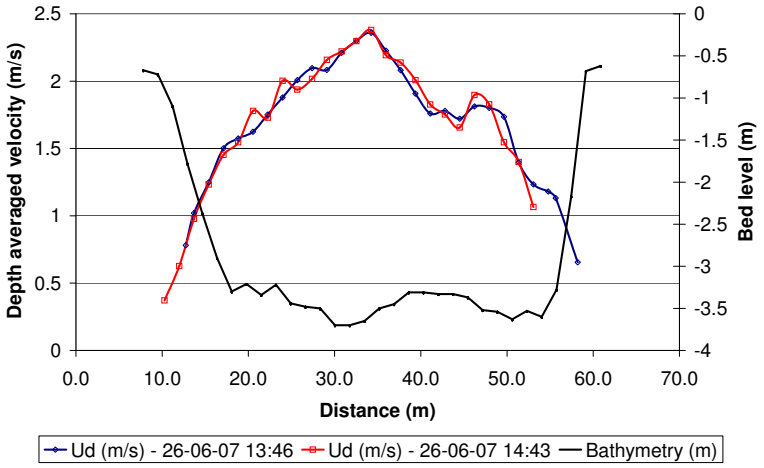

Figure 6.18: Depth averaged velocity at Derby Saint Mary's - 26-06-2007 at 13:46 and 14:43

The two depth-averaged velocity profiles are very similar and exhibit relative differences of less than 5%, thereby suggesting that the flow was in a steady state condition. The peak velocity occurs at the center of the main channel and is 2.36 m/s and 2.38 m/s for the measurements carried out at 13:46 and 14:43 respectively. The depth-velocity profile is not symmetrical as the profile has lower values near the right floodplain. This deficit in velocity could be attributed to the denser vegetation on the right bank.

The log-law was fitted to the velocity profiles obtained at both locations for the central part of the channel. The measurements exhibit much less noise than the data collected on the river Rhône. The better quality of the Derby Saint Mary's data set can be explained by the use of the stationary mode. The 6-second measuring time, the averaging of 6 profiles and the use of the same measurement grid ensure a greater consistency in the results. The results are presented in Table 6.8.

The water profile and the bed slope are not known at both location. However, the friction slope S_f can be calculated based on the results presented in Table 6.8. The

Table 6.8: Estimation of shear velocity and roughness at Derby St Mary's

	Derby St Mary's (13:42)	Derby St Mary's (14:38)
Average Z_0 (m)	0.0066	0.0067
Average bed shear stress T_B (N/m2)	13.71	14.23
Average goodness to fit R^2	0.91	0.91

roughness height k_s can be calculated from Equation 6.10, assuming that the vertical gradient of the mean streamwise velocity follows a logarithmic law:

$$\frac{U}{U_*} = \frac{1}{\kappa} \ln\left(\frac{z}{k_s}\right) + 8.5 \tag{6.10}$$

Hence the value of k_s can therefore be determined by combining Equations 6.10 and 6.5, as $k_s = Z_0 e^{8.5\kappa}$. One obtains a k_s value of 0.219 m. The corresponding Manning's n values can be calculated using Equation 6.11:

$$n = \frac{k_s^{\frac{1}{6}}}{8.25 * \sqrt{g}} \tag{6.11}$$

A Manning's n value of 0.030 is obtained. This Manning's n value corresponds to the normal value of a clean, straight full stage channel according to Chow (1959), thus giving some credits to the calculations. Then using Manning's Equation 6.12 to calculate the friction slope S_f one obtains a friction slope S_f equal to 1/2050.

$$U = \frac{H_{mc}^{\frac{2}{3}} S_0^{\frac{1}{2}}}{n} \tag{6.12}$$

The variation of the bed shear stress obtained from the log-law fitting are presented in the Figure 6.19. In Figure 6.19, the bed shear stress was calculated using Equation 6.6 and normalised by the average bed shear stress across the section.

The results vary between $0.7\tau_{Bmean}$ and $1.4\tau_{Bmean}$, which is of comparable amplitude to the variations observed with the Rhône River ADCP data.

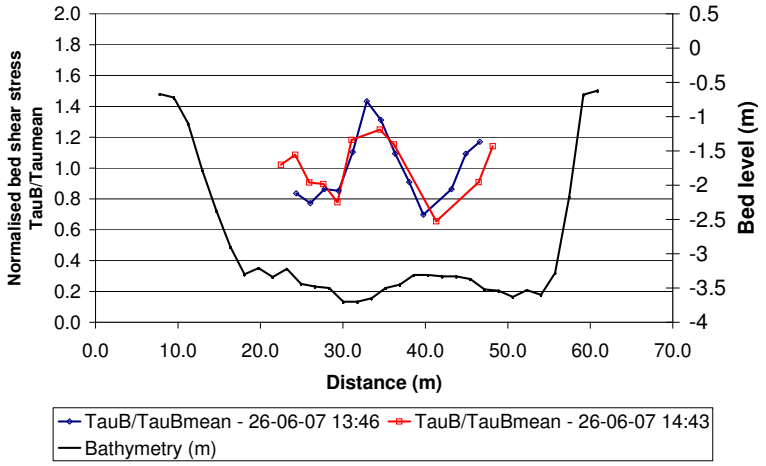

Figure 6.19: Boundary shear stress derived from log-law at Derby Saint Mary's - 26-06-2007 at 13:46 and 14:43

6.4.3.3 Secondary currents and vorticity

The normalized mean longitudinal velocity distribution and the vorticity distribution are presented with the secondary flow vectors (V,W) in Figure 6.20.

The strength of secondary currents $\frac{\sqrt{V^2+W^2}}{U}$ is 8 % on average with a standard deviation of 4 %. They are stronger than the typical values observed in laboratories. The link between secondary currents and boundary shear stress is not evident in these results, although the ascending secondary currents in the region of y=40m and y=31m match the decrease in boundary shear stress shown in Figure 6.19.

The extremes in vorticity values are observed near the sideslope area. On the left floodplain, the vorticity normalised by its maximum value has "pockets" with values lower than -0.60 and can exceed 0.80 on the right sideslope, while it remains between -0.30 and +0.35 in the centre region of the channel. This pattern is similar to that observed in the river Rhône. Secondary currents in the sidelsope areas of compound channel have been observed on numerous occasions in laboratories (Nezu and Nakagawa, 1993;

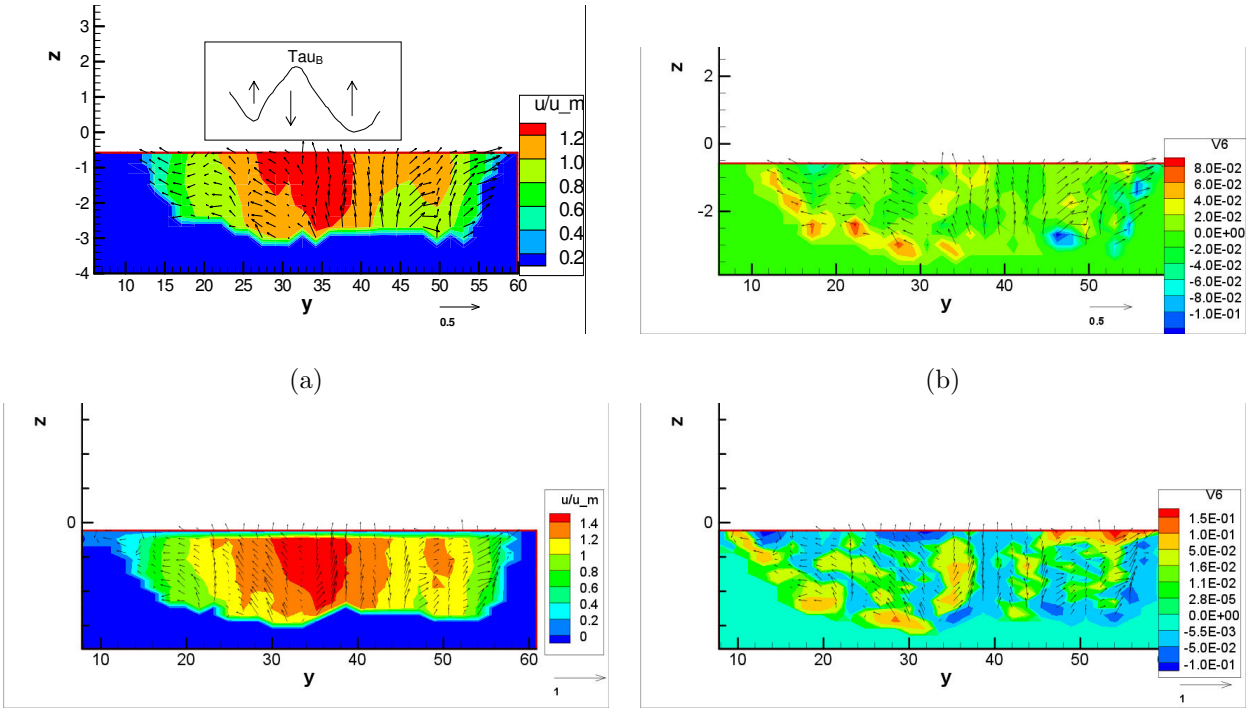

(a) (b)

(c) (d)

Figure 6.20: Isovels of streamwise velocity and vorticity with secondary currents vectors at Derby Saint Mary's on 26-06-2007 at 13:46 (a) and (b), and 13:43 (c) and (d) respectively.

Shiono and Knight, 1991; Sun, 2006). The vegetation has also been observed to intensify the secondary currents in the sideslope region (Kang and Choi, 2006b). Kang and Choi (2006a) noted that the strength of the secondary flow increases with the vegetation density on the floodplain. The stronger secondary currents near the sideslope are responsible for the higher values in vorticity.

6.5 Conclusion

ADCP measurements were carried out in the river Rhône in April 2006 for two over-banks flows and ADP measurements were also carried out in June 2007 in the river Derwent for one over-bank flow.

Transverse profiles were taken at four cross-sections in the area of Pierre-Bénite on the 4^{th} and the 11^{th} of April 2006. The data from the different profiles were combined to obtain the mean velocity components. The depth-averaged velocity was calculated and the bed shear stress was determined in the centre part of the main channel using the logarithmic law of the wall. The cross-section averaged bed shear stress values derived from the log-law are generally found to be in close agreement with the theoretical cross-section averaged values. The lateral variations of the bed shear stress can be significant, from 0.7 up to 1.3 times the mean bed shear stress.

Secondary currents were found to be of higher magnitudes when compared to typical values corresponding to uniform flows in straight compound channels as they vary between 7% and 12% with local maxima up to 25%-35%. Secondary flow was found to be dependent on the vorticity, hence future investigations on secondary flow circulation should investigate the link with vorticity further. Correlations of ascending or descending currents with bed shear stress gave mixed results as the areas of decreasing bed shear stress proved difficult to relate to upflows areas. The highest secondary current values and the highest vorticity values are located on the side slopes.

The methodology used to postprocess the data measured in the river Rhône was applied to the river Derwent at Derby Saint Mary's data. The postprocessing of the results was simplified due to the use of a fixed measurement grid for all profiles. Six profiles were combined for two river crossings carried out approximately at a one-hour interval. The depth averaged-velocity profiles derived from the two sets of data were identical within 5 %, thereby suggesting that the flow was in a steady state. The secondary currents were found to be stronger than that usually observed in straight compound channel in laboratories and their strength was 8 % on average. The boundary shear stress exhibits large variations, from 0.7 to 1.4 times the mean bed shear stress.

There are a number of limitations in this study. The limitations include the absence of a more accurate device to measure flow velocity, the limited number of transects avail-

able per cross-section and the unknown bed load condition at the time of measurement in the river Rhône. Nevertheless, the analysis provides an insight into flow patterns for overbank flow conditions in one of large rivers in France.

While the stationary mode developed by SonTek requires a structure to be able to move and stop the boat across the river at fixed locations, the quality of the data seems to benefit from such methodology. A comparison of typical vertical profiles of the mean longitudinal velocity collected for both the Rhône data set in France by the CNR and at Derby by SonTek is provided in figure 6.21. The profiles collected with the Stationary mode generally appear to be much smoother.

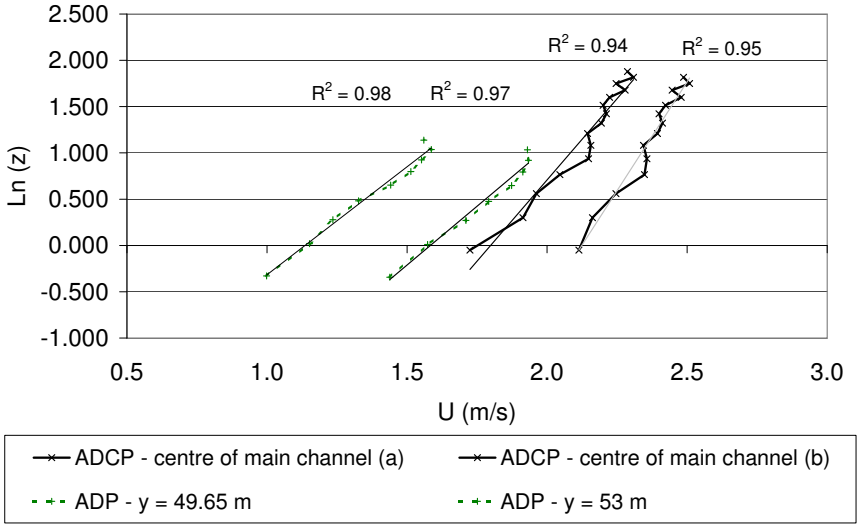

Figure 6.21: Sample of velocity profiles from the River Rhône and from the River Derwent datasets

There are three possible explanations to the previous observation:

First, six profiles were combined at Derby St Mary's instead of four on the river Rhône. As explained in 6.2.2, the greater the number of profiles available to be com-

bined, the lesser the dispersion on the data.

Secondly, the fact that the measurements are carried out at the exact same location with reference to a fixed structure also ensures that the velocity direction is accurate. For the Rhône data, the ADCP were used in Mode 12, that is in multiple ping mode. In Mode 1 a ping is transmitted and received, converted to a velocity profile in earth coordinates and recorded. However, the conversion to velocity in earth coordinates involves a substantial amount of overhead time. When the Mode 12 is used to enable multiple pinging, the assumption is made that the ADCP is quasi immobile during the averaging of several pings. The velocity is then converted to earth coordinates. By eliminating the overhead consumed on each ping, the ADCP can ping much faster and average several measurements in the same time as a Mode 1 ping - thereby reducing the standard deviation of the measurement. However, this also implies that the direction of the velocity vector can be affected to some degrees during the measurements, even though much care has been taken to keep the heading of the ADCP constant throughout the measurements.

Finally, the assumption of the fixed bed in the Rhône data during the flood event can also be questioned to some degree. However, the discharge calculated from the velocity measurements matched the discharge on the existing rating curve for the corresponding water levels.

CHAPTER 7

Numerical Modeling of One Line of Emergent Vegetation on the Edge of Floodplain in Straight Compound Channels

7.1 Introduction

The analysis of the experimental and field data collected during this research was presented in Chapters 4, 5 and 6. This Chapter deals with the numerical modelling of the investigated flows and sums up the main characteristics of flow patterns.
The main two objectives of this Chapter are:

- to assess the ability of the Shiono and Knight Method and Telemac-2D to model compound channel flows with vegetated floodplain. In this research, the SKM was modified to incorporate the impact of drag force while the modelling capabilities of Telemac-2D were investigated. The results of the modified SKM and Telemac-2D modelling are presented in Sections 7.2 and 7.3 respectively.

- to summarise the phenomenology of the studied flows. Defining flow patterns are presented based on the experimental data and the numerical modelling. Three modes, depending on the level of interaction between the main channel and the floodplain, can be distinguished. The results of this synthesis are presented in Section 7.4.

In this Chapter, the depth-averaged velocity U_d is written as U in order to simplify the presentation of equations.

7.2 SKM Modelling

In this section, the SKM is modified to model flows in straight compound channels with vegetation. First, the development of the modified SKM is outlined following theoretical considerations. The proposed SKM is then applied to the data collected in laboratory. Then, a numerical code incorporating the newly formulated SKM is presented. This code was used to model the field data collected with ADCP, in a river with irregular channel geometries. Finally, for discussion purposes, the laboratory flow cases studied in Loughborough were also modelled with a more standard SKM approach. The results obtained with the more standard SKM are considered and the overall modelling strategy behind the SKM is addressed.

7.2.1 Development of the SKM in Presence of Vegetation on the Floodplain

7.2.1.1 Theoretical considerations

As described in Section 2.4.6.2, a modified SKM version (written as Equation 7.1) was proposed by Rameshwaran and Shiono (2007) to account for the impact of vegetation. Vegetation was modelled as a momentum sink term in the Navier Stokes Equation.

$$\underbrace{\frac{\partial H\left(\rho UV\right)_d}{\partial y}}_{\text{I}} = \underbrace{\rho g H So}_{\text{II}} + \underbrace{\frac{\partial H\overline{\tau}_{yx}}{\partial y}}_{\text{III}} + \underbrace{\tau_b\left(1+\frac{1}{s^2}\right)^{\frac{1}{2}}}_{\text{IV}} - \underbrace{\sum_i \frac{1}{2}\rho\left(C_D S_F A_P\right)_i U^2}_{\text{V}} \qquad (7.1)$$

where Term I is the advection term $\Gamma = \frac{\partial H(\rho UV)_d}{\partial y}$, Term II is the gravity term, Term III is the transverse shear stress term, Term IV is the boundary shear stress term and Term V is the drag force term. This Equation was developed into Equation 7.2.

$$\rho g H So + \rho \frac{\partial}{\partial y}\left(\rho H \overline{\epsilon_t} \frac{\partial U}{\partial y}\right) + \rho \frac{f}{8} U^2 \left(1 + \frac{1}{s^2}\right)^{\frac{1}{2}} - \frac{1}{2}\frac{\rho N C_D S_F D H U^2}{DL} = 0 \qquad (7.2)$$

The model required for inputs a calibrated friction factor (f), the secondary current term Gamma (Γ), the depth-averaged eddy viscosity ($\overline{\epsilon_t}$) and the drag coefficient and the shading factor that define the drag force component ($C_D X S_f$).

In a departure from previous studies involving the SKM, it is proposed that the advection term be set to zero. This decision will be discussed further in this chapter. In order to account for turbulence due to drag force in the flow field, the depth-averaged turbulent eddy viscosity $\overline{\epsilon_t}$ is split as a bottom turbulence eddy viscosity $\overline{\epsilon_{tb}}$ and a turbulence drag eddy viscosity $\overline{\epsilon_d}$ as shown in Equation 7.3.

$$\overline{\epsilon_t} = \overline{\epsilon_{tb}} + \overline{\epsilon_d} \qquad (7.3)$$

With some degree of success, an Elder formulation has been used as a depth-averaged eddy viscosity ϵ_t in many recent studies (Shiono *et al.*, 2009; Sun, 2008; Terrier *et al.*, 2008b). In these studies, the non-dimensional eddy viscosity λ was used as a constant parameter, the characteristic length L defining ϵ_t was taken as the local depth, and the characteristic velocity U as the shear velocity. In this proposed SKM, ϵ_{tb} is kept as an Elder formulation so that $\epsilon_{tb} = \lambda U_* H$. The friction velocity U_* remains related to a bed friction parameter taken as the Darcy-Weisbach friction factor f, with $U_* = \left(\frac{f}{8}\right)^{\frac{1}{2}} U$.

Turbulence activity generated by vegetation is related to the wakes spreading laterally over the water depth. Hence, it is suggested that ϵ_d be also modelled through an Elder model, in which the characteristic length L remains the local water depth H. The characteristic velocity U is defined as a so-called "apparent drag velocity" U_D. As proposed in Equation 7.4, U_D can be related to a friction drag parameter f_d similar to the bed friction f, and to the local velocity U.

$$U_D = \lambda \left(\frac{f_d}{8}\right)^{\frac{1}{2}} U \tag{7.4}$$

ϵ_d is defined in Equation 7.5.

$$\epsilon_d = HU_D = \lambda \left(\frac{f_d}{8}\right)^{\frac{1}{2}} HU \tag{7.5}$$

Hence, the final depth-averaged turbulent shear stress term in the proposed SKM can be expressed in Equation 7.6.

$$\overline{\tau_{xy}} = \rho(\epsilon_{tb} + \epsilon_d)\frac{\partial U}{\partial y} = \lambda\rho \left(\sqrt{\frac{f}{8}} + \sqrt{\frac{f_d}{8}}\right) HU\frac{\partial U}{\partial y} \tag{7.6}$$

7.2.1.2 Equation of the proposed SKM

To summarise, the proposed modified SKM is presented in Equation 7.7.

$$\rho g H So + \rho\frac{\partial}{\partial y}\left[\lambda\left(\sqrt{\frac{f}{8}} + \sqrt{\frac{f_d}{8}}\right) H^2 U\frac{\partial U}{\partial y}\right] + \rho\frac{f}{8}U^2\left(1 + \frac{1}{s^2}\right)^{\frac{1}{2}} - \frac{1}{2}\frac{\rho N C_D S_F D H U^2}{DL} = 0 \tag{7.7}$$

This equation is solved to obtain the lateral depth-averaged velocity and boundary shear stress distributions across the channel.

7.2.1.3 Analytical solution of the proposed SKM

Equation 7.7 is a second order linear ordinary differential equation and admits analytical solution.

In order to solve Equation 7.7, the analytical solutions for the depth-averaged velocity are required for each region in the channel. The channel has been subdivided into four sections, as shown in Figure 7.1; 1) The main channel, 2) The side slope, 3) The region of the rods, and 4) The floodplain. For simplicity, the region of the rods was assumed to involve no overlap onto the side slope. This assumption was correct for smooth rods but in reality, there was a slight overlap when brushes were used in Series

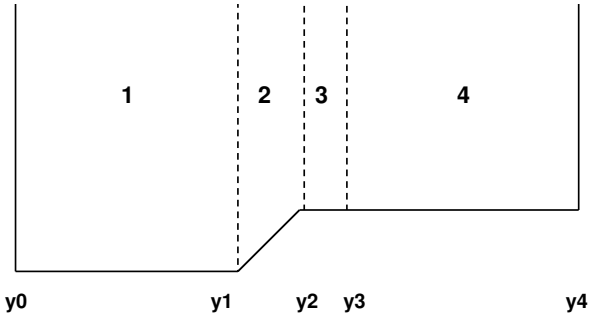

Figure 7.1: Subdivisions of the channel in the resolution of the modified SKM 2B.

The solution for each subdivisions are given by Equations 7.8 to 7.11. In this presentation of the analytical solution, the advection term Γ is kept as this is used later for discussions. This term is simply set to zero in the proposed SKM.

$$(U_1(y))^2 = A_1 e^{\gamma_1 y} + A_2 e^{-\gamma_1 y} + \frac{8gHS_0}{f}(1-\beta) \tag{7.8}$$

$$(U_2(y))^2 = A_3 \xi^{\alpha} + A_4 \xi^{-\alpha-1} + \omega\xi + \beta \tag{7.9}$$

$$(U_3(y))^2 = A_5 e^{\gamma_2 y} + A_6 e^{-\gamma_2 y} + \frac{8gHS_0}{\frac{f}{8} + \frac{1}{2}\frac{N}{L}C_D S_F H}(1-\beta) \tag{7.10}$$

$$(U_4(y))^2 = A_7 e^{\gamma_1 y} + A_8 e^{-\gamma_1 y} + \frac{8gHS_0}{f}(1-\beta) \tag{7.11}$$

where

$$\gamma_1 = \frac{1}{H}\left[\frac{\left(\frac{f}{8}\right)}{\frac{\lambda}{2}\left(\sqrt{\frac{f}{8}} + \sqrt{\frac{f_d}{8}}\right)}\right]^{\frac{1}{2}} \tag{7.12}$$

$$\gamma_2 = \frac{1}{H}\left[\frac{\left(\frac{f}{8} + \frac{1}{2}\frac{N}{L}HC_D\right)}{\frac{\lambda}{2}\left(\sqrt{\frac{f}{8}} + \sqrt{\frac{f_d}{8}}\right)}\right]^{\frac{1}{2}} \tag{7.13}$$

$$\beta = \frac{\Gamma}{\rho g H S_0} \tag{7.14}$$

$$\xi = H - \frac{y-b}{s} \tag{7.15}$$

$$\alpha = -\frac{1}{2} + \frac{1}{2}\left[1 + s(1+s^2)^{\frac{1}{2}}\frac{f}{8}\frac{1}{\lambda\left(\sqrt{\frac{f}{8}} + \sqrt{\frac{f_d}{8}}\right)}\right]^{\frac{1}{2}} \tag{7.16}$$

$$\omega = \frac{gS_0}{\frac{(1+s^2)^{\frac{1}{2}}}{s}\left(\frac{f}{8}\right) - \frac{\lambda}{s^2}\left(\sqrt{\frac{f}{8}} + \sqrt{\frac{f_d}{8}}\right)} \tag{7.17}$$

In order to solve the modified SKM, the coefficients A_i, ($i \in [1, 2, ..., 8]$), need to be determined. The following 8 boundary conditions are used for that purpose:

$$\begin{cases} U_{1(y=y0)} = U_{Left\ wall} \\ U_{1(y=y1)} = U_{2(y=y1)} \\ \dfrac{\partial U_1}{\partial y}_{(y=y1)} = \dfrac{\partial U_2}{\partial y}_{(y=y1)} \\ U_{2(y=y2)} = U_{3(y=y2)} \\ \dfrac{\partial U_2}{\partial y}_{(y=y2)} = \dfrac{\partial U_3}{\partial y}_{(y=y2)} \\ U_{3(y=y3)} = U_{4(y=y3)} \\ \dfrac{\partial U_3}{\partial y}_{(y=y3)} = \dfrac{\partial U_4}{\partial y}_{(y=y3)} \\ U_{y=y4} = U_{Right\ wall} \end{cases} \tag{7.18}$$

The first and the last boundary conditions refer to the definition of wall velocities. The six other boundary conditions express the continuity of velocity and its derivative between the subdivisions. It should be noted that other boundary conditions might be needed in cases where depth-averaged velocities present a discontinuity at the interface of the compound channel with no sloping main channel banks for example. In such cases, the continuity of apparent shear force should be used as a boundary condition. This continuity is expressed in Equation 7.19.

$$\tau_a H - \tau_w (H - h) = \tau_a h \tag{7.19}$$

Analytical expressions for the coefficients A_i $i \in 1, 8$ can be found so that a full analytical solution for the modified SKM can be written. However, its is more convenient to solve numerically the modified SKM. The system of equations defined by 7.8 to 7.18 can be written as Equation 7.20.

$$EA = B \tag{7.20}$$

where:

$$E = \begin{pmatrix} 1 & 1 & 0 & 0 & 0 & 0 & 0 & 0 \\ e_{2,1} & e_{2,2} & e_{2,3} & e_{2,4} & 0 & 0 & 0 & 0 \\ e_{3,1} & e_{3,2} & e_{3,3} & e_{3,4} & 0 & 0 & 0 & 0 \\ 0 & 0 & e_{4,3} & e_{4,4} & e_{4,5} & e_{4,6} & 0 & 0 \\ 0 & 0 & e_{5,3} & e_{5,4} & e_{5,5} & e_{5,6} & 0 & 0 \\ 0 & 0 & 0 & 0 & e_{6,5} & e_{6,6} & e_{6,7} & e_{6,8} \\ 0 & 1 & 0 & 0 & e_{7,5} & e_{7,6} & e_{7,7} & e_{7,8} \\ 0 & 0 & 0 & 0 & 0 & 0 & e_{8,7} & e_{8,8} \end{pmatrix}$$

$$A = \begin{pmatrix} A_1 \\ A_2 \\ A_3 \\ A_4 \\ A_5 \\ A_6 \\ A_7 \\ A_8 \end{pmatrix} \qquad B = \begin{pmatrix} b_{1,1} \\ b_{2,1} \\ b_{3,1} \\ b_{4,1} \\ b_{5,1} \\ b_{6,1} \\ b_{7,1} \\ b_{8,1} \end{pmatrix}$$

In order to obtain the coefficients A_i, the system of equations presented in Equation 7.20 is solved via a simple inverse matrix method, as shown in Equation 7.21.

$$A = E^{-1} B \tag{7.21}$$

The expression of the 26 coefficients of matrix E and of the 8 coefficients of matrix B are provided in Appendix C.

7.2.1.4 Input model parameters

In order to solve Equation 7.7 to obtain the depth-averaged velocity U, the model requires the drag coefficient C_D, the shading factor S_F, the local friction and drag friction factors f and f_d respectively and the dimensionless eddy viscosity as input parameters. Wall velocities also need to be determined. The methodology used to estimate these parameters is presented below.

Bulk drag coefficient

Nepf (1999) showed that the drag coefficient in a array of cylinders is suppressed due to wake interaction, as discussed in Section 2.5.4. In a similar way to Rameshwaran and Shiono (2007), the bulk drag coefficient ($C_D S_F$), taking account of the shading effects on the downstream rod, is determined from Nepf (1999) and is 0.715 for $\frac{L}{D} = 8.0$, 1.015 for $\frac{L}{D} = 16.0$ and is estimated to be 1.20 for $\frac{L}{D} = 32.0$.

Darcy-Weisbach friction factor

The Darcy-Weisbach friction factor f was estimated using the standard Colebrook-White equation (Equation 5.5), following the methodology exposed in Chapter 5. A detailed comparison was presented for the three LMFA flow cases in Section 5.2.2.2. On average, the calculated friction factors differed by 6.4%, 2.6% and 1.4% for Dr=0.21, Dr=0.43 and Dr=0.44 respectively.

For the Loughborough flow cases, the friction factors calculated using the same standard Colebrook-White equation compared favorably with the experimental friction factors in the main channel. However, a better represent of the friction factor was obtained on the floodplain through the calibrated Colebrook-White equation presented in Equation 7.22. In Equation 7.22, a coefficient of 7.75 was used in the second denominator of the *log* term, instead of 12.3 normally used in the standard Colebrook-White equation. The results between the calculated and the experimental averaged friction factors in the main channel and in the floodplain are summarised in Figure 7.2 for the Loughborough

and LFMA flumes.

$$f = \frac{1}{\left[-2log\left(\frac{3.02\nu}{\sqrt{128gH^3So}} + \frac{k_s}{7.75H}\right)\right]^2} \tag{7.22}$$

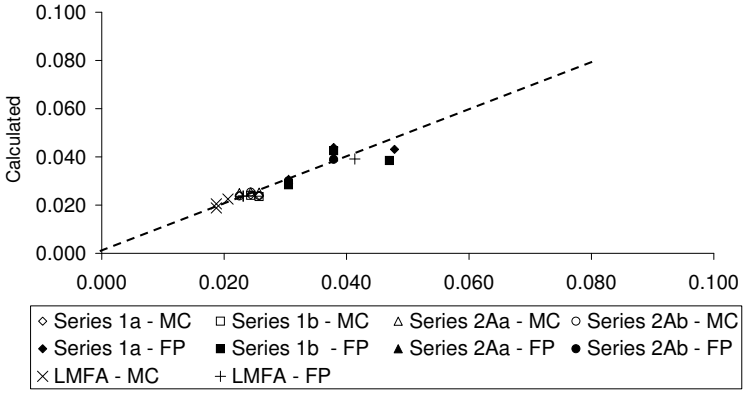

Figure 7.2: Comparison between calculated friction factor and friction factors derived from data

Wall velocities

Wall velocities can be imposed on the wall boundary as these give a more accurate velocity near the wall boundaries (Sun, 2008). The mean wall velocity can be determined from the measured wall shear stress $\overline{\tau_{wall}}$ using the logarithmic-overlap layer equation (Equation 7.23). In order to determine the mean wall velocity, the y coordinate y^+ normalised by the viscous length $\frac{\nu}{U_{*,wall}}$ was set to 30 (White, 1999).

$$U_{wall} = \frac{1}{\kappa}\left(ln(30) + 5.5\right)U_{*,wall} \tag{7.23}$$

where $\frac{1}{\kappa} = \frac{1}{0.41}$ and $U_{*,wall}$ is the mean wall shear velocity, defined as $U_{*,wall} = \frac{\sqrt{\overline{\tau_{wall}}}}{\rho}$.

If τ_{wall} is not known, an approximation is required to set up wall velocities. As a rule of thumb, it was found that τ_{wall} could be approximated by $0.7\tau_B$ to $0.8\tau_B$ for the studied

cases.

Turbulent eddy viscosity

In the proposed SKM, the turbulent eddy viscosity ϵ_t is made of the bottom turbulence eddy viscosity ϵ_t and a turbulence drag eddy viscosity ϵ_d. Both require the dimensionless eddy viscosity λ to be defined. In this study, λ is kept constant, equal to the standard value $\frac{\kappa}{6} = 0.0683$. The friction drag coefficient f_d can be adjusted across the section as a calibration parameter. It is, however, possible to determinate f_d from its theoretical definition. In the proposed SKM, the transverse shear stress is split between the contributions of bottom turbulence and drag turbulence, as presented in Equation 7.24.

$$\frac{\partial H\tau_{xy}}{\partial y} = \rho\frac{\partial}{\partial y}\left[H^2\lambda\left(\underbrace{\left(\frac{f}{8}\right)^{\frac{1}{2}}}_{\text{A}} + \underbrace{\left(\frac{f_d}{8}\right)^{\frac{1}{2}}}_{\text{B}}\right)U\frac{\partial U}{\partial y}\right] \tag{7.24}$$

where A is the contribution to apparent shear force τ_{ab} due to bottom generated turbulence and B is the contribution to apparent shear force τ_{ad} due to drag force F_D per unit area. The friction drag coefficient can be found by scaling the momentum equation by stating that the transverse shear stress term balances the resistance due to the array of rods

$$\left(\frac{\partial H\tau_{xy}}{\partial y}\right)_{y=y_{int}} \simeq -\frac{F_D}{2} \tag{7.25}$$

Assuming that $H\tau_{xy}$ has a linear variation between y_{int} up to $y = y_{u_{max}}$, where the maximum velocity occurs and $\tau_{xy} = 0$, one obtains Equation 7.26.

$$\frac{-\rho\epsilon_d H\frac{\partial U}{\partial y}}{(y_{int} - y_{u_{max}})} \simeq -\frac{F_D}{2} \tag{7.26}$$

Since $\epsilon_d = \lambda\sqrt{\frac{f_d}{8}}HU$, the friction drag f_d can be determined so that:

$$f_d \simeq 2\left[(y_{int} - y_{u_{max}})\,\frac{F_D}{\lambda\rho H^2 U\frac{\partial U}{\partial y}}\right]^2 \tag{7.27}$$

It should be noted that in the case of a rectangular main channel, the wall shear stress τ_{wall} needs to be taken into account in the calculation of the transverse shear stress at the rod.

A word on porosity

As shown in Section 4.4, the calculated porosity values remain higher than 0.998. For simplicity, it is therefore decided that porosity will not be explicitly included in the modelling.

7.2.1.5 Sensitivity of the model to the friction drag f_d

A sensitivity analysis carried out on f_d is presented in Figure 7.3, in which f_d is set to 0, 0.15 and 10.0 for a relative water depth of 0.25 in the Loughborough flume. For this relative depth, the Darcy-Weisbach friction factors f derived using the Colebrook-White Equation are 0.026 and 0.048 in the main channel and floodplain respectively.

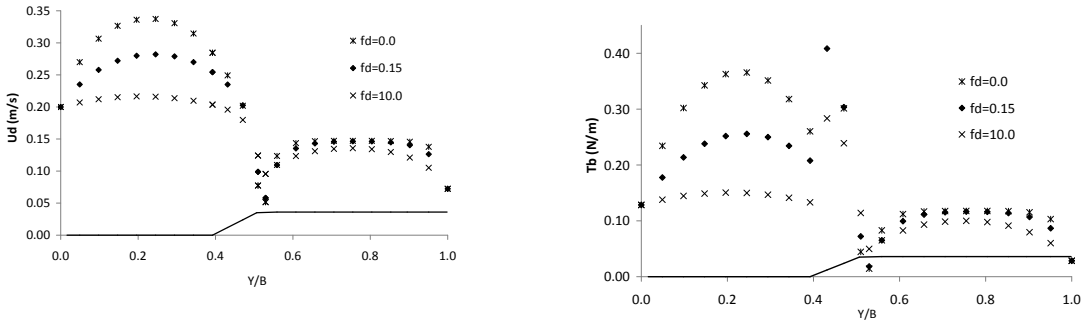

(a) (b)

Figure 7.3: Illustration of the sensitivity of f_d for a relative water depth of 0.25 in Loughborough flume for (a) U_d (b) τ_B

Decreasing f_d from 0.15 to 0 decreased the main channel flow by 28.7% and the floodplain flow by 7.8% while increasing f_d from 0.15 to 10.0 increased the main channel flow by 9.7% and the floodplain flow by 5.7%.

The same sensitivity test was carried out for the higher relative depth of 0.51, once more by varying f_d from 0 to 0.15 and 10.0. This time, decreasing f_d from 0.15 to 0 decreased the main channel flow by 27.7% and the floodplain flow by 20.5% while increasing f_d from 0.15 to 10.0 increased the main channel flow by 20.4% and the floodplain flow by 23.9%. At low relative depth, the flow rate in the main channel therefore appears more sensitive to f_d than in the floodplain.

7.2.2 Application of the modified Shiono and Knight Method (SKM) to Laboratory Experimental Data set

7.2.2.1 Calibrated Friction Drag factors

The values of f_d used to calibrate the model for the Loughborough and LMFA flow cases are presented in Table 7.4. A single value of f_d has been applied across the section as this was seen to provide satisfactory results.

Table 7.1: Values of f_d used in the SKM modelling of the Loughborough and LMFA flow cases

Relative depth	Series 1a	Series 1b	Series 2Aa	Series 2Ab	Series 2Ba	Series 2Bb	Relative depth	LMFA
0.25	1.469	0.653	0.367	0.104	2.000	2.650	0.22	0.104
0.35	0.653	0.235	0.180	0.059	1.280	2.500	0.43	0.069
0.51	0.163	0.041	0.080	0.015	0.367	1.672	0.44	0.115

Figure 7.4 illustrates the variations of f_d in function of relative depths in the Loughborough flow cases. For smooth rods, f_d increases with diameter and rod density and decreases with relative depth. It can be seen from Table 7.4 that f_d follows the same trends for the LMFA flow cases, as f_d increases when the relative water depth and the spacing ratio decrease.

The values of f_d for Series 2B, when bristles are added to the rods, are higher than for the corresponding smooth rod cases. This increase in drag friction corresponds to an

increase in flow resistance due to the additional drag generated by foliage. However, while f_d decreases with relative depth, f_d is actually found to increase when density decreases, which correlates the decrease in flow rate observed when the density of brushes is also decreased.

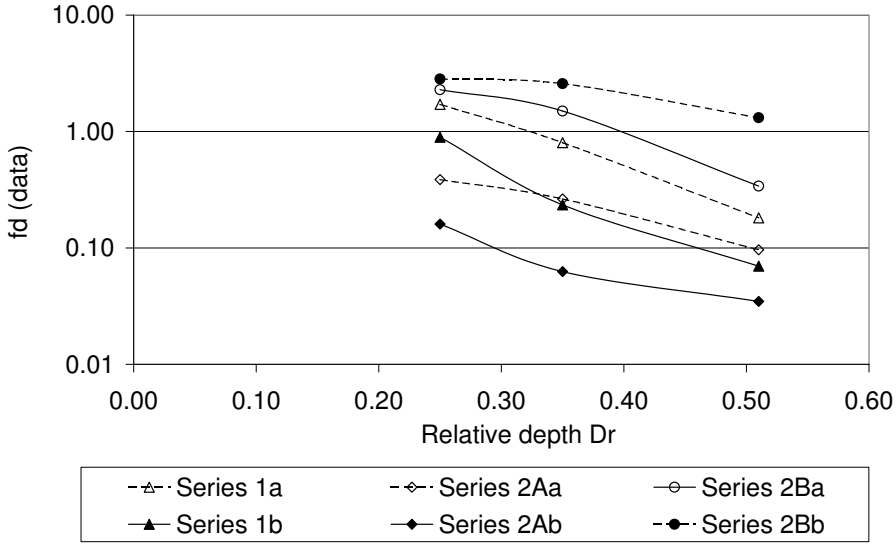

Figure 7.4: Variation of experimental values of f_d in function of relative depth

As mentioned, in Section 7.2.1.4, a comparison can be made between the calibrated values of f_d used in the SKM modelling, presented in Table 7.4, and the values of f_d derived from the experimental data through Equation 7.27. The results of this comparison are presented in Figure 7.5 for the 18 flow cases of Series 1, 2A and 2B, the 6 flow cases presented in Sun and Shiono (2009) and the 3 flow cases obtained in LMFA. Experimental values of f_d were derived from the main channel experimental data.

The skew towards slightly larger experimental values of f_d mainly comes from Series 2B, which suggests that brushes would perhaps require a specific treatment to optimize the results.

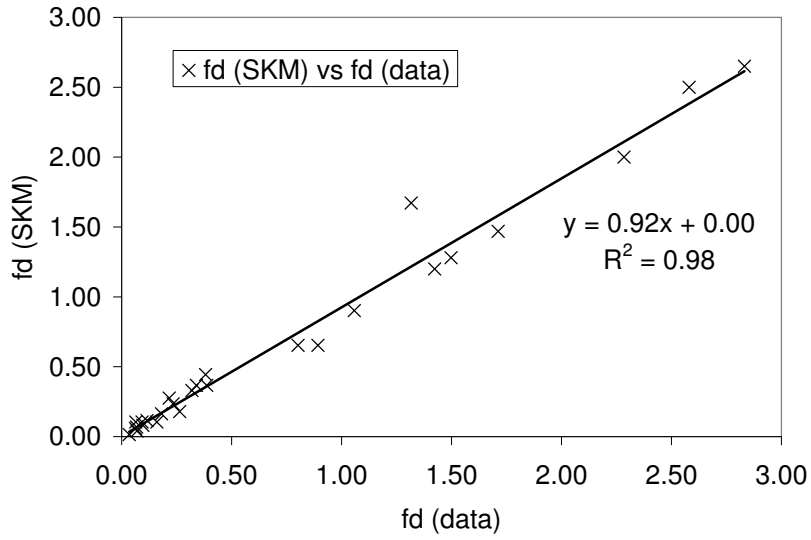

Figure 7.5: Values of f_d used in the SKM modelling against experimental f_d values normalised by the average modelled friction factor

7.2.2.2 Results of lateral depth-averaged velocity and boundary shear stress distributions

The profiles of the modelled and measured depth-averaged velocity and bed shear stress across a section are presented. Overall, the results show that modelled depth-averaged velocity and bed shear stress agree reasonably well with the measured data. Depth-average velocities are better predicted compared to boundary shear stress. Predictions of boundary shear stress could be optimized by refining the modelling of the Darcy-Weisbach friction factors for each rod configurations.

Loughborough flow cases

The lateral distributions of depth-averaged velocity and boundary shear stress are presented for smooth rods in Figures 7.6, 7.7 and 7.8, for relative depths of 0.25, 0.35 and 0.51 respectively.

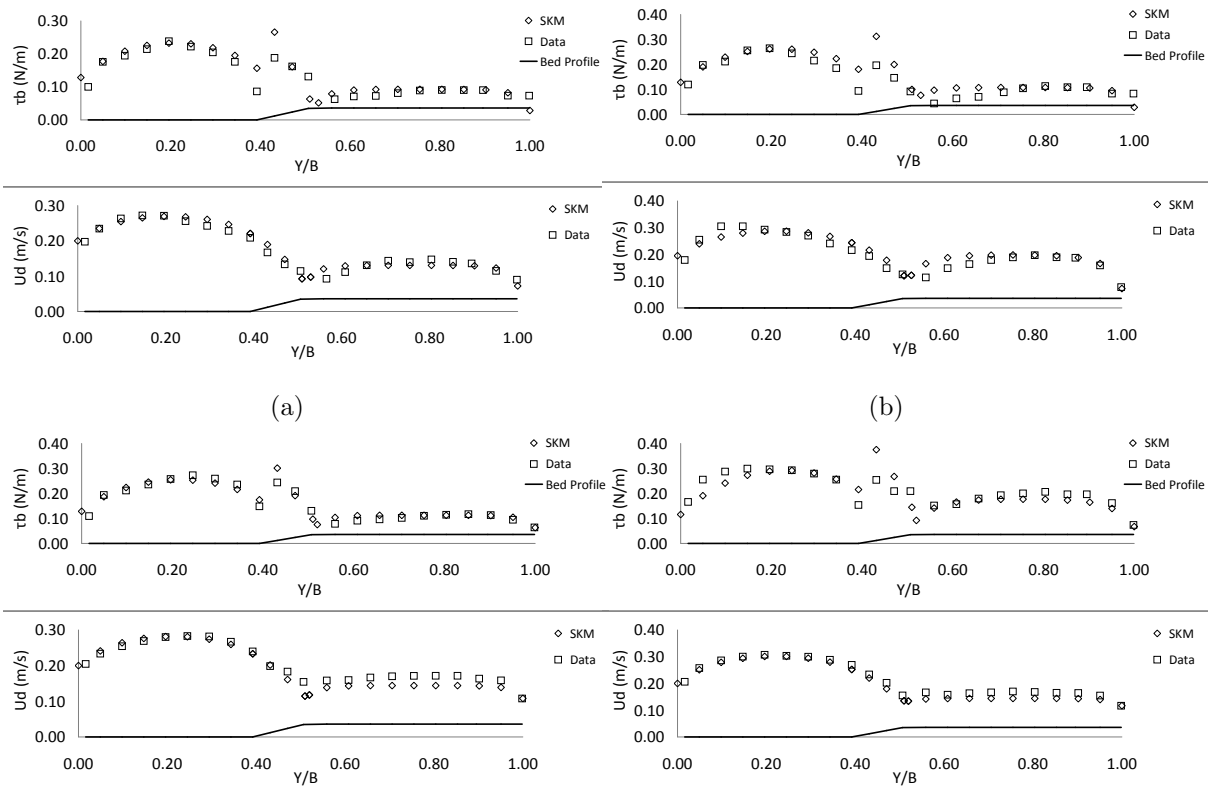

Figure 7.6: SKM results for τ_B (top) and U_d (bottom) for (a) Series 1a (b) Series 1b (c) Series 2Aa and (c) Series 2Ab

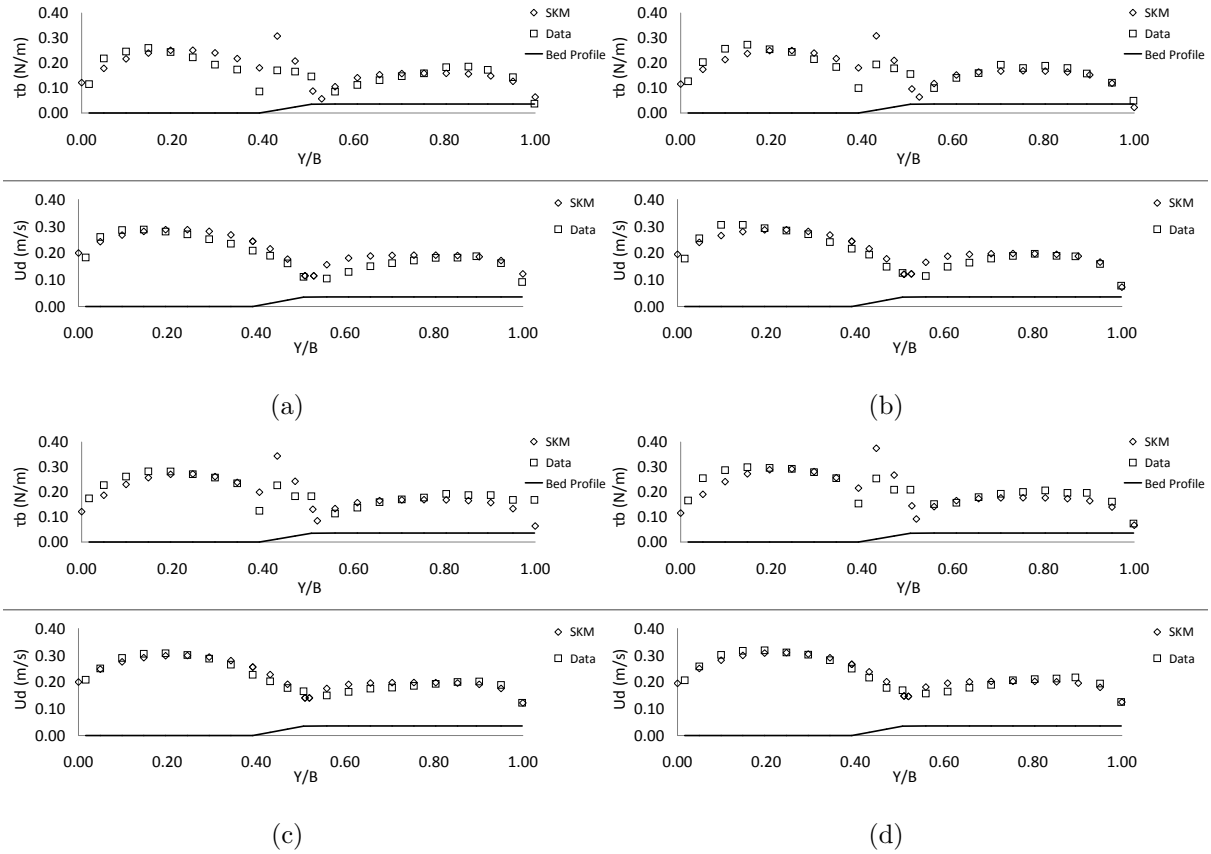

(a) (b)

(c) (d)

Figure 7.7: SKM results for τ_B (top) and U_d (bottom) for (a) Series 1a (b) Series 1b (c) Series 2Aa and (c) Series 2Ab

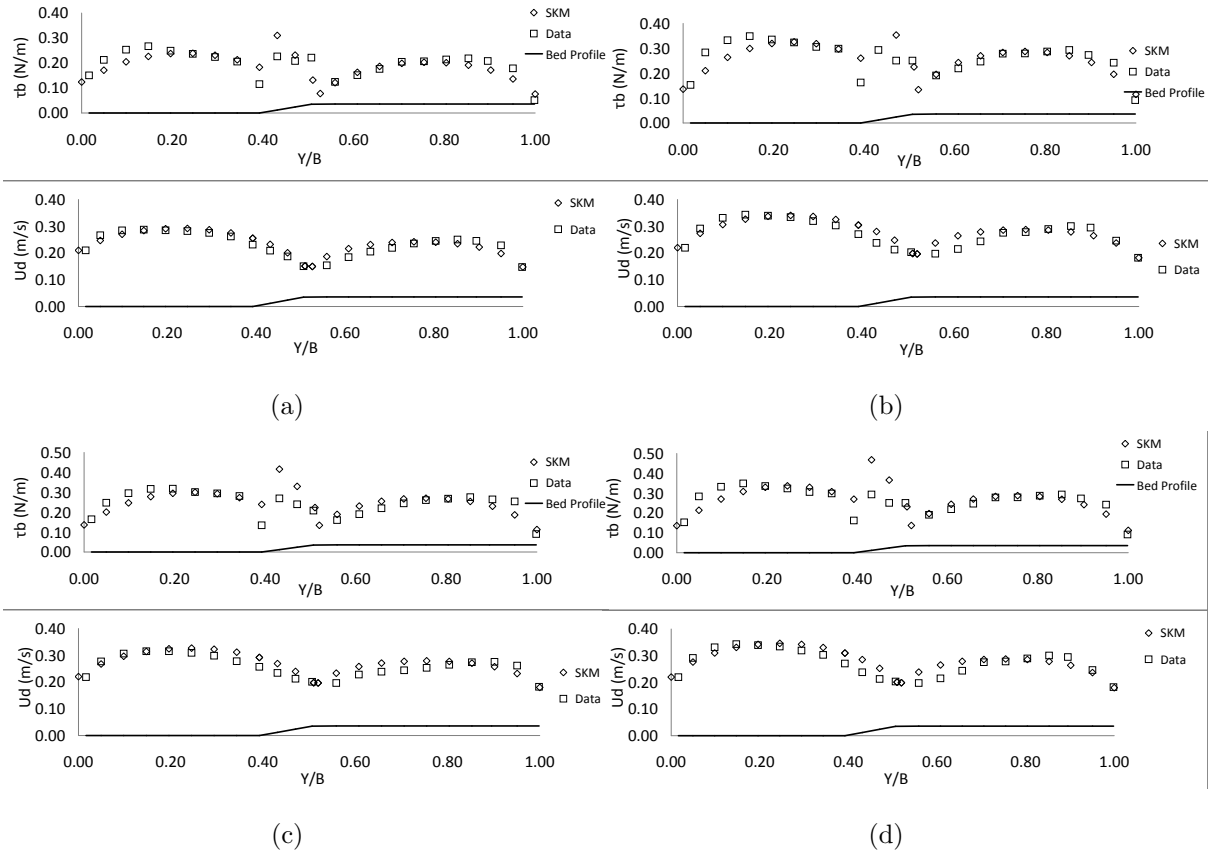

Figure 7.8: SKM results for τ_B (top) and U_d (bottom) for (a) Series 1a (b) Series 1b (c) Series 2Aa and (c) Series 2Ab

LMFA flow cases

The results of the modified SKM applied to the LMFA experiments are presented in Figure 7.9.

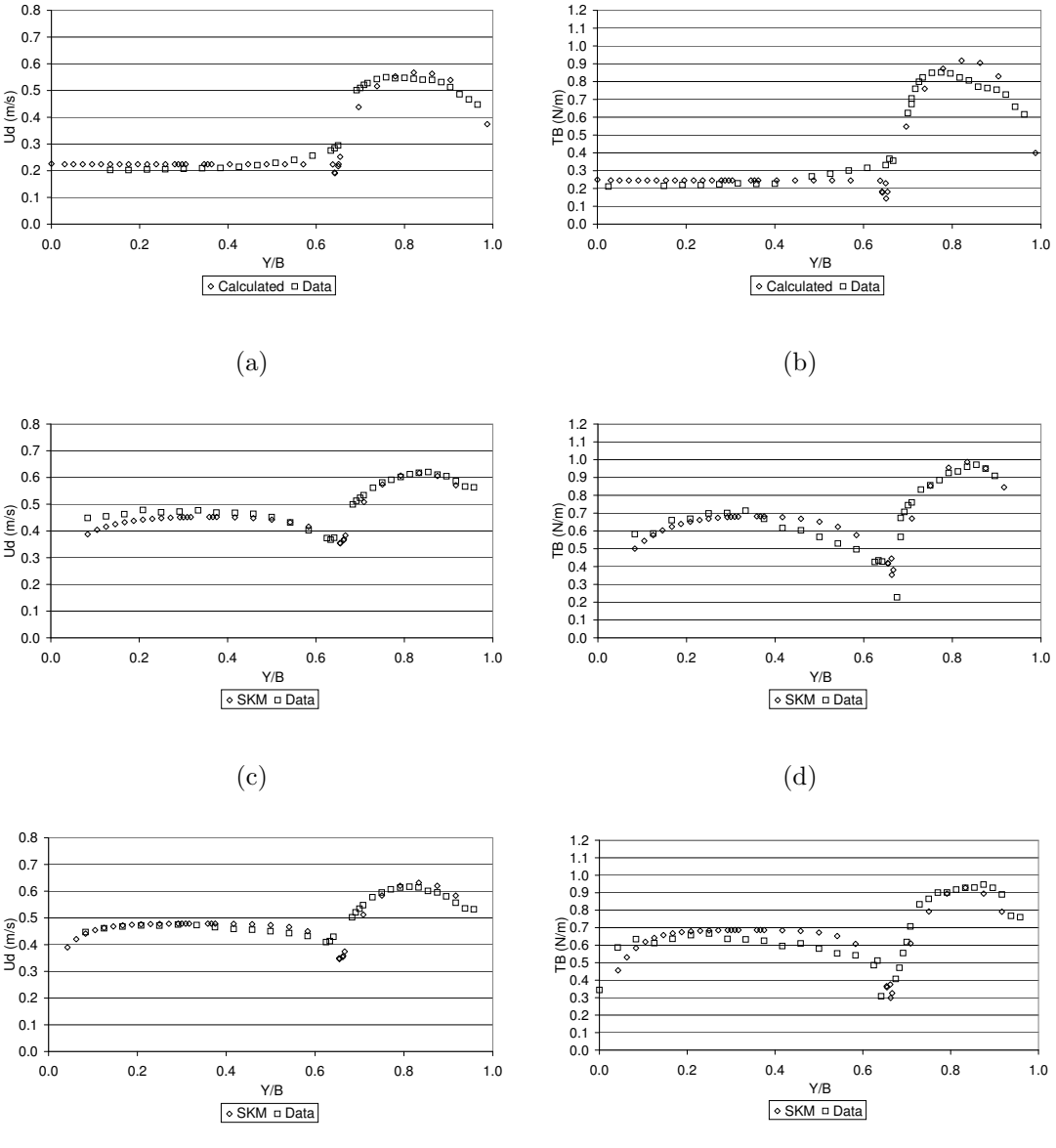

Figure 7.9: SKM results of depth-averaged velocity and boundary shear stress for (a) and (b) Dr=0.22 ; (c) and (d) Dr=0.43; (e) and (f) Dr=0.44

7.2.2.3 Results of flow predictions

In order to assess the performance of the model in terms of stage-discharge, the modelled discharges are compared with measured discharges.

Table 7.2 presents the percentage relative difference with all flow cases in Loughborough and LFMA. Flow predictions compared to experimental flow values are all within 5% for smooth rods. The worst predictions are obtained for Series 2Bb, which strengthens the presumption that foliage should maybe require a different modelling strategy. However, the results remain satisfactory as all flow predictions are within 6% of the measured discharges.

Table 7.2: Percentage relative difference with experimental flows (%)

Relative depth	Series 1a	Series 1b	Series 2Aa	Series 2Ab	Series 2Ba	Series 2Bb	Relative depth	LMFA
0.25	-1.20	3.10	1.16	4.92	-4.60	-2.40	0.22	0.53
0.35	3.14	1.68	4.80	3.85	-5.94	-3.78	0.43	-3.26
0.51	0.34	3.45	3.14	-0.29	-2.76	-5.18	0.44	0.65

7.2.3 Validation of the modified Shiono and Knight Method (SKM) to Field Data

7.2.3.1 Numerical modelling of the Shiono and Knight method

The analysis in Chapter 6 showed that strong secondary currents and vorticity was observed in the channel, particularly on the side slopes. This pattern was attributed to the presence of vegetation along the river banks, which enhanced the turbulence anisotropy and the secondary currents. In order to apply the proposed SKM to the irregular geometry of the river Rhône's main channel, a numerical code was developed

in Fortran. The main steps of the algorithm used in this Fortran code are outlined below.

1. Data input

   First the channel geometry, roughness and water level are read in an input data file. This data file also contains the non-dimensional eddy viscosity, the bulk drag coefficient, the friction drag coefficient and the advection term if the latter is required.

2. Interpolation onto an appropriate mesh

   The channel geometry is interpolated onto a regular mesh whose space step is specified. Similarly, each of the terms required to define the SKM, such as the friction drag coefficient and the bulk drag coefficient, are also interpolated onto that mesh.

3. The Matrix coefficients A and B are defined.

   Each term of the SKM is discretised using centered schemes. The system obtained after discretisation is linear, has for unknown U^2 and can be written in the form of a tri-diagonal matrix system AX=B. The subdiagonal, the diagonal and the superdiagonal of the resultant tri-diagonal matrix are defined, as well as the matrix of constants B.

4. The tri-diagonal matrix is solved using a Gauss elimination method

   The square of the depth-averaged velocity at the different locations is solved. The depth-averaged velocity profile can therefore be computed.

5. The results are computed and exported

   The boundary shear stress, turbulent shear stress and drag force are calculated from the solution and exported.

Details of the discretisations are now given. The equation of the SKM can be rewritten as Equation 7.28:

$$gHS_0 - \frac{\Gamma}{\rho} = \frac{f}{8}\left(1+\frac{1}{s^2}\right)^{\frac{1}{2}} - \frac{\partial}{\partial y}\left[\frac{\lambda}{2}\left(\sqrt{\frac{f}{8}}+\sqrt{\frac{f_d}{8}}\right)H^2\frac{\partial U^2}{\partial y}\right] - \frac{1}{2}\left(NC_DHD\right)U^2 \quad (7.28)$$

For a given element i of the mesh:

The gravity term is discretised into: $\rho g H S_0 = \rho g H_i S_0$. This term is part of the matrix of constant B.

The boundary shear stress term is discretised into $f_i\left(1+\frac{1}{s_i^2}\right)^{\frac{1}{2}}U_i^2$, where s_i is the side slope at the mesh element i. This term is part of the matrix diagonal.

Gamma, if used, is discretised into Γ_i and also composes the matrix of constant B_i so that $B_i = gH_iS_0 - \frac{\Gamma_i}{\rho}$.

The drag force term is decomposed into $\frac{NDH_iU_i^2}{2}$. This term is part of the matrix diagonal.

The turbulent shear stress term is discretised through Equation 7.29:

$$\begin{aligned}
\frac{\partial}{\partial y}\left\{\frac{\lambda}{2}\left[\left(\frac{f}{8}\right)^{\frac{1}{2}}+\left(\frac{f_d}{8}\right)^{\frac{1}{2}}\right]H^2\frac{\partial U^2}{\partial y}\right\} &= \frac{H_i^2}{2}\left[\left(\frac{f_i}{8}\right)^{\frac{1}{2}}+\left(\frac{f_{d,i}}{8}\right)^{\frac{1}{2}}\right]\frac{U_{i+1}^2-U_{i-1}^2}{\Delta y}\left(\frac{\lambda_{i+1}-\lambda_{i-1}}{\Delta y}\right) \\
&+ \frac{H_i^2}{2}\lambda_i\frac{U_{i+1}^2-U_{i-1}^2}{\Delta y}\left[\left(\frac{f_{d,i}}{8}\right)^{\frac{1}{2}}+\left(\frac{\left(\frac{f_{i+1}}{8}\right)^{\frac{1}{2}}-\left(\frac{f_{i-1}}{8}\right)^{\frac{1}{2}}}{\Delta y}\right)\right] \\
&+ \frac{H_i^2}{2}\lambda_i\frac{U_{i+1}^2-U_{i-1}^2}{\Delta y}\left[\left(\frac{f_i}{8}\right)^{\frac{1}{2}}+\left(\frac{\left(\frac{f_{d,i+1}}{8}\right)^{\frac{1}{2}}-\left(\frac{f_{d,i-1}}{8}\right)^{\frac{1}{2}}}{\Delta y}\right)\right] \\
&+ \frac{\lambda_i}{2}\left[\left(\frac{f_i}{8}\right)^{\frac{1}{2}}+\left(\frac{f_{d,i}}{8}\right)^{\frac{1}{2}}\right]\frac{U_{i+1}^2-U_{i-1}^2}{\Delta y}\left(\frac{H_{i+1}^2-H_{i-1}^2}{\Delta y}\right) \\
&+ \frac{\lambda_i}{2}\left[\left(\frac{f_i}{8}\right)^{\frac{1}{2}}+\left(\frac{f_{d,i}}{8}\right)^{\frac{1}{2}}\right]H_i^2\left(\frac{U_{i+1}^2-2U_i^2+U_{i-1}^2}{4(\Delta y)^2}\right)
\end{aligned} \quad (7.29)$$

By rearranging the terms of the discretised elements of the SKM, one obtains a tri-diagonal system of the form:

$$A = \begin{pmatrix} ad_1 & asp_1 & 0 & \cdots & \cdots & 0 \\ asb_2 & ad_2 & asp_2 & \ddots & \cdots & \vdots \\ 0 & \ddots & \ddots & \ddots & \ddots & \vdots \\ \vdots & \ddots & \ddots & \ddots & \ddots & 0 \\ \vdots & \ddots & \ddots & asb_{n-1} & ad_{n-1} & asp_n \\ 0 & \cdots & \cdots & 0 & asb_n & ad_n \end{pmatrix}$$

7.2.3.2 Input parameters

Bulk drag coefficient

As mentioned in Section 3.2.3, the density of trees on the floodplain of the study reach was estimated following a survey of the vegetation carried out in June 2007. The results of the survey estimated that there were 3 trees per 10 m^2 with an average tree diameter of 0.5 m. This estimation was used to calculate the drag force term. By assimilating the trees to experimental rods, the bulk drag coefficient C_D can be determined from Nepf (1999) using the same method as that used for the laboratory data. For a spacing ratio of approximately 10, the diminution in the drag coefficient due to the wakes generated by the upstream rods leads to a bulk drag coefficient of approximately 0.77. Vegetative conditions on the floodplain were assumed to be homogeneous with a constant density of trees.

Darcy-Weisbach friction factor

In Chapter 6, the log-law analysis was applied in the main channel to obtain a characteristic roughness length Z_0 and Z_0 was found to vary between 0.032 m to 0.072 m. A roughness coefficient k_s can be estimated based on Z_0, by identifying the log-law used in the log-law analysis (Equation 6.5) with Equation 7.30.

$$\frac{U}{U_*} = \frac{1}{\kappa} \ln\left(\frac{z}{k_s}\right) + 8.5 \tag{7.30}$$

The standard Colebrook-White equation (Equation 5.5) can then be applied to calculate the Darcy-Weisbach friction factor f. For the upstream cross-section for

example, f is 0.065 and 0.069 for the low and high flood events respectively. In the floodplain, k_s was increased to 12.3 m in order to account for the increased roughness conditions and the resulting low velocity. k_s was interpolated linearly on the sideslope, to represent the transition between the main channel and floodplain roughness.

Turbulent eddy viscosity

The dimensionless eddy viscosity coefficient λ was kept constant and taken as 0.0683. The friction drag coefficient f_d was used as a calibration parameter. The calibrated values of f_d are presented in Table 7.3. For comparisons, friction drag values were also derived from the processed field data using Equation 7.27. In Equation 7.27, the values of U, H and $\frac{dU}{dy}$ were averaged from the processed data. The drag force F_D was calculated using the same analytical formulae as the one that was applied in the numerical modelling code, with values of averaged values of H and U on the vegetated floodplain.

Table 7.3: Values of the friction drag f_d used in the SKM modelling of the river Rhône data and derived from data

Case	f_d used in SKM modelling	Approximate f_d derived from data
pk7.1 04-04-06	6.0	8.3
pk7.7 04-04-06	5.0	8.2
pk7.1 11-04-06	2.5	4.5
pk7.85 11-04-06	2.0	4.1

The friction drag values used in the SKM modelling remain of the same order of magnitude than those derived from the processed data.

7.2.3.3 Sensitivity of the model to drag friction factor f_d

To illustrate the impact of the drag friction f_d on the depth-averaged velocity profile, f_d is set to 0.0, 6.0, 30.0 and 100.0 for the low flood event in the upstream section. The results are presented in Figure 7.10 (a), with the calibrated value of f_d being chosen

as 6.0. f_d plays its most significant part on the side slope, where the effects of vegetation and of the resulting enhanced secondary currents are strongest. By definition, the drag friction f_d is associated to the gradient of depth-averaged velocity, which also explains its influence in these areas. In addition, it can be seen that a very high value of f_d such as 100.0 has for effect to increase the overall resistance in the channel as the depth-averaged velocity decreases. A change of f_d from 0.0 to 30.0 leads to a decrease in depth-averaged velocity of 22% on average on the right side slope, near the vegetated interface. On the other hand, depth-averaged velocity is only decreased by a further 4% following a change of f_d from 30.0 to 100.0. This lower sensitivity of the parameter f_d compared to the experimental cases is the result of the high roughness values used on the sideslope and the floodplain, which control flow resistance. f_d decreases when relative depth increases, which correlates the experimental observations.

7.2.3.4 Results

The lateral distributions of the depth-averaged velocity are presented in Figure 7.10 for the upstream sections. The boundary shear stress distributions are presented in Appendix D.

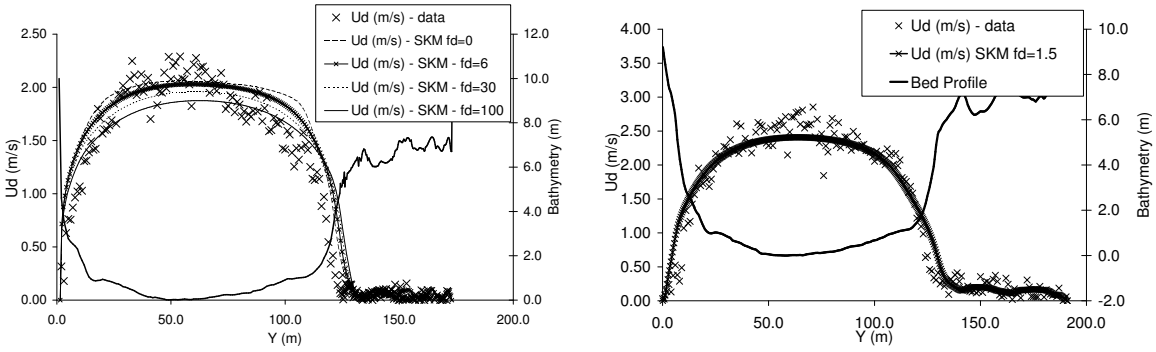

(a) (b)

Figure 7.10: Depth-averaged velocity derived from SKM for (a) pk=7.1 - 04-04-2006 (b) pk=7.1 - 11-04-2006

The modelled lateral depth-averaged velocity profiles compare relatively well with the profiles derived from field data, especially for the high flow event. However, the roughness applied to the side slope of the right bank for the low flow event is underestimated. A better fit could have been obtained with a higher Darcy-Weisbach friction factor applied in this area.

7.2.4 Discussion: Comparison of the Proposed SKM with a more Traditional Approach using the Advection Term

A second version of the SKM was tested to allow comparison with the results of the proposed SKM for the Loughborough flow cases. In a more standard approach, the SKM was kept in its original form, i.e. with the turbulence shear stress term reduced to the bottom turbulence shear term. The models were calibrated through the use of the advection term Γ. In addition, a local friction drag at the rod $f_{d,rod}$ was included to account for the local increased friction due to the line of rods. This version is a variation of the SKM version exposed in Shiono *et al.* (2009) and is presented in Equation 7.31.

$$\tau_{xy} = \rho(\epsilon_t + \epsilon_d) = \lambda \left(\sqrt{\frac{f}{8}} + \sqrt{\frac{f_i}{8}} \right) HU \tag{7.31}$$

where

$$f_i = \begin{cases} f_{d,rod}, & \text{at the rod} \\ 0, & \text{elsewhere} \end{cases} \tag{7.32}$$

7.2.4.1 Input parameters

The input parameters in this SKM version were the same as those used for the proposed SKM except that values for the advection term and friction drag factor at rods were required. The calibrated values used in the modelling of the Loughborough flow cases are given in Table D.1, in Appendix D.

7.2.4.2 Sensitivity analysis of advection term Γ and the drag friction factor at rods $f_{d,rod}$

Figure 7.11 illustrates the sensitivity of the the depth-averaged velocity to the parameters Γ and $f_{d,rod}$.

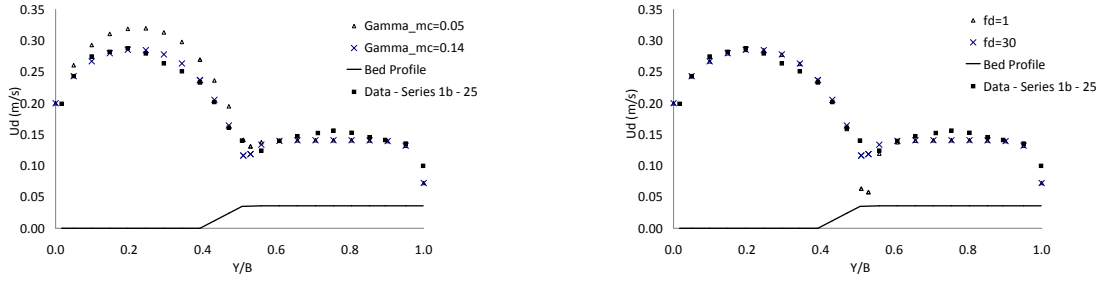

(a) (b)

Figure 7.11: Illustration of the sensitivity of Γ_{mc} and $f_{d,rod}$ on the results (a) Γ_{mc} is changed from 0.14 to 0.05 and $f_d = 30$ is kept constant (b) f_d is changed from 1 to 30 and $\Gamma_{mc} = 0.14$ is kept constant

When Γ increases, the depth-averaged velocity decreases and conversely. The friction factor $f_{d,rod}$ might be seen as a fortuitous way to compensate for the uncertainties in the analytical formulae to represent the effects of wakes.

7.2.4.3 Results

The lateral distributions of depth-averaged velocities and of the second version of the SKM are presented in Appendix D.

The relative difference with the experimental flows is given in Table 7.4. All the calculated flows are within 4% of their corresponding experimental values.

Table 7.4: Percentage relative difference with experimental flows

Relative depth	Series 1a	Series 1a	Series 2Aa	Series 2Ab	Series 2Ba	Series 2Bb
0.25	3.90	-1.63	1.48	3.38	0.82	-2.72
0.35	-3.68	0.76	0.00	3.60	0.16	-3.15
0.51	-1.41	-1.14	-3.58	-2.21	-1.33	-3.54

7.2.4.4 Relation between the advection term and drag force

Figure 7.12 presents the variations between Γ and drag force F_D with linear trends fitted to all distributions. In the floodplain, the linear regression coefficients vary between 96.6% and 99.8%. In the main channel, they are over 90% for all cases.

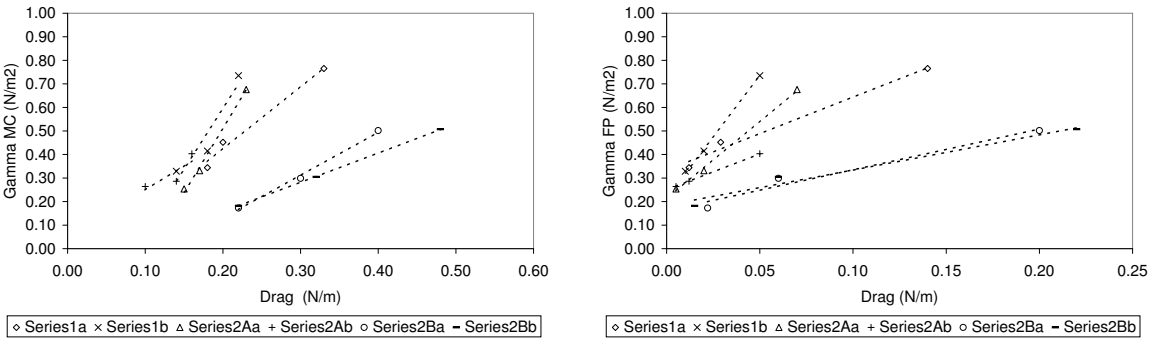

(a) (b)

Figure 7.12: Variations of Γ_{mc} and Γ_{fp} with drag force F_D (a) Γ_{mc} (b) Γ_{fp}

Figures 7.13 present the variations of β_{fp} and β_{mc} with relative depth. The variations of β_{mc} for the smooth rods do not vary significantly with relative depth except for Series 1a, i.e. for the dense case of 6 mm diameter rods. However, β_{fp} increases significantly with relative depth, almost linearly, for all smooth rod cases. This last pattern correlates the finding of Rameshwaran and Shiono (2007) who observed a linear variation of the advection term with relative depth in the floodplain.

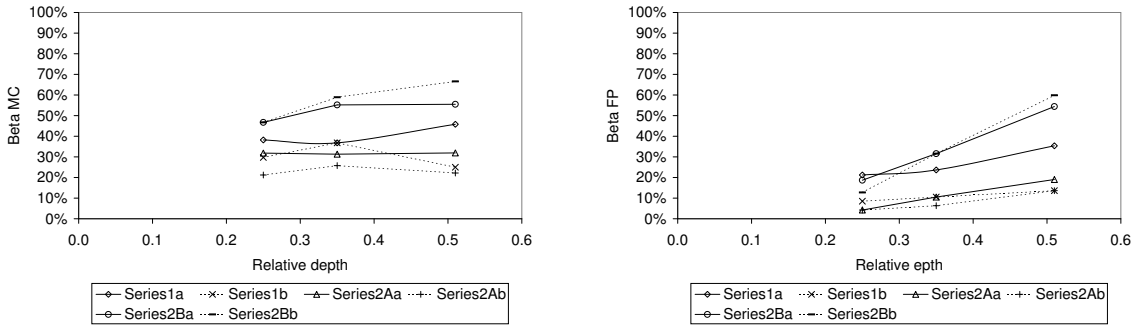

(a) (b)

Figure 7.13: Variations of β_{mc} and β_{fp} with relative depth (a) β_{mc} (b) β_{fp}

7.2.4.5 Conclusion on the use of the drag friction factor versus advection term

The results obtained for the Loughborough flow cases demonstrate that the proposed SKM can be used in order to make flow prediction and to estimate the lateral distribution of depth-averaged velocity and boundary shear stress. In the proposed SKM, the drag friction factor f_d used to calibrate the model can be derived from experimental data. The trends in f_d appear consistent with the different tested flow cases. f_d is seen to decrease when diameter, density and relative depth increase, relative depth being the most influential factor. On the other hand, a more standard SKM modelling that incorporates the advection term $\frac{\partial \rho HUV}{\partial y}$ and a the drag friction factor at rods $f_{d,rod}$ also gives very satisfactory results. Relations defining the variations of the advection term can be derived from the results for each case, as the advection term is seen to increase linearly in the main channel and in the floodplain when compared to relative depth. The advection term appears to be linked with drag force, which also varies linearly with relative depth. However, the theoretical considerations leading to the proposed SKM and that define the added turbulence drag term appear more directly related to the experimental results. It is felt that the advection term requires more experimental investigations, with the direct measuring of transverse velocity for example. Hence, the proposed SKM with the drag friction factor and the advection term set to zero, as defined in Equation 7.24, is favored.

7.3 Telemac-2D

This Section presents the Telemac-2D modelling of flow cases studied in the laboratories. First, a description of the models set up is highlighted. The turbulence models available in Telemac-2D are then introduced and the results of sensitivity tests carried out on selected key parameters are exposed. Then, the results of Large Eddy Simulations (LES) performed for three flow cases in Loughborough are presented and the simulated unsteady flow characteristics are discussed. The four turbulence models available in Telemac-2D were applied to two flow cases studied in LMFA and the results of these simulations are reported. Finally, an alternative option for the modelling of the rods is presented.

7.3.1 Introduction

Telemac-2D is a finite-element-based model of free surface flow solving the 2-D Saint-Venant equations in their non-conservative form. The model was developed by the National Hydraulics Laboratory of Electricité de France (EDF) and has been successfully applied internationally to engineering research and practice.
The second-order partial differential equations for depth-averaged free surface, derived from the full three-dimensional Navier-Stokes equations, are presented in Equations 7.33,7.34,7.35:

$$\frac{\partial h}{\partial t} + \mathbf{u}.grad(h) + h.div(\mathbf{u}) = 0 \tag{7.33}$$

$$\frac{\partial u}{\partial t} + \mathbf{u}.grad(u) = -g\frac{\partial Z}{\partial x} - \frac{1}{h}div(h\nu_t grad(u)) + S_x \tag{7.34}$$

$$\frac{\partial v}{\partial t} + \mathbf{u}.grad(v) = -g\frac{\partial Z}{\partial x} - \frac{1}{h}div(h\nu_t grad(v)) + S_y \tag{7.35}$$

in which h is the water depth, u and v are the velocity components, Z is the free surface elevation, and S_x and S_y are the source or sink terms in dynamic equation.

Hereinafter, ν_t denotes the depth averaged turbulent eddy viscosity. The model calculates water depth and velocity in the x and y directions at each computational node. An extensive description of Telemac-2D modelling system can be found in Hervouet (2003).

7.3.2 Model set-up

7.3.2.1 Mesh generation

In Telemac-2D the mesh is generated via a pre-processor package called Matisse. The geometry is interpolated on unstructured triangular mesh. In order to ensure that the interpolated geometry is correct, some constraints are imposed on Matisse so that boundaries such as the main channel and floodplain interface are accurately defined and forced into the mesh. The explicit definition of the rods in the model, entered manually as islands, constrains significantly the mesh generator. As a result, some poorly proportioned triangles can be locally generated. The mesh were therefore reviewed and adjusted manually where needed so that triangles were not elongated by a ratio greater than 5:1, thus respecting the rule of thumb given in Wilson *et al.* (2002).

Telemac-2D cannot handle vertical steps. Therefore, a steep slope of 5.6° was generated to model the step between the main channel and the floodplain in the rectangular cross-section of the LMFA flume.
The mesh were locally refined near the wall boundaries and in the rod area to better represent the rapidly changing flow patterns occurring in these areas.

7.3.2.2 Boundary conditions

Upstream, the inflows in the main channel and floodplain as measured by the flowmeters were used as boundary conditions. A constant depth was applied downstream, based on the experimental measurements. Slip and non-slip boundary conditions can be applied to the boundaries in Telemac-2D. When non-slip boundary conditions are applied, the longitudinal velocity and the transverse velocity are set to zero on the walls. For slip

boundary conditions, the transverse gradient of longitudinal velocity and the transverse velocity are set to zero, i.e. (Equation 7.36):

$$\frac{\partial U}{\partial y} = 0, V = 0 \tag{7.36}$$

Slip conditions were found to improve the results significantly and were favored in the modelling. Nevertheless, Telemac-2D generally performed unsatisfactorily near the wall boundaries, even with the slip condition imposed and despite refining the mesh in these areas. Therefore, wall velocities derived from the law of the wall were recurrently imposed as this led to some improvement in the results. This is discussed further in section 7.3.4.3.

7.3.2.3 Other general set up parameters

After investigations, a timestep of 0.005 s was used during the simulations for all cases except when the LES turbulence model was applied. A smaller timestep of 0.0025 s was used with LES turbulence models as this was seen to encourage eddy generation and improved the resolution of periodic flow structures in the output of LES results. These relatively small timesteps also helped to keep the Courant numbers low during the simulations. The Courant number is defined by Equation 7.37:

$$Cr = \frac{u\Delta t}{\Delta X} \tag{7.37}$$

where u is the local velocity, Δt is the timestep and ΔX is the mesh size of the element considered. Courant numbers during the simulations were typically in the range $0.1 \sim 0.4$. The highest Courant numbers were observed in the rod area, which is where the mesh size is the most refined, locally reaching up to $0.6 \sim 0.8$.

The initial conditions were applied by setting the water profile parallel to the bed slope via a Fortran subroutine. The initial depth was chosen to replicate the relative depths studied in experiments.

The roughness was specified throughout the domain via a Manning's n number. Different roughness can be applied to the domain via a Fortran subroutine. The Manning coefficient applied to the studied cases varied between 0.009 (in LMFA flume) to 0.011 (in Loughborough flume).

7.3.3 Turbulence modelling in Telemac-2D

Four turbulence closure schemes are available in Telemac-2D, namely constant eddy viscosity model, Elder model, $k-\epsilon$ model and Large Eddy Simulation (LES). These four turbulence models were tested for two LMFA flow cases for a spacing ratio of $\frac{L}{D} = 32$, for the shallow case (Dr = 0.22) and the deeper case (Dr = 0.43). The LES turbulence model was applied to the three flow cases of Series 2Ab studied in Loughborough.

7.3.3.1 Constant eddy viscosity

The simplest, in its formulation, eddy viscosity model to be used is the constant eddy viscosity model. Telemac-2D modelling with the constant eddy viscosity model was carried out using a single value of ν_t across the domain. This means that an overall viscosity coefficient (molecular and turbulent viscosity) is applied to the whole domain. Hence, the value of the constant eddy viscosity is expected to be greater than the physical value molecular value of $10^{-6}\ m^2/s$.

In Telemac-2D, the value of constant eddy viscosity has an impact on secondary currents. A low value of eddy viscosity will tend to dissipate only small eddies while high values will also dissipate large eddies.

The calibrated values of ν_t for the dense rod case of $\frac{L}{D} = 32$ for Dr = 0.22 and Dr = 0.43 were $10^{-4}\ m^2/s$ and $5.10^{-4}\ m^2/s$ respectively. These values are in the range $10^{-4}\ m^2/s$ to $10^{-3} m^2/s$ given by Wilson *et al.* (2002). The difference between the eddy viscosity used for cases Dr = 0.22 and Dr = 0.43 might seem significant. However,

such variations for eddy viscosity are also in the range of the variations presented in Shiono and Knight (1991) (Figure 16) between cases Dr=0.196 and Dr=0.400 for the experiments carried out in the Flood Channel Facility.

7.3.3.2 Elder model

The Elder model in Telemac-2D allows the use of different viscosity values for both the longitudinal (x) and transverse (y) directions (ν_x and ν_y respectively), through dimensionless dispersion coefficients α_x and α_y that need to be specified. The turbulent diffusion coefficients ν_x and ν_y are given by Equations 7.38 and 7.39.

$$\nu_x = \alpha_x h U_* \qquad (7.38) \qquad\qquad \nu_y = \alpha_y h U_* \qquad (7.39)$$

In the modelling, the initial runs were carried out with values of (α_x, α_y) taken as $(6.0, 0.6)$, as recommended by Wilson *et al.* (2002). These values were then adjusted and treated as a calibration parameter.

The calibrated values of (α_x, α_y) for $\frac{L}{D} = 32$ and for Dr = 0.22 and Dr = 0.43 were $(5.0, 0.35)$ and $(6.0, 0.6)$ respectively.

7.3.3.3 k-epsilon model

The $k-\epsilon$ model describes the turbulent eddy viscosity ν_t as a function of the turbulent kinetic energy k and the rate of dissipation ϵ, as defined in Equation 7.40:

$$\nu_t = c_\mu \frac{k^2}{\epsilon} \qquad (7.40)$$

here c_μ is a constant equal to 0.09. The standard constants of the $k-\epsilon$ transport equations are used within Telemac-2D (Hervouet, 2003) and no turbulence parameter calibration was carried out in the model set-up.

Relation 7.40 assumes an equilibrium between the production of turbulence and its dissipation. The parameter k is a measure of the turbulence intensity while ϵ is closely

related to a length scale L characterising turbulent motion.

The set of depth-averaged equations defining the $k-\epsilon$ model in Telemac-2D reads:

$$\frac{\partial k}{\partial t} + u_i \frac{\partial k}{\partial x_i} = \frac{1}{h} div\left(h \frac{\nu_t}{\sigma_k} \overrightarrow{grad}(k)\right) + P - \epsilon + P_{kv} \tag{7.41}$$

$$\frac{\partial \epsilon}{\partial t} + u_i \frac{\partial \epsilon}{\partial x_i} = \frac{1}{h} div\left(h \frac{\nu_t}{\sigma_\epsilon} \overrightarrow{grad}(\epsilon)\right) + \frac{\epsilon}{k}\left[C_{1\epsilon} P - C_{2\epsilon}\epsilon\right] + P_{\epsilon v} \tag{7.42}$$

The production terms (which always remain positive) are calculated with the gradients of horizontal velocity components:

$$P = \nu_t \left(\frac{\partial u_i}{\partial x_j} + \frac{\partial u_j}{\partial x_i}\right) \frac{\partial u_i}{\partial x_j} \tag{7.43}$$

where $C_{1\epsilon}$ and $C_{2\epsilon}$ are equal to 1.44 and 1.92 respectively and the terms P_{kv} and $P_{\epsilon v}$ are defined by:

$$P_{kv} = C_k \frac{u_*^3}{h} \tag{7.44}$$

$$P_{\epsilon v} = C_\epsilon \frac{u_*^4}{h^2} \tag{7.45}$$

with $C_k = \frac{1}{\sqrt{C_f}}$ and $C_\epsilon = 3.6 \frac{C_{2\epsilon}\sqrt{C_\mu}}{C_f^{\frac{3}{4}}}$. C_f is the bottom friction coefficient and u_* is the shear velocity.

When the $k-\epsilon$ model is used, the velocity diffusivity coefficient remains set to the molecular value of $10^{-6}\ m^2/s$.

7.3.3.4 Large Eddy Simulations (LES)

The essence of LES lies in the separation of the velocity field into a resolved and a sub-grid part. The mean flow and the large energy containing structures are computed directly, while the influence of small scale structures is computed through sub-grid models.

Lesieur *et al.* (2005) gave a comprehensive review of LES. Let Δx be a scale characteristic of the computational mesh. To eliminate the sub-grid scales and filter the high frequency structures, a filter function $G_{\Delta x}(\overrightarrow{x})$ is applied to a quantity $f(\overrightarrow{x},t)$. This filtering operation corresponds to the convolution of $f(\overrightarrow{x},t)$ by $G_{\Delta x}(\overrightarrow{x})$. $G_{\Delta x}(\overrightarrow{x})$ has for expression 7.46:

$$\overline{f}(\overrightarrow{x},t) = \int f(\overrightarrow{y},t)G_{\Delta x}(\overrightarrow{x}-\overrightarrow{y})d\overrightarrow{y} = \int f(\overrightarrow{x}-\overrightarrow{y},t)G_{\Delta x}(\overrightarrow{y})d\overrightarrow{y} \tag{7.46}$$

The quantity f is made of a resolvable scale part $\overline{f}$ and a sub-grid scale part f', as laid out in Equation 7.47:

$$f = \overline{f} + f' \tag{7.47}$$

In LES, the modelling of turbulence is directly linked to the computational mesh size Δx. As $\Delta x \to 0$ LES becomes closer to Direct Numerical Simulation (DNS). One advantage of LES is that it captures the unsteady effects of the modelled flow better than the Reynolds-averaged Navier Stokes (RANS) approaches and it remains less computationally expensive than DNS.

Applying the filter function to the continuity and momentum equations leads to :

$$\overline{\frac{\partial u_i}{x_i}} = 0 \tag{7.48}$$

$$\overline{\frac{\partial u_i}{\partial t}} + \frac{\partial}{\partial x_j}(\overline{u_i u_j}) = -\frac{1}{\rho}\frac{\partial \overline{p}}{\partial x_i} + \frac{\partial}{\partial x_i}\left(2\nu\overline{S_{ij}} + T_{ij}\right) \tag{7.49}$$

where S_{ij} is the filtered-field deformation tensor as defined in Equation 7.50 and T_{ij} (Equation 7.51) is the sub-grid stresses tensor responsible for momentum exchange between the subgrid and the filtered scales.

$$S_{ij} = \frac{1}{2}\left(\frac{\partial \overline{u_i}}{\partial x_j} + \frac{\partial \overline{u_j}}{\partial x_i}\right) \tag{7.50}$$

$$T_{ij} = \overline{u_i u_j} - \overline{u_i}\,\overline{u_j} \tag{7.51}$$

The sub-grid stresses are often expressed using models inspired of RANS modelling such as an eddy viscosity model. The most widely used sub-grid model remains the Smagorinsky model, developed by Smagorinsky (1963). This is the model implemented in Telemac-2D. Similar to the mixing length concept in RANS equations, Smagorinsky proposed that the sub-grid eddy viscosity ϵ_{se} be proportional to the characteristic sub-grid scale Δl and to a characteristic subgrid velocity $v_{\Delta x}$ as expressed by Equation 7.52. This assumption can be seen as a transposition of Prandtl's assumption, who proposed that the eddy viscosity arising in RANS modelling be proportional to a mixing length multiplied by a turbulence characteristic velocity scale.

$$v_{\Delta x} = \Delta l |\overline{S}| \tag{7.52}$$

Δl and $|\overline{S}|$ can be expressed by Equations 7.53 and 7.54 respectively.

$$\Delta l = \sqrt{\Delta x \Delta y} \tag{7.53}$$

where Δx and Δy are the grid size in the x and y directions respectively.

$$|\overline{S}| = \sqrt{2\overline{S_{ij}S_{ij}}} \tag{7.54}$$

with $\overline{S_{ij}}$ already defined in Equation 7.50. Thus, the sub-grid eddy viscosity ϵ_{se} as proposed by Smagorinsky has for expression Equation 7.55.

$$\epsilon_{se} = (C_S \Delta l)^2 |\overline{S}| \tag{7.55}$$

where C_S is the Smagorinsky constant and is normally 0.1. In this work, the default value of 0.1 was kept for C_S to calculate the LES eddy viscosity.

Since the simulations in LES are unsteady, the mean values of the variables need to be calculated. This is achieved by time-averaging the results so that the mean value $\overline{f}$ of a quantity f at location (x,y) is calculated by Equation 7.56:

$$\overline{f(x,y)} = \frac{1}{T}\sum f(x,y,t) \tag{7.56}$$

where T is a period of time sufficiently large for the mean to remain constant. Figure 7.14 shows the test results of depth-averaged velocity for different periods of time T and the corresponding relative discrepancies between the tested durations. The test presented was carried out for Series 2Ab-35. The relative differences in depth-averaged velocity between $T = 45$ s, $T = 60$ s and $T = 75$ s shown in Figure 7.14 do not exceed 4%. In this work, T was taken as 60 s.

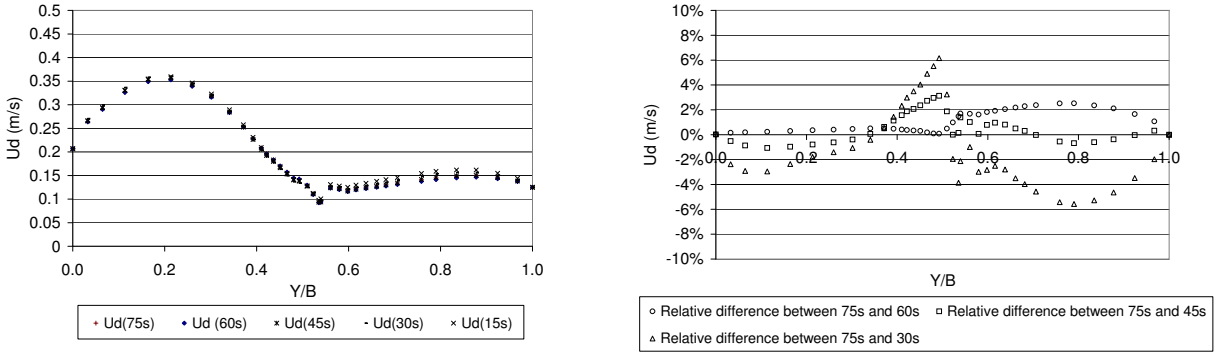

(a) (b)

Figure 7.14: (a) Depth-averaged velocity from LES for Series 2Ab-35 (b) Relative differences between durations T

7.3.4 Sensitivity tests

7.3.4.1 Introduction

It is crucial to assess the sensitivity of a number of parameters when performing 2D numerical modelling of shallow flows. The main aim of the sensitivity analysis is to ensure that the results generated by the numerical code are related to the physics of the modelled flows, under the assumptions made by the numerical code used, as opposed to numerical quirks.

This Section presents the relevant results of the tests carried out on the sensitivity of the mesh density and the advection scheme. Results on the influence of boundary conditions on solid wall boundaries are also presented as this was shown to be of importance in the modelled flows.

7.3.4.2 Influence of the mesh

The rods were modelled using octagons. The orientation of the octagons on the modelling was tested by rotating the rods for the dense case at LMFA as shown in Figure 7.15.

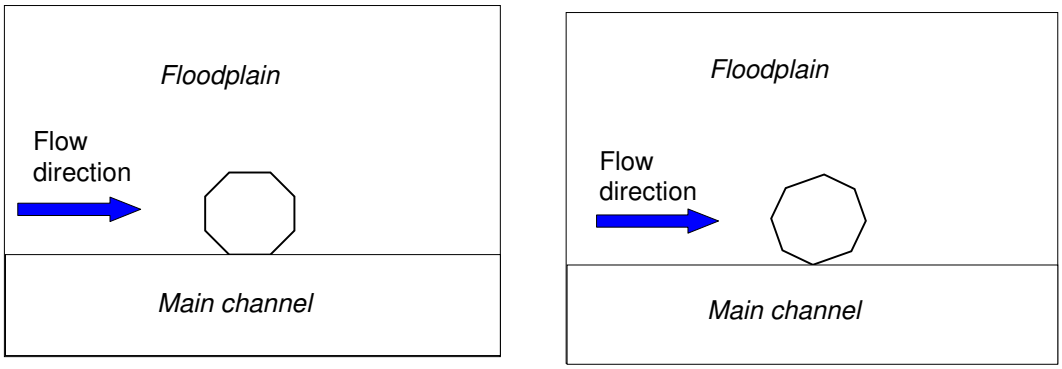

(a) (b)

Figure 7.15: Modelling of the rods within Telemac-2D as (a) Octogons with the upstream side perpendicular the flow (b) Octogons rotated by 22.5 °

The results of the depth-averaged velocity between two rods in the measuring section are presented in Figure 7.16. The relative difference between the depth-averaged velocity for both cases is shown on the right axis. It can be seen that the results are almost identical with relative differences of less than 1.5% except in the rod area in the floodplain, where the relative difference peaks at 6.7%. The depth-averaged velocities appear higher when the side of the octagon is rotated and is not perpendicular to the flow. The simulated results using the rotated configuration are closer to the measured data. Therefore, this configuration was adopted.

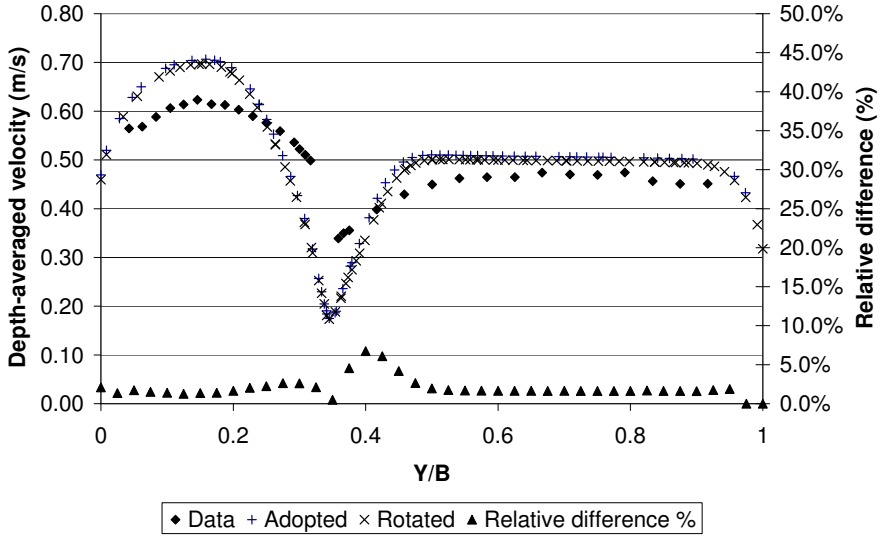

Figure 7.16: Effect of rod modelling on depth-averaged velocity for a relative depth of 0.44 and $\frac{L}{D} = 16$

It is important to verify that the mesh used is sufficiently refined so that the code used is not sensitive to the mesh density. Three densities of mesh were tested at the initial stages of the modelling in both the LMFA and Loughborough flumes. A summary of the results carried out in the LMFA flume is given. The details of the three different mesh in LFMA are given in Table 7.5.

Table 7.5: Description of the mesh used in LMFA

Mesh case	Number of elements	Number of nodes	Average element size near rods and boundaries (m)	Element size in floodplain and main channel (m)
Less dense	37686	19260	0.018	0.0035
Intermediate density	28365	55753	0.012	0.025
Dense mesh	184080	92943	0.006	0.012

The influence of the mesh resolution on the velocity is presented in Figure 7.17 for a $k - \epsilon$ turbulence model for the rod case $Dr = 0.44$ and $\frac{L}{D} = 8.0$.

The results were linearly interpolated on a grid spacing coinciding with the measuring grid spacing. The tested mesh densities did not significantly influence the water depth. The water depth results for the intermediate density mesh and dense mesh remained within 0.4%. The less dense mesh remained within 0.8% of the results from the denser mesh.

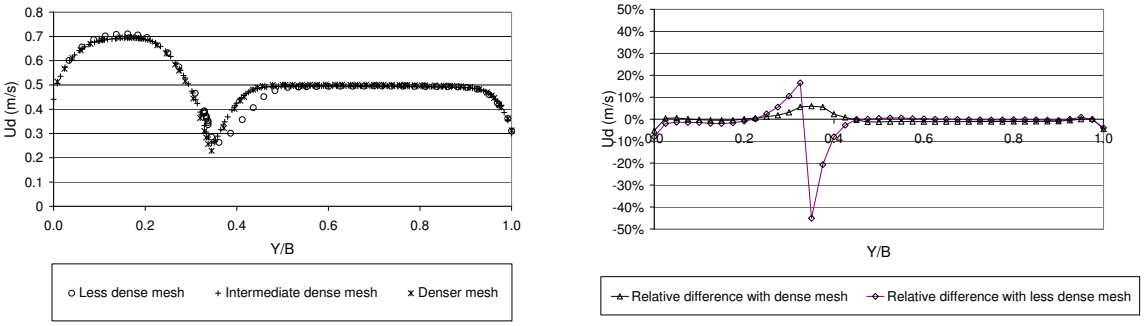

(a) (b)

Figure 7.17: Impact of mesh density on Depth-averaged velocity (a) Depth-averaged velocity profiles (b) Relative differences

The influence of the mesh on the depth-averaged velocity profiles proved to be limited outside the rod area. However, some very notable differences are observed in the region where the rods are located. The less dense mesh is too coarse to adequately model the change in velocity occurring in the rod area. The relative difference reaches 45.1% at the interface on the floodplain between the coarse and dense mesh. On the other hand, the results between the intermediate density mesh and the dense mesh are all within 5% relative difference.

A test on the mesh sensitivity was also performed using the LES turbulence model. This turbulence model is by definition sensitive to the mesh resolution. The relative difference between the intermediate mesh and the dense mesh are shown in Figure 7.18.

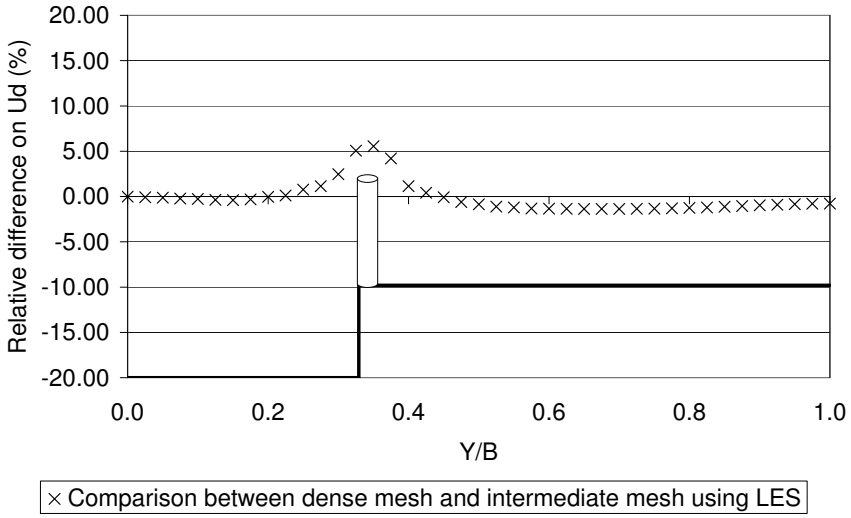

Figure 7.18: Impact of mesh density on depth-averaged velocity with LES turbulence model for 0.44 and $\frac{L}{D} = 16$

The relative difference between the two mesh densities remains mostly within a 1.5% difference and is only marginally greater than 5.0%, reaching 5.35% in the rod area near the floodplain.

The refined and intermediate density mesh performed similarly for the different tested rod densities so that in this study, rod density did not have any significant effect on the choice of mesh density for the numerical results to be grid independent. However, only two rod densities were tested for a given flume geometry.

The intermediate density mesh was adopted in LMFA because it performed appropriately and the gain saved in running time was substantial.

7.3.4.3 Influence of boundary conditions at wall boundaries

Simulations were first performed following the recommendations of Sun (2006) i.e. using non-slip boundary conditions. According to Sun (2006), non-slip boundary conditions

improve velocity predictions while they do not affect boundary shear stress distributions significantly. However, it was evident that the use of non-slip boundary conditions on walls constrains the velocity so severely that the transverse depth-averaged velocity profile "plunges" unrealistically near the wall boundaries compared to experimental data. This is demonstrated in Figure 7.19, which presents the LES results obtained by Sun (2006).

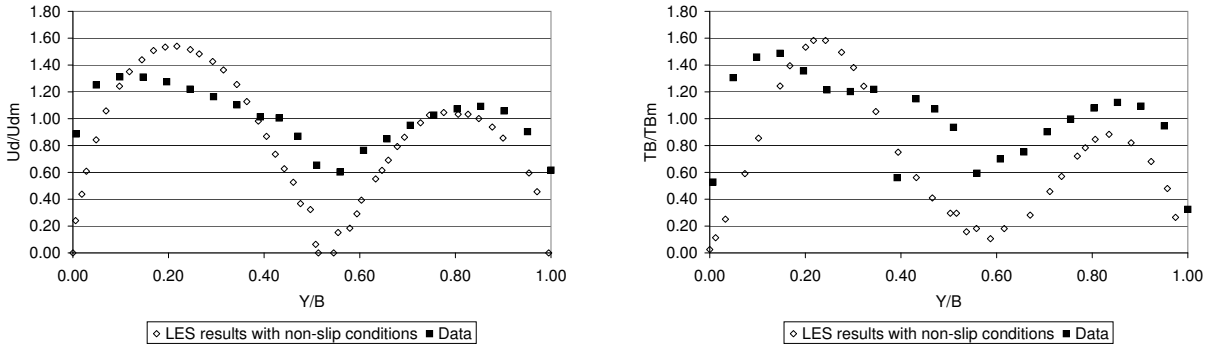

(a) (b)

Figure 7.19: LES modelling results for Dr=0.51 and $\frac{L}{D} = 4$ (Sun, 2006) (a) depth-averaged velocity and (b) Boundary shear stress

On this basis, slip boundary conditions perform better near the wall boundaries although they might still poorly define the wall velocities. One solution to this was to change the boundary conditions at the wall by imposing the wall velocity, noted as U_{wall}, using the experimental results. Velocities at the wall were determined following the same methodology as that used in the SKM modelling and presented in Section 7.2.1.4. Equation 7.23 was used to calculate U_{wall}.

The use of wall velocities as boundary condition was seen to improve the results mainly near the wall boundaries. Figure 7.20 gives an example of the impact of wall boundary conditions on the results. In this LMFA simulation, the wall velocity was imposed

on the main channel sidewall while the slip condition was imposed on the floodplain sidewall.

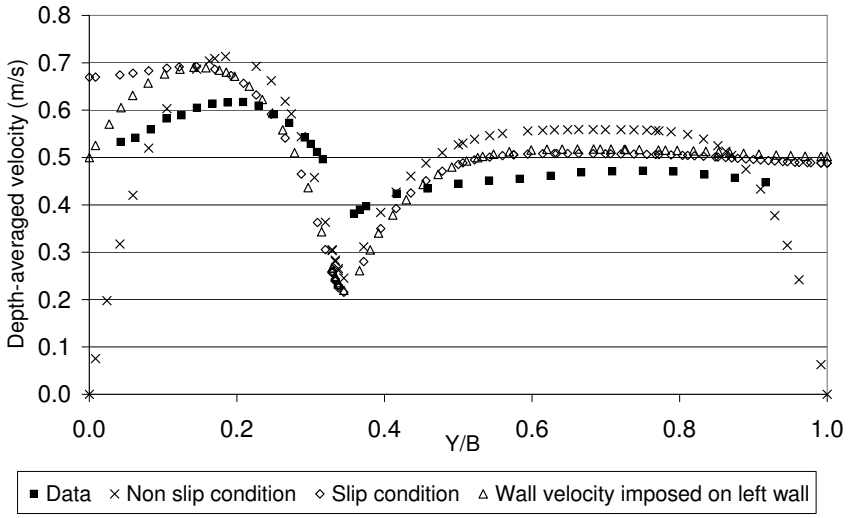

Figure 7.20: Effect of wall boundary conditions on depth-averaged velocity for a relative depth of 0.43 and $\frac{L}{D} = 32$ in LMFA

Imposing wall velocity on the left wall has not for sole effect to improve the depth-averaged velocity profile on the edge. When non-slip boundary conditions are used, the underprediction of velocity near the wall boundaries means that the velocity tends to be even more significantly overestimated in the main channel and in the floodplain to compensate for the loss of flow prediction at the edges.

7.3.4.4 Influence of the advection scheme

The solution algorithm of Telemac-2D is based on the operator-splitting technique and is described in depth in Hervouet (2007). The solving of the solution algorithm requires two steps, namely the discretization of the advection terms and the discretization of the diffusion terms.

The first step starts by solving the non conservative 2-D Saint-Venant equations for depth and velocity. Telemac-2D offers to treat the discretization of the advection scheme with the Method of Characteristics (MOC) or the Streamline Upwind Petrov-Galekin (SUPG) formulation. The Method of Characteristics (MOC) is the default scheme in Telemac-2D. The MOC and SUPG schemes were both tested in this research.

The MOC is well suited to the hyperbolic nature of the non conservative formulation of the Saint-Venant equations. In the MOC scheme, the flow variable f at time t^{n+1} at the node M is assumed to be equal to that at time t^n at the node Q obtained by retracing backwards the trajectory from point M by going back in time interval dt. The MOC is the fastest scheme to discretize the advection problem, but it induces advection error due to the linear interpolation involved to calculate the trajectories of characteristics and can compromise mass conservation.

In the SUPG scheme, the finite element formulation contains test functions bent in the direction of current. These test functions, compared to the Petrov-Galerkin method, are linear but discontinuous. They contain an additional stabilisation term which is applied in the direction of current and enhances mass conservation as well as numerical stability (Hervouet, 2007).

Rameshwaran and Shiono (2003a) tested the MOC and SUPG in Telemac-2D in meandering channel. Rameshwaran and Shiono (2003a) calibrated the models for each advection scheme and this was achieved by adjusting the Manning coefficients. As mentioned by Rameshwaran and Shiono (2003a), uniform flow can be achieved in Telemac-2D by changing either the roughness (via a Manning coefficient in this case) or the eddy viscosity. The decision to use roughness instead of eddy viscosity was based on the assumption that eddy viscosity has a negligible influence on depth-averaged velocity (Rameshwaran and Shiono, 2003b). The maximum difference in roughness between the MOC and SUPG schemes tested was 22%.

The results presented in Rameshwaran and Shiono (2003a) are significant because they reveal that the use of a calibrated Manning' s n value is partly conditioned by the numerical scheme chosen by the modeller. A calibrated Manning's n value warrants correct water surface profiles. However, the modeller then needs to be careful when deriving bed shear stress values. In Telemac-2D, bed shear stress is proportional to the square of Manning's n. Hence, for a given numerical scheme, assuming that the equivalent Manning's n recreates the velocity field and the water surface profile with a discrepancy in Manning's n of 22% leads to a discrepancy in boundary shear stress of 39%.

Figure 7.21 illustrates the impact of constant eddy viscosities on the water surface elevations for the deeper case and $\frac{L}{D} = 32$ in LFMA. These results were obtained using the constant eddy viscosity turbulence model. When the turbulent eddy viscosity is increased significantly, from $10^{-4}\ m^2/s$ to $10^{-3}\ m^2/s$, the water surface elevation also increases, in this case by up to 22.4%. A turbulent eddy viscosity with a value which is too high will introduce artificial diffusion to the flow field and therefore leads to incorrect results. When the values of the Manning's n coefficient are known exactly, from experimental investigations for example, calibration through eddy viscosity should possibly be favored.

The MOC and SUPG advection schemes were compared for the deeper and less dense case in LFMA with the $k - \epsilon$ turbulence model. The influence of the advection scheme was also compared without including the rods in the mesh but with the drag force term added in the rod area. This test was also performed for the narrow flume in Loughborough for Series 2Ab-51, with the LES turbulence model. The models were calibrated using the SUPG scheme and then reran using the MOC scheme for comparison.

Table 7.6 shows the relative difference in depth at the measuring section when the same roughness and eddy viscosity are used for both advection schemes. The mass balance value is defined as the percent of the ratio of the predicted discharge to the

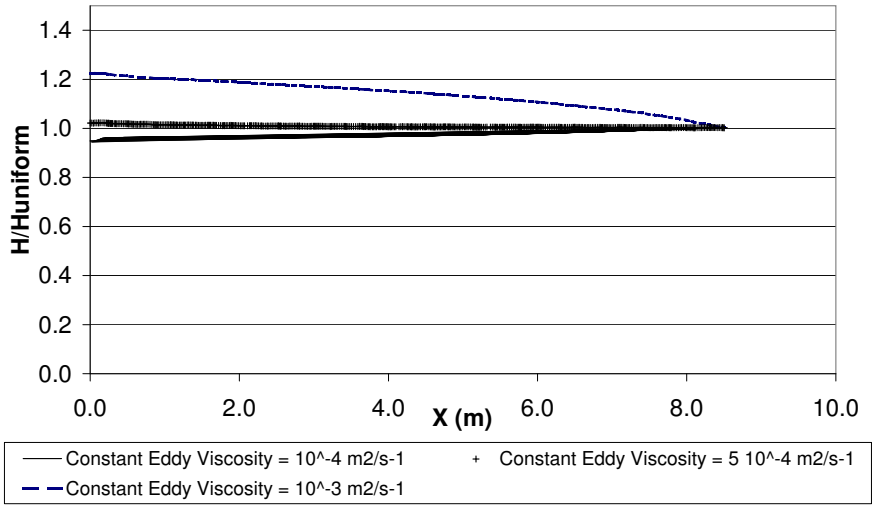

Figure 7.21: Effect of constant eddy viscosity on water surface elevation for a relative depth of 0.43 and $\frac{L}{D} = 32$

prescribed discharge.

Table 7.6: Influence of advection scheme on water depth at measuring section

Mesh case	Advection scheme	Relative difference with measured flow depth (%)	Mass balance (%)
Dr = 0.43, $\frac{L}{D}$=32.0 - rods included in mesh - $k-\epsilon$	SUPG	-1.18	1.33
Dr = 0.43, $\frac{L}{D}$=32.0 - rods included in mesh - $k-\epsilon$	MOC	4.31	1.59
Dr = 0.43, $\frac{L}{D}$=32.0 - rods modelled as drag force - $k-\epsilon$	SUPG	1.36	0.61
Dr = 0.43, $\frac{L}{D}$=32.0 - rods modelled as drag force - $k-\epsilon$	MOC	0.612	1.36
Dr = 0.51, $\frac{L}{D}$=16.0 - LES	SUPG	-0.1	0.64
Dr = 0.51, $\frac{L}{D}$=16.0 - LES	MOC	-2.9	1.78

The water depths computed at the measuring section remain relatively close to each other, within 5%, but these changes in water depth indicate that the models do need to be recalibrated to improve predictions.
The results exhibit no major discrepancies in terms of mass conservation between the MOC and the SUPG schemes, with the SUPG scheme marginally improving mass conservation. In the simulations, mass balance values using the SUPG scheme were typically in the order of 1 %. However, some of the values encountered in the modelling were slightly higher than the common criterion of ±1% for RANS modelling.

Figure 7.22 shows the impact of advection scheme on depth-averaged velocity and boundary shear stress at the measuring section in Loughborough for Dr = 0.51 and $\frac{L}{D} = 16.0$.

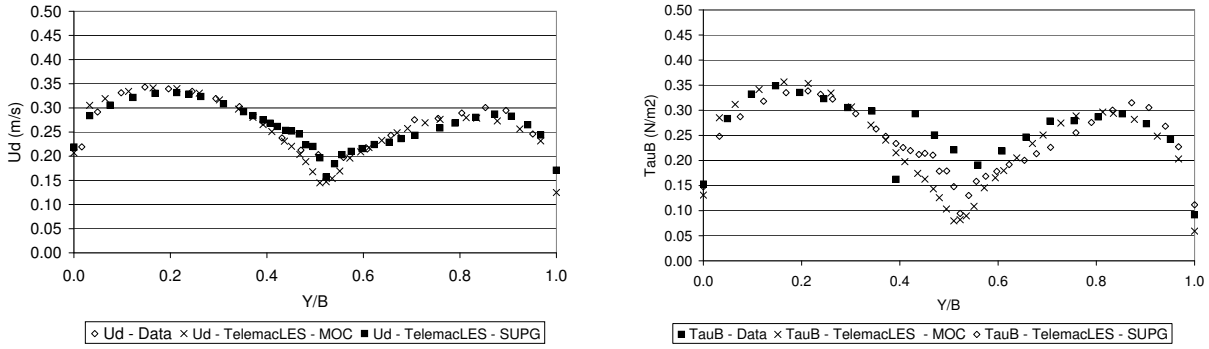

(a) (b)

Figure 7.22: LES modelling results for MOC and SUPG schemes for Dr=0.25 and $\frac{L}{D} = 16$ (a) Depth-averaged velocity and (b) Boundary shear stress

The velocity and boundary shear stress are similar in the main channel and floodplain but are clearly greater underestimated by the MOC advection scheme in the rod area. This may be due to the nature of the flow field between two rods, characterised by the presence of secondary flow circulation, which is less well represented by the MOC

advection scheme.

The results confirm Rameshwaran and Shiono (2003a) findings that the advection scheme in Telemac-2D has some noticeable impact on the results. For this research, the SUPG numerical scheme was used in the numerical modelling of vegetation in Telemac-2D, mainly because it induced less errors in mass balance and gave a better representation of the flows in the rod area.

7.3.5 Telemac-2D Results of Large Eddy Simulations in Loughborough University

This section presents the Large Eddy Simulation turbulence modelling with Telemac-2D of three flow cases studied experimentally in the Loughborough flume. The unsteady flow modelling was carried out with the 3 mm diameter rods and $\frac{L}{D} = 16.0$ spacing ratio of Series 2Ab flow cases.

7.3.5.1 Mean parameters

Figures 7.23, 7.24 and 7.25 present the lateral distributions of depth-averaged velocity and boundary shear stress for Series 2Ab-25, Series 2Ab-35 and Series 2Ab-51 respectively.

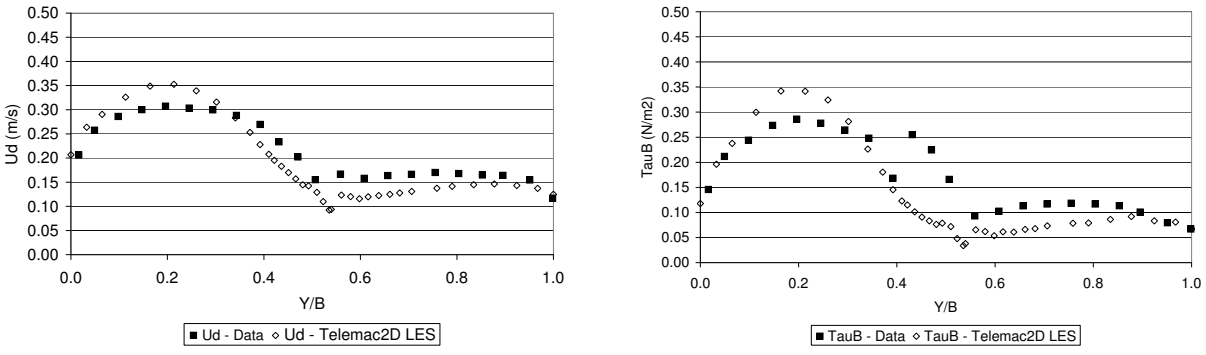

(a) (b)

Figure 7.23: LES modelling results for Series 2Ab-25 (a) U_d and (b) τ_B

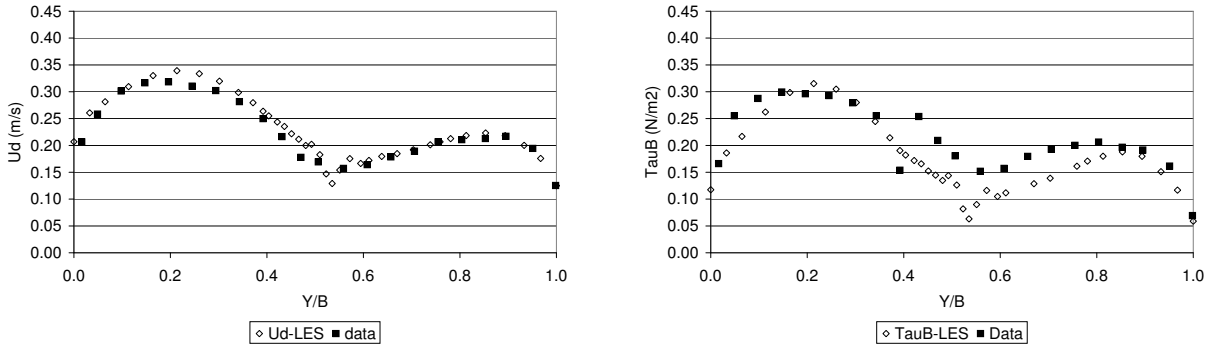

(a) (b)

Figure 7.24: LES modelling results for Series 2Ab-35 (a) U_d and (b) τ_B

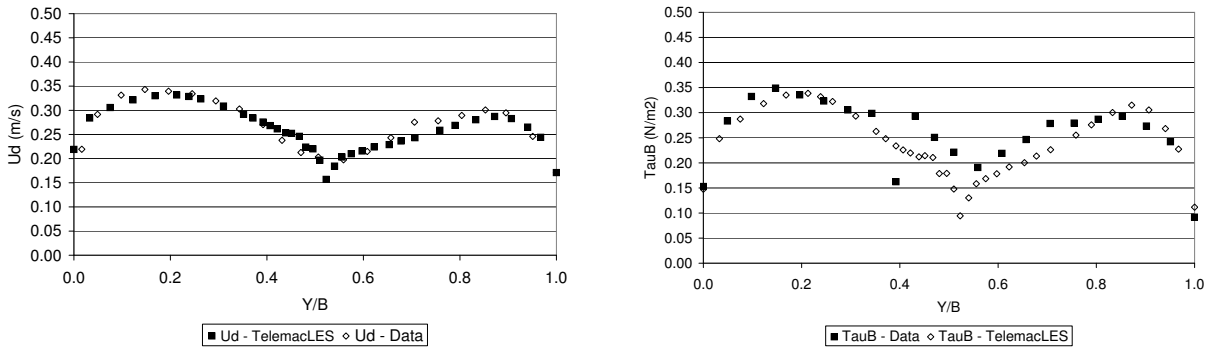

(a) (b)

Figure 7.25: LES modelling results for Series 2Ab-51 (a) U_d and (b) τ_B

Table 7.7 presents the amplitude of relative difference of depth-averaged velocity in the main channel between y = 0.01 m and y = 0.105 m and in the floodplain for y = 0.175 m and y = 0.295 m, i.e. excluding the measured data points closest to the wall boundaries.

The prediction of depth-averaged velocity tends to improve when the relative depth increases. The predictions of depth averaged velocity remain below 6% above a relative

Table 7.7: Relative differences between depth-averaged velocity results modelled with LES Telemac-2D and experimental data for Series 2Ab

Case	Average relative difference in main channel (%)	Average relative difference in floodplain (%)
Dr=0.25	9.53	18.22
Dr=0.35	5.01	1.98
Dr=0.51	2.25	3.05

depth of 0.35 and are satisfying.

Table 7.8 presents the amplitude of relative difference of boundary shear stress in the main channel between y = 0.01 m and y = 0.105 m and in the floodplain for y = 0.175 m and y = 295 m, i.e. excluding the datapoints closest to the wall boundaries.

Table 7.8: Relative differences between boundary shear stress results modelled with Telemac-2D LES and experimental data for Series 2Ab

Case	Average relative difference in main channel (%)	Average relative difference in floodplain (%)
Dr=0.25	11.51	27.26
Dr=0.35	4.12	20.16
Dr=0.51	3.71	11.51

The bed shear stress is better modelled in the main channel and results improve when the relative depth increases, which is consistent with the modelling of depth-averaged velocity. However, the predictions of average bed shear stress in the floodplain remain above 10% at best.

The standard SKM assumes that the term $\rho H(UV)$ varies linearly in the main channel and the floodplain, allowing SKM users to define the advection term, its gradient, as a constant per sub-section. For example, constant values of the advection term were used in the SKM modelling presented for discussion in Section 7.2.4. This assumption

was verified in the Flood Channel Facilities in the absence of vegetation (Shiono and Knight, 1991). However, this assumption should also be verified in presence of vegetation as the wake structure and drag force alter the flow field in the channel. Figure 7.26 shows the variations of $\rho H(UV)$ for Series 2Ab-51.

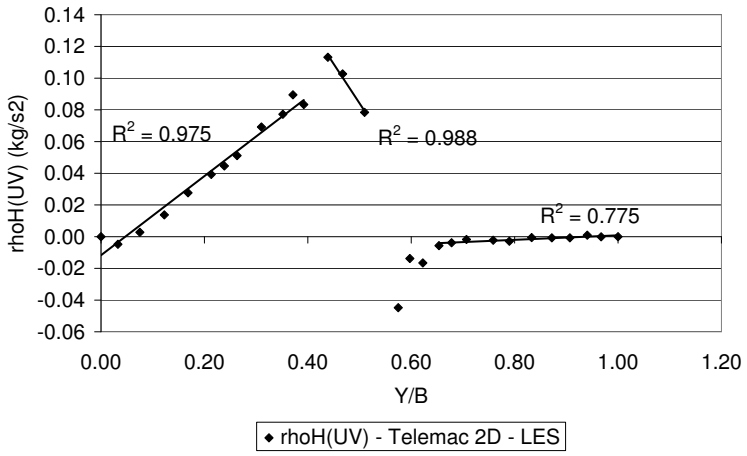

Figure 7.26: Transverse variations of $\rho H(UV)$ for Dr=0.51, $\frac{L}{D} = 16$ with the 3 mm rods

$\rho H(UV)$ varies linearly in the main channel and on the side slope, with linear regression coefficients of 97.5% and 98.8% respectively. Therefore, the assumption that the advection term is constant holds. The results suggest that a different Gamma coefficient on the sideslope than on the main channel would possibly improve the modelling. On the floodplain, however, $\rho H(UV)$ oscillates and the linear regression coefficient is only 77.5%.

From Figure 7.26, the values of the advection term can be calculated. In the main channel, taking the gradient of $\rho H(UV)$ over the whole subsection, $\Gamma_{mc} = 0.21$ and in the floodplain, $\Gamma_{fp} = 0.05$. With these values, a value of f_d taken as 0.035 applied in the brush area (region 3) gives the best results. The Telemac-2D LES value of Γ in the

main channel is higher than the corresponding calibrated value presented in Section 7.2 i.e. 0.16 while in the floodplain the values are both equal to 0.05. The calibrated value of f_d is smaller than the value presented in Section 7.2. This can be explained by the higher advection term simulated by the Telemac-2D LES modelling and used as input in this SKM modelling.

7.3.5.2 Shear stress modelling

Using LES, it is possible to distinguish the contribution to shear stress made by larger turbulence structures (τ_{LE}) and smaller turbulent structures (τ_{SE}). τ_{LE} and τ_{SE} can be calculated using Equations 7.57 and 7.58.

$$\tau_{LE} = \frac{1}{T}\rho\Sigma(U - \overline{U})(V - \overline{V}) \tag{7.57}$$

$$\tau_{SE} = \rho\overline{\epsilon_{SE}}\frac{\partial\overline{U}}{\partial y} \tag{7.58}$$

where $\overline{\epsilon_{SE}}$ is the mean sub-grid eddy viscosity. Figure 7.27 presents the lateral variations of τ_{LE} and τ_{SE} normalised by ρU_*^2 for Series 2Ab-51.

τ_{SE} is typically in the order of O $\left(0.01\rho U_*^2\right)$, which is two orders of magnitude smaller than τ_{LE}. This suggests that the contribution of sub-grid eddies can be neglected under the studied shallow flow conditions. This correlates Sun (2006)'s results obtained with LES Telemac-2D modelling in compound channel flow with vegetation on the floodplain.

7.3.5.3 Spatial flow fluctuations

Figure 7.28 presents the instantaneous spatial distributions of longitudinal and transverse velocities U and V, their product UV, vorticity, free surface elevation and boundary shear stress between x=7.0 m and x=9.0 m for Series 2Ab-25, corresponding to Dr=0.25 and 3 mm diameter rods, at a time T when large coherent structures have fully developed. In this case, T was taken as T=195 s. In Figure 7.28, the velocity

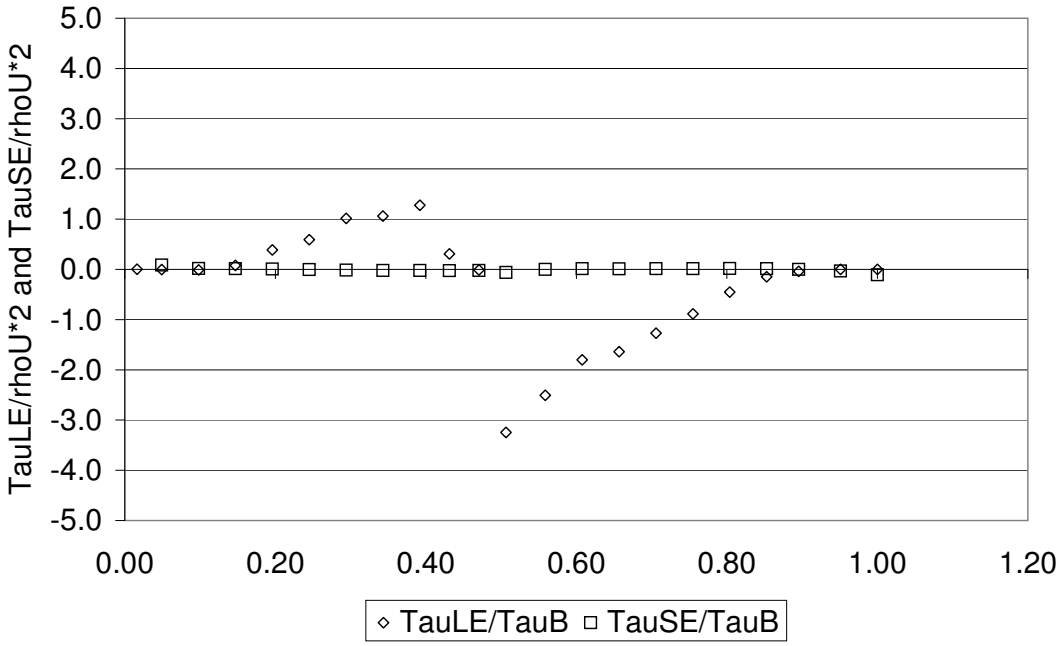

Figure 7.27: LES simulation results presenting lateral variations of τ_{LE} and τ_{SE} for Series 2Ab-51

and bed shear stress are normalised by the mean velocity and mean bed shear stress respectively. The comparison of these results shows the impact of large eddies on the hydraulic behaviour of the studied case and is discussed in the following paragraphs.

The areas of high longitudinal velocity can be observed in Figure 7.28a in the center parts of the main channel and of the floodplain. To each high velocity area in the main channel corresponds a low velocity area in the floodplain, approximately symmetrical to the interface, and viceversa. The lowest streamwise velocity occurs in the rod area, as the rods cause flow retardation. The effects on streamwise velocity of the wakes, generated in the trail of the rods, appear to be more pronounced in the floodplain than they are in the main channel.

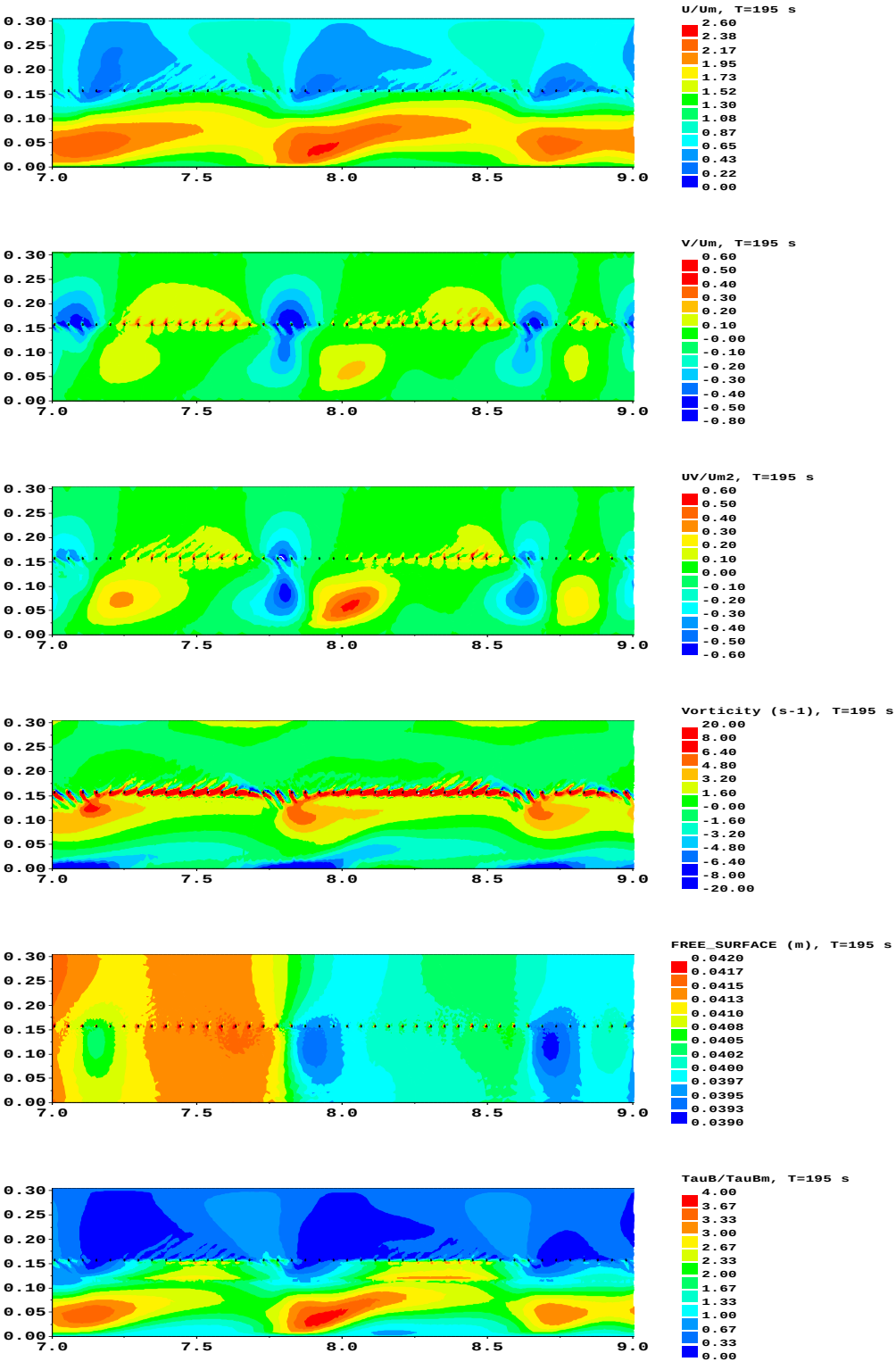

Figure 7.28: Series 2Ab-Dr=0.25 (a) U/Um (b) V/Um (c) UV/Um2 (d) Vorticity (s-1) (e) Free surface elevation (f) TB/TBm

In Figure 7.28b, positive and negative transverse velocity areas are found alternatively stretching either side of the interface. This is a clear indication of periodic motions in this region. Unsurprisingly, the impact of wakes is visible near the rods in the floodplain when the transverse velocity is positive and in the main channel when the transverse velocity in negative. The highest magnitude of transverse velocity V occurs in the central regions of the main channel and floodplain as well as around the rods. This pattern is different from the corresponding no rod case where the maxima of transverse velocity only occur in the vicinity of the interface.

The role of UV in the SKM has already been highlighted in this chapter through the so called advection term. Figure 7.28c shows that the spatial distribution of UV is similar to that of the transverse velocity. The values of UV normalised by U^2 fall in the range -0.6 to 0.6.

Figure 7.28d illustrates vehemently that the highest vorticity values are found near the rod. In the main channel, the magnitude of vorticity is strongest on the sideslope, which is similar to the pattern observed in Chapter 6 with the collected field data.
In the region bordering the vegetation, the vorticity remains positive while away from the interface, the vorticity is negative. This supports Ikeda and McEwan (2009b) who also reported that vorticity reached its highest maximum near the vegetated interface of their studied straight compound channel.

Figure 7.28e reveals that the lower and higher values of free surface occur at the start of the main channel sideslope, as well as round the rods. In the no vegetation case, the lower and higher values of free surface are only observed alternatively around the main channel and floodplain junction (Sun, 2006).

The highest values of bed shear stress are found in the main channel and floodplain central regions, as seen in Figure 7.28f. When the bed shear stress is high in the centre

of the main channel, it is low in the center of the opposite floodplain and vice-versa. This pattern is similar to that observed for the longitudinal velocity. Interestingly, the bed shear stress distribution on the sideslope differs from that of the main channel. The lower and higher values of bed shear stress on the sideslope are shifted in the longitudinal direction compared to the corresponding lower or higher values in the main channel center. The sideslope is the area of the main channel where both the wake actions and the vorticity are the strongest, thus modifying the patterns of the no vegetation flow case.

Figure 7.29 shows the streamwise advection of large coherent structures between T=193 s and T=194.5 s between 7.0 and 9.0 m. The core of the main upstream structure is located at x=8.173 m and y=0.179 m on the floodpain side and T=193 s. Inspection of the time series shows that it then moves to the main channel side at x=8.363 m and y=0.181 m at T=194 s. This means that the mean relative advection speed of these coherent structures is approximately 0.19 m/s. The mean velocity across the section between T=193 s and T=194.5 s is 0.18 m/s and is 0.13 m/s at the interface.

The trajectories of 8 particles of water after 60 s, released between y = 0.060 m and 0.246 m at x = 6.0 m, are presented in Figure 7.30. All the trajectories exhibit some wavy patterns

In this example, five particles move from the floodplain to the main channel or vice-versa. Three of these particles have been released in the floodplain and two in the main channel. The particle released at y = 0.205 m moves from the floodplain to the main channel from x = 7 m at space intervals of the order of 5 to 11 times the distance L between two rod.

The two particles moving from the main channel to the floodplain and back to the main channel were those released for $y < 0.10\ m$. Interestingly, their stay on the floodplain is very short and they travel back to the floodplain with sharp angles within a distance of 3 L.

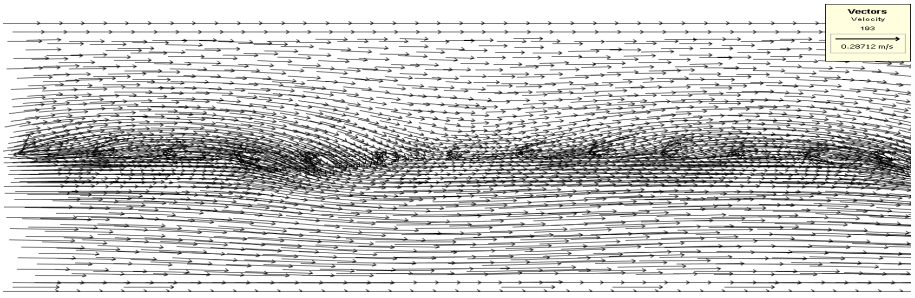

(a)

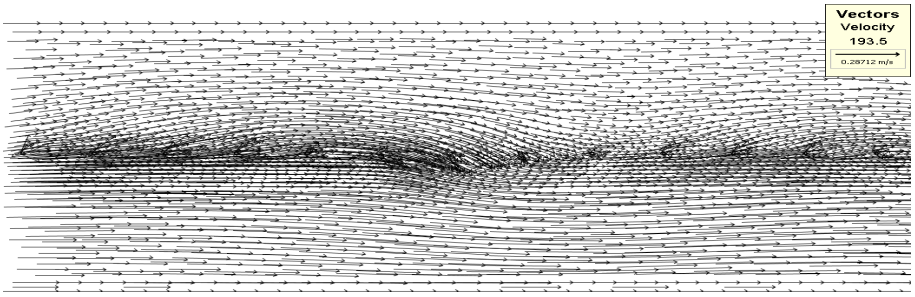

(b)

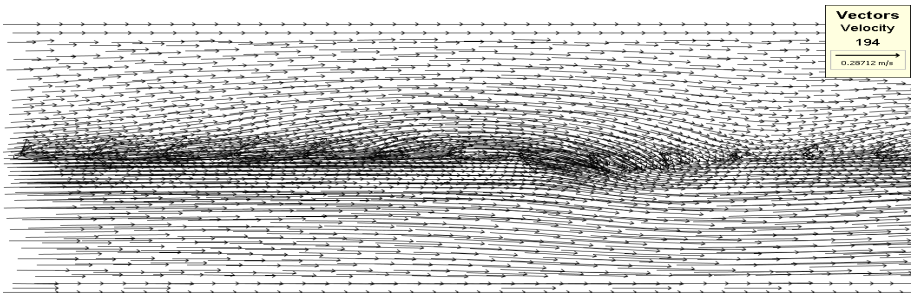

(c)

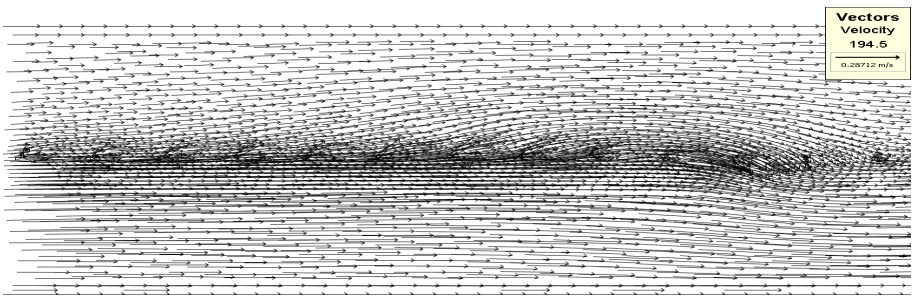

(d)

Figure 7.29: Velocity vectors at T = (a) 193 s (b) 193.5 s (c) 194 s (d) 194.5 s

The two particles released the closest to the rod on the floodplain move the slowest as they do not reach the end of the flume after 60 s.

This example illustrates the complex flow patterns generated by the rods placed on the floodplain. The somewhat periodic patterns of water particles travelling back and forth the sub-sections correspond to the alternating patterns of positive and negative vorticities presented in Figure 7.28d. Vorticity itself is the result of the combined effects of momentum transfer, secondary currents and wake action due to drag.

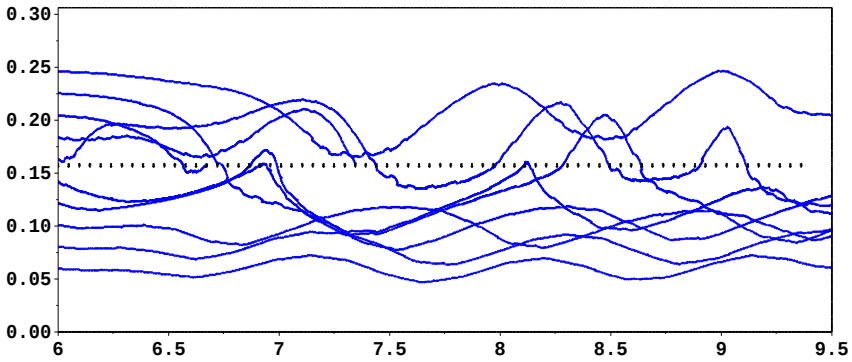

Figure 7.30: Trajectories of 8 particles of water released at x=6 m between x=6 m and x= 9.5m after 60 s

7.3.5.4 Temporal flow fluctuations

Figure 7.31 (a-f) shows the respective time-series of the longitudinal velocity (U) and lateral velocity (V) normalised by U^2, UV normalised by U^2, vorticity, water depth (H) and bed shear stress τ_B normalised by τ_{Bm} at the interface of the measuring section, mid distance between two rods. Figure 7.31a shows that U varies mostly within $\pm$ 55% of its mean value. White and Nepf (2007) found a similar order of magnitude ($\approx \pm$ 50%) when analysing the fluctuations in streamwise velocity. From Figure 7.31b, the time scale of the periodic pattern of lateral velocity V can be calculated. Between T=140.8 s and T=149 s, 4 periods of lateral velocity can be observed. This corresponds to a timescale of 2.05 s and a frequency of 0.49 Hz. UV and the vorticity follow the same periodic pattern.

Inspection of water depth patterns in Figure 7.31e reveals 4 periods of water depths between 140.2 s and 148.2 s. This corresponds to a timescale of 2.0 s and a frequency of 0.50 Hz. Taking the mean longitudinal velocity of 0.123 m/s , the Strouhal number corresponding to the calculated frequency can be determined using Equation 5.12. One obtains St=0.012, which is characteristic of the range of Strouhal numbers found experimentally in LFMA after analysis of water surface time-series (in Section 5.2.2.6). The time series of U, V and H simulated by LES are similar to the corresponding temporal variations for the flow case presented by White and Nepf (2007) in Section 2.4.4. For this flow case, a Strouhal number of approximately 0.045 can also be calculated following the same methodology.

The LES modelling suggests good correlation between the velocity field and the water surface fluctuations. These results suggest that simple instrumentation, such as the pressure gauge used in LMFA to record water surface fluctuations, might be suitable to deduce turbulence timescale in presence of vegetation.
The variations of the water depth are approximately comprised between $\pm 7.5\%$ of the mean water depth. On a vegetated floodplain flow which is flooded to a depth of 2 m, this corresponds to variations in water depths of ± 15 cm. Such variations in water surface fluctuations are significant and have consequences for the design of engineering flood defence schemes. For example, this would have to be accounted for in the design of setback embankments on the floodplain, which are currently often one of the preferred options under the "Making Space for Water" policy adopted by the Department for Environment, Food and Rural Affairs (DEFRA, 2004).

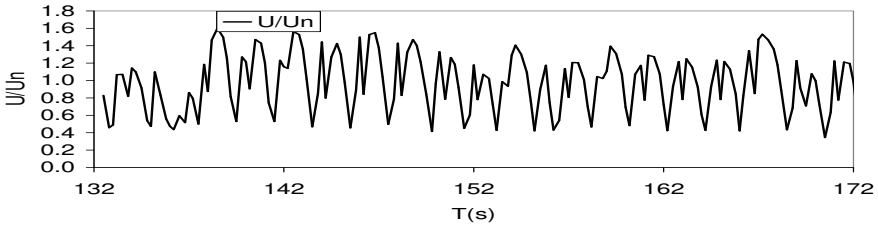

(a)

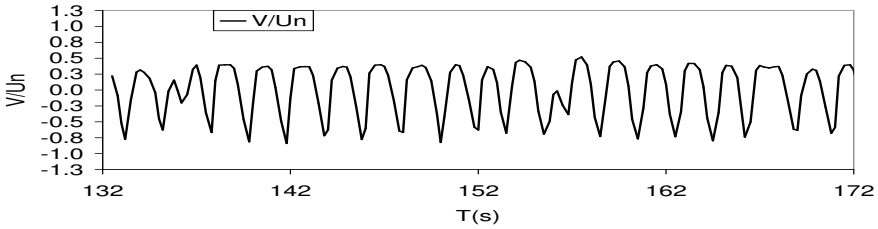

(b)

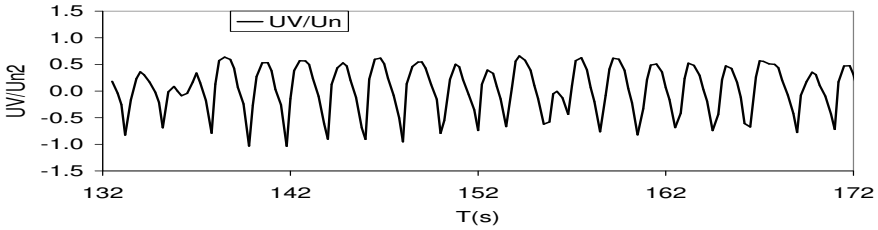

(c)

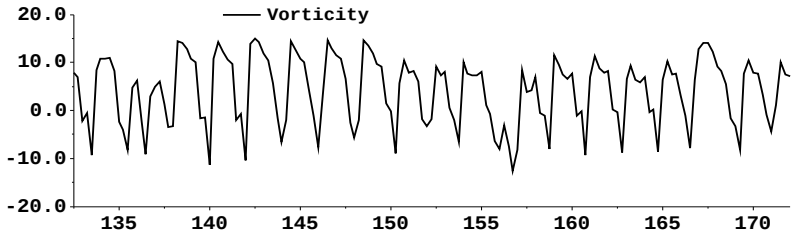

(d)

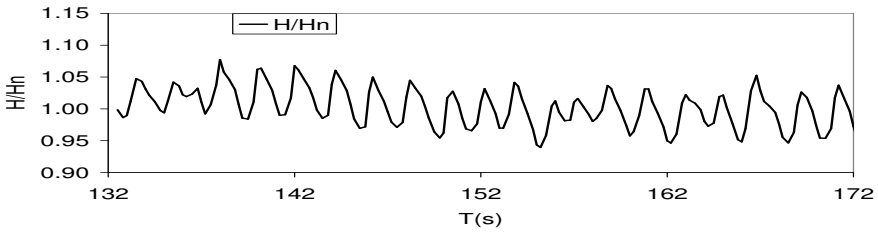

(e)

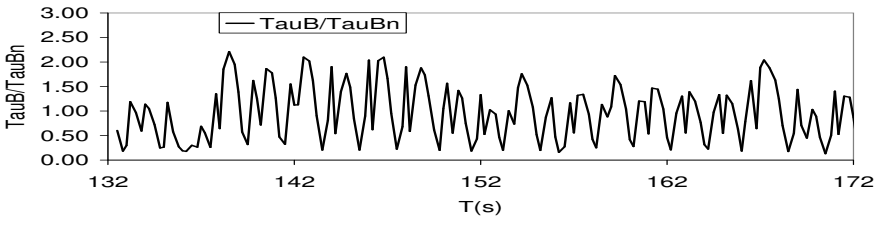

(f)

Figure 7.31: Case 2a Dr=0.25 (a) U/Um (b) V/Um (c) UV/Um2 (d) Vorticity (s-1) (e) Water depth (f) TB/TBm

7.3.5.5 Is Large Eddy Simulation worth the effort?

By definition, Large Eddy Simulations can be expected to perform well for flows in which the dominant processes occur in the resolved large scales. As stated by Pope (2004), the most compelling case for LES can be made for momentum transfer in shear flows at high Reynolds numbers. For these flows, LES provides a suitable model for the cascade of energy described by Kolmogorov, dominantly from the resolved large scale to the statistically isotropic small scales. LES would therefore seem to be a reasonable approach to model the studied flows of one-line of rods along the main channel and indeed, LES modelling appeared to satisfactorily reproduce the flow cases of Series 2Ab studied in Loughborough.

Another strong case for LES lies in the capture of unsteady effects. Numerical results obtained from RANS models such as a $k - \epsilon$ model might be misleading to the engineer as they give a static view of the flow field. Results obtained from LES demonstrate the significance, or not, of large eddies present in the simulated flow field. The modelled fluctuations of the water surface can give useful indications to flood defence engineers in the design of embankments. The correct representation of large eddies also bears consequences in terms of pollutant transport and bank erosion for example.

However, Telemac-2D using LES has a tendency to generate eddies that might appear too regular and neat. Figure 7.32 shows typical time-series of transverse velocities from Telemac-2D LES compared with LS-PIV in the narrow flume of Loughborough for Series 2Ab-51.
The time-series generated by Telemac-2D LES are characteristic of a periodic sinusoidal signal. On the other hand, the results from LS-PIV are much more irregular and probably more representative of the range of coherent structures observed near the vegetated interface.

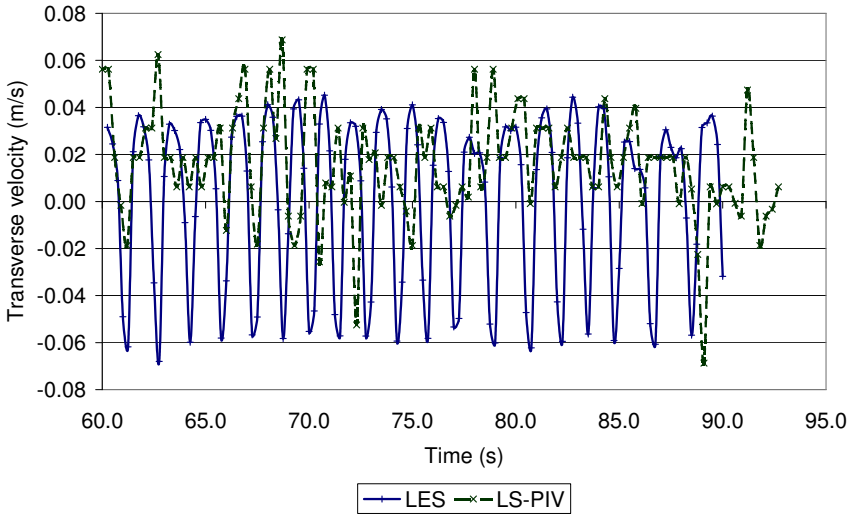

Figure 7.32: Comparison between typical transverse velocity time-series modelled with Telemac-2D LES and derived from LS-PIV for Series 2Ab-51

7.3.6 Application of Telemac-2D to the modelling of the LMFA flow cases

In this section, the influence of the different turbulence models presented in 7.3.3 is assessed against the two experimental flow cases obtained in LMFA for a spacing ratio $\frac{L}{D}$ of 32.0.

7.3.6.1 Note on Large Eddy Simulation for the LMFA flow cases

The Large Eddy Simulation turbulence model did not generate coherent structures in the LMFA flume, despite numerous attempts that include the use of finer mesh, smaller timesteps or longer running time. A test simulation was run with a less steep longitudinal slope of 0.001 instead of 0.0018 for the shallow flow case. This led to the formation of coherent structures beginning to develop in approximately the last 2 meters of the flume, thereby suggesting that the steep slope of the LFMA flume tends to suppress the formation of eddies. Coherent structures require some length to develop and in Telemac-2D that length seems to exceed the physical length of the flume. During

experiments, no eddies could be observed for the deeper cases which is similar to the LES Telemac-2D results. However, eddies where clearly observed for the shallower case during experiments and this could not be reproduced with the LES modelling. A finer mesh than those tested might have been necessary to achieve this. Another solution, not tested in this research, might have been to introduce a hydrograph as upstream boundary condition built as the superposition of a constant inflow and perturbations. Nonetheless, while no coherent structures were generated by LES turbulence model, wavy water surface profiles started to appear from x=5 m for the shallow case, as seen in Figure 7.33, but not for the deeper flow case. This wavy water surface profile was typical in the LES simulations of the flow cases studied in Loughborough, for which coherent structures were simulated.

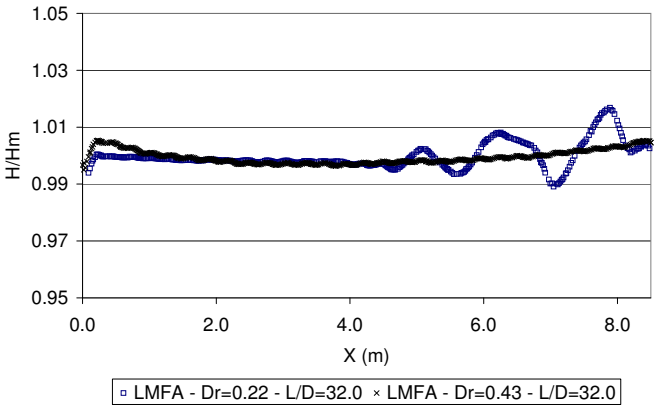

Figure 7.33: Instantaneous simulated water depths with LES along the LMFA channel normalised by the averaged depth for Dr=0.22 and Dr=0.43, $\frac{L}{D} = 32$

7.3.6.2 Influence of turbulence models on the mean parameters

The depth-averaged velocity results for the two simulated LMFA flow cases are given in Figure 7.34. The calibrated values for the different turbulence models parameters were presented in Section 7.3.3.

Once calibrated, all four turbulence models led to relatively similar depth-averaged velocity predictions. They all significantly underestimated velocity in the rod area, while overestimating the velocity in the main channel and the floodplain. The $k-\epsilon$ model performed best in the rod area, with velocity at the interface greater by 25.5% 16.5% and 23.1% than the constant eddy viscosity, Elder and LES models respectively for the shallow case. The constant eddy viscosity model best modelled the velocity in the floodplain while the $k-\epsilon$ best modelled the velocity in the main channel. Conversely, these two turbulence models worst modelled velocity in the other respective sub-section. In absence of rods at the interface, predictions in Telemac-2D tend to overestimate velocity in the floodplain and underestimate it in the main channel (Wilson *et al.*, 2002). However, in presence of rods along the interface, velocity is largely underestimated in the vicinity of the interface and velocity is overestimated in the center of main channel and floodplain.

The bed shear stress results for the LMFA simulations are given in Figures 7.35. They correlate the modelled depth-averaged velocity profiles.

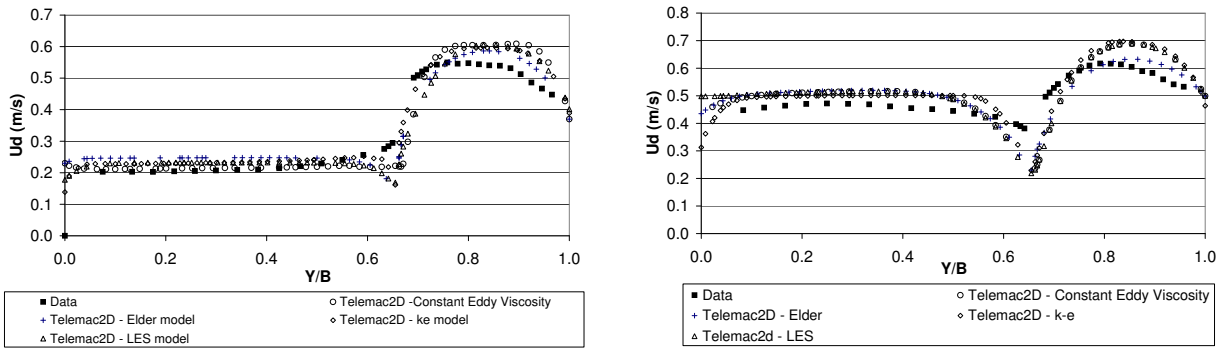

(a) (b)

Figure 7.34: Influence of turbulence modelling on depth-averaged velocity profiles for $\frac{L}{D} = 32$ (a) Dr=0.22 and (b) Dr=0.43

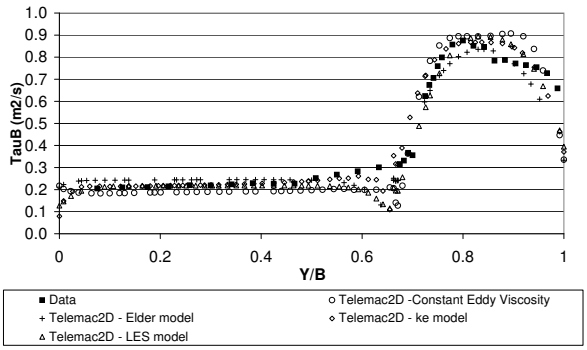

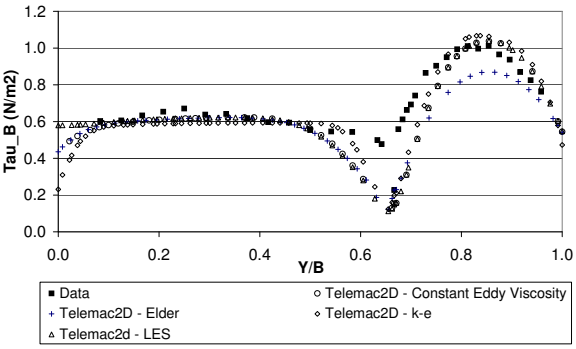

(a) (b)

Figure 7.35: Influence of turbulence modelling on boundary shear stress profiles for $\frac{L}{D} = 32$ (a) Dr=0.22 and (b) Dr=0.43

The difference $\rho g H S_0 - \tau_B$ normalised by $\rho g H S_0$ from the LMFA simulations are given in Figures 7.36. Interestingly, the $k - \epsilon$ turbulence model is the model that best recreated the strongest momentum transfer observed between the main channel and the floodplain in the shallow case. Indeed, the simulated differences $\rho g H S_0 - \tau_B$ only become negative in the floodplain with this turbulence model, thus reproducing well the experimental results. The other turbulence models predict a "drop" in the difference near the interface but this drop is not significant enough to account for the more significant momentum transfer observed experimentally. At the interface, the difference $\rho g H S_0 - \tau_B$ normalised by $\rho g H S_0$ is 14.67% higher than the experimental values for the $k - \epsilon$ model.

The $k - \epsilon$ turbulence model simulated stronger transverse velocity V than all the other models in the vegetated region, with $|V| = O(10^{-2})$m/s, which is one order of magnitude higher than the other turbulence model predictions. This might be an indication of why momentum transfer is better simulated by the $k - \epsilon$ turbulence model. With LES failing to generate coherent structures, the $k - \epsilon$ turbulence model seems to best capture the velocity gradients between the vegetated interface and the sub-sections.

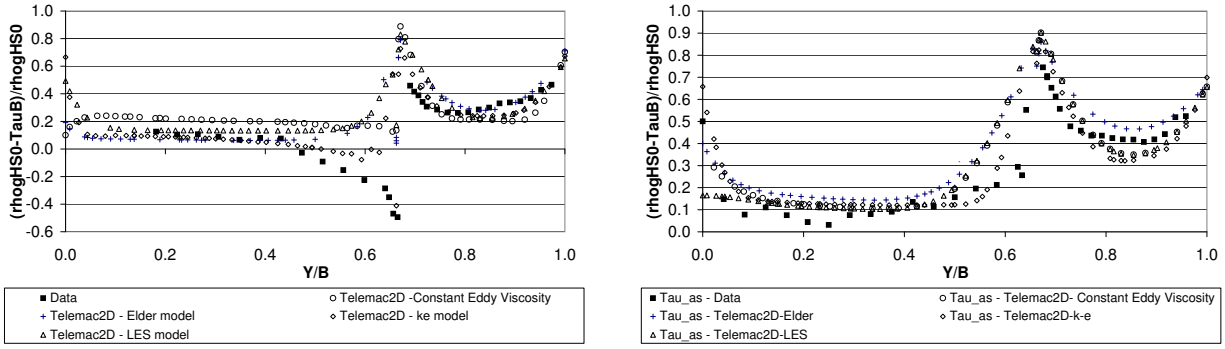

(a) (b)

Figure 7.36: $(\rho g H S_0 - \tau_B)$ normalised by $\rho g H S_0$ for $\frac{L}{D} = 32$ (a) Dr=0.22 and (b) Dr=0.43

The apparent shear stress results for the LMFA simulations are given in Figure 7.37. No significant differences appear in the predictions of apparent shear stress by the four turbulence models for the deeper case. All turbulence models greatly underestimated the apparent shear stress in the main channel while predictions in the floodplain were better. For the shallow case however, apparent shear stress was overestimated across most of the channel, with the $k - \epsilon$ model giving the best predictions.

7.3.6.3 Modelling of the rods: explicit modelling versus drag force modelling

Telemac-2D offers the capability to model the drag of a structure via a subroutine without having to include the structure explicitly in the mesh. This is a significant advantage compared to many other packages that do not offer this option. In large scale river flow modelling, forests for example are commonly modelled in two dimensions by increasing the roughness in order to account for the effects of drag. This is, for example, the approach adopted by the Conveyance Estimation System (McGahey and Samuels, 2003) which is recommended by the Environment Agency on flood modelling projects

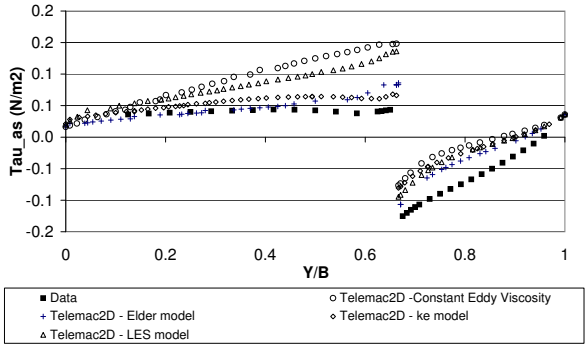

(a)

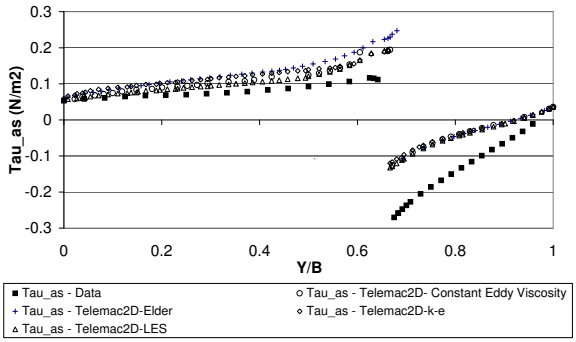

(b)

Figure 7.37: Apparent shear stress for the different turbulence models tested for $\frac{L}{D} = 32$ (a) Dr=0.22 and (b) Dr=0.43

in England and Wales. However, Rameshwaran and Shiono (2007) showed that such practice could be highly detrimental for bed shear stress predictions, especially where roughness is dominated by drag forces. In Telemac-2D, the effect of rods can instead be modelled in the drag force term by using the results of field surveys.
In Telemac-2D, the drag force is modelled as Equation 7.59 so that the term $\frac{F_D}{\rho H}$ is added to the momentum equations.

$$\frac{F_D}{\rho H} = -\frac{N}{A} C_D \frac{D}{2} U_D^2 \tag{7.59}$$

The code therefore requires as input:

- the number of structures (N) per unit of area $(A)\frac{N}{A}$
- the diameters (D) of the structures
- the drag coefficient C_D

A test was performed in the deeper case of LMFA, using the $k-\epsilon$ model. The drag force was applied to the floodplain along the main channel where the rods were located in the experiments. The results of depth-averaged velocity and boundary shear stress lateral distributions are presented in Figure 7.38.

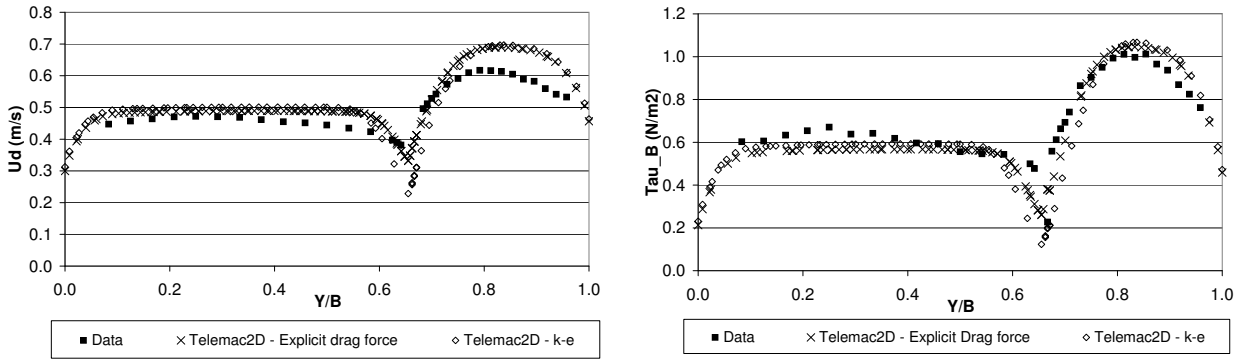

(a) (b)

Figure 7.38: Explicit modelling of drag force applied to the rod area for flow case Dr=0.43 and $\frac{L}{D} = 32$ (a) Depth-averaged velocity and (b) Boundary shear stress

The inflows used in the modelling overestimated the experimental inflows by approximately 5%. The results are sensibly the same as with the explicit modelling of rods in the main channel and in the floodplain. However, in the rod area, the modelling of drag force as a source term added to the momentum equations led to better prediction of velocity and boundary shear stress. Near the rod interface, the modelling of rods as islands underestimated velocity by 27.83% at $\frac{Y}{B} = 0.358$ compared to relative error of 4.93% without rods. The underestimation of velocity in the vegetated area may be caused by numerical diffusion as this area proves to be the most challenging to model numerically.

7.4 Phenomenology of Flows in Straight Compound Channel with an Array of Rods along the Main Channel

The experiments in the narrow trapezoidal flume of Loughborough and in the steep larger rectangular flume of the LMFA laboratory, the analysis of the collected field data, as well as the numerical modelling have highlighted some important features of the flow structure in a straight compound channel with rods on the edge of the floodplain. It is therefore possible to draw out an overall picture of this flow structure,

as illustrated in Figure 7.39.

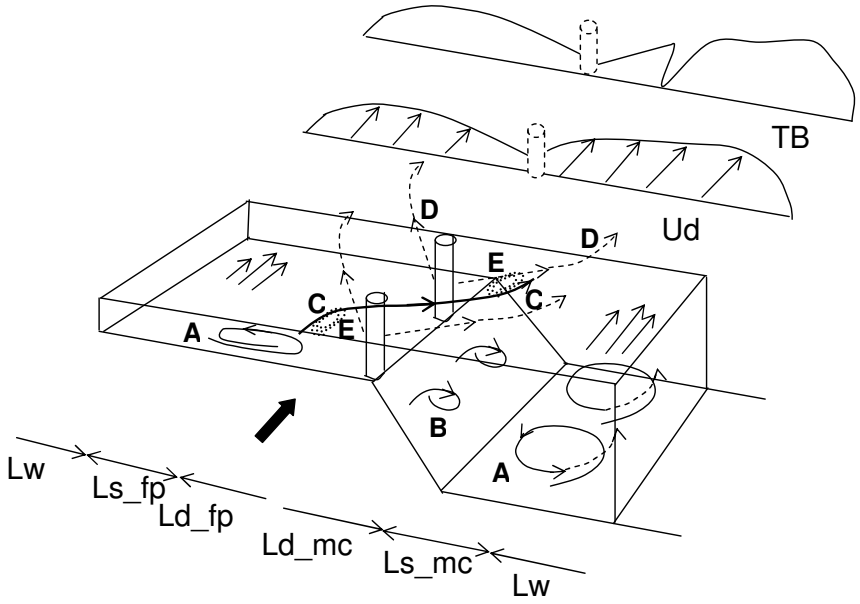

Figure 7.39: Suggested Flow structure in straight compound channel with rods on the edge of floodplain

Five flow mechanisms are represented in Figure 7.39.

1. Secondary circulation from Prandtl's second kind (represented by the letter A) This secondary circulation is observed in straight compound channel without vegetation (Shiono and Knight, 1991). In presence of one-line vegetation along the main channel, such secondary circulation would be observed outside the area of influence of drag force, noted as L_S, typically in channels with large aspect ratios. In the narrow flume of Loughborough such secondary circulation is unlikely to occur. Three dimensional measurements would be needed to confirm the existence of this flow mechanism in presence of vegetation in the LMFA flume.

2. Secondary circulation generated by two-layer flow (represented by the letter B)

   In the main channel, within the length of influence of drag force Ld_{mc}, the action of drag force locally creates a layer on top of the flowing main channel flow.

Secondary currents due to the wakes are strong in this area and entrain the flow in the sublayer to rotate towards the outside walls. Due to the lack of three dimensional measurements and three dimensional numerical modelling, this could not be verified with the collected experimental data. This mechanism contributes to the increased vorticity values observed on the side slope of the field data presented in Chapter 6.

3. Planform coherent structures advected from floodplain to main channel and vice-versa (represented by the letter C)

   This mechanism was observed for all cases in Loughborough experiments and was described in Section 4.4.3. In LMFA, planform coherent structures were observed for the lower relative depth only. At higher relative depths however, the streamlines created by seedings on the water surface did not highlight such interaction between the subsections.

4. Wake action in the main channel and the floodplain (represented by the letter D)

   This is the most obvious flow mechanism, visually evident when observing the deformations of the free surface or applying seedings on the water free surface. The line of rods acts as an array of bluff bodies generating a strong wake action on either side of the interface. The wake action was seen to increase with relative depth, a pattern that was particularly clear in LFMA where the rods with the largest diameter (9 mm) were used. For the deeper cases of LMFA, the effects of wakes were such that no LS-PIV data could be collected near the rods as seeding was pushed towards the sidewalls.

5. Eddying motion (represented by the letter E)

   This mechanism was observed for all cases in Loughborough and was described in Section 4.4.3. In LMFA, such motion was also observed for the shallow case.

The lengths L_w, $L_{d,fp}$ and $L_{d,mc}$ represent the lengths of dominant influence of the

wall shear stress, floodplain drag and main channel drag respectively. The length $L_{s,fp}$ represents the difference between the floodplain width and $L_{d,fp}$, and $L_{s,mc}$ between the main channel width and $L_{d,mc}$. In the case of a narrow channel such as the Loughborough flume, $L_{s,mc}$, and $L_{s,fp}$ are expected to be zero. However, for large aspect ratio such as the LMFA flume, $L_{s,fp}$, and $L_{s,mc}$ represent the area far enough from the wall and the vegetation at the interface to exhibit characteristics of a large straight channel without vegetation.

The phenomenona C, D and E were observed in the experiments and have been described in Chapters 4 and 5. However, secondary circulations illustrated as A and B could not be measured as the studied flows proved too shallow for the instrumentation available (such as ADV) during experiments. Nonetheless, results provided towards the end of this research from an experiment carried out in Kansai University (Shiono *et al.*, 2009) confirmed the presence of secondary circulation in the main channel and in the floodplain in the case of one-line of rods placed along a rectangular main channel. In Kansai, the experiment was carried out with rods of squared sections placed along the interface of the main channel for a relative water depth of 0.48. The aspect ratio of the flume used in Kansai was 5.95, which lies between the aspect ratios of the Loughborough and LMFA flumes. The vector graph is presented in Figure 7.40. One secondary circulation cell extending across the floodplain is clearly visible. In the main channel two secondary cells can also be distinctively observed: one extending across the main channel and one, much smaller, located at the bottom corner near the interface.

From the five flow patterns described above, three different modes can be made out from the set of experiments carried out. These modes are illustrated in Figure 7.41.

They are described in more detailed in the following paragraphs:

1. Limited momentum transfer between the main channel and the floodplain

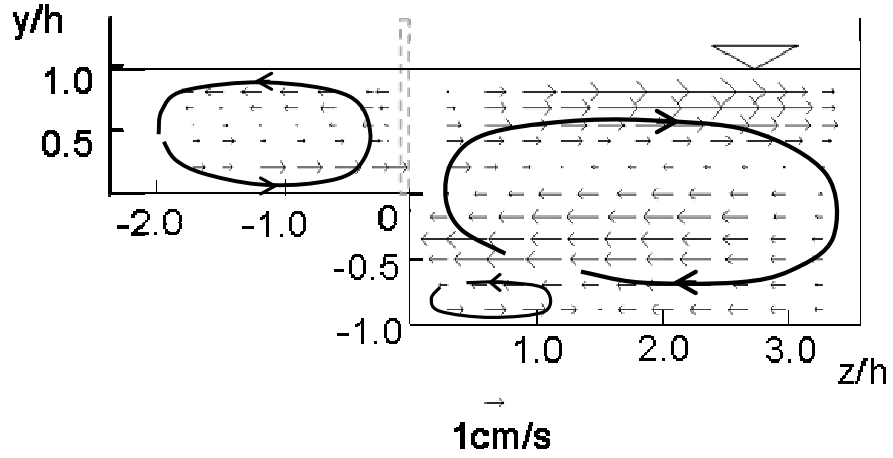

Figure 7.40: Suggested Flow structure in straight compound channel with rods, after Shiono et al. (2009)

This mode is characterised by the absence of coherent structures moving from one sub-section to another, i.e. from the main channel to the floodplain and conversely. The wake action from the rods is dominant and extends well into the main channel and floodplain. The rods act somewhat like a wall between the sub-sections. Eddying motion is not observed on the surface. This mode was observed in the steep slope of the LMFA channel, at the high relative depths of 0.43 and 0.44, and in the case of the brushes in Loughborough. This mode was simulated numerically with Telemac-2D LES, for which no planform vortices moving either side of the line of rods was observed.

2. Significant momentum transfer between the main channel and the floodplain with limited effect of rods

   Opposite to the previous mode, the flow structure of this mode is close to that of a straight compound channel in the absence of vegetation and a unique shear layer is observed. This can happen in cases where the spacing between rods is large for example. Planform vortices along the interface are seen and a shear layer can develop. Strong momentum transfer being the main channel and the floodplain

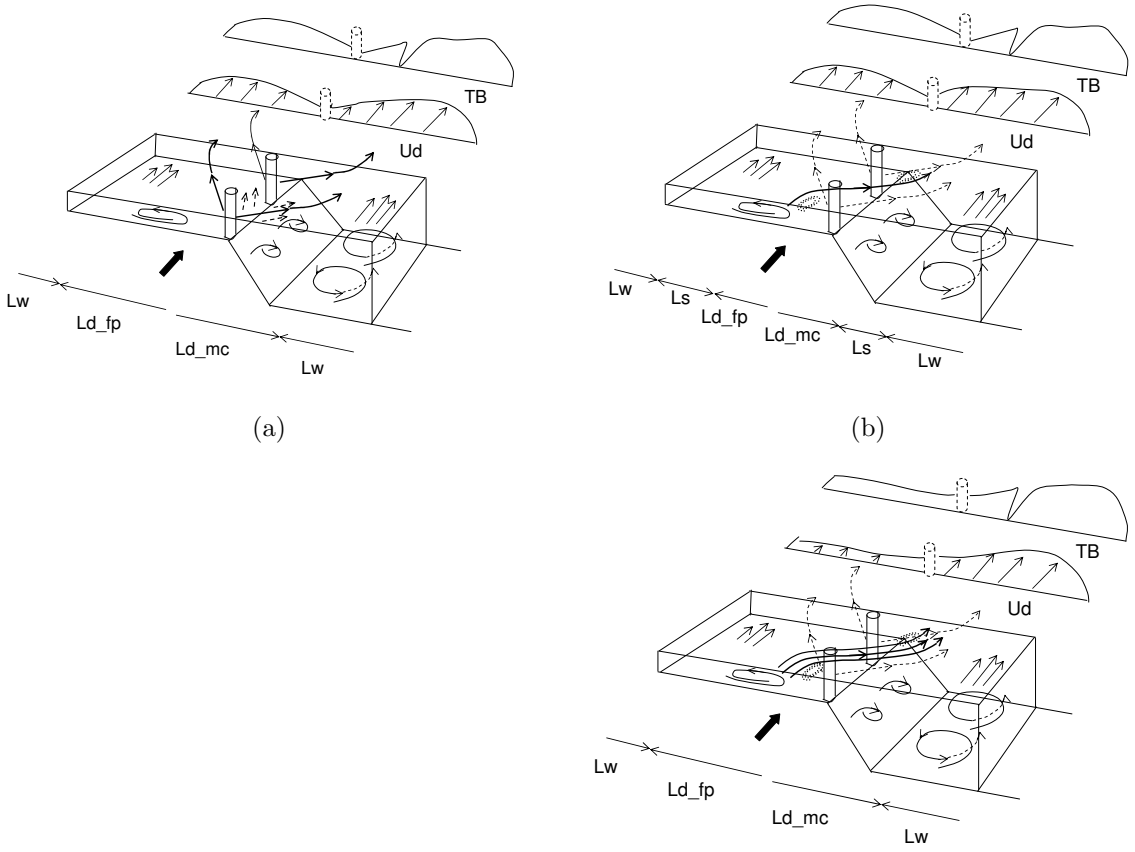

Figure 7.41: Three different modes identified with one-line of rods along the main channel, based on the degree of interaction between the sub-sections (a) Wake dominated mode, (b) Intermediate mode (c) Mode characterised by a more limited impact of rods

takes place. This strong momentum transfer is reflected in the difference $\rho gHS - \tau_B$ changing sign between the main channel and the floodplain, as it becomes negative on the floodplain. However, the magnitude of bed shear stress decreases as drag force also acts as a resistive force. Water surface suppresses w' while u' and v' increase due to the turbulence created by the drag exerted in the x-y plan. The experiment carried out in LMFA for the shallow case of Dr=0.22 illustrates this mode.

3. Intermediate mode with main channel and floodplain interacting through momentum exchange and secondary circulation

Planform vortices are observed moving between the main channel and the floodplain. However, two very distinct shear layers either side of the line of vegetation can be observed. Wake action is clearly visible but coexists with planform vortices. Momentum transfer between the main channel and the floodplain is more limited. The experiments carried out in Loughborough university with the smooth rods fall into that category.

7.5 Conclusions

The physical processes taking place in compound channel flows with one-line of rods at the interface are fully three-dimensional, as demonstrated in Section 7.4. These processes include horizontal planform structures driven by secondary currents and momentum transfer, horizontal eddies, transversal secondary circulation and wakes generated by drag force. It is therefore important to consider that depth-averaged two dimensional numerical models such as the SKM and Telemac-2D are limited and fundamentally imperfect.

A new version of the Shiono and Knight Method was tested by introducing a friction drag coefficient and setting the advection term to zero. Turbulence activity generated by the rods is related to the wakes spreading laterally over the water depth. Hence, the term accounting for turbulence in the SKM, i.e. the transverse shear stress term, was complemented with a turbulence drag term. An Elder formulation was adopted to model this turbulence drag term, and a friction drag coefficient f_d was introduced in the same way as the dimensionless Darcy-Weisbach friction coefficient f was introduced in the original SKM (Shiono and Knight, 1991). This friction drag coefficient can be derived from the experimental dataset. In this research, the evolution of the friction drag was found to be consistent with the evolution of rod diameter, rod density and relative depth.

For discussion, another approach was tested whereby the advection term was retained as a calibration parameter, in a similar way to Rameshwaran and Shiono (2007). A

local friction drag was introduced in the rod area. The advection term was seen to increase with rod density for smooth rods. Also, a larger magnitude of the advection term was required, both in the main channel and in the floodplain, when brushes were used compared to smooth cylinders at the same rod density. The advection term increases more significantly in the flow cases with brushes, compared to cases with smooth cylinders, when the rod density decreases. The advection term is sometimes referred to as the secondary flow term in literature (Knight *et al.*, 2007), and its variations can be related to secondary current activity to some extent. In the standard version of the SKM, an increase in secondary current magnitude due to a greater vegetation density would be reflected by an increase in the magnitude of advection term Γ.

Although the experimental data set was best reproduced through the calibration with the advection term, the proposed SKM is favored as it can be more closely related to the experimental data and to physical processes.

The numerical modelling of flows was also simulated in Telemac-2D. Sensitivity tests showed that attention needed to be paid to the mesh density in the vicinity of the rods. The tested coarse mesh underestimated results in this area by up to 45.1% while results in the main channel and floodplain remained similar to those obtained with denser mesh.

The SUPG advection scheme was seen to perform better in the rod region as it led to less underestimation for the flow velocity compared to the MOC scheme. Mass balance was only marginally improved with the SUPG scheme, the MOC scheme offering a similar performance. Non-slip conditions were inadequate to simulate the near wall flow conditions as they force the velocity to "dive" near the wall. Slip boundary conditions improved the results but the best results were obtained by imposing wall velocity directly on the wall boundaries through the logarithmic-overlap layer law (White, 1999).

LES simulations were performed for the three Loughborough flows of Series 2Ab. The results proved to be satisfactory for all cases although the predictions were seen to improve when relative depth increases. The unsteady flow patterns generated by Telemac-

2D LES turbulence model exhibited realistic time and length scales although these appeared somewhat too neat and regular. This tendency to generate rather idealised periodic flow structures is particularly evident when comparing LS-PIV and Telemac-2D time series of the lateral velocity near the rod interface. The characteristic time period of large structures was 0.50 Hz for Series 2Ab-25.

The four turbulence models available in Telemac-2D, namely the constant eddy viscosity, Elder, $k-\epsilon$ and the LES models, were compared for two LMFA flow cases. Once each model was calibrated, the comparison of the computed mean flow parameters did not highlight significant discrepancies although the results obtained with the $k-\epsilon$ turbulence model were better in the rod area. The $k-\epsilon$ model simulated higher secondary currents values in the rod region compared to the other turbulence models. For LMFA flow cases, the LES model did not generate fully developed coherent structures. The comparison of the overall water surface profiles suggests that the generation process of coherent structures is initiated in the shallow case but not in the deeper case. This is in agreement with the experimental flow visualisation carried out with seedings for the deeper case. However, the planform coherent structures observed experimentally in the shallow case could not be reproduced with the Telemac-2D LES model.

The typology of the flow field influenced by the presence of rods on the edge of the floodplain can be more closely defined. Three modes can be observed, related to the influence of the drag effects on the flow structure. Each of these modes is dominated by different flow patterns, from the wake dominated patterns observed in the deeper case of the LMFA, to the limited impact exerted by rods in the shallow LMFA flow case where the compound channel approaches a no rod case. More research is necessary to define the boundaries characterising these three modes of interaction between the main channel and the floodplain.

CHAPTER 8

Conclusion and Future Research Prospects

This Chapter draws conclusions about the research objectives. Section 8.1 summarises the important observations and new findings from this research while Section 8.2 recommends future research prospects.

8.1 Conclusions

This thesis dealt with flows in straight compound channel with rods placed on the edge of the floodplain. This configuration was investigated by conducted appropriate experiments in Loughborough University Frank Gibbs and LMFA laboratories, with field studies in the Rhône and Derwent rivers, and by numerical modelling.

8.1.1 Experimental investigations

A Pitot tube, a micro-propeller and a Preston tube were used to measure the mean velocity and the boundary shear stress in the trapezoidal compound channel of Loughborough University and in the rectangular compound channel of LMFA. In Loughborough, 12 flow cases were considered by placing one line of smooth 3 mm and 6 mm diameter rods on the edge of floodplain and further 6 flow cases were investigated with brushes.

In LMFA, three flow cases were investigated with 9 mm diameter smooth wooden rods.

In the narrow flume of Loughborough, the impact of both smooth rods and brushes on the velocity and boundary shear stress distributions proved to be significant. Both depth-averaged velocity and boundary shear stress were reduced, particularly in the rod area. In the smooth rod cases, the maximum velocity in both the main channel and floodplain moved away from the interface as rod density, rod diameter and relative water depth were increased. In LMFA, similar results were obtained for the two deeper flow cases modelled. For the shallow and less dense LFMA flow case, the lateral distribution of depth-averaged velocity approached that of the no rod case.

In Loughborough, the influence of rod diameter, spacing and relative depths were investigated and it emerged that relative depth was the most influential parameter on the configurations tested. This is because drag force and the effects of wakes and of Prandtl's second kind's secondary currents due to the presence of rods increase significantly with relative depth. The magnitude of turbulence intensity in the lateral direction also increases as a result, but the turbulence intensity in the vertical direction remains similar due to the free surface. Consequently, the overall turbulence anisotropy is enhanced. Secondary currents are, therefore, strengthened at higher relative depths regardless of rod density.

Nevertheless, both rod diameter and spacing need to be taken into account in planning riparian vegetation as both are shown in this study to have a significant impact on boundary shear stress. A decrease in diameter from 6 mm to 3 mm had more impact on the measured boundary shear stress than an increase in the spacing ratio from 8.0 to 16.0. When rod diameter was doubled, boundary shear stress was 17.3% greater on average compared to 13.2% when the spacing ratio was halved.
The addition of foliage, modelled using brushes, led to some counter intuitive results and changed some of the flow behaviour from that observed in smooth rods. In partic-

ular, an increase in brush density resulted in increased flow rates for the same relative water depth. This result suggests that simply increasing the vegetative density on the edge of floodplain on the assumption that this will systematically lead to increased flow capacity is not valid.

The distribution of apparent shear force remained linear in both the floodplain and the main channel. This pattern was observed both in Loughborough and LMFA flumes. The amplitude of apparent shear stress was seen to increase with relative depth. The flow cases with brushes (Series 2B) exhibited the highest amplitude of apparent shear stress, due to the increase in drag and turbulent activity generated by foliage.

Drag force values derived from the force balance method varied approximately linearly with relative depth for all configurations. These values differed from those calculated with the analytical formulae $\left(F_D = \frac{1}{2}\frac{\rho C_D S_f A_P H U_{d,p}^2}{\frac{L}{D}}\right)$. The best results were obtained with the analytical formulae for the flow cases using 3 mm diameter rods and a spacing ratio $\frac{L}{D} = 8.0$ (Series 2Aa), with an average relative difference between the two methods of 13.8%. The worst fits were obtained for the flow cases using the 6 mm diameter rods (Series 1). In LMFA, the analytical formulae also produced different results compared to force balance at the higher relative water depths, overestimating the drag force by 25.6% and 51.2% for the spacing ratio of $\frac{L}{D}$=16 and 32 respectively. The best fit was obtained for the shallow relative water depth of 0.25 (22.6%). The discrepancy between the drag force values obtained by force balance and the analytical formulae are largely attributed to misrepresentative bulk drag coefficients that do not adequately account for shading effects. Caution is therefore required when applying the analytical formulae to derive the values of drag force in such arrangements.

For all Loughborough flow cases, the visualization of the free surface flow revealed a complex flow structure made up of three dominant patterns. Wake action in the trail of the rods, visible through light reflection, was more pronounced at higher relative

depths. Planform coherent structures were advected from the main channel to the floodplain and vice-versa while eddies in the vicinity of rods were also observed by sieving seeding on the water free surface.
In LMFA, planform vortices were discovered moving from one sub-section to another for the shallow case. However, these planform vortices were not observed for the deeper cases, where the wakes generated by the rods were the dominant flow characteristic.Comparison of the differences between $\rho g H S_0 - \tau_B$ for the three LMFA cases revealed significant discrepancies correlating the flow visualization. $\rho g H S_0 - \tau_B$ remained positive across the section for the deeper cases while this difference changed sign between the main channel and the floodplain for the shallow flow case. Hence, these results confirm that momentum transfer between the floodplain and the main channel is dependent upon the density of rods and the relative water depth.

8.1.2 Field data investigations

ADCP measurements were carried out in the river Rhône in April 2006 for two over-banks flows and ADP measurements were also carried out in June 2007 in the river Derwent for one over-bank flow. The measurements took place in areas where the river channels could be approximated to straight compound channels with vegetated floodplain.

The depth-averaged velocity was calculated and the bed shear stress was determined in the centre parts of the main channel using the logarithmic law of the wall. The cross-section averaged bed shear stress values derived from the log-law were generally found to be in close agreement with the theoretical cross-section averaged values, the difference between both values lying below or around 5%. The lateral variations of the bed shear stress proved to be significant, ranging from 0.7 to 1.4 times the mean bed shear stress.

Secondary currents were found to be of higher magnitudes when compared to typical

values corresponding to uniform flows in straight compound channels, varying between 7% and 12% with local maxima rising to 25%-35%. The highest secondary current values and the highest vorticity values were located on the side slopes, which is where the effects of floodplain vegetation on the edge of floodpain would be expected to generate the strongest anisotropic turbulence.

8.1.3 Numerical modelling

8.1.3.1 Quasi two dimensional modelling with the Shiono and Knight Method

The SKM was extended to model the effects of flow resistance in the compound channel. As turbulence activity is related to the wakes spreading laterally over the water depth, the term accounting for turbulence in the model, i.e. the transverse shear stress term was complemented with the addition of a turbulence drag term. An Elder formulation was introduced for this turbulence drag term, and a friction drag coefficient f_d was introduced in a similar way to that in which the dimensionless friction coefficient f was introduced in the original SKM (Shiono and Knight, 1991). The advection term was set to zero as the recommendation of van Prooijen *et al.* (2005) was adopted. This proposed SKM version was tested on the 18 flow cases measured during this research in Loughborough, the 6 cases presented in Sun and Shiono (2009) and the 3 flow cases measured in LMFA. A correlation of 98% was found between the values of the friction drag coefficients derived through experiments and the calibrated values used in the SKM. The evolution of the friction drag was found to be consistent with the evolutions of rod diameter, rod density and relative depth.

For discussion, a second version of the SKM was tested by retaining the advection term as a calibration parameter, in a similar way to the method proposed in Rameshwaran and Shiono (2007). A local friction drag coefficient $f_{d,rod}$ was introduced in the rod area. The advection term was seen to increase with rod density for smooth rods. Furthermore, a larger magnitude of the advection term was required to calibrate the model, both in the main channel and in the floodplain, when brushes were used compared to

smooth cylinders at the same rod density. From a qualitative view, the assumed link between the advection term and secondary currents seemed well established. It also appeared clear that the advection term was related to drag force.

Flow rates derived from both methods were satisfactory. The experimental data set was best reproduced through the calibration with the advection term, i.e. with the second version of the SKM. Nevertheless, the proposed SKM, which assumes the advection term to be negligible, is favored for the present study as it can be more closely related to the experimental data and to physical processes. The advection term remains to be solved by experimental investigations.

8.1.3.2 Telemac-2D numerical modelling

Modelling results in the region of the rods were significantly affected by the mesh resolution, and to a lesser extent by the choice of advection scheme. Non-slip conditions were inadequate in simulating the near wall flow conditions as they constrain the velocity to "dive" near the wall. While slip boundary conditions improved the results, the best predictions of mean parameters were obtained by imposing wall velocities directly on the wall boundaries through a law of the wall.

The Large Eddy Simulations performed for the three Loughborough flow cases of Series 2Ab yielded satisfactory results for all cases. The predictions were seen to improve when relative depth was increased. The relative difference in depth-averaged velocity in the main channel varied from 9.53% to 2.25% for Dr=0.25 to Dr=0.51 respectively while it varied from 18.22% to 3.05% in the floodplain.

The time series of streamwise and transverse velocities U, V, and water depth H generated with the LES turbulence model revealed near periodic fluctuations. The amplitudes of oscillations were significant relative to the mean. The depth-averaged velocity varied within $\pm 55\%$ of its mean value U_{mean} for the shallow flow case of Dr=0.25.

These results have some similarities with the time series presented in White and Nepf (2007). The Telemac-2D time series generated by LES might have a tendency to generate rather idealised periodic flow structures. This is particularly evident when comparing the modelling results with LS-PIV time series of lateral velocity near the rod interface. Nevertheless, these unsteady flow patterns generated by the Telemac-2D LES turbulence model exhibited realistic time and length scales for the modelled coherent structures.

The four turbulence models available in Telemac-2D, namely the constant eddy viscosity, Elder, $k-\epsilon$ and the LES models, were compared for two LMFA flow cases with spacing ratio of 32. In the rod area, the best results were obtained with the $k-\epsilon$ turbulence model. All models significantly underestimated velocity in the vicinity of the rods. The $k-\epsilon$ model simulated higher secondary currents values in the rod region compared to the other turbulence models.

8.1.4 Overall flow characteristics of one line of emergent rods on the edge of a floodplain

The physical processes taking place in compound channel flows with one-line of rods on the edge of a floodplain are fully three-dimensional and complex. Nevertheless, a typology of the flow field influenced by the presence of rods on the edge of floodplain can be more closely defined following these investigations. Five flow patterns were identified during this research. Three of them were directly observed, namely eddying motion, wake action in the main channel and floodplain, and planform coherent structures advected from floodplain to main channel and vice-versa. Two more were suspected, these being secondary circulation in the transverse plan and the secondary circulation from Prandtl's second kind.

Although not measured in this study, secondary circulation in the transverse plane and induced by the rods was measured in Kansai University in a similar context. Despite

the use of square rods in Kansai University, the comparable spacing ratio, rod Reynolds number and compound channel's aspect ratio used in that study suggest that such secondary circulation, suspected in the investigated flow cases, should take place.

Three flow modes were observed, related to the influence of the drag effects on the flow structure. Each of these modes is dominated by different flow patterns, from the wake dominated patterns observed in the deeper case of the LMFA, to the limited impact exerted by rods in the shallow LMFA flow case, where the compound channel flow characteristics approach those of a no rod case.

8.2 Future Research Prospects

It is felt that the flow structure caused by one line of emergent rods in straight compound channels is now better understood. The combination of experimental, field and numerical investigations to explore this configuration confirms how such a synergy can help the researcher in fluvial hydraulics. Nevertheless this research has highlighted a number of areas that require further assessment and additional scientific research. Such topics are summarised below as recommendations for future research prospects.

1. Direct drag force measurements and turbulence measurements would ensure that all the components of force balance equation and of the SKM are known quantities. Drag force needs to be measured on a single rod and then on the downstream rod of aligned emergent rods for various relative depths. Such measurements would help to understand how transverse shear in compound channels affects drag coefficient. Similarly, turbulence should be measured through sophisticated non-intrusive technology such as PIV in order to provide a better picture of the turbulence generated by the emergent rods in the compound channel.

2. More confrontation with field data is necessary to allow for comparison with laboratory data. Robust field data will become more and more available with further technological advances in instrumentation. This will provide more insight into

the impacts of riparian emergent vegetation on secondary currents and vorticity.

3. The unsteady flow patterns generated by the LES turbulence model of Telemac-2D need to be further tested against direct turbulence measurements. In particular, a thorough comparison of time and length scales of vorticies would be useful in assessing the relevance of the LES turbulence model of Telemac in two dimensions. The model would then have applications in water quality modelling for example, in assessing the risks of main channel pollution spreading to the floodplain. Similarly, the role of such vortical structures in the transport of sediment could be numerically assessed.

4. The proposed quasi two dimensional SKM model requires further assessment against more diverse vegetative conditions. In particular, the effects of the drag friction coefficient f_d requires more testing. Such research is currently under way at Loughborough University.

5. The range of straight compound channels studied in this work needs to be broadened. Many parameters which could be the determinants for the flow structure, such as the channel aspect ratio, the wall roughness, the main channel side slope, require further investigation. A research programme exploring these parameters would give a more comprehensive understanding of the flow mechanisms highlighted in this study. There is also scope to extend the current research and modelling work to non prismatic geometry. Experiments on the effects of one line of rods placed on the edge of a converging floodplain are under way at Loughborough University.

APPENDIX A

Establishment of Uniform Flow Conditions in Straight Compound Channels

A.1 Introduction

There has been recently increasing concern about the uniformity of flow at measuring sections in straight compound channel experiments (Terrier *et al.*, 2008a). Experiments have usually been carried out with the same total head at the inlet of the main channel and floodplain and as a result the velocities entering into the main channel and onto the floodplain are also the same. As flow enters onto the floodplain, the floodplain discharge exceeds the discharge for a uniform flow condition, hence mass transfer towards the main channel progressively occurs along the flume until flow becomes uniform for both main channel and floodplain.

This appendix investigates the influence of inlet conditions, relative depth, floodplain width and one-line vegetation on the length required for a uniform flow distribution to be achieved in compound channel flumes.

The quasi one-dimensional model the Independent Sub-Sections Method (ISM), the two-dimensional model Telemac-2D and a three-dimensional numerical model have been used to simulate experiments conducted at LMFA (France) and at UCL (Belgium) dealing with the impact of relative depth on that issue. The ISM and the three-dimensional code have been subsequently used to investigate more upstream conditions and floodplain width configurations at the LMFA. The impact of one-line vegetation on flow development is also discussed as this is central to this thesis.

Section A.2 formulates the issue of flow development while Section A.3 lays out the methodology adopted. The results are presented and discussed in Section A.4.

A.2 Formulation of the Problem

A.2.1 Definition of uniform flow

In free-surface flow, the component of the weight of water in the downstream direction causes acceleration of flow (if the bottom slope is positive), whereas the shear stress at the channel bottom and sides generates resistance to flow. Depending upon the relative magnitude of these accelerating and decelerating forces, the flow may accelerate or decelerate. If the channel is long and prismatic, then the flow accelerates or decelerates for a distance until the accelerating and resistive forces are equal. From that point on, the flow depth and velocity remain constant and the flow is called uniform.

In practice, uniform flow is set up in laboratory flumes by:

1. Adjusting the flow depth so that it remains constant in the vicinity of the measuring section. This is verified by measuring the flow at different cross-sections;
2. Ensuring that the mean velocity, measured for a sufficient time remains constant near the measuring section. This is achieved by comparing the isovels at different cross-sections.

The distance L_u for mass transfer to decay and the flow distribution along the channel to remain stable can be significant. Experiments on straight compound channels carried out by Bousmar *et al.* (2005) and Proust (2005) highlight that in some cases a length longer than the physical length of the flumes used in experiments might be required to equilibrate the discharge distribution between main-channel and floodplain subsections. While it has previously been known that a distance is required for the boundary-layer development (Schlichting and Gersten, 1968), discussions on this topic have been limited in the literature. Schlichting suggested a criteria of 100 times the flow depth to be used for boundary-layer development. This criteria was determined for flow over a rectangular plate. For compound channels, a criteria of 150 times H can be found in literature (Tominaga and Nezu, 1991). This criteria assumes that the flow distribution remains constant and that turbulence has developed.

A.2.2 The significance of verifying uniform flow conditions: a practical case study

One might wonder how stringent one shall be when ensuring uniform flow conditions have been achieved during an experiment. Measuring flow depth with accuracy in a large flume with a point-gauge might prove difficult if the water surface is particularly wavy.

In two-dimensional flow, the Reynolds equations, derived from the Navier-Stokes equations are:

$$U\frac{\partial U}{\partial x} + W\frac{\partial U}{\partial z} = g\sin\alpha - \frac{\partial}{\partial x}\left(\frac{P}{\rho}\right) + \frac{\partial(-u^2)}{\partial x} + \frac{\partial(-uw)}{\partial z} + \nu\nabla^2 U \tag{A.1}$$

$$U\frac{\partial W}{\partial x} + W\frac{\partial W}{\partial z} = -g\cos\alpha - \frac{\partial}{\partial z}\left(\frac{P}{\rho}\right) + \frac{\partial(-uw)}{\partial x} + \frac{\partial(-w^2)}{\partial z} + \nu\nabla^2 U \tag{A.2}$$

where P is the mean pressure, α is the angle of the channel slope to horizontal. In uniform flow conditions, W=0 and the partial derivatives according to x are zero. By depth integrating A.2 and combining the result with Equation A.1, one obtains (Nezu and Nakagawa, 1993):

$$\tau_B = \rho g h \sin\alpha - \rho g h \cos\alpha \frac{dh}{dx} \tag{A.3}$$

The first term on the right hand side of Equation A.3 is the two dimensional value of bed shear stress for uniform flow conditions. The term $\left(\sin\alpha - \cos\alpha \frac{dh}{dx}\right)$, appearing on the right hand side, is the energy gradient.

Let us consider a flow depth of 0.064 m and 0.013 m in the main channel and in the floodplain respectively. Assuming a longitudinal slope of 1 in 1000 and a variation in depth of -0.0005 m within 1 m, one obtains $\rho g h \cos\alpha \frac{dh}{dx} = 0.3136 N/m^2$ and $0.0637 N/m^2$ for the main channel and floodplain respectively. The corresponding two-dimensional values of the bed shear stress are $0.6278 N/m^2$ and $0.1275 N/m^2$. In other words, the boundary shear stress is decreased by 50% compared to its uniform flow value.

The contribution of decreasing or increasing flow depth term to the two-dimensional value of bed shear stress are independent of the flow depth, but depend on the bed longitudinal slope and the longitudinal variations of flow depth.

To put the above results into perspective, it should be noted that a water gradient that is different from that of a bed slope will normally be clearly apparent in the measurements. The waviness of the free surface is more likely to lead to local inaccuracies while the overall flume gradient should remain correct. Nonetheless, this simplistic approach illustrates the importance of setting up a constant flow depth with the maximum possible accuracy.

A.2.3 The importance of inlet conditions in compound channel flumes

A unique tank is commonly used for the upstream inlet of the main channel and floodplains in experimental flumes. Therefore, experiments on flow in compound channels

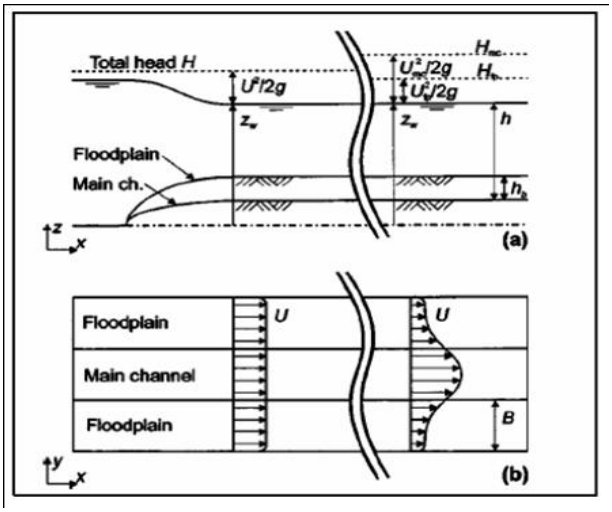

Figure A.1: Water surface, head and velocity profiles in a compound channel flume with classical inlet, near inlet and at distance d/s: a) side view b) plan view (after Bousmar *et al.*, 2005)

have usually been carried out with the same total head at the inlet of the main channel and floodplain. As the water level z_w across the section is almost constant, the kinetic head $\frac{U^2}{2g}$ and the velocities entering into the main channel and onto the floodplain are also the same (A.1) or, in practice, almost identical. As flow enters onto the floodplain, the floodplain discharge exceeds the discharge for a uniform flow condition, hence mass transfer towards the main channel progressively occurs along the flume until flow becomes uniform for both main channel and floodplain (Bousmar *et al.*, 2005). Mass transfer can be observed until the downstream end of the channel if the channel is not long enough.

Evidence that uniform flow conditions are not always actually achieved is provided in Figure A.2 where the evolution of the depth-averaged velocity is given at different locations along the flume for a relative depth of 0.2 in the flume located in the Companie National du Rhône laboratory. This Figure provides a typical example of flow development in a straight compound channel with a unique upstream tank. The upstream floodplain velocity, which exceeds the velocity corresponding to uniform flow conditions, exhibit a clear deceleration along the flume. On the other hand, the main

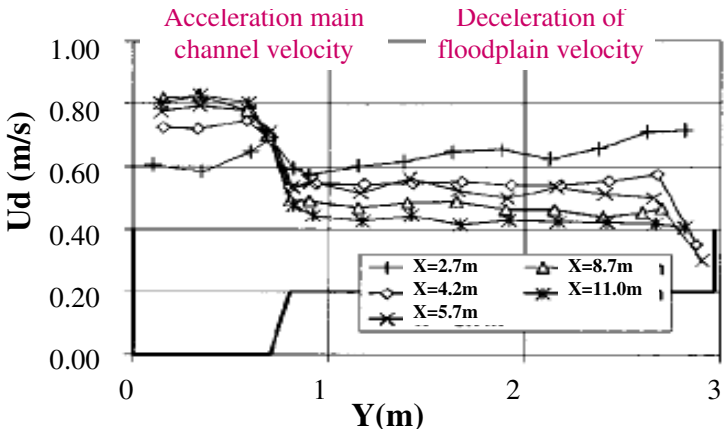

Figure A.2: CNR flume, discharge Q=150 L/ s: transverse distribution of the floodplain depth-averaged velocity U_d at given stations x (after Proust, 2005)

channel velocity is gradually increasing until a uniform flow distribution is achieved. For some configurations and relative depths, experiments carried out with a unique inlet tank have shown that the physical length of the flume can exceed the length required for uniform flow conditions to be achieved (Proust, 2005).

One solution to that issue, suggested by Bousmar *et al.* (2005), is to use separate inlets for both the floodplain and the main channel as shown in Figure A.3. With the help of this device and with different flowmeters fitted to each subsection, a flow distribution close to the uniform flow condition can be chosen.

A number of parameters can influence the length required for a uniform flow distribution to be achieved. Among them are the roughness of the flume, the relative depth, the floodplain width, the inlet and outlet conditions. In this study, the relative depth, the inlet conditions, the floodplain width and the impact of one-line vegetation are investigated.

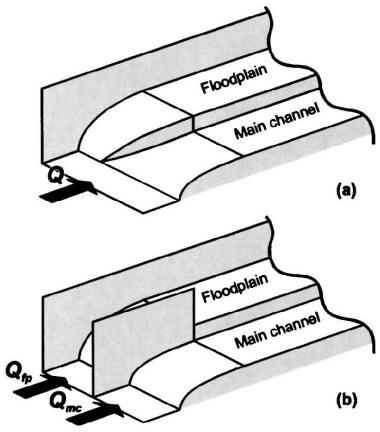

Figure A.3: Compound-channel flume inlet: a: Classical inlet common for main channel and floodplain, with curved transition zone; and b: separate inlets (after Bousmar *et al.*, 2005)

A.3 Methodology: Experimental and Numerical Modelling Investigations

A.3.1 Overview

The methodology adopted to investigate this issue is the described below.

The experiments performed in straight compound channel at the Laboratory of Acoustic and Fluid Mechanics (LMFA, France) and presented in Bousmar *et al.* (2005) were modelled numerically. The experiments carried out at the Catholic University of Louvain (UCL, in Belgium) were also included in the analysis for validation purposes. These experiments aimed at investigating the influence of relative depth and inlet conditions on the length necessary to achieve a uniform flow distribution. The quasi one-dimensional model Independent Sub-Sections Method (ISM) (Proust *et al.*, 2006), the two-dimensional commercial software Telemac-2D (Hervouet, 2003) and a three-dimensional numerical model (Vyas, 2007) have been used to simulate the experiments. The first objective of the numerical modelling was therefore to obtain base

Table A.1: Main characteristics of the UCL and LFMA FLumes

Flume	*LMFA*	*UCL*
Type	Asymmetrical	Symmetrical
Length (m)	8.0	10.0
Total width (m)	1.2	1.2
Slope	0.0018	0.00099
Floodplain width (m)	0.8	0.4
Bankfull depth (m)	0.051	0.050
Roughness	Smooth	Smooth

models calibrated by the experimental results and to investigate numerically the impact of relative depths and inlet conditions. The second objective was to use the existing models to investigate the impact of floodplain width on flow development. Finally, the impact of one-line vegetation on flow development is succinctly illustrated through the use of experimental data.

A.3.1.1 Experimental data

The characteristics of the flumes used for the experiments are presented in table (A.1). The LMFA flume has a length of 7.95 m, a total width of 1.2 m and a height of 0.4 m. The simulated experiments were conducted with a floodplain width of 0.8 m and a main channel width of 0.4 m. The slope was 1.8 $10^{-3} m/m$. The Manning's n roughness was $0.0091 m^{-\frac{1}{3}} s$ in the main channel and varied between $0.0089 m^{-\frac{1}{3}} s$ and $0.0096 m^{-\frac{1}{3}} s$ in the floodplain.

Experiments in UCL were staged in order to analyse the evolution of flow distribution over a longer distance than the physical flume length. This was achieved by using variable opening screens that enabled upstream control of each subsection supply. The first experiment was carried out without controlling flow at the inlet. Flow distribution was measured at the outlet. This was subsequently set at the inlet by upstream flow control, so that the experiment could be carried over one more flume length. This

Table A.2: Flow conditions investigated at LMFA flume

Total Flow (L/s)	Percentage increase in u/s floodplain flow (%)	Water Depth (m)	Relative Depth
17.3	56	62	0.09
24.7	53	72	0.18
24.7	38	72	0.18
36.3	32	85	0.27

Table A.3: Flow conditions investigated at UCL flume

Total Flow (L/s)	Percentage increase in u/s floodplain flow (%)	Water Depth (m)	Relative Depth
10.0	67	61.1	0.18
14.0	48	68.6	0.29
24.0	32	85.3	0.40

process was repeated until a uniform flow distribution could be achieved.

In LMFA, separate inlets were used so that the upstream floodplain and main channel flows could be supplied separately at the inlet of the flume. In order to investigate the impact of an unbalanced upstream flow distribution, the upstream floodplain flow was increased compared to its uniform flow value for a given total flow.

The flow conditions investigated in LMFA and UCL are presented in Tables (A.2 and A.3) respectively.

Telemac-2D was used for the simulation of the experiments in UCL while the ISM and the three-dimensional model were used to simulate all the experiments presented in Table (A.3). Uniform flow was considered as achieved when the relative difference between the computed flow distribution and the experimental uniform flow distribution presented discrepancies lower than 1%. A brief description of the different configurations of numerical models used in this study is presented below.

A.3.1.2 Numerical modelling

The decision to use three different types of numerical models was made in order to allow comparison of the results.

The Independent Subsections Method

The Independent Subsections Method (ISM), solves a system of ordinary differential equations (ODE) composed of three momentum equations and one equation of mass conservation. This system of ODE calculates the water level and the mean velocity in the main channel and on the floodplain. The ISM explicitly models the shear stress at the interface and the momentum exchange. A full description of the ISM is provided in Proust (2005).

Telemac-2D

The hydraulic model applied in this study was Telemac-2D. A more comprehensive presentation of Telemac-2D is given in Chapter 7. For the simulations, an Elder formulation was adopted for the modelling of turbulence with the eddy viscosity across the channel calibrated as $0.5U_*H$ for Q=10 L/s and Q=14 L/s, and $0.4U_*H$ for Q=24 L/s while the eddy viscosity along the channel was kept as $6.0U_*H$ for all three cases. A Manning's n coefficient of 0.01 was applied to the whole domain. The total modelled length was 30 m. The mesh resolution was 50 mm except in the interface area where it was 20 mm.

Vyas three dimensional model

A detailed description of the finite volume three dimensional model used in this analysis is given in Vyas (2007). The code is based on Patenkar and Spalding (1995) and is using a collocated finite volume discretization. The code solves the Reynolds Averaged Navier-Stokes equations coupled with the continuity equation. The pressure-velocity coupling is achieved using the SIMPLE algorithm of Patenkar and Spalding

(1972). The governing equations were solved with the linear $k-\epsilon$ model of Rodi (1993) to calculate the Reynolds stresses and thus simulate the turbulent flows.

A.3.1.3 Impact of the floodplain width on the establishment length

Once validated against the experimental data, the three-dimensional model described above was used in order to test new configurations in the LMFA flume with a floodplain width of 0.4 m and 0.6 m instead of 0.8 m. The purpose was to verify whether a narrower floodplain would decrease the transition length required to achieve uniform flow conditions. The total inflows for the so-called uniform cases were derived using Debord formulae as this was also used during experiments at the LMFA laboratory with a reasonable degree of success. The assumption $U_{mc} = U_{fp}$ was applied upstream for the boundary conditions, in relation to the problem formulation presented in Section A.2

The additional simulations are described in the following table (A.4):

Table A.4: Additional simulations investigating the impact of floodplain width in the LFMA flume

Floodplain width (m)	Relative depth	Q_{total} (L/s)	Q_{fp} (L/s)	Q_{mc} (L/s)	$\frac{Q_{fp}}{Q_{total}}$ (%)
0.4	0.2	34.78	2.07	32.71	5.94
0.4	0.3	45.021	3.22	31.56	9.27
0.4	0.4	61.384	3.22	31.56	9.27
0.6	0.2	26.444	4.73	40.29	5.94
0.6	0.3	35.564	6.52	38.50	14.49
0.6	0.4	50.3182	7.23	37.79	16.06

A.3.1.4 Impact of one line vegetation on the establishment length

In LMFA, water depth and velocity were measured at different sections along the channel in the cases with rods placed at the interface of the compound channel. The flow

conditions are summarised in Table A.5. These results are used to assess the influence of the rods on flow development.

Table A.5: Experimental conditions in LMFA

Configuration	Q_{total} (L/s)	Relative depth	Averaged Water depth in main channel (m)
No rod	17.3	0.21	0.0649
9mm rod - $\frac{L}{D} = 32$	17.3	0.22	0.0657
No rod	36.3	0.42	0.0649
9mm rod - $\frac{L}{D} = 32$	36.3	0.43	0.0657
9mm rod - $\frac{L}{D} = 16$	36.3	0.44	0.0663

A.4 Results

A.4.1 Impact of relative depth and inlet conditions

The computed evolution of floodplain discharge (as percentage of total discharge Q) for the LMFA and the UCL flumes is presented in Figures A.4 and A.5. The graphs show the evolution of the ratio $\frac{Q_{fp}}{Q_total}$ along the channel so as to enable direct comparison with Proust (2005).

During the experiments, a uniform flow distribution was achieved in UCL within the physical length of the flume for Q=10 L/s. The upstream flow control enabled the determination of a uniform flow establishment length Lu for Q=14 L/s and Q=24 L/s as the downstream flow of the first experiment was used as an upstream condition in second and third experiments. This clearly illustrates the impact of a unique upstream reservoir on the establishment of a uniform flow. In LMFA, where separate inlets were used to increase the floodplain flow compared to its uniform flow value, mass transfer was observed over the whole length of the flume.

The results obtained from the ISM and the three-dimensional model were in good agreement with the experimental results at LMFA where flow distributions within a relative

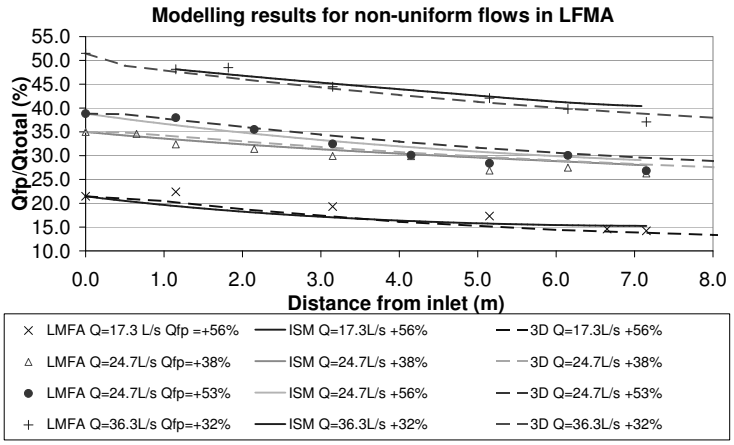

Figure A.4: Evolution of the ratio $\frac{Q_{fp}}{Q_total}$ Modelling vs Experimental Results in LMFA

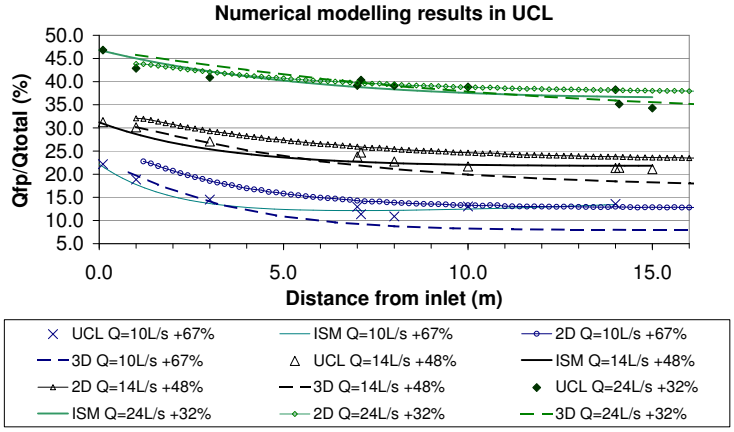

Figure A.5: Evolution of the ratio $\frac{Q_{fp}}{Q_total}$ Modelling vs Experimental Results in UCL

error of 5% were obtained for all simulations. The ISM, the two and three dimensional models also computed flow distribution within 5% of the experimental results for the higher discharge Q=24 L/s in the UCL flume. However, while the ISM computed flow distributions close to the experimental results for Q=10 L/s and Q=14 L/s, the three-dimensional model computed a lower floodplain flow distribution for both results, with relative errors of 40% and 17% respectively.

Mass transfer decreasing from the floodplain to the main channel are observed for all the numerical simulations for the given upstream conditions as was observed during the experiments. It is interesting to note that the ISM and the three-dimensional model computed similar water depth profiles with small variations (typically less than 2 mm) in the water depth. These small variations imply that mass transfer can occur with very small changes in the water depth. Such changes are notably difficult to measure in large flumes, particularly during experiments for which the water surface is not perfectly smooth. As observed experimentally, the computed flows in the flume require some distance to reach their uniform flow distributions. Depending on the stringency of the criteria used to define a uniform flow and the level of destabilisation of the upstream flow distribution, the flumes in both LMFA and UCL can appear to be too short for a uniform flow to be reached when using a unique reservoir. However, when using separate inlets in the LMFA, a uniform flow distribution within the floodplain and the main channel is reached within the first two meters of the flume.

In order to characterise the length required for the mass transfer along the channel to have fully stabilised, additional simulations were carried out with different floodplain flows given upstream, corresponding to different levels of destabilisation for Q=24.7 L/s at LMFA. The results are presented in Figure A.6. It must be noted that the ISM numerical simulations for which floodplain flows are given upstream with a value below that of a uniform floodplain flow do not have corresponding experiments.

Figure A.6 highlights how significant the upstream conditions can be to stabilise the flow distribution in the flume. The use of separate inlets drastically shortens the distance Lu as the uniform flow distribution can be directly given upstream. On the other hand, Lu increases drastically if the upstream floodplain flow differs significantly from its uniform flow value. The flume appears to be too short to meet the uniform flow criteria if the upstream floodplain inflow is more than 35% of its uniform flow value. In the case of the example presented above, the uniform flow distribution is achieved within

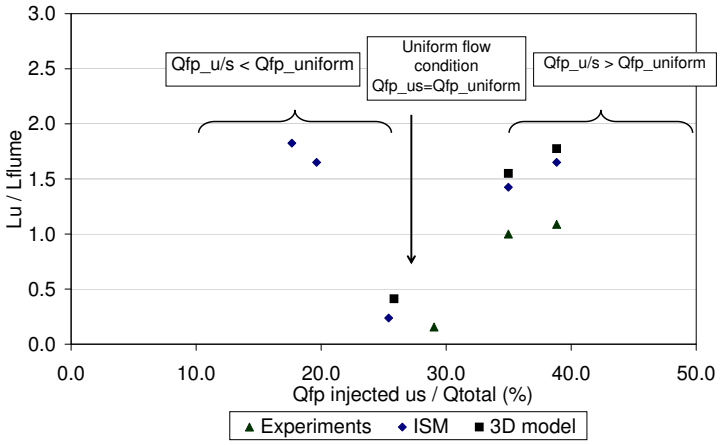

Figure A.6: Length necessary in LMFA flume for the flow distribution to stabilise for Q=24.7 L/s in function of the upstream floodplain flow Q_{fp}

the first few meters of the flume if separate inlets are used. The LMFA experimental flow Q=24.7 L/s for which Qfp has been increased to 53% with the separate inlets has an upstream flow distribution similar to that of a unique reservoir situation. The upstream floodplain and main channel velocities are close to each other (Umc=0.49m/s and Ufp=0.43m/s). For this experiment, Lu is equal to 8.5m as opposed to 1.15m when separate inlets are used.

A.4.2 Impact of floodplain width

Figures A.7 presents the evolution of the ratio $\frac{L_u}{B_{fp}}$ as a function of relative depth, assuming a unique inlet is used upstream and that as a result $U_{mc} = U_{fp}$. The results show that L_u increases with relative depth for all floodplain width. The increases are approximately linear for the three simulated floodplain width.

Intuitively, it was thought before the simulations that L_u would decrease significantly with the floodplain width B_{fp} for a given relative depth. However, this does not appear in the results.

The assumption $U_{mc} = U_{fp}$ does not lead to the same "excess" of inflow upstream

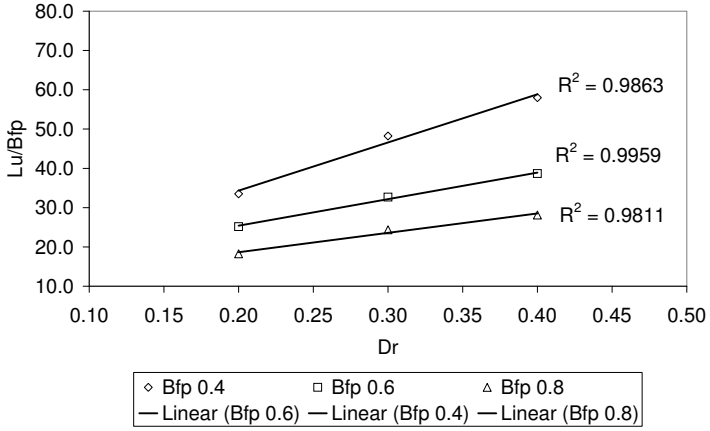

Figure A.7: L_u normalised by B_{fp} as a function of relative depth assuming a unique inlet is used

in the floodplain (or equivalently, to the same deficiency of inflow in the main channel). Figure A.8 presents the evolution of the ratio $\frac{L_u}{B_{fp}}$ normalised by the excess of floodplain flow $\frac{Q_{fp,us}}{Q_{fp,uniform}}$, where $Q_{fp,us}$ is the upstream floodplain flow and $Q_{fp,uniform}$ is the floodplain uniform flow.

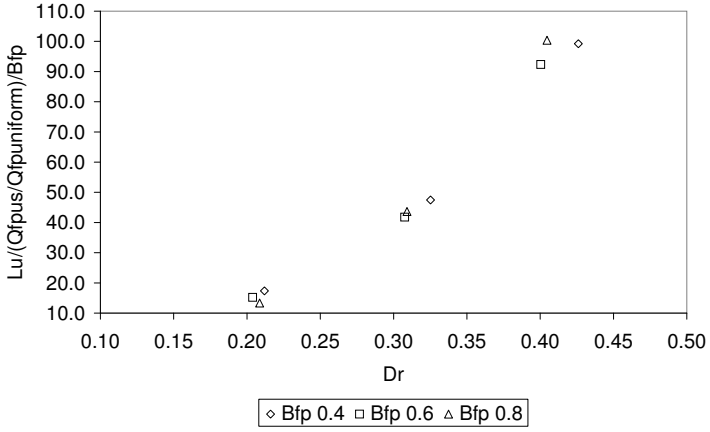

Figure A.8: L_u normalised by B_{fp} and $\frac{Q_{fp,us}}{Q_{fp,uniform}}$ as a function of relative depth assuming a unique inlet is used

While the ratio $\frac{L_u Q_{fp,us}}{B_{fp} Q_{fp,uniform}}$ increases with relative depth, the results appear sim-

ilar for the different floodplain widths simulated. Hence, the condition $U_{mc} = U_{fp}$ upstream leads to discrepancies in the upstream and uniform flow distributions that vary with the floodplain width.

A.4.3 Impact of one-line vegetation

The first notable impact of the line of rods is on the evolution of the water depth. Figure A.9 presents the average water depth in the main channel and in the floodplain ($H_{mean}(x)$), at different stations x, minus the uniform water depth ($H_{uniform}$) for the rod case $\frac{L}{D} = 32$ and the no rod case. The results show that rods have a slight tendency to smooth out the longitudinal average water depth profile. The difference $H_{mean}(x) - H_{uniform}$ lies between ± 1 mm between 3.0 m and 7.0 m. However, for the no rod case, this is only the case between 4.8 m and 6.2 m and the discrepancies are greater along the channel.

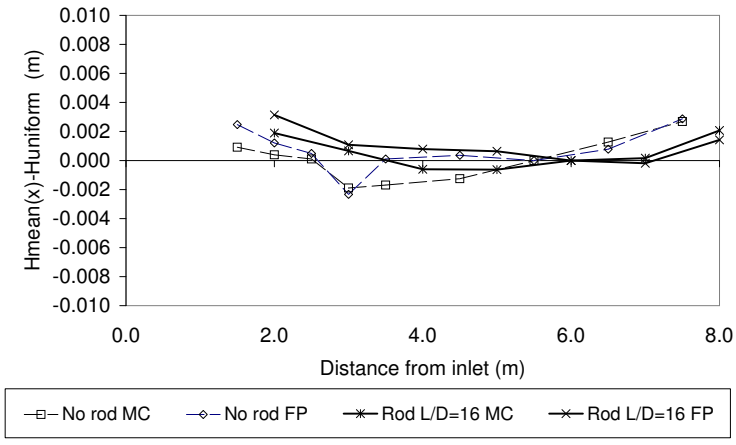

Figure A.9: L_u normalised by B_{fp} and $\frac{Q_{fp,us}}{Q_{fp,uniform}}$ as a function of relative depth assuming a unique inlet upstream

The impact of rods on depth-averaged velocity profiles is more limited. Figure A.10 presents the depth average velocity profiles between 1.5 m and 7.5 m for the no rod and

rod case for $\frac{L}{D} = 16$. No significant discrepancy can be observed between 4.5 m and 6.5 m for both sets of profiles, and discrepancies between the depth-averaged velocity in this region which remain respectively within 5%. Nevertheless, the profiles converge quicker between Y=0.7 m and 0.9 m near the interface, especially in the floodplain. In the presented rod case, the depth-averaged velocity profile converges from x=2.5 m while in the nor rod case the shear layer appears developed only from the x=3.5 m profile.

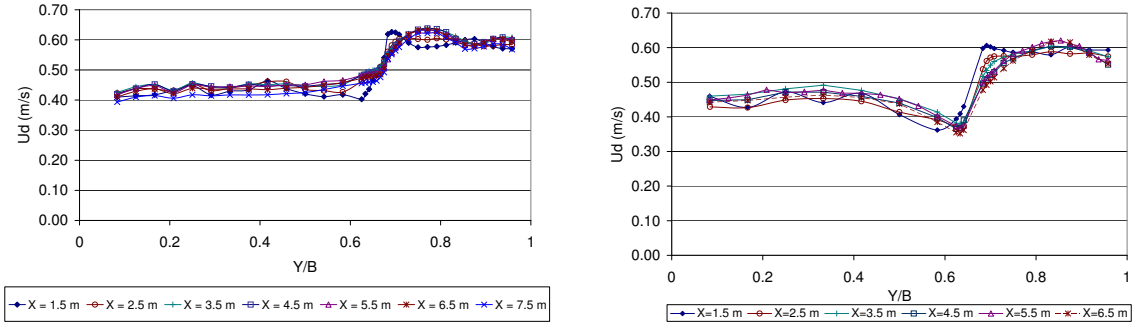

(a) (b)

Figure A.10: (a) (b) Depth-averaged Velocity profiles between 1.5 m and 7.5 m (a) No rod case (b) Rods spaced at $\frac{L}{D} = 16$.

A.5 Discussion and Conclusion

A.5.1 Discussion

Bousmar *et al.* (2005) compared results in the literature and issued a guideline to define the necessary transition length required to achieve uniform flow conditions in straight compound channels. A non-dimensional length was used, defined as the ratio between the distance from upstream of the first measuring station L_m and the floodplain width B_fp. They suggested that the ratio $\frac{L_m}{B_{fp}}$ should be greater than 35. The idea underlying that guideline is that for a larger floodplain width, the mass transfer is supposed to

require a longer establishment length. However, in Bousmar *et al.* (2005) the definition of uniform flow is flawed by the fact that an absolute difference of $\frac{Q_{fp}}{Q_{total}}$ is considered to define L_u.

One limitation of the three dimensional numerical modelling might lie in the use of a linear $k-\epsilon$ model. However, while the linear $k-\epsilon$ model is not capable of accurately predicting the normal Reynolds stresses and cannot reproduce the secondary currents generated by the anisotropy of turbulence (Speziale (1987)), it has been regarded as sufficient for the objectives of the current analysis. Indeed, one of the primary objectives of this work was to quantify the length necessary to obtain a constant flow distribution along the flume. Rameshwaran and P. (2003) highlighted that a three dimensional model with a linear $k-\epsilon$ model could reproduce reasonably well the flow field yet noticing that discrepancies existed at the interface between the main channel and the floodplain. It is however reasonable to tackle the issue of mass transfer in flow development with the linear $k-\epsilon$ model as a first step and anisotropic turbulence models can be used in future research.

This issue of uniform flow seems restricted to straight compound channels only. In other configurations, when an obstacle lies in the floodplain for instance, the latter would force mass transfer to occur predominantly in the upstream part of the flume facility so that the influence of the upstream inflow is localized on a small distance from upstream. Similar comments apply to meandering channels and also to the case of one-line vegetation along the channel.

A.5.2 Conclusions

Numerical modelling was carried out using the Independent Sub-sections Method (ISM), the two-dimensional commercial software Telemac-2D and a three-dimensional model in order to investigate the establishment of uniform flow in experimental flumes. The

experiments carried out at LMFA and UCL flumes were simulated by the three different numerical models. The ISM computed flow distributions along the channel which were within 5% of relative error with all experimental flow distributions. The three-dimensional model also computed flow distributions within 5% of all experimental flow distributions at the LMFA. Telemac-2D, only used to model the UCL experiments, simulated flow distribution similar to the experimental flow distribution, the largest discrepancy being 9% for Q=14L/s. The most significant discrepancy in flow distribution was obtained between the three-dimensional model and the flow Q=10 L/s at UCL (40%).

Clearly, flow depth measurements alone are not enough to verify the uniformity of a flow. As was demonstrated, excess flow from the floodplain can be transferred towards the main channel with water depths quasi identical to that of uniform flow conditions. The use of separate inlet conditions as an upstream control has proved to significantly shorten the length Lu required for no mass transfer. This type of upstream control enables the establishment of a uniform flow distribution within the first few meters of a flume. If an upstream flow distribution is too different from the uniform flow distribution, Lu might exceed the physical length of a flume.

The length required for the flow distribution along the channel to become stable increases with the relative depth Dr. The experimental results suggest that this length is about 3.9m for Dr=0.18, 12.4m for Dr=0.29 and 16.0m for Dr=0.40 in the UCL flume. The ISM and the three-dimensional numerical models both confirm the same trends. The hypothetical case of an upstream floodplain flow given below its uniform flow value was also simulated. Mass transfer from the main channel to the floodplain was observed and some length comparable to the length observed for increased floodplain flows was also necessary to achieve a uniform flow distribution.

Rods placed on the edge of the floodplain tend to smooth out the water profiles

along the channel. In particular, depth-averaged velocity profiles were seen to converge more rapidly along the flume near the main channel - floodplain interface compared to the no rod case. Further away from this interface, differences between the evolutions of depth-averaged velocity profiles are more subdued. This particular phenomenon can be regarded as a consequence of the greater mixing generated by the rods. As a result, the lengths required to achieve uniform flow conditions in the no rod case can be kept for the rod case.

APPENDIX B

Complementary Information on Experimental Dataset

This Appendix presents the isovels of all the experiments carried out in Loughborough University. The results are shown in Figures B.1 to B.5.

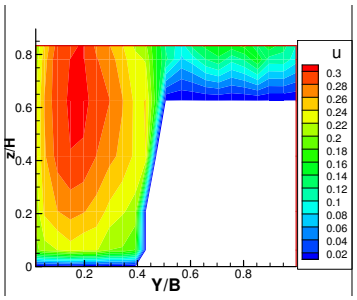

(a)

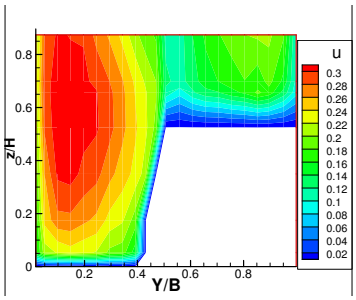

(b)

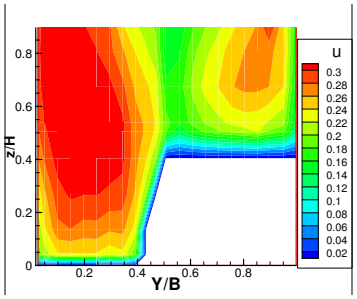

(c)

Figure B.1: Isovels for Series 1a (a) Dr=0.25 (b) Dr=0.35 (c) Dr=0.51

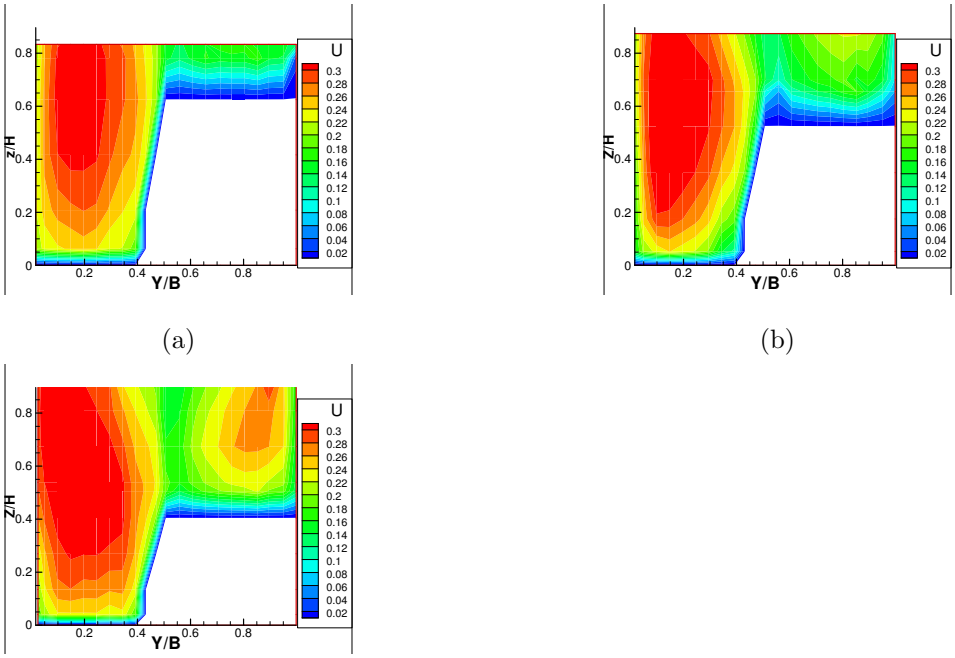

(a) (b)

(c)

Figure B.2: Isovels for Series 1b (a) Dr=0.25 (b) Dr=0.35 (c) Dr=0.51

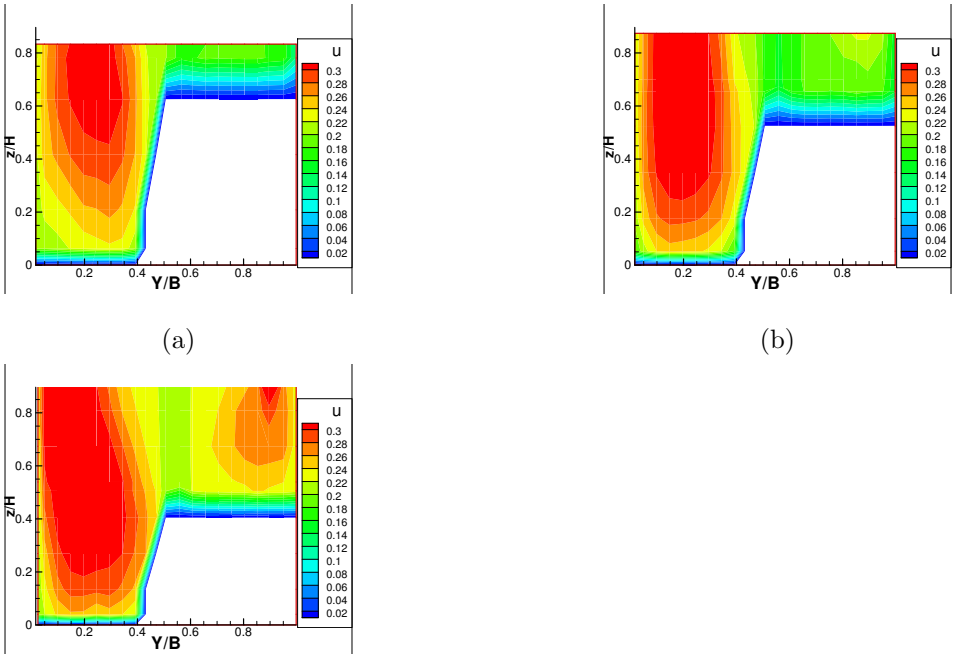

(a) (b)

(c)

Figure B.3: Isovels for Series 2Aa (a) Dr=0.25 (b) Dr=0.35 (c) Dr=0.51

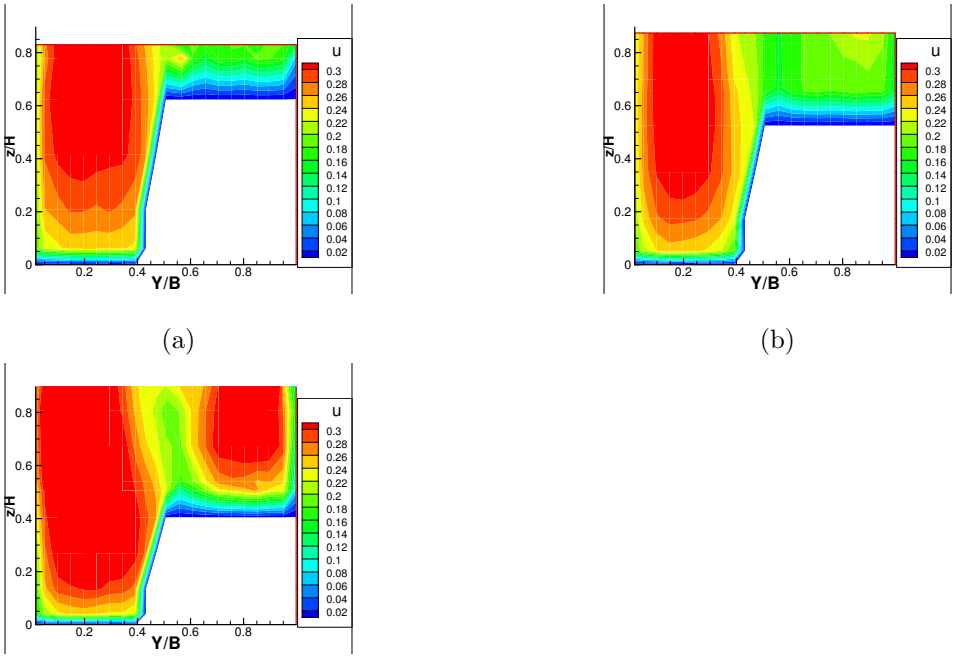

(a) (b)

(c)

Figure B.4: Isovels for Series 2Ab (a) Dr=0.25 (b) Dr=0.35 (c) Dr=0.51

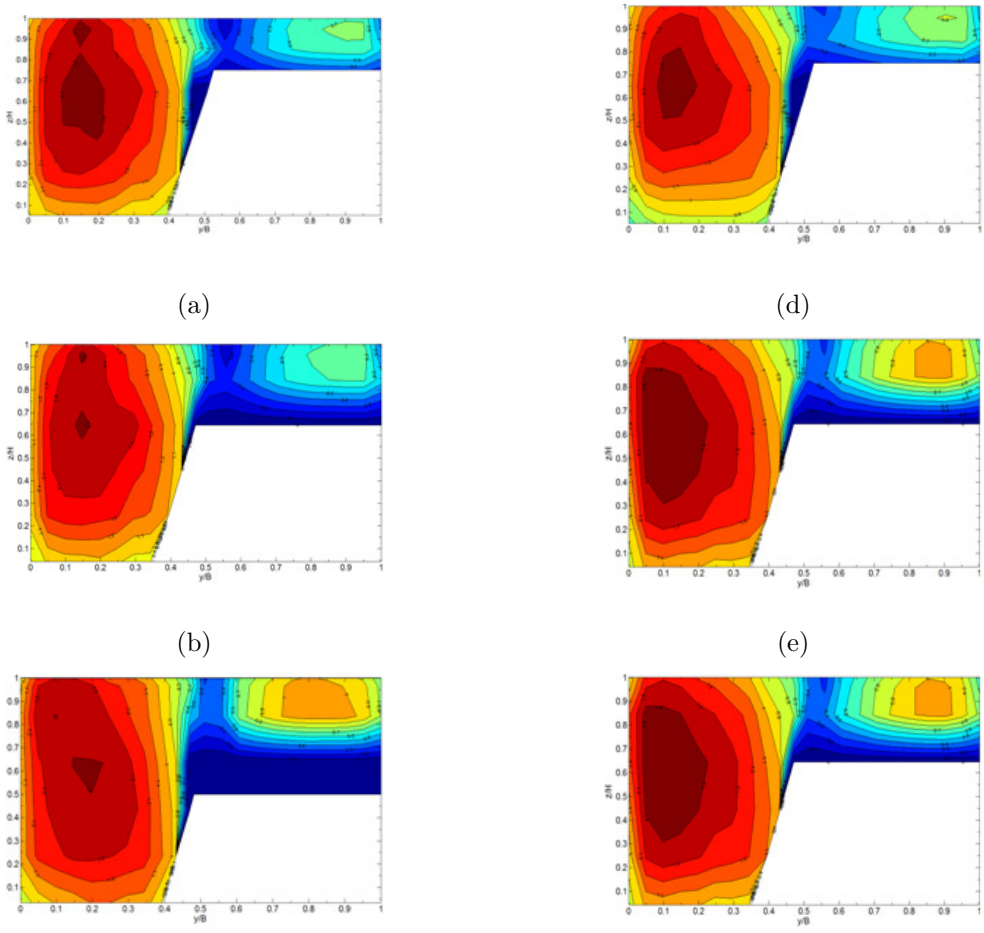

(a) (d)

(b) (e)

(c) (f)

Figure B.5: Isovels for cases (a) (b) (c) Series 2Ba-25 to 51 and (d) (e) (f) Series 2Bb-25 to 51

Figure B.6 presents the rods used in the experiments and a detailed picture of the brush used in the experiments for Series 2B.

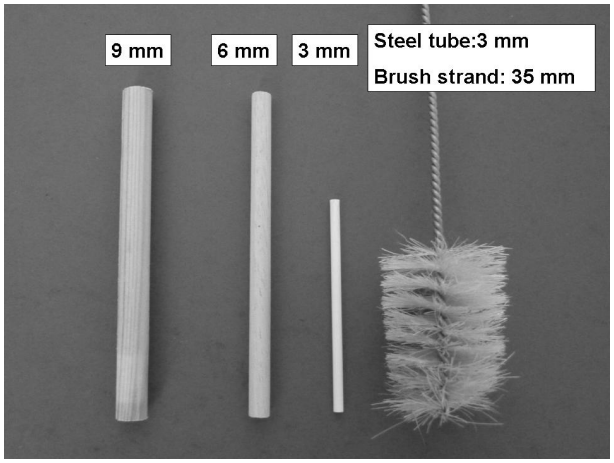

(a)

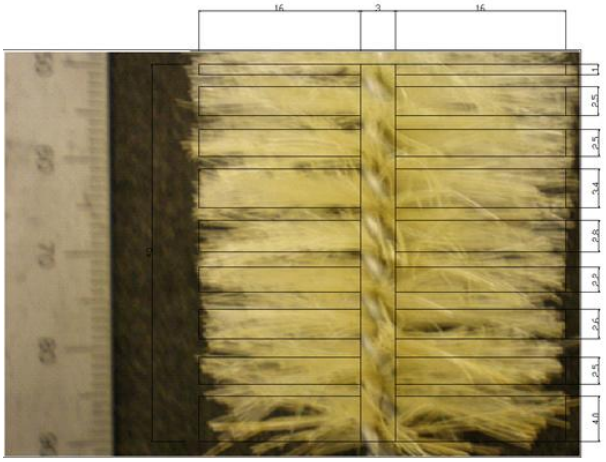

(b)

Figure B.6: (a) Summary photograph of the rods used in the experiments; from left to right: the 9 mm, 6 mm, 3 mm and the brush (b) Detailed picture of the brush used in the experiments

APPENDIX C

Detailed Resolution of the Modified SKM

This Appendix presents the expressions of the different coefficients required to solve the modified SKM presented in Chapter 7. The system of equations solved by the proposed SKM can be written as Equation 7.20 in the form $EA = B$. In the trapezoidal cross-section case of the Loughborough flume, the matrix E requires 26 coefficients to be fully defined.

$$e_{2,1} = e^{\gamma_1 y_1} \quad \text{(C.1)}$$
$$e_{2,2} = e^{-\gamma_1 y_1} \quad \text{(C.2)}$$
$$e_{2,3} = -\xi_1^{\alpha_1} \quad \text{(C.3)}$$
$$e_{2,4} = -\xi_1^{-\alpha_1 - 1} \quad \text{(C.4)}$$
$$e_{3,1} = \gamma_1 e^{\gamma_1 y_1} \quad \text{(C.5)}$$
$$e_{3,2} = -\gamma_1 e^{-\gamma_1 y_1} \quad \text{(C.6)}$$
$$e_{3,3} = \alpha_1 \xi_1^{\alpha_1 - 1} \quad \text{(C.7)}$$
$$e_{3,4} = (\alpha_1 - 1)\xi_1^{-\alpha_1 - 2} \quad \text{(C.8)}$$
$$e_{4,3} = -\xi_2^{\alpha_1} \quad \text{(C.9)}$$
$$e_{4,4} = -\xi_2^{-\alpha_1 - 1} \quad \text{(C.10)}$$
$$e_{4,5} = e^{\gamma_2 y_2} \quad \text{(C.11)}$$
$$e_{4,6} = -e^{-\gamma_2 y_2} \quad \text{(C.12)}$$
$$e_{5,3} = -\alpha_1 \xi_2^{\alpha_1 - 1} \quad \text{(C.13)}$$
$$e_{5,4} = (\alpha_1 + 1)\xi_2^{-\alpha_1 - 2} \quad \text{(C.14)}$$
$$e_{5,5} = -\gamma_2 e^{\gamma_2 y_2} \quad \text{(C.15)}$$
$$e_{5,6} = \gamma_2 e^{-\gamma_2 y_2} \quad \text{(C.16)}$$
$$e_{6,5} = e^{\gamma_2 y_3} \quad \text{(C.17)}$$
$$e_{6,6} = e^{-\gamma_2 y_3} \quad \text{(C.18)}$$
$$e_{6,7} = -e^{\gamma_1 y_3} \quad \text{(C.19)}$$
$$e_{6,8} = -e^{-\gamma_1 y_3} \quad \text{(C.20)}$$
$$e_{7,5} = \gamma_2 e^{\gamma_2 y_3} \quad \text{(C.21)}$$
$$e_{7,6} = -\gamma_2 e^{-\gamma_2 y_3} \quad \text{(C.22)}$$
$$e_{7,7} = -\gamma_1 e^{\gamma_1 y_3} \quad \text{(C.23)}$$
$$e_{7,8} = \gamma_1 e^{-\gamma_1 y_3} \quad \text{(C.24)}$$
$$e_{8,7} = e^{\gamma_1 y_4} \quad \text{(C.25)}$$
$$e_{8,8} = e^{-\gamma_1 y_4} \quad \text{(C.26)}$$

with $\xi_1 = H_{mc}$ and $\xi_2 = H_{fp}$.

The 8 coefficients of the matrix of constants B are given below.

$$\begin{cases} b_{1,1} = \dfrac{8gH_{mc}S_0}{f}(1-\Gamma) + U^2_{Left\ wall} \\ b_{2,1} = H_{mc}\omega + \eta - \dfrac{8gH_{mc}S_0}{f}(1-\beta) \\ b_{3,1} = -\omega \\ b_{4,1} = \dfrac{8gH_{fp}S_0}{f}(1-\Gamma) - H_{fp}\omega - \eta \\ b_{5,1} = \omega \\ b_{6,1} = \dfrac{8gH_{fp}S_0}{f}(1-\Gamma) - \dfrac{8gHS_0}{\frac{f}{8} + \frac{1}{2}\frac{N}{L_T}C_D S_F H}(1-\beta) \\ b_{7,1} = 0 \\ b_{8,1} = \dfrac{8gH_{fp}S_0}{f}(1-\Gamma) + U^2_{Right\ wall} \end{cases} \tag{C.27}$$

APPENDIX D

Complementary SKM Modelling Results

D.1 Input Parameters of SKM Including Advection Term for the Loughborough Flow Cases

Table D.1: Parameters used in the second version of the SKM modelling of the Loughborough experiments

Parameter	Relative depth	Series 1a	Series 1b	Series 2Aa	Series 2Ab	Series 2Ba	Series 2Bb
Γ_{mc}	0.25	0.18	0.14	0.15	0.10	0.22	0.22
	0.35	0.20	0.20	0.17	0.14	0.30	0.32
	0.51	0.33	0.28	0.23	0.16	0.40	0.48
Γ_{fp}	0.25	0.03	0.01	0.01	0.005	0.022	0.015
	0.35	0.03	0.02	0.02	0.01	0.06	0.06
	0.51	0.14	0.05	0.07	0.05	0.20	0.22
f_d	0.25	37.0	37.0	37.0	37.0	65.0	65.0
	0.35	4.1	1.0	4.1	1.0	16.3	7.1
	0.51	1.5	0.2	1.5	0.04	5.9	0.2

D.2 Results of SKM Including the Advection Term for Loughborough Flow Cases

Figures D.1, D.2 and D.3 present the results of the second SKM version including the advection term for relative depths of 0.25 to 0.51 in Loughborough University.

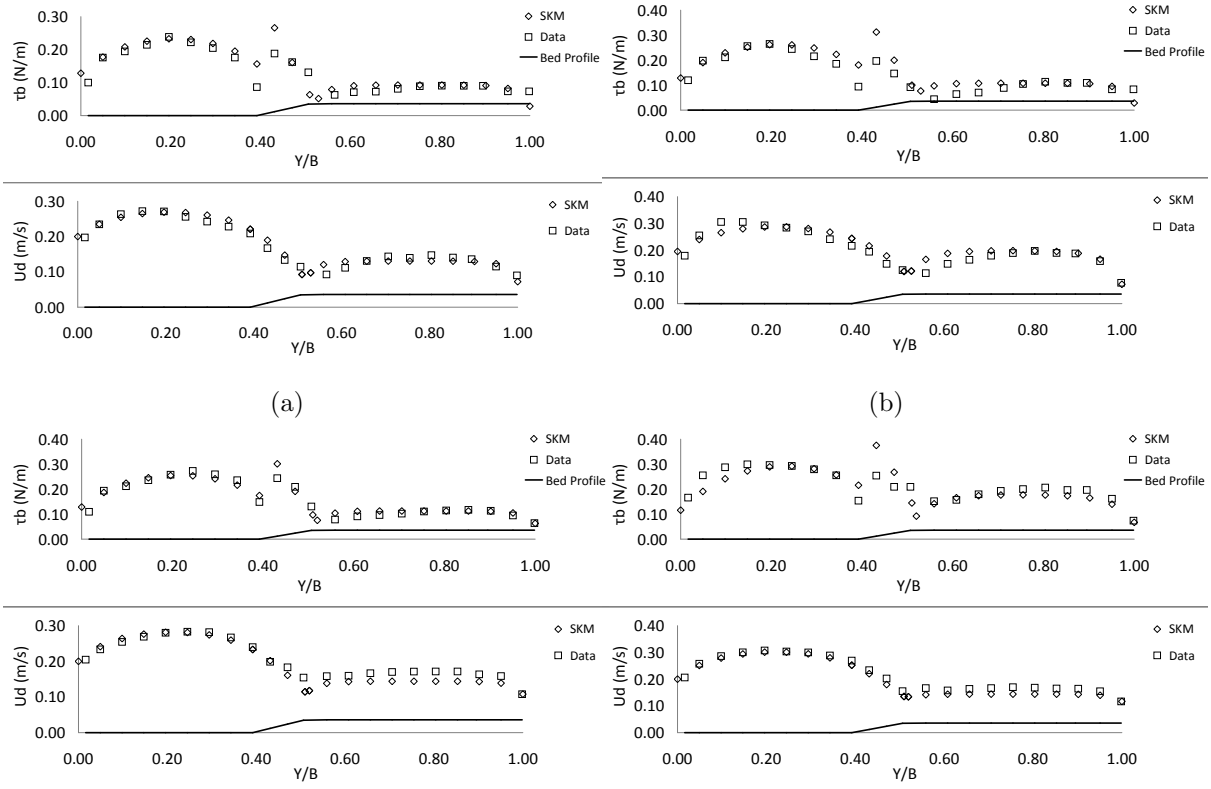

(a) (b)

(c) (d)

Figure D.1: SKM results for τ_B (top) and U_d bottom for Dr=0.25 (a) Series 1a (b) Series 1b (c) Series 2Aa and (c) Series 2Ab

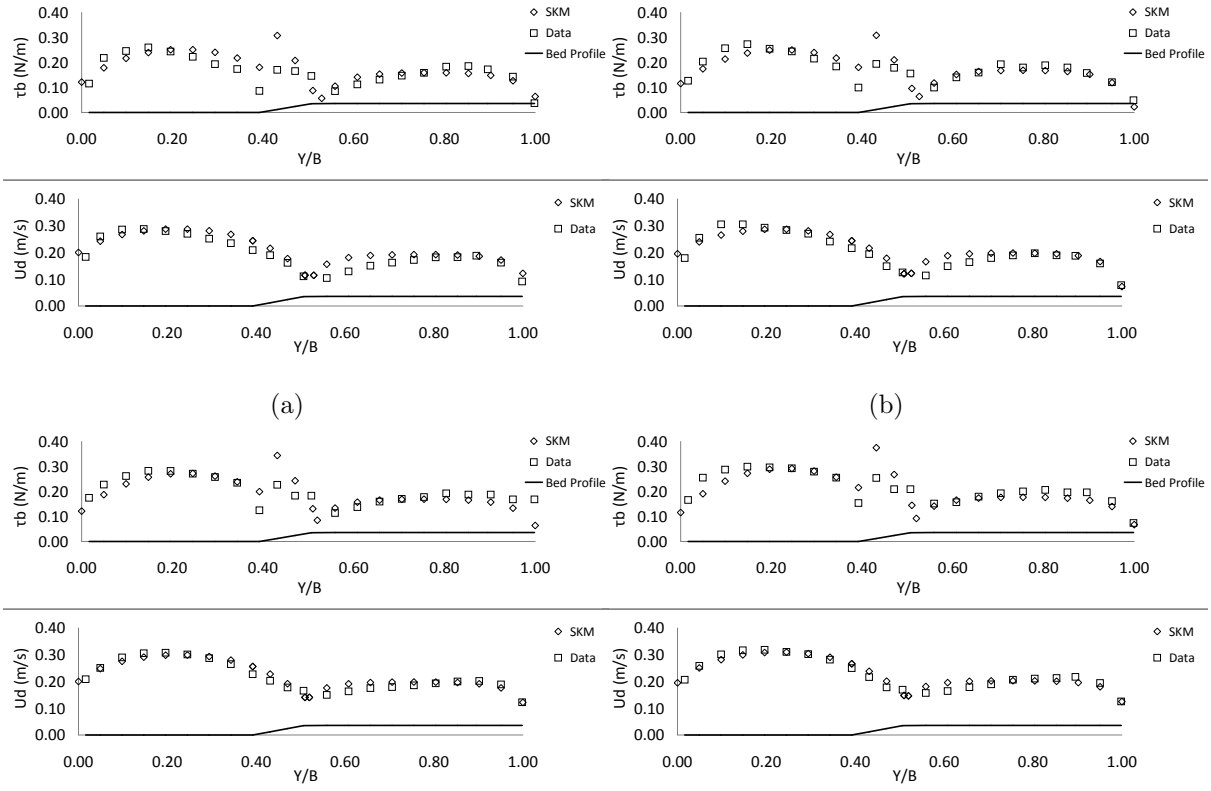

Figure D.2: SKM results for τ_B (top) and U_d bottom for Dr=0.35 (a) Series 1a (b) Series 1b (c) Series 2Aa and (c) Series 2Ab

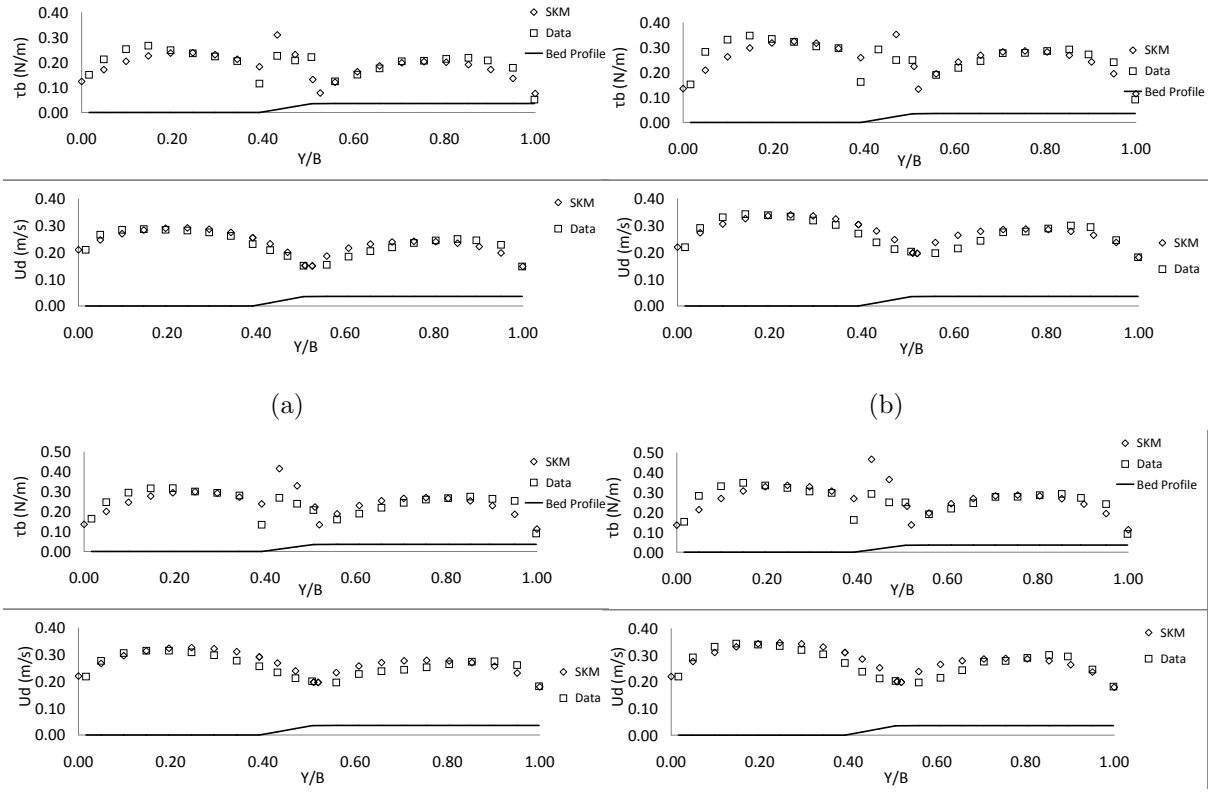

Figure D.3: SKM results for τ_B (top) and U_d bottom for Dr=0.51 (a) Series 1a (b) Series 1b (c) Series 2Aa and (c) Series 2Ab

D.3 Results of SKM Including the Advection Terms derived from LES

Figure D.4 presents the results of the SKM modelling with the advection term derived Telemac-2D LES modelling.

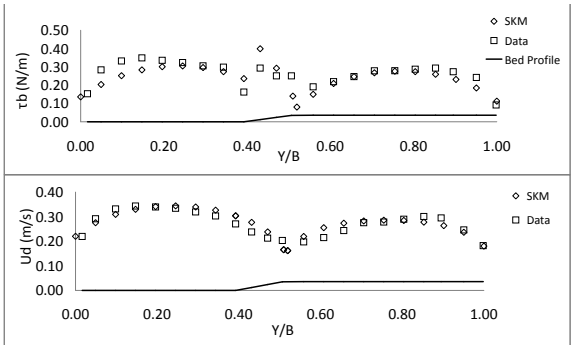

Figure D.4: SKM results with the advection term as simulated by Telemac-2D LES modelling for Series 2Ab-51

D.4 Complementary results on the application of the SKM to field data

The predicted bed shear stress normalised by $\rho g H S_0$ are presented in Figure D.5 for the low and high flow events at the upstream section.

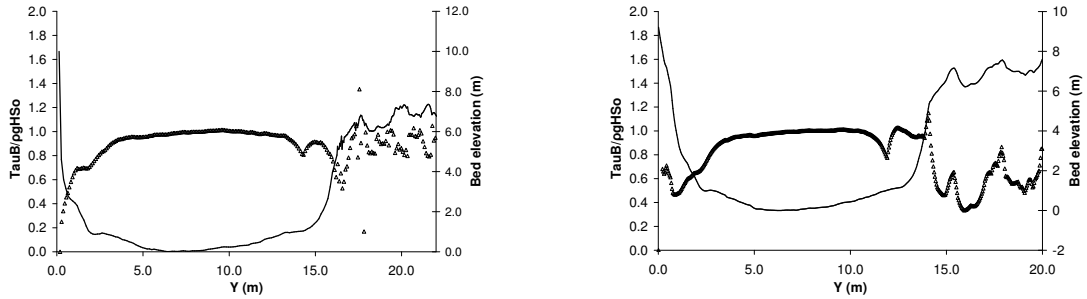

(a) (b)

Figure D.5: Variations of τ_B normalised by $\rho g H S_0$ for (a) low flow event (04-04-06) (b) high flow event (11-04-06)

References

Abril, J. and Knight, D. (2004). Stage-discharge prediction for rivers in flood applying a depth-averaged model. *Journal of Hydraulic Research*, **42**, 616–629. 6.3.4.1

Ackers, P. (1991). Hydraulic design of straight compound channels. Report SR281, 2 Vols., HR Wallingford Ltd. 4.4.2, 5.2.2.2

Appell, G. (1996). Design and tests of a real time sontek adp system. In *OCEANS '96. MTS/IEEE. 'Prospects for the 21st Century'. Conference Proceedings*, 289–292. 6.4.1.1

Armanini, A., Righetti, M. and Grisenti, P. (2005). Direct measurement of vegetation resistance in prototype scale. *Journal of Hydraulic Research*, **43**, 481–487. 2.4.2.2

Babaeyan-Koopaei, K., Ervine, D., Carling, P. and Cao, Z. (2002). Velocity and turbulence measurements for two overbank flow events in river severn. *Journal of Hydraulic Engineering*, **128**, 891–900. 6.3.4.2

Berz, G. (2000). Flood disasters : lessons from the past - worries for the future. In *Proceedings of the 28th Congress of IAHR, Post congress volume, Graz, Austria*, 9–16. 1.1

Bousmar, D. (2002). *Flow modelling in compound channels - Momentum transfer between main channel and prismatic or non prismatic floodplains*. Ph.D. thesis, Université catholique de Louvain-la-Neuve, Belgium. 2.4.6.3, 2.7

Bousmar, D., Rivière, N., Proust, S., Paquier, A., Morel, R. and Zech, Y. (2005). Upstream discharge distribution in compound channel flumes. *Journal of Hydraulic Engineering*, **131**, 408–412. A.2.1, A.2.3, A.2.3, A.3.1, A.5.1

Carr, M. and Rehmann, C. (2007). Measuring the dispersion coefficient with acoustic doppler current profilers. *Journal of Hydraulic Engineering*, **133**, 977–982. 6.2.1

Chow, V. (1959). *Open-Channel Hydraulics*. McGraw-Hill Companies. 6.4.3.2

Christodoulou, G. (1992). Apparent shear stress in smooth compound channels. *Water resources management*, **6**, 235–247. 2.3.6, 2.3.6, 4.4.4

Crawley, D. and Nickling, W. (2003). Drag partition for regularly-arrayed rough surfaces. *Boundary-Layer Meteorology*, **107**, 445–468. 2.4.5

Darby, S.E. (1999). Effect of riparian vegetation on flow resistance and flood potential. *Journal of Hydraulic Engineering*, **125**, 443–454. 2.4.3

DEFRA (2004). Making space for water. Defra Publications. 7.3.5.4

Dinehart, R. and Burau, J. (2005). Repeated surveys by acoustic doppler current profiler for flow and sediment dynamics in a tidal river. *Journal of Hydrology*, **314**, 1–21. 6.2.1

Dinehart, R.L. (2003). Spatial analysis of adcp data in streams. In *Proceedings of the workshop, Sediment Monitoring Instrument and Analysis Research, Flagstaff, AZ*, 8. 6.2.1, 1

Fukuoka, S. and Watanabe, A. (1997). Horizontal structures of flood flow with dense vegetation clusters along main channel banks. In *Proceedings of the 27th Congress of IAHR, B2, San Francisco*, 1408–1413. 5.3

Gioia, G. and Bombardelli, F. (2002). Scaling and similarity in rough channel flows. *Physical Review Letters*, **88**, 0145011–0145014. 4.4.2

Gordon, R. (1996). *Accoustic Doppler current profiler principles of operation: a practical primer*. RD Instruments. 1

Guillermo, P., Kim, S., Stoesser, T. and Rodi, W. (2008). Turbulence structures on the flow through emergent vegetation. In *Advances in Hydro-science and engineering IAHR, ICHE, Nagoya, Japan*, 239–240. 2.4.6.3

Hauet, A. (2006). *Estimation de débit and mesure de vitesse en rivière par Large Scale Particle Image Velocimetry*. Ph.D. thesis, Institut National Polytechnique de Grenoble, France. 3.3.7.1

Hauet, A., Creutin, J. and Belleudy, P. (2007). Sensitivity study of large-scale particle image velocimetry measurement of river discharge using numerical simulation. *Journal of Hydrology*, **349**, 178–190. 3.3.7.2

Heanen, A., Myers, W. and Lyness, J. (2004). The conveyance capacity of compound channels with large scale floodplain roughness. In *River Flow 2004, Napoli, Italy*, 459–468. 4.4.4

Helmio, T. (2002). Unsteady 1d flow model of compound channel with vegetated floodplains. *Journal of Hydrology*, **269**, 89–99. 4.4.4

Hervouet, J. (2003). *Hydrodynamique des écoulements a surface libre*, vol. 1, chap. R ésolution des équations de Saint-Venants, in French, 89–117. Presses de l'Ecole Nationale des Ponts et Chaussées. 7.3.1, 7.3.3.3, A.3.1

Hervouet, J. (2007). *Free surface flows*, vol. 1, chap. Equations of free surface hydrodynamics, 62–68. Presses de l'Ecole Nationale des Ponts et Chaussées. 7.3.4.4

Hetz, A. (1991). Vortex shedding over five in-line cylinders. *Journal of Fluids and Structures*, **5**, 243–257. 2.5.2, 5.2.2.6

Hubble, T., Docker, B. and Rutherfurd, I. (2009). The role of riparian trees in maintaining riverbank stability: A review of australian experience and practice. *Ecological Engineering*, **Article in Press**. 1.2

Huthoff, F. and Augustin, D. (2006). Hydraulic resistance of vegetation. Final Project Report, University of Twente. 4.4.2

Igarashi, T. (1984a). Characteristics of the flow around two circular cylinders arranged in tandem. *Bulletin of Japanese Society of Mechanical Engineers*, **27**, 2380–2387. 3.2.3, 3.2.3.2

Igarashi, T. (1984b). Characteristics of three cylinders arranged in line. *Bulletin of Japanese Society of Mechanical Engineers*, **27**, 2397–2404. 2.5.4

Ikeda, S. (1981). Self-formed straight channels in sandy beds. *Journal of Hydraulic Division*, **107**, 389–456. 2.2.4, 2.3.5

Ikeda, S. and McEwan, I. (2009a). *Flow and sediment transport in compound channels*. IAHR Monograph Series. 2.4.6.1, 2.7

Ikeda, S. and McEwan, I. (2009b). *Flow and Sediment Transport in Compound Channels*, vol. 1, chap. Flow Structure, 56–60. IAHR Monographs. 7.3.5.3

Islam, N. (2001). The open approach to flood control: the way to the future in bangladesh. *Futures*, **33**, 783–802. 1.1

James, C. and Wark, J. (1992). Conveyance estimation for meandering channels. Report SR329, HR Wallingford Ltd., UK. 2.2.3

James, C., Goldbeck, U., Patini, A. and Jordanova, A. (2008). Influence of foliage on flow resistance of emergent vegetation. *Journal of Hydraulic Research*, **46**, 536–542. 2.4.2.2, 4.4.9.2

James, C.S. and Makoa, M. (2006). Conveyance estimation for channels with emergent vegetation boundaries. *Proceedings of the Institution of Civil Engineers*, **159**, 235–243. 2.4.3

Jarvela, J. (2002). Determination of flow resistance of vegetated channel banks and floodplains. In *River Flow 2002, Louvain-la-neuve, Belgium*, 311–318. 2.4.2.1, 2.4.2.2

Jarvela, J. (2004). Determination of flow resistance caused by non-submerged woody vegetation. *International Journal of River Basin Management*, **2**, 61–70. 2.4.2.2

Jordanova, A. and James, C. (2003). Experimental study of bed load transport through emergent vegetation. *Journal of Hydraulic Engineering*, **129**, 474–478. 2.4.5

Jordanova, A., James, C.S. and Birkhead, A. (2006). Practical estimation of flow resistance through emergent vegetation. *Proceedings of the Institution of Civil Engineers*, **159**, 173–181. 4.4.4

Kang, H. and Choi, S. (2006a). Reynolds stress modelling of rectangular open-channel flow. *International Journal for Numerical Methods in Fluids*, **51**, 1319–1334. 2.2.2, 2.2.3, 6.4.3.3

Kang, H. and Choi, S. (2006b). Turbulence modelling of compound open-channel flows with and without vegetation on the floodplain using the reynolds stress model. *Advances in Water Resources*, **29**, 1650–1664. 2.3.3, 2.4.4, 6.4.3.3

Knight, D. and Demetriou, J. (1983). Flood plain and main channel flow interaction. *Journal of Hydraulic Engineering*, **109**, 1073–1092. 2.3.4

Knight, D., Demetriou, J. and M.E., H. (1984). Boundary shear in smooth rectangular channels. *Journal of Hydraulic Engineering*, **110**, 405–422. 2.2.4

Knight, D., Yuen, K. and Al-hamid, A. (1994). *Mixing and Transport in the Environment*, vol. 1, 51–87. K. Beven, Chatwin P. C. and Millbank J. H. (Eds), John Wiley and Sons Ltd. 2.3.4

Knight, D.W. and Shiono, K. (1996). *River channel and floodplain hydraulics*, vol. 1, chap. Floodplain processes, 139–181. Anderson, Walling and Bates (Eds), J. Wiley. 2.3.2, 2.3.4

Knight, D.W., Omran, M. and Tang, X. (2007). Modeling depth-averaged velocity and boundary shear in trapezoidal channels with secondary flows. *Journal of Hydraulic Engineering*, **133**, 39–47. 2.2.3, 6.3.2.2, 7.5

Kolmogorov, K. (1941). Dissipation of energy under locally isotropic turbulence. *Dokl. Akad. Nauk SSSR*, **32**, 0145011–0145014. 4.4.2, 4.4.2

Landcare Notes, a. (1998). Watercourse re-vegetation using indigenous plants. State of Victoria publications. 3.2.3.2

Le Coz, J., Paquier, A., Chastan, B. and Dramais, G. (2007). Emploi des profileurs acoustiques a effet doppler (adcp) pour etudier la tructure des ecoulements en riviere. In *Congres Francais de Mecanique, Grenoble*. 6.2.1, 6

Lesieur, M., Metais, O. and Comte, P. (2005). *Large-eddy simulations of turbulence*. Cambridge University Press, Cambridge. 2.4.6.3, 2.7, 7.3.3.4

Martin, N. (2007). Riversurveyors stationary method used in unseasonal summer flood conditions a sign of climate change? Application Note, SonTek Ltd. 6.4.1.3

McGahey, C. and Samuels, P. (2003). Methodology for conveyance estimation in two-stage straight, skewed and meandering channels. In *Proceedings of the XXX Congress of the International Association for Hydraulic Research*, Vol. C1. 7.3.6.3

Muste, M., Yu, K. and Spasojevic, M. (2004). Practical aspects of adcp data use for quantification of mean river flow characteristics; part I: Moving vessel measurements. *Flow Measurement and Instrumentation*, **15**, 1–16. 1.3, 6.2.1, 2, 5

Myers, R. and Elsawy, E. (1975). Boundary shear in channel with flood plain. *Journal of Hydraulic Engineering*, **101**, 933–946. 2.3.4, 2.3.4

Myers, W. (1978). Momentum transfer in a compound channel. *Journal of Hydraulic Research*, **16**, 139–150. 2.3.2, 2.3.6

Nadaoka, K. and Yagi, H. (1998). Shallow-water turbulence modelling and horizontal large-eddy computation of river flow. *Journal of Hydraulic Engineering*, **124**, 493–500. 2.4.6.3

Naot, D. and Rodi, W. (1982). Calculation of secondary currents in channel flow. *Journal of the Hydraulics Division*, **108**, 948–968. 2.2.2, 2.2.3, 2.2.3

NAOT, D., NEZU, I. AND NAKAGAWA, H. (1996). Hydrodynamic behavior of partly vegetated open channels. *Journal of Hydraulic Engineering*, **122**, 625–633. 2.4.3, 2.4.4

NEPF, H. (1999). Drag, turbulence, and diffusion in flow through emergent vegetation. *Water Resources Research*, **35**, 479–489. 2.4.3, 2.5.4, 4.4.7, 4.4.9.2, 7.2.1.4, 7.2.3.2

NEPF, H.M., SULLIVAN, J.A. AND ZAVISTOSKI, R.A. (1997). A model for diffusion within an emergent plant canopy. *Limnol. Oceanogr.*, **42**, 85–95. 2.5.3

NEZU, I. AND NAKAGAWA, H. (1984). Cellular secondary currents in a straight conduit. *Journal of Hydraulic Engineering*, **110**, 173–193. 6.3.4.2

NEZU, I. AND NAKAGAWA, H. (1993). *Turbulence in Open-Channel FLows*, vol. 1, chap. Three-Dimensional flow structures driven by turbulence, 87–110. IAHR. 2.2.2, 2.3.3, 7, 6.3.4.3, 6.4.3.3, A.2.2

NEZU, I. AND ONITSUKA, K. (2001). Turbulent structures in partly vegetated open-channel flows with lda and piv measurements. *Journal of Hydraulic Research*, **39**, 629–642. 2.4.4, 2.4.5, 2.4.5, 4.4.5, 4.4.7

NEZU, I., TOMINAGA, A. AND NAKAGAWA, H. (1993). Field measurements of secondary currents in straight rivers. *Journal of Hydraulic Engineering*, **119**, 598–614. 6.3.4.2

PASCHE, E. AND ROUVE, M. (1985). Hydrodynamic behavior of partly vegetated open channelsoverbank flow with vegetatively roughened floodplains. *Journal of Hydraulic Engineering*, **111**, 1262–1278. 2.4.3, 4.4.5

PATEL, V.C. (1965). Calibration of the preston tube and limitations on its use on pressure gradients. *Journal of Fluid Mechanics*, **23**, 185–208. 3.3.6.1, 3.3.6.2

PATENKAR, S. AND SPALDING, D. (1972). A calculation procedure for heat mass and momentum transfer in three-dimensional parabolic flows. *International Journal of Heat and Mass Transfer*, **15**, 1787–1806. A.3.1.2

Patenkar, S. and Spalding, D. (1995). Efficiency and accuracy aspects of a full-multigrid simple algorithm for three-dimensional flows. *Numerical Heat Transfer, Part B Fundamentals*, **31**, 23–42. A.3.1.2

Pope, S.B. (2004). Ten questions concerning the large-eddy simulation of turbulent flows. *New Journal of Physics*, **6**, 1–24. 7.3.5.5

Prandtl, L. (1952). *Essentials of fluid dynamics*. Blackie, London, UK. 2.2.3

Preston, J.H. (1954). The determination of turbulent skin friction by means of pitot tubes. *Journal of the Royal Aeronautical Society*, **58**, 109–121. 3.3.6.1

Proust, S. (2005). *Ecoulements non-uniformes en lit composés: effets de variations de largeur du lit majeur, in French*. Ph.D. thesis, Cemagref. 2.7, 5.2.2.2, A.2.1, A.2.3, A.3.1.2, A.4.1

Proust, S., Bousmar, D., Rivière, N., Paquier, A. and Zech, Y. (2006). A methodology for computing non-uniform flows in compound channels. In *Proceedings of RiverFlow Conference, Lisbon, Portugal*, 405–413. 3.2.2.2, A.3.1

Purseglove, J. (1988). *Taming the Flood: History and Natural History of Rivers and Wetlands*. Oxford University Press. 1.1

Rameshwaran, P. and P., N. (2003). Three-dimensional numerical simulation of compound channel flows. *Journal of Hydraulic Engineering*, **129**, 645–652. A.5.1

Rameshwaran, P. and Shiono, K. (2003a). Computer modelling of two-stage meandering channel flows. *Proceedings of the Institution of Civil Engineers*, **156**, 325–339. 7.3.4.4, 7.3.4.4

Rameshwaran, P. and Shiono, K. (2003b). Modelling of meandering channels for overbank flow. *Proceedings of the Institution of Civil Engineers*, **156**, 225–233. 7.3.4.4

Rameshwaran, P. and Shiono, K. (2007). Quasi two-dimensional model for straight overbank flows through emergent vegetation on floodplains. *Journal of Hydraulic*

Research, **45**, 302–315. 2.4.6.1, 2.4.6.2, 2.4.6.2, 2.6, 5.2.2.2, 7.2.1.1, 7.2.1.4, 7.2.4.4, 7.3.6.3, 7.5, 8.1.3.1

Rodi, W. (1993). *Turbulence models and their application in hydraulics: a state of the art review*. IAHR Monograph Series, Taylor and Francis. A.3.1.2

Schlichting, H. and Gersten, K. (1968). *Boundary-layer Theory*. 6th Ed., McGraw-Hill, New York. 2.4.2.1, 2.4.2.2, 4.4.9.1, A.2.1

Sellin, R.H.J. (1964). A laboratory investigation into the interaction between the flow in the channel of a river and that over its flood plain. *La Houille Blanche*, **7**, 793–801. 2.3.2

Shiono, K. and Knight, D. (1991). Turbulent open channel flow with variable depth across the channel. *Journal of Fluid Mechanics*, **222**, 617–646. 2.3.3, 2.3.4, 2.3.4, 2.3.5, 2.3.6, 2.3.6, 2.4.6.2, 2.4.6.2, 4.2, 4.4.7, 4.4.7, 4.4.8, 4.4.8, 4.5, 5.2.2.2, 5.2.2.2, 5.2.2.3, 5.2.2.3, 6.4.3.3, 7.3.3.1, 7.3.5.1, 1, 7.5, 8.1.3.1

Shiono, K. and Knight, D.W. (1989). Transverse and vertical reynolds shear stress measurements in a shear layer region of a compound channel. In *Proc. 7th Int. Symp. On Turbulent Shear Flows, Stanford, U. S. A.*, 28.1.1 28.1.6. 2.3.3

Shiono, K., Ishigaki, T., Kawanaka, R. and Heatlie, F. (2009). Influence of one line vegetation on stage-discharge rating curves in compound channel. In *IAHR, Vancouver, Canada*, 459–468. 3.2.3.2, 7.2.1.1, 7.2.4, 7.4

Sime, L., Ferguson, R. and Church, M. (2007). Estimating shear stress from moving boat acoustic doppler velocity measurements in a large gravel bed river. *Water Resources Research*, **43**, 1–12. 6.2.1

Slaouti, A. and Stansby, P. (1992). Flow around two circular cylinders by the random-vortex method. *Journal of Fluids and Structures*, **6**, 641–670. 2.5.2

Smagorinsky, J. (1963). General circulation experiments with the primitive equations i: The basic experiment. *Monthly Weather Review*, **91**, 99–164. 7.3.3.4

Smits, A. (2001). *A Physical Introduction to Fluid Mechanics, second printing*. John Wiley and Sons. 2.4.2.1

Speziale, C. (1987). On linear k-l and k-e models of turblence. *Journal of Fluid Mechanics*, **178**, 459–475. A.5.1

Stoesser, T., Guillermo, P., Rodi, W. and Panayiotis, D. (2009). Large eddy simulation of turbulent flow through submerged vegetation. *Earth and Environmental Science*, **78**, 347–365. 2.4.6.3

Sun, X. (2006). *Flow characteristics in compound channels with and without vegetation*. Ph.D. thesis, Civil Engineering Deparment, Loughborough University, UK. 2.3.4, 2.4.6.3, 2.6, 2.6, 3.2.1.2, 3.2.3.1, 3.2.3.2, 4.3, 4.3, 4.4.2, 6.3.4.3, 6.4.3.3, 7.3.4.3, 7.3.5.2, 7.3.5.3

Sun, X. (2008). Modelling of velocity and boundary shear stress for one-line vegetation along the edge of floodplain compound channel. In *Advances in Hydro-science and engineering IAHR, ICHE, Nagoya, Japan*, 213–214. 2.6, 2.6, 7.2.1.1, 7.2.1.4

Sun, X. and Shiono, K. (2009). Flow resistance of one-line emergent vegetation along the floodplain edge of a compound open channel. *Advances in Water Resources*, **32**, 430–438. 2.6, 2.6, 4.3, 1, 4.4.5, 4.4.8, 4.4.9.2, 4.4.9.3, 4.4.9.3, 4.5, 5.2.2.4, 7.2.2.1, 8.1.3.1

Sutardi and Ching, C. (2001). Effect of tube diameter on preston tube calibration curves for the measurement of wall shear stress. *Experimental thermal and fluid science*, **24**, 93–97. 3.3.6.2

Tamura, H., Kiya, M. and Arie, M. (1980). Vortex shedding from a circular cylinder in moderate-reynolds-number shear flow. *Journal of Fluid Mechanics*, **141**, 721–735. 2.5.3

Terrier, B. (2010). Example of experiments carried out in Loughborough with saw dust used as seeding. Website, `http://www.youtube.com/watch?v=AKiAQxjvkyA`. 4.4.3

Terrier, B., Proust, S., Bousmar, D., Shiono, K. and Paquier, A. (2008a). Investigations on the establishmnent of uniform flow in compound channel flumes. In *Advances in Hydro-science and engineering IAHR, ICHE, Nagoya, Japan*, 211–212. A.1

Terrier, B., Shiono, K., Proust, S., Paquier, A. and Françon, S. (2008b). Flow structure in straight compound channel section of river rhône in france for overbank flow. In *River Flow 2008, Cesme, Turkey*, 1–10. 7.2.1.1

Terrier, B., Robinson, S., Shiono, K. and Paquier, A. (2010). Influence of vegetation to boundary shear stress in open channel for overbank flow. In *River Flow 2010, Braunschweig, Germany*, 1–8. 4.4.4

Thomson, J. (1878). On the flow of water in uniform regime in rivers and other open channels. *Proceedings of the Royal Society of London*, **28**, 113–127. 2.2.2

Tominaga, A. and Nezu, I. (1991). Turbulent structure in compound open-channel flows. *Journal of Hydraulic Engineering*, **117**, 21–41. 2.3.3, 2.3.3, 2.3.4, A.2.1

Tominaga, A., Nezu, I., Ezaki, K. and Nakagawa, H. (1991). Turbulent structure in compound open-channel flows. *Journal of Hydraulic Engineering*, **117**, 21–41. 2.2.3

Tsubaki, R. and Fujita, I. (2007). Large scale piv software user manual. Kobe University. 3.3.7.1

Tsujimoto, T. (1992). Spectral analysis of velocity and water surface fluctuations appearing in an open channel with vegetated and non-vegetated regions in a cross-section. In *Proceedings of the Sixth IAHR International Symposium on Stochastic Hydraulics, Taipei*, 361–368. 2.4.3

van Prooijen, B.C., Battjes, J.A. and Uijttewaal, W.S.J. (2005). Momentum exchange in straight uniform compound channel flow. *Journal of Hydraulic Engineering*, **131**, 175–181. 2.7, 4.4.7, 4.4.7, 4.4.9.4, 5.2.2.3, 5.2.2.3, 5.2.2.3, 8.1.3.1

VINCENT, K. (2005). *Investigating the causes of the decline of the urban House Sparrow Passer domesticus population in Britain*. Ph.D. thesis, De Montfort University, UK. 3.2.3.1

VYAS, K. (2007). *Multigrid Modelling of 3D Anisotropic Turbulent Flow in Compound Meandering Channels*. Ph.D. thesis, Civil Engineering Department, Loughborough University, UK. A.3.1, A.3.1.2

WANG, J. (2006). Drag reduction of a circular cylinder using an upstream rod. *Flow, Turbulence and Combustion*, **76**, 83–101. 2.5.4

WANG, Z. AND CHENG, N. (2005). Secondary flows over artificial bed strips. *Advances in Water Resources*, **28**, 441–450. 2.2.2

WHITE, B. AND NEPF, H. (2007). Shear instability and coherent structures in shallow flow adjacent to a porous layer. *Journal of Fluid Mechanics*, **593**, 1–32. 2.4.4, 7.3.5.4, 8.1.3.2

WHITE, F. (1999). *Fluid Mechanics Fourth Edition*, vol. 1, chap. 6, 335–338. McGraw-Hill Publishing International Editions. 7.2.1.4, 7.5

WILLIAMSON, C.H.K. (1992). The natural and forced formation of spot-like vortex dislocations in the transition of a wake. *Journal of Fluid Mechanics*, **243**, 393–441. 2.5.3

WILSON, C., BATES, P. AND HERVOUET, J. (2002). Comparison of turbulence models for stage-discharge rating curve prediction in reach-scale compound channel flows using two-dimensional finite element methods. *Journal of Hydrology*, **257**, 42–58. 7.3.2.1, 7.3.3.1, 7.3.3.2, 7.3.6.2

YUEN, K. (1989). *A study of boundary shear stress, flow resistance and momentum transfer in open channels with simple and compound trapezoidal cross sections*. Ph.D. thesis, University of Birmingham, UK. 2.3.4

ZDRAVKOVICH, M. (1977). Review of flow interference between two circular cylinders in various arrangements. *Journal of Fluids Engineering - Transactions of the ASME*, **99**, 618–633. 2.5.2

ZDRAVKOVICH, M. (1987). The effects of interference between circular cylinders in cross flow. *Journal of Fluids and Structures*, **1**, 239–261. 2.5.1